

# Advanced Nanomaterials for Energy-Related Applications

Guest Editors: Xiaogang Han, Quan-Hong Yang, Junyou Yang,  
Taeseup Song, Jiayu Wan, and Cristina Flox





---

# **Advanced Nanomaterials for Energy-Related Applications**

Journal of Nanomaterials

---

## **Advanced Nanomaterials for Energy-Related Applications**

Guest Editors: Xiaogang Han, Quan-Hong Yang, Junyou Yang, Taeseup Song, Jiayu Wan, and Cristina Flox



---

Copyright © 2015 Hindawi Publishing Corporation. All rights reserved.

This is a special issue published in "Journal of Nanomaterials." All articles are open access articles distributed under the Creative Commons Attribution License, which permits unrestricted use, distribution, and reproduction in any medium, provided the original work is properly cited.

## Editorial Board

Domenico Acierno, Italy  
Katerina Aifantis, USA  
Sheikh Akbar, USA  
Nageh K. Allam, USA  
Margarida Amaral, Portugal  
Martin Andersson, Sweden  
Raul Arenal, Spain  
Ilaria Armentano, Italy  
Vincenzo Baglio, Italy  
Lavinia Balan, France  
Thierry Baron, France  
Andrew R. Barron, USA  
Reza Bayati, USA  
Hongbin Bei, USA  
Daniel Bellet, France  
Stefano Bellucci, Italy  
Enrico Bergamaschi, Italy  
Samuel Bernard, France  
D. Bhattacharyya, New Zealand  
Sergio Bietti, Italy  
Giovanni Bongiovanni, Italy  
Theodorian Borca-Tasciuc, USA  
Mohamed Bououdina, Bahrain  
Torsten Brezesinski, Germany  
C. Jeffrey Brinker, USA  
Christian Brosseau, France  
Philippe Caroff, Australia  
Victor M. Castaño, Mexico  
Albano Cavaleiro, Portugal  
Bhanu P. S. Chauhan, USA  
Shafiq Chowdhury, USA  
Jin-Ho Choy, Korea  
Kwang-Leong Choy, UK  
Yu-Lun Chueh, Taiwan  
Elisabetta Comini, Italy  
Giuseppe Compagnini, Italy  
David Cornu, France  
Miguel A. Correa-Duarte, Spain  
P. Davide Cozzoli, Italy  
Shadi A. Dayeh, USA  
Luca Deseri, USA  
Yong Ding, USA  
Philippe Dubois, Belgium  
Alain Dufresne, France  
Zehra Durmus, Turkey

Joydeep Dutta, Oman  
Ali Eftekhari, USA  
Jeffrey Elam, USA  
Samy El-Shall, USA  
Ovidiu Ersen, France  
Claude Estournès, France  
Andrea Falqui, KSA  
Matteo Ferroni, Italy  
E. Johan Foster, USA  
Ilaria Fratoddi, Italy  
Wolfgang Fritzsche, Germany  
Alan Fuchs, USA  
Miguel A. Garcia, Spain  
Siddhartha Ghosh, Singapore  
P. K. Giri, India  
Russell E. Gorga, USA  
Jihua Gou, USA  
Jean M. Greneche, France  
Smrati Gupta, Germany  
Kimberly Hamad-Schifferli, USA  
Simo-Pekka Hannula, Finland  
Michael Harris, USA  
Yasuhiko Hayashi, Japan  
F. Hernandez-Ramirez, Spain  
Michael Z. Hu, USA  
Nay Ming Huang, Malaysia  
Shaoming Huang, China  
David Hui, USA  
Zafar Iqbal, USA  
B. Jeyadevan, Japan  
Xin Jiang, Germany  
Rakesh Joshi, Australia  
Jeong-won Kang, Korea  
Hassan Karimi-Maleh, Iran  
Antonios Kelarakis, UK  
Alireza Khataee, Iran  
Ali Khorsand Zak, Iran  
Philippe Knauth, France  
Ralph Krupke, Germany  
C. Kübel, Germany  
Prashant Kumar, UK  
Michele Laus, Italy  
Eric Le Bourhis, France  
Burtrand Lee, USA  
Jun Li, Singapore

Meiyong Liao, Japan  
Shijun Liao, China  
Silvia Licocchia, Italy  
Wei Lin, USA  
Jun Liu, USA  
Zainovia Lockman, Malaysia  
Nico Lovergine, Italy  
Jim Low, Australia  
Jue Lu, USA  
Songwei Lu, USA  
Ed Ma, USA  
Laura M. Maestro, Spain  
Gaurav Mago, USA  
Muhamamd A. Malik, UK  
Devanesan Mangalaraj, India  
Sanjay R. Mathur, Germany  
Tony McNally, UK  
Yogendra Mishra, Germany  
Paulo Cesar Morais, Brazil  
Paul Munroe, Australia  
Jae-Min Myoung, Korea  
Rajesh R. Naik, USA  
Albert Nasibulin, Russia  
Toshiaki Natsuki, Japan  
Koichi Niihara, Japan  
Natalia Noginova, USA  
Sherine Obare, USA  
W.-C. Oh, Republic of Korea  
Atsuto Okamoto, Japan  
Abdelwahab Omri, Canada  
Ungyu Paik, Republic of Korea  
Piersandro Pallavicini, Italy  
Edward A. Payzant, USA  
Alessandro Pegoretti, Italy  
Ton Peijs, UK  
O. Perales-Pérez, Puerto Rico  
Jorge Pérez-Juste, Spain  
Alexey P. Popov, Finland  
Philip D. Rack, USA  
Peter Reiss, France  
Orlando Rojas, USA  
Marco Rossi, Italy  
Ilker S. Bayer, Italy  
Cengiz S. Ozkan, USA  
Sudipta Seal, USA



---

Shu Seki, Japan  
V. Šepelák, Germany  
Huaiyu Shao, Japan  
Prashant Sharma, USA  
Donglu Shi, USA  
Bhanu P. Singh, India  
Surinder Singh, USA  
Vladimir Sivakov, Germany  
Ashok Sood, USA  
Adolfo Speghini, Italy  
Marinella Striccoli, Italy  
Xuping Sun, KSA  
Ashok K. Sundramoorthy, USA  
Angelo Taglietti, Italy

Bo Tan, Canada  
Leander Tapfer, Italy  
Valeri P. Tolstoy, Russia  
Muhammet S. Toprak, Sweden  
Ramon Torrecillas, Spain  
Takuya Tsuzuki, Australia  
Tamer Uyar, Turkey  
Bala Vaidhyanathan, UK  
Luca Valentini, Italy  
Rajender S. Varma, USA  
Ester Vazquez, Spain  
Antonio Villaverde, Spain  
Ajayan Vinu, Australia  
Ruibing Wang, Macau

Shiren Wang, USA  
Yong Wang, USA  
Magnus Willander, Sweden  
Ping Xiao, UK  
Zhi Li Xiao, USA  
Yangchuan Xing, USA  
Doron Yadlovker, Israel  
Yoke K. Yap, USA  
Kui Yu, Canada  
William W. Yu, USA  
Michele Zappalorto, Italy  
Renyun Zhang, Sweden

# Contents

**Advanced Nanomaterials for Energy-Related Applications**, Jiayu Wan, Taeseup Song, Cristina Flox, Junyou Yang, Quan-Hong Yang, and Xiaogang Han  
Volume 2015, Article ID 564097, 2 pages

**Classical Behavior of Alumina (Al<sub>2</sub>O<sub>3</sub>) Nanofluids in Antifrogen N with Experimental Evidence**, M. Saleemi, S. Vanapalli, N. Nikkam, M. S. Toprak, and M. Muhammed  
Volume 2015, Article ID 256479, 6 pages

**Synthesis of Renewable Energy Materials, Sodium Aluminum Hydride by Grignard Reagent of Al**, Jun-qin Wang, Jian-feng Gao, Zhi-gang Wu, Guo-li Ou, and Yu Wang  
Volume 2015, Article ID 296486, 5 pages

**Preparation and Microwave Absorbing Properties of an Electroless Ni-Co Coating on Multiwall Carbon Nanotubes Using [Ag(NH<sub>3</sub>)<sub>2</sub>]<sup>+</sup> as Activator**, Qiao-ling Li, Xiao-yong He, Yue-qing Zhang, and Xiao-feng Yang  
Volume 2015, Article ID 404698, 7 pages

**Fabrication of an Antireflective Nanodome Array with High Packing Density for Photovoltaic Applications**, Jiseok Lim, Sun-Mi Lee, Ho-Young Jang, and Seok-Min Kim  
Volume 2015, Article ID 561586, 6 pages

**Graphene-Tapered ZnO Nanorods Array as a Flexible Antireflection Layer**, Taeseup Song  
Volume 2015, Article ID 925863, 6 pages

**Synthesis and Structural Characterization of Al<sub>2</sub>O<sub>3</sub>-Coated MoS<sub>2</sub> Spheres for Photocatalysis Applications**, S. V. Prabhakar Vattikuti and Chan Byon  
Volume 2015, Article ID 978409, 9 pages

**Synthesis and Characterization of Molybdenum Disulfide Nanoflowers and Nanosheets: Nanotribology**, S. V. Prabhakar Vattikuti and Chan Byon  
Volume 2015, Article ID 710462, 11 pages

**Preparation and Application of Fluorescent Carbon Dots**, Jun Zuo, Tao Jiang, Xiaojing Zhao, Xiaohong Xiong, Saijin Xiao, and Zhiqiang Zhu  
Volume 2015, Article ID 787862, 13 pages

**A Review on Fault Mechanism and Diagnosis Approach for Li-Ion Batteries**, Chao Wu, Chunbo Zhu, Yunwang Ge, and Yongping Zhao  
Volume 2015, Article ID 631263, 9 pages

**Study of the Electroless Deposition of Ni for Betavoltaic Battery Using PN Junction without Seed Layer**, Jin Joo Kim, Young Rang Uhm, Byoung Gun Choi, and Kwang Jae Son  
Volume 2015, Article ID 283291, 5 pages

**Enhanced Photovoltaic Properties of the Solar Cells Based on Cosensitization of CdS and Hydrogenation**, Hongcai He, Kui Yang, Shuangshuang Ren, Tao Liu, and Ning Wang  
Volume 2015, Article ID 109865, 6 pages



---

**Enhancement of Electrochemical Stability about Silicon/Carbon Composite Anode Materials for Lithium Ion Batteries**, Wei Xiao, Chang Miao, Xuemin Yan, Qing Sun, and Ping Mei  
Volume 2015, Article ID 926256, 6 pages

**Cauliflower-Like  $\text{Co}_3\text{O}_4$ /Three-Dimensional Graphene Composite for High Performance Supercapacitor Applications**, Huili Liu, Xinglong Gou, Yi Wang, Xuan Du, Can Quan, and Tao Qi  
Volume 2015, Article ID 874245, 9 pages

## Editorial

# Advanced Nanomaterials for Energy-Related Applications

Jiayu Wan,<sup>1</sup> Taeseup Song,<sup>2</sup> Cristina Flox,<sup>3</sup> Junyou Yang,<sup>4</sup>  
Quan-Hong Yang,<sup>5,6</sup> and Xiaogang Han<sup>1</sup>

<sup>1</sup>Department of Materials Science and Engineering, University of Maryland, College Park, MD 20742, USA

<sup>2</sup>School of Materials Science and Engineering, Yeungnam University, Gyeongsan 712-749, Republic of Korea

<sup>3</sup>Catalonia Institute for Energy Research, Jardins de les Dones de Negre, el, Sant Adrià de Besòs, 08930 Barcelona, Spain

<sup>4</sup>State Key Laboratory of Material Processing and Die & Mould Technology, Huazhong University of Science and Technology, Wuhan 430074, China

<sup>5</sup>School of Chemical Engineering and Technology, Tianjin University, Tianjin 300072, China

<sup>6</sup>Engineering Laboratory for Functionalized Carbon Materials, Graduate School at Shenzhen, Tsinghua University, Shenzhen 518055, China

Correspondence should be addressed to Xiaogang Han; hanxg@umd.edu

Received 7 September 2015; Accepted 14 September 2015

Copyright © 2015 Jiayu Wan et al. This is an open access article distributed under the Creative Commons Attribution License, which permits unrestricted use, distribution, and reproduction in any medium, provided the original work is properly cited.

Energy has been the cornerstone of sustainable development of our economy and society. The dramatic demand on energy supply to be as unrestricted as possible, however, leads to conflicting feedback loops on the ecological environment. Thus, research is appealing worldwide to diminish the negative environmental consequences of energy consumption. This includes energy saving, generation, harvest, conversion, and storage. Nanomaterials and nanostructures provide unique mechanical, electrical, and optical properties and have played an important role in recent advances in energy-related applications.

In this special issue, we report the current progress on the preparation and the usage of nanomaterials for energy-related applications. In these aspects, we will cover a broad range of subjects from nanomaterial synthesis and characterization to energy-related demonstration and relevant technologies and device. Specifically, we focused on the synthesis of nanomaterials and their application in Li-ion batteries and optoelectronic devices.

(1) *Nanomaterials for Optoelectronic/Photochemical Devices.* World energy consumption largely relies on the combustion of fossil fuels. However, the traditional way is neither sustainable nor environmentally benign. Renewable energy generation devices, such as solar cells, thermoelectronic devices, are

widely investigated to replace fossil fuels. Nanomaterials have played an essential role in developing novel energy generation devices. The unusual quantum effect at nanoscale benefits the electron transport and band engineering in nanomaterials, which brings about an excellent performance for devices [1, 2].

In this special issue, we specifically focused on the nanomaterials/nanostructures for optoelectronic/photochemical devices. The papers “Graphene-Tapered ZnO Nanorods Array as a Flexible Antireflection Layer” and “Fabrication of an Antireflective Nanodome Array with High Packing Density for Photovoltaic Applications” reported the utilization of ZnO/graphene nanocomposite and nanodome structure as antireflection layer for solar cells, respectively. The nanofeature reduced the Fresnel reflection and increased the transmitted light through the solar cell. The paper “Enhanced Photovoltaic Properties of the Solar Cells Based on Cosensitization of CdS and Hydrogenation” reported the CdS quantum dots sensitized TiO<sub>2</sub> porous nanocrystal with enhanced photovoltaic performance. The paper “Synthesis and Structural Characterization of Al<sub>2</sub>O<sub>3</sub>-Coated MoS<sub>2</sub> Spheres for Photocatalysis Applications” reports the photocatalytic behavior of Al<sub>2</sub>O<sub>3</sub> decorated MoS<sub>2</sub> nanospheres; the enhanced performance of nanostructured Al<sub>2</sub>O<sub>3</sub>/MoS<sub>2</sub>

to bulk composite indicates it is a promising candidate for removal of pollutant from waste water.

(2) *Nanomaterials for Energy Storage.* Renewable energy storage has been ubiquitously utilized in the modernized world, such as portable electronics, electrical vehicles, and grid scale energy storage. Li-ion batteries, which obtain the highest massive/volumetric energy density among all existing technologies, have attracted most attention both in academia and industry. Still, in order to pursue Li-ion batteries with higher energy density and power density, novel materials and structures with high specific capacity and high rate performance are needed.

For example, the specific capacity for Si anode is 4200 mAh/g, 10 times larger than that of graphite (376 mAh/g). However, large amount of Li insertion in Si caused a 400% volume change, thus resulting in severe pulverization problem/unstable solid electrolyte interphase (SEI) formation during cycling for bulk Si as Li-ion battery anode. To solve this problem, Si in various nanostructures is utilized; the best performed one achieved stable cycling of more than 2000 cycles [3, 4]. The other advantage of nanomaterials for energy storage devices is that they obtain a large specific surface area. Large surface area is good for the accessibility of electrolyte, which is beneficial to the fast charge/discharge for Li-ion batteries and ultracapacitors [5].

In this special issue, we reported the exciting results of nanomaterials for energy storage applications. In the paper “Enhancement of Electrochemical Stability about Silicon/Carbon Composite Anode Materials for Lithium Ion Batteries,” W. Xiao et al. reported the Si/C composite as anode for Li-ion batteries. This composite delivers a high charge capacity of 791.7 mAh/g at a current density as high as 500 mAh/g. In the paper “Cauliflower-Like  $\text{Co}_3\text{O}_4$ /Three-Dimensional Graphene Composite for High Performance Supercapacitor Applications,” H. Liu et al. reported a 3D  $\text{Co}_3\text{O}_4$ /graphene nanocomposite. In this composite,  $\text{Co}_3\text{O}_4$  is used as active capacitor electrode and graphene is served as conductive additive and mechanical support. This composite shows an excellent specific capacity of 863 F/g in 6 M KOH at the rate of 1 mV/s.

(3) *Synthesis of Nanomaterials for Energy Applications.* Materials synthesis is the basis of nanomaterial applications in energy fields. Thus, this special issue also collected work focusing on synthesis of nanomaterials including Ni-Co-coated carbon nanotubes (“Preparation and Microwave Absorbing Properties of an Electroless Ni-Co Coating on Multiwall Carbon Nanotubes Using  $[\text{Ag}(\text{NH}_3)_2]^+$  as Activator”), carbon dots (“Preparation and Application of Fluorescent Carbon Dots”),  $\text{MoS}_2$  nanoflowers and nanosheets (“Synthesis and Characterization of Molybdenum Disulfide Nanoflowers and Nanosheets: Nanotribology”), sodium aluminum hydride (“Synthesis of Renewable Energy Materials, Sodium Aluminum Hydride by Grignard Reagent of Al”), and nanocomposite of  $\text{Al}_2\text{O}_3$ /Antifrogen N (“Classical Behavior of Alumina ( $\text{Al}_2\text{O}_3$ ) Nanofluids in Antifrogen N with Experimental Evidence”). All these materials were demonstrated for various energy applications such as

microwave adsorption (“Preparation and Microwave Absorbing Properties of an Electroless Ni-Co Coating on Multiwall Carbon Nanotubes Using  $[\text{Ag}(\text{NH}_3)_2]^+$  as Activator”), heat transfer (“Classical Behavior of Alumina ( $\text{Al}_2\text{O}_3$ ) Nanofluids in Antifrogen N with Experimental Evidence”), lubrication (“Synthesis and Characterization of Molybdenum Disulfide Nanoflowers and Nanosheets: Nanotribology”), and photocatalysis (“Classical Behavior of Alumina ( $\text{Al}_2\text{O}_3$ ) Nanofluids in Antifrogen N with Experimental Evidence”). The synthesis methods involved electroless deposition (“Preparation and Microwave Absorbing Properties of an Electroless Ni-Co Coating on Multiwall Carbon Nanotubes Using  $[\text{Ag}(\text{NH}_3)_2]^+$  as Activator”), solvothermal reaction (“Synthesis and Characterization of Molybdenum Disulfide Nanoflowers and Nanosheets: Nanotribology”), and traditional solid chemical reaction (“Synthesis of Renewable Energy Materials, Sodium Aluminum Hydride by Grignard Reagent of Al”).

Jiayu Wan  
Taeseup Song  
Cristina Flox  
Junyou Yang  
Quan-Hong Yang  
Xiaogang Han

## References

- [1] M. Law, L. E. Greene, J. C. Johnson, R. Saykally, and P. Yang, “Nanowire dye-sensitized solar cells,” *Nature Materials*, vol. 4, no. 6, pp. 455–459, 2005.
- [2] W. Bao, J. Wan, X. Han et al., “Approaching the limits of transparency and conductivity in graphitic materials through lithium intercalation,” *Nature Communications*, vol. 5, article 4224, 2014.
- [3] H. Wu, G. Chan, J. W. Choi et al., “Stable cycling of double-walled silicon nanotube battery anodes through solid-electrolyte interphase control,” *Nature Nanotechnology*, vol. 7, no. 5, pp. 310–315, 2012.
- [4] J. Wan, A. F. Kaplan, J. Zheng et al., “Two dimensional silicon nanowalls for lithium ion batteries,” *Journal of Materials Chemistry A*, vol. 2, no. 17, pp. 6051–6057, 2014.
- [5] P. Simon and Y. Gogotsi, “Materials for electrochemical capacitors,” *Nature Materials*, vol. 7, no. 11, pp. 845–854, 2008.

## Research Article

# Classical Behavior of Alumina ( $\text{Al}_2\text{O}_3$ ) Nanofluids in Antifrogen N with Experimental Evidence

M. Saleemi,<sup>1,2</sup> S. Vanapalli,<sup>3</sup> N. Nikkam,<sup>1</sup> M. S. Toprak,<sup>1</sup> and M. Muhammed<sup>1</sup>

<sup>1</sup>Department of Materials and Nano Physics, KTH Royal Institute of Technology, 16440 Kista Stockholm, Sweden

<sup>2</sup>Department of Materials and Environmental Chemistry, Stockholm University, 106 91 Stockholm, Sweden

<sup>3</sup>Faculty of Science & Technology, University of Twente, 7500 AE Enschede Twente, Netherlands

Correspondence should be addressed to M. Saleemi; mohsins@kth.se and S. Vanapalli; s.vanapalli@utwente.nl

Received 13 February 2015; Revised 19 May 2015; Accepted 22 June 2015

Academic Editor: Cristina Flox

Copyright © 2015 M. Saleemi et al. This is an open access article distributed under the Creative Commons Attribution License, which permits unrestricted use, distribution, and reproduction in any medium, provided the original work is properly cited.

A nanofluid is a suspension containing nanoparticles in conventional heat transfer fluids. This paper reports on an investigation of alumina ( $\text{Al}_2\text{O}_3$ ) nanoparticles in Antifrogen N, also called AFN, which is a popular antifreeze coolant consisting primarily of ethylene glycol and other additives to impede corrosion. The base carrier fluid is 50% by weight of water and 50% by weight of AFN. We systematically measured the nanomaterials and heat transfer data of nanofluids for four different size particles, namely, 20, 40, 150, and 250 nm alumina particles. The pH of all the nanofluids is adjusted to have a stable dispersion. The material characterizations include SEM and DLS particle measurements. We measured thermal conductivity, viscosity, and heat transfer coefficient in developing flow of the nanofluids. We observed that these nanofluids behave as any other classical fluids in thermally developing flow and classical heat transfer correlations can be used to completely describe the characteristics of these nanofluids.

## 1. Introduction

Heat transfer fluids with enhanced cooling characteristics is a subject of active research in several laboratories [1]. Nanofluid is the dispersion of nanoparticles in conventional coolants [2, 3]. Numerous studies performed in our lab and elsewhere studied nanofluids prepared with coolants, such as water and ethylene glycol (EG) [4–10]. EG based nanofluids have a distinct advantage in cooling applications compared to water based coolant due to the possibility of operating these fluids down to  $-80^\circ\text{C}$  [11, 12]. Antifrogen N (AFN) is a commercial coolant, which is a clear liquid with tinted pale yellow color and consists of monoethylene glycol as base component. Furthermore, AFN contains effective corrosion inhibitors and prevents scaling in commonly used metal surfaces in heat transfer equipment. It is used as a heat transfer medium for several applications, such as closed hot water heating systems and heat pumps and is widely used as cooling brine in industrial refrigeration equipment. AFN is a good freeze resistant coolant similar to EG. A mixture of AFN with water (minimum 20% by volume) can be used in a temperature

range of  $+150^\circ\text{C}$  to  $-50^\circ\text{C}$ . AFN is a commercial product of Clarinet and all the details were obtained from the published materials data sheet [13].

Alumina ( $\text{Al}_2\text{O}_3$ ) nanoparticles are a preferred choice in preparing nanofluids due to the maturity of production on a large scale and lower cost and are environmentally friendly. Therefore, alumina based nanofluids are investigated extensively in many laboratories and are identified as one of the best candidates for a nanofluid based coolant [14]. Water based  $\text{Al}_2\text{O}_3$  nanofluids are reported to show improved thermal performance (ranging from 2 to 10%) with a particle size of 40 nm [15, 16]. However, the conclusions in the literature seem not to agree with ethylene glycol as a base fluid. Timofeeva and coworkers [17] investigated different morphologies of  $\text{Al}_2\text{O}_3$  nanoparticles in water-EG mixture as base fluid. They report a 15% increase in thermal conductivity with platelet  $\text{Al}_2\text{O}_3$  nanoparticles (7% volume of solid content). The enhancement of thermal conductivity reduced to 3% when the alumina content is reduced to 1%. Maïga et al. showed reported heat transfer coefficient increase to 70% in a 7.5% volume of particles (roughly 22% by weight)

[18]. Similarly, Murshed et al. reported that 80 nm size  $\text{Al}_2\text{O}_3$  nanoparticles dispersed in EG increased by only 3.5% and 6% in effective thermal conductivity for 0.5 vol % and 1 vol %, respectively [19]. Few other literatures presented comparable results that larger particle size in the EG based  $\text{Al}_2\text{O}_3$  nanofluids gives more enhancement in thermal conductivity [20, 21].

Beck and coworkers [20–23] examined, theoretically and experimentally, the effect of particle size in water, EG, and water-EG mixtures. Their experimental results, measured at 25°C for 2 vol % and 3 vol % of 16 nm  $\text{Al}_2\text{O}_3$  particles dispersed in ethylene glycol, showed thermal conductivity enhancement of 6% and 9%, respectively, whereas particles of 245 nm size with the same particle concentrations (2 vol % and 3 vol %) achieved 8% and 14% improvement in thermal performance [24]. Their second study for water EG mixture (50-50 vol %) based nanofluids have showed similar behavior; as the particle size increases from 10 to 50 nm, the thermal conductivity increases with higher solid content. For instance, 3 vol %  $\text{Al}_2\text{O}_3$  particles with 10 and 50 nm in water EG mixture enhances the thermal conductivity ratio to 5% and 7% measured at room temperature [22, 23]. However, these investigations are not conclusive about the optimum particle size of a EG based nanofluid. Moreover, we have not found any published literature on an AFN based nanofluid, although this is the most commonly used coolant in the heat equipment industry.

The aim of this paper is to perform a systematic study of the influence of alumina nanoparticle size on the thermal performance of the nanofluid made with water and AFN mixture. Four different sizes of commercially available  $\text{Al}_2\text{O}_3$  nanoparticles, namely, 20 nm (Disp-Al20), 40 nm (Disp-Al40), 150 nm (Disp-Al150), and 250 nm (Disp-Al250) particles, are selected for this study. To the best of our knowledge this is the first report of nanofluids prepared with water and AFN mixture as a base fluid. Thermal conductivity, viscosity, and forced convective heat transfer measurements were performed on these nanofluids.

## 2. Description of Experiments

The alumina ( $\text{Al}_2\text{O}_3$ ) nanoparticles (Disp-Al20, Disp-Al40, Disp-Al150, and Disp-Al250) are procured from NanoPhase Nanoengineered Products, Romeville, IL, USA. Nanofluids are prepared by dispersing 9 weight % quantity of alumina nanoparticles into the base fluid (water-AFN 50/50 wt%). These mixtures were subjected to mechanical shaker for thirty minutes without any additives or surfactant and the pH of the solution is adjusted to a value of 8, to provide electrostatic dispersion strength for nanoparticles and to avoid agglomeration of the particles. The produced nanofluids remained stable for several hours on the shelf and no sedimentation has been observed during the flow measurements.

The thermal conductivity of the base fluid and the nanofluids are measured using a thermal property analyser based on hot wire method, KD2 Pro (Decagon Devices Inc.). A sample holder whose temperature is controlled with a thermal bath is used to improve the accuracy of the measurements. Each data point is acquired in an interval

of 15 minutes. An average of at least 50 measurement points is taken for each fluid. The relative viscosity of the nanofluids is measured using a rotational type viscometer. Forced convective heat transfer experiments are performed with the base fluid and the nanofluids. The heating section is a circular tube of nominal inner diameter of 4 mm and a length of 0.45 m. The inlet and outlet fluid temperature and the wall temperatures are measured (at regular intervals of 0.05 m) with thermocouples. The mass flow rate of the fluid pumped into the heated tube is also measured. The experimental setup details are described in this reference [25].

## 3. Results and Discussion

**3.1. Physicochemical Characterizations.** The morphology and particle size are characterized with a scanning electron microscopy (SEM), Zeiss Ultra 55. Figures 1(a)–1(d) show SEM micrographs of the four alumina powders (Disp-Al20, Disp-Al40, Disp-Al150, and Disp-Al250). The average particle size was measured with image J software using more than three hundred particles. The results are shown in Table 1. Figure 1(a) reveals spherical morphology of Disp-Al20 sample with an average particle size of  $22 \text{ nm} \pm 12 \text{ nm}$ . Few particles of the size in the range of 60 to 80 nm are also observed. Disp-Al40 sample also contains spherical particles with an average size of  $52 \text{ nm} \pm 10 \text{ nm}$  as shown in Figure 1(b). However, the SEM micrographs of Figures 1(c) and 1(d) reveal irregular morphology and a wide distribution of primary particle size. It is important to note that SEM particle size analysis shows slight differences in particle size and morphology compared to the supplier quoted data.

Hydrodynamic (DLS) particle size is determined with Beckman Coulter Delsa NanoC setup. Figure 2 presents DLS particle size with the intensity distribution curves. DLS particle sizes for Disp-Al20 and Disp-Al40 nanofluids have shown narrow distribution over the range of 10 to 60 nm and 30 to 90 nm, respectively. DLS particle size is slightly bigger than the primary particle size and this increment is due to the interaction of solid and liquid content. DLS curves of Disp-Al150 and Disp-Al250 samples have shown wide distribution of particles, which correspond with the variance in size and the irregular morphology, as observed in SEM micrographs. Morphology, primary particle size, and average DLS size results are summarized in Table 1.

**3.2. Thermophysical Properties.** Figure 3 shows the ratio of thermal conductivity (TC) and viscosity of the four nanofluids to the base fluid of Antifrogen N and water mixture. Disp-Al20  $\text{Al}_2\text{O}_3$  nanofluid has the lowest increase in TC, about 3% with a large viscosity increase, 90% compared to the base fluid. TC enhancement in Disp-Al40  $\text{Al}_2\text{O}_3$  nanofluid is 6% while the viscosity increased to 50%. The viscosity of the nanofluids decreased with the increase in particle size. The thermal conductivity of Disp-Al150 nanofluid is the highest among all the measured nanofluids, about 11%. The thermal conductivity of Disp-Al250 actually decreases compared to Disp-Al150, which is due to the sedimentation of large particles. The measured values of thermal conductivity and viscosity are shown in Table 2.

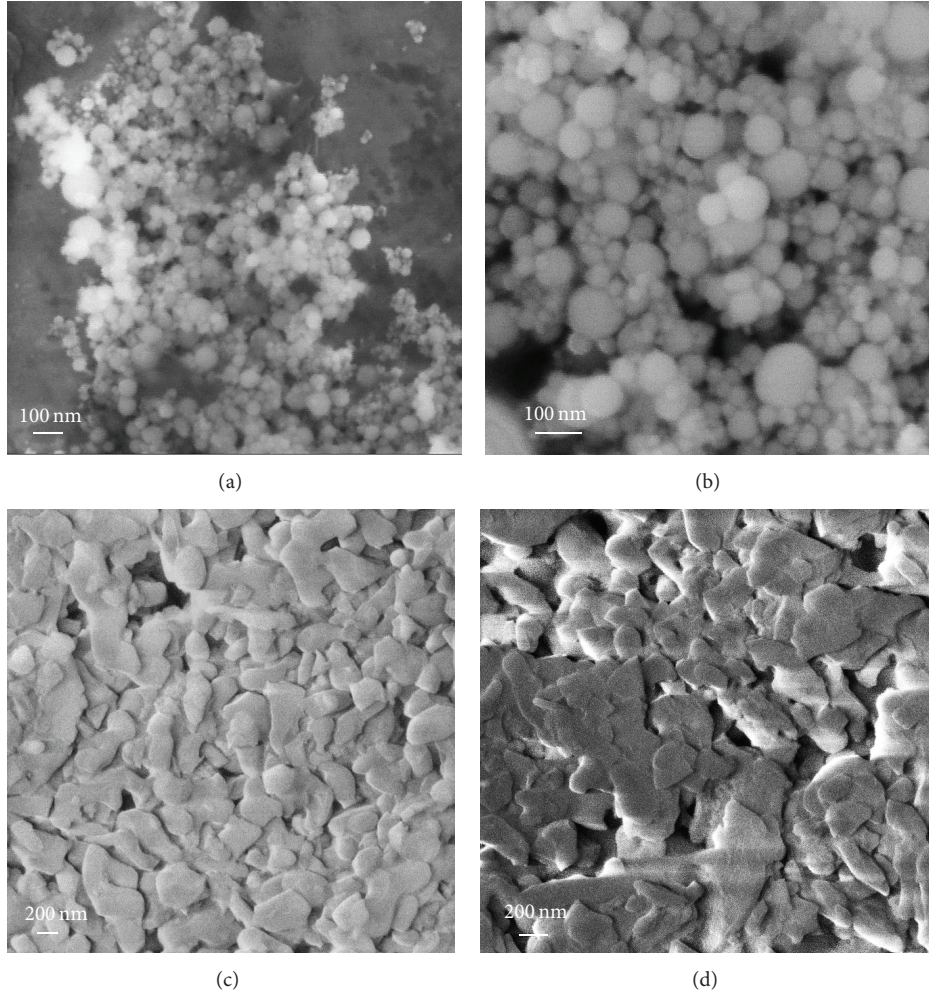


FIGURE 1: SEM micrographs of (a) Disp-Al20, (b) Disp-Al40, (c) Disp-Al150, and (d) Disp-Al250 samples.

TABLE 1: Material properties of  $\text{Al}_2\text{O}_3$  nanofluids.

Sample ID	Size (supplier)	SEM average particle Size	Morphology	DLS average particle Size
Disp-Al20	20 nm	$22 \pm 10$ nm	Spherical	25 nm
Disp-Al40	40 nm	$52 \pm 10$ nm	Spherical	50 nm
Disp-Al150	150 nm	$165 \pm 20$ nm	Irregular	170 nm
Disp-Al250	250 nm	$275 \pm 25$ nm	Irregular	285 nm

The effective specific heat capacity of the mixture is calculated based on the basic principle of the mixture rule as

$$c_{p,\text{mix}} = xc_{p,\text{particle}} + (1-x)c_{p,\text{fluid}}. \quad (1)$$

$c_{p,\text{particle}}$  and  $c_{p,\text{fluid}}$  are obtained from manufacturer specifications. The calculated specific heat capacity of the nanofluids is shown in Table 2. The specific heat capacity of the nanofluids is lower than the base fluid by about 7%.

**3.3. Flow Experiments.** Efficient heat transfer in the laminar flow occurs in the thermal entrance region. The objective of these flow experiments is to answer the question: Does the

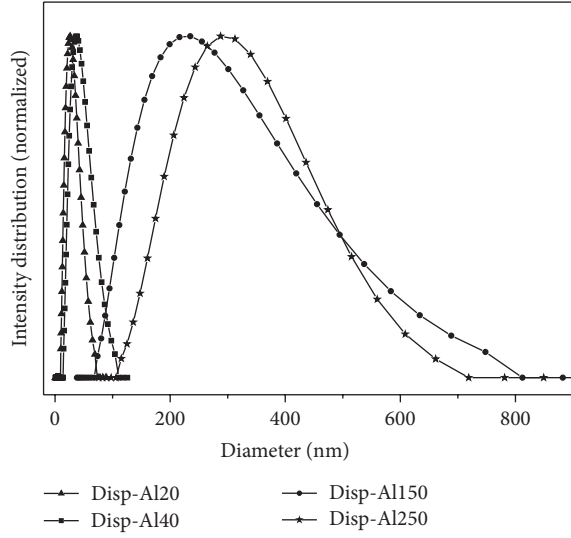
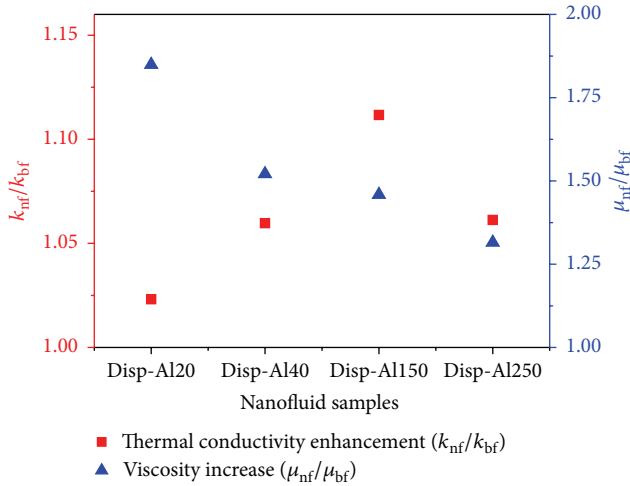
addition of nanoparticles to a coolant alter the classical thermal behavior in a thermally developing flow? A correlation for the Nusselt number,  $\text{Nu}$  for laminar flow heat transfer in the thermal entrance regions, was provided by Incropera and DeWitt [26]:

$$\text{Nu} = 1.86 \left( \frac{\text{RePr}}{L/D} \right)^{1/3} \left( \frac{\mu}{\mu_0} \right)^{0.14}. \quad (2)$$

Flow experiments are performed in a test rig, the details of which are described in another publication of the author [25]. The length of the heated test section is 0.45 m and the inner diameter of the tube is 4 mm. The length of the entry region,  $L_{\text{entrance}}$ , before a temperature profile is fully established in the

TABLE 2: Thermophysical properties of the base fluid and nanofluids.

Properties	AFN/water	Disp-Al20	Disp-Al40	Disp-Al150	Disp-Al 250
Specific heat $C_p$ (J/kgK)	3250	3037	3037	3037	3037
Viscosity $\mu$ (mPa·s)	4.513	8.345	6.864	6.583	5.936
Thermal conductivity $k$ (W/m·K)	0.3887	0.3977	0.4119	0.4321	0.4125

FIGURE 2: DLS curves from  $\text{Al}_2\text{O}_3$  nanofluid samples.FIGURE 3: Effect of particle size on thermal conductivity and viscosity of  $\text{Al}_2\text{O}_3$  based NFs.

presence of a fully developed hydrodynamic boundary layer is

$$L_{\text{entrance}} = 0.05 \cdot D \cdot \text{Re} \cdot \text{Pr}. \quad (3)$$

The Reynolds number range of the tests is between 100 and 500 and the Prandtl number is between 37 and 43. Putting these figures into the above equation produces the limits for  $L_{\text{entrance}}$  between 0.74 and 4.3 m. As the length of the heated section in the test rig is 0.45 m it can be concluded that

the temperature profile is not fully developed in the test rig. This can be further checked by examining the temperature difference between the wall and the fluid. In the case of constant heat flux heat transfer the temperature difference between the tube wall and the fluid is constant when the temperature profile is fully developed. The measured temperature differences indeed do not stabilize along the length of the heated section.

Further analysis of the measurement data is based on the approach often used by heat exchanger designers to plot the data in a standard form, that is, of  $\text{Log}_{10}(\text{Stanton Prandtl})^{2/3}$  against  $\text{Log}_{10}(\text{Reynolds number})$ . This has been done for the base fluid of Antifrogen N and for the four nanofluids tested. Figure 4(a) shows the data containing 50 points for the entire test results. The Antifrogen N and water base fluid results fall to the right of the graph as they have the highest Reynolds number due to a low viscosity. It is interesting to note that all the points for the four nanofluids and the base fluid fall on a single line indicating that it is the base fluid that is controlling the heat transfer. Any anticipated change in the heat transfer performance of the nanofluids due to a modification of the temperature profile, leading to a nonclassical behavior, is not apparent from this graph. The nanofluids are behaving as any classical fluid in the thermally developing flow. The equation of the line in Figure 4(b) can be expressed as

$$\text{Log StPr}^{2/3} = -0.6862 \text{Log Re} - 0.6761. \quad (4)$$

Substituting the definition of Stanton number into the above equation and using the value of  $D = 0.004$  m and  $L = 0.45$  m give a relation between Nu and Re:

$$\text{Nu} = 1.02 \text{Re}^{0.314} \left( \frac{\text{Pr}}{L/D} \right)^{1/3}. \quad (5)$$

This relation compares well to the Seider Tate equation for thermally developing flow given in (2). Therefore the experimental results confirm a classical relationship between Nusselt number and Reynolds number for nanofluids. The Nusselt number is plotted in Figure 4(b).

## 4. Conclusion

The following conclusions can be drawn from the systematic analysis of alumina nanofluids comprising Antifrogen N and water mixture as a basefluid.

- (i) The thermal conductivity enhancement decreases as the particle size decreases below about 170 nm. This finding is consistent with a decrease in the thermal conductivity of alumina nanoparticles with decreasing particle size, which can be attributed to phonon

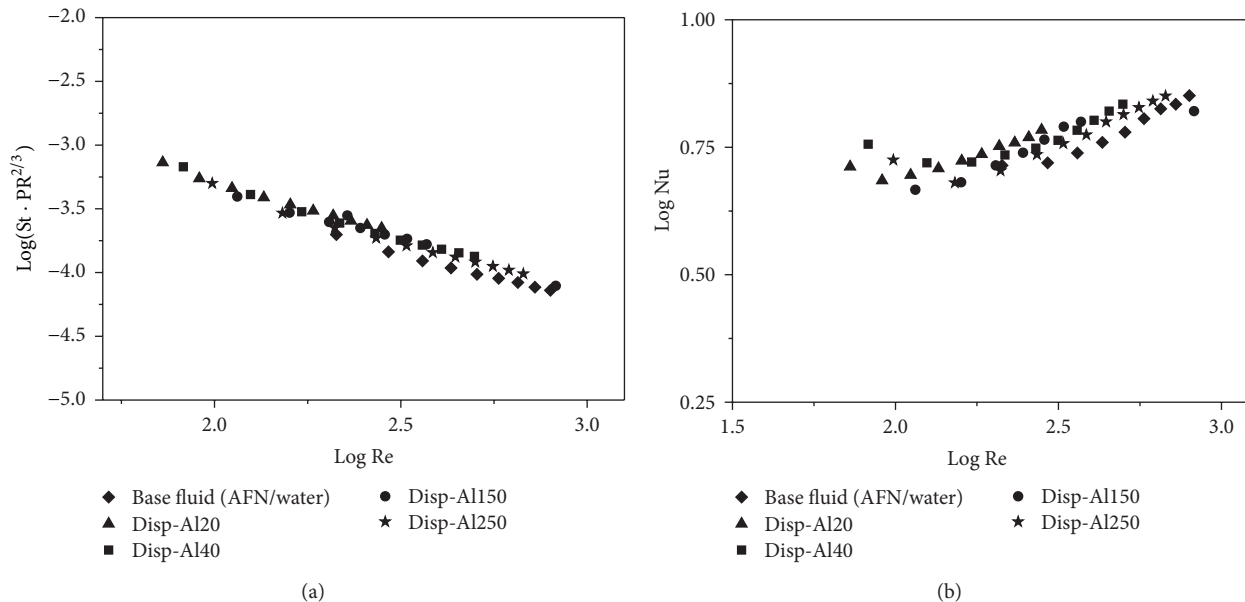


FIGURE 4: Classical behavior of  $\text{Al}_2\text{O}_3$  nanofluid; (a) Reynolds versus Nusselt number, (b) Reynolds versus Prandtl number.

scattering at the solid-liquid interface. Nanofluids with 285 nm size nanoparticles also show lower thermal conductivity enhancement, which could be attributed to the sedimentation of nanoparticles. Hence, there exists an optimum size of the nanoparticles for enhancement of thermal conductivity.

- (ii) The viscosity of nanofluids decreases with increasing particle size.
- (iii) Flow experiments in a developing flow show that the alumina nanofluids behave as a classical fluid. Any anticipated improvement in the heat transfer performance due to change in temperature profile in the developing flow is not observed in our experiments.

## Notation

- $A$ : Area ( $\text{m}^2$ )  
 $v$ : Velocity ( $\text{m/s}$ )  
 $c_p$ : Specific heat at constant pressure ( $\text{J/kg}\cdot\text{K}$ )  
 $D$ : Diameter ( $\text{m}$ )  
 $h$ : Heat transfer coefficient ( $\text{W/m}^2\cdot\text{K}$ )  
 $k$ : Thermal conductivity ( $\text{W/m}\cdot\text{K}$ )  
 $L$ : Length ( $\text{m}$ )  
 $m$ : Mass flow rate ( $\text{kg/s}$ )  
 $\text{Nu}$ : Nusselt number,  $hD/k$  (—)  
 $\text{Pr}$ : Prandtl number,  $c_p\mu/k$  (—)  
 $Q$ : Heat transfer rate ( $\text{J/s}$ ,  $\text{W}$ )  
 $\text{Re}$ : Reynolds number,  $\rho vD/\mu = m \cdot D/A \cdot \mu$  (—)  
 $\text{St}$ : Stanton number,  $\text{Nu}/\text{Re}\cdot\text{Pr}$  (—)  
 $T$ : Temperature ( $\text{K}$ )  
 $\rho$ : Density ( $\text{kg/m}^3$ )  
 $\mu$ : Viscosity ( $\text{Pa}\cdot\text{s}$ )  
 $x$ : Mass fraction of nanoparticles (—).

## Conflict of Interests

The authors declare that there is no conflict of interests regarding the publication of this paper.

## Acknowledgments

The financial support from the EC-FP7 frame work Project, NanoHex (Grant Agreement no. 2228882), and Swedish research Council for project VR-NanoHex (Enhanced Nanofluid Heat Exchange) is gratefully acknowledged.

## References

- [1] S. K. Das and S. U. S. Choi, "A review of heat transfer in nanofluids," *Advances in Heat Transfer*, vol. 41, pp. 81–197, 2009.
- [2] M. N. M. Zubir, A. Badarudin, S. N. Kazi et al., "Experimental investigation on the use of reduced graphene oxide and its hybrid complexes in improving closed conduit turbulent forced convective heat transfer," *Experimental Thermal and Fluid Science*, vol. 66, pp. 290–303, 2015.
- [3] E. Sadeghinezhad, H. Togun, M. Mehrali et al., "An experimental and numerical investigation of heat transfer enhancement for graphene nanoplatelets nanofluids in turbulent flow conditions," *International Journal of Heat and Mass Transfer*, vol. 81, pp. 41–51, 2015.
- [4] G. Paul, T. Pal, and I. Manna, "Thermo-physical property measurement of nano-gold dispersed water based nanofluids prepared by chemical precipitation technique," *Journal of Colloid and Interface Science*, vol. 349, no. 1, pp. 434–437, 2010.
- [5] J. A. Eastman, S. U. S. Choi, S. Li, W. Yu, and L. J. Thompson, "Anomalous increased effective thermal conductivities of ethylene glycol-based nanofluids containing copper nanoparticles," *Applied Physics Letters*, vol. 78, no. 6, pp. 718–720, 2001.
- [6] S. U. S. Choi, Z. G. Zhang, W. Yu, F. E. Lockwood, and E. A. Grulke, "Anomalous thermal conductivity enhancement in

- nanotube suspensions,” *Applied Physics Letters*, vol. 79, no. 14, pp. 2252–2254, 2001.
- [7] P. Keblinski, S. R. Phillpot, S. U. S. Choi, and J. A. Eastman, “Mechanisms of heat flow in suspensions of nano-sized particles (nanofluids),” *International Journal of Heat and Mass Transfer*, vol. 45, no. 4, pp. 855–863, 2001.
- [8] N. Nikkam, M. Ghanbarpour, M. Saleemi, M. S. Toprak, M. Muhammed, and R. Khodabandeh, “Thermal and rheological properties of micro- and nanofluids of copper in diethylene glycol—as heat exchange liquid,” *MRS Proceedings*, vol. 1543, pp. 165–170, 2013.
- [9] N. Nikkam, M. Saleemi, E. B. Haghighi et al., “Fabrication, characterization and thermo-physical property evaluation of SiC nanofluids for heat transfer applications,” *Nano-Micro Letters*, vol. 6, no. 2, pp. 178–189, 2014.
- [10] N. Nikkam, E. B. Haghighi, M. Saleemi et al., “Experimental study on preparation and base liquid effect on thermo-physical and heat transport characteristics of  $\alpha$ -SiC nanofluids,” *International Communications in Heat and Mass Transfer*, vol. 55, pp. 38–44, 2014.
- [11] N. Nikkam, M. Ghanbarpour, M. Saleemi et al., “Experimental investigation on thermo-physical properties of copper/diethylene glycol nanofluids fabricated via microwave-assisted route,” *Applied Thermal Engineering*, vol. 65, no. 1-2, pp. 158–165, 2014.
- [12] E. B. Haghighi, N. Nikkam, M. Saleemi et al., “Shelf stability of nanofluids and its effect on thermal conductivity and viscosity,” *Measurement Science and Technology*, vol. 24, no. 10, Article ID 105301, 2013.
- [13] P. Maschines, “Heat Transfer Fluids,” 49, pp. 1–21, 2013.
- [14] V. Sridhara and L. N. Satapathy, “Al<sub>2</sub>O<sub>3</sub>-based nanofluids: a review,” *Nanoscale Research Letters*, vol. 6, article 456, 2011.
- [15] E. B. Haghighi, M. Saleemi, N. Nikkam et al., “Cooling performance of nanofluids in a small diameter tube,” *Experimental Thermal and Fluid Science*, vol. 49, pp. 114–122, 2013.
- [16] B. Sahin, G. G. Gültekin, E. Manay, and S. Karagoz, “Experimental investigation of heat transfer and pressure drop characteristics of Al<sub>2</sub>O<sub>3</sub>-water nanofluid,” *Experimental Thermal and Fluid Science*, vol. 50, pp. 21–28, 2013.
- [17] E. V. Timofeeva, J. L. Routbort, and D. Singh, “Particle shape effects on thermophysical properties of alumina nanofluids,” *Journal of Applied Physics*, vol. 106, no. 1, Article ID 014304, 2009.
- [18] S. E. B. Maïga, C. T. Nguyen, N. Galanis, and G. Roy, *Hydrodynamic and Thermal Behaviours of a Nanofluid in a Uniformly Heated Tube*, Computational Studies, WIT Press, 2004.
- [19] S. M. S. Murshed, K. C. Leong, and C. Yang, “Investigations of thermal conductivity and viscosity of nanofluids,” *International Journal of Thermal Sciences*, vol. 47, no. 5, pp. 560–568, 2008.
- [20] H. Xie, J. Wang, T. Xi, Y. Liu, F. Ai, and Q. Wu, “Thermal conductivity enhancement of suspensions containing nanosized alumina particles,” *Journal of Applied Physics*, vol. 91, no. 7, pp. 4568–4572, 2002.
- [21] B. LotfizadehDehkordi, S. N. Kazi, M. Hamdi, A. Ghadimi, E. Sadeghinezhad, and H. S. C. Metselaar, “Investigation of viscosity and thermal conductivity of alumina nanofluids with addition of SDBS,” *Heat and Mass Transfer*, vol. 49, no. 8, pp. 1109–1115, 2013.
- [22] M. P. Beck, Y. Yuan, P. Warrier, and A. S. Teja, “The effect of particle size on the thermal conductivity of alumina nanofluids,” *Journal of Nanoparticle Research*, vol. 11, no. 5, pp. 1129–1136, 2009.
- [23] M. P. Beck, Y. Yuan, P. Warrier, and A. S. Teja, “The thermal conductivity of alumina nanofluids in water, ethylene glycol, and ethylene glycol + water mixtures,” *Journal of Nanoparticle Research*, vol. 12, no. 4, pp. 1469–1477, 2010.
- [24] M. P. Beck, T. Sun, and A. S. Teja, “The thermal conductivity of alumina nanoparticles dispersed in ethylene glycol,” *Fluid Phase Equilibria*, vol. 260, no. 2, pp. 275–278, 2007.
- [25] S. Vanapalli and H. J. M. T. Brake, “Assessment of thermal conductivity, viscosity and specific heat of nanofluids in single phase laminar internal forced convection,” *International Journal of Heat and Mass Transfer*, vol. 64, pp. 689–693, 2013.
- [26] F. P. Incropera and D. P. DeWitt, *Fundamentals of Heat and Mass Transfer*, Wiley, 2000.

## Research Article

# Synthesis of Renewable Energy Materials, Sodium Aluminum Hydride by Grignard Reagent of Al

Jun-qin Wang, Jian-feng Gao, Zhi-gang Wu, Guo-li Ou, and Yu Wang

School of Science, North University of China, Taiyuan 030051, China

Correspondence should be addressed to Jian-feng Gao; [jianfenggao@163.com](mailto:jianfenggao@163.com)

Received 19 May 2015; Accepted 12 July 2015

Academic Editor: Xiaogang Han

Copyright © 2015 Jun-qin Wang et al. This is an open access article distributed under the Creative Commons Attribution License, which permits unrestricted use, distribution, and reproduction in any medium, provided the original work is properly cited.

The research on hydrogen generation and application has attracted widespread attention around the world. This paper is to demonstrate that sodium aluminum hydride can be synthesized under simple and mild reaction condition. Being activated through organics, aluminum powder reacts with hydrogen and sodium hydride to produce sodium aluminum hydride under atmospheric pressure. The properties and composition of the sample were characterized by FTIR, XRD, SEM, and so forth. The results showed that the product through this synthesis method is sodium aluminum hydride, and it has higher purity, perfect crystal character, better stability, and good hydrogen storage property. The reaction mechanism is also discussed in detail.

## 1. Introduction

Hydrogen is considered as one of the most important energy carriers for future energy vectors because of the higher energy storage density, environmental friendliness, and broadened sources [1]. Complex metal hydride composites in the form of  $ABH_4$ , where A is an alkali metal and B is a group III element, have been widely studied in solution as proton acceptors to enhance  $H_2$  adsorption abilities.  $NaAlH_4$  is different from any other metal hydrides and borohydrides with similar structures since it is capable of reversibly storing  $H_2$  after doping with transition metals (e.g., Ti, Fe, or Zr) [2, 3].  $NaAlH_4$  is one of the most useful solid hydrogen storage materials [4]. It could be produced by many methods such as liquid-phase synthesis method [5, 6], solid-phase synthesis method [7], and milling synthesis [8]. However, all these synthesis methods have some disadvantages [4, 9], like lower yield rate, higher consumption of raw material, higher temperature and higher pressure, and so forth [10], which make them difficult for industrial production.

This paper will describe a simple and efficient method to synthesize sodium aluminum hydride under moderate condition. The synthesis could be split into two steps. First, aluminum powder is activated by organics to produce activated aluminum. Secondly, the activated aluminum reacts

with hydrogen and sodium hydride to produce final product [11]. The raw material for this synthesis method is easy to get, and the utilization of the raw material and yield rate are really high. All these features of the synthesis demonstrate that this method is promising for the industrialization of sodium aluminum hydride [12, 13]. It is established that hydrogen storage material sodium alanate can be obtained from low cost starting materials [4].

## 2. Experimental

**2.1. Reagents and Materials.** Aluminum powder (granularity, 200, purchased from Beijing Chemical Reagent Factory) was dried in a vacuum oven. Anhydrous aluminum chloride (purchased from Tianjin Chemical Reagent Factory) and iodine (purchased from Zhengzhou Chemical Reagent Factory) were sealed and stored in a dark environment as the initiator. In addition, commercial NaH (purity 60%, purchased from Aladdin) was stored under  $N_2$  atmosphere to prevent oxygen/moisture exposure. Toluene and tetrahydrofuran (THF) (AR, purchased from Tianli Chemical Reagent Co. Ltd.) were distilled over sodium metal under  $N_2$  atmosphere to remove water.  $H_2$  (purity 99.999%, purchased from Taiyuan Industrial Gases Factory) was removed moisture through a scrubber, as the purpose of a protective and reaction

gas. Several freeze-pump-thaw cycles were performed for halogenated hydrocarbons (AR, purchased from Tianjin Chemical Reagent Factory) to remove trace amounts of  $O_2$  and water.

**2.2. Synthesis Method.** All reactions were carried out under anhydrous and oxygen-free environment (hydrogen circumstance). Since there are some impurities in aluminum powder and NaH surface wrapping in mineral oil, their dosage should be slightly more than the theoretical value. Aluminum powder 2 g, exact amounts of anhydrous aluminum chloride and iodine, and freshly sealed halogenated hydrocarbons 8 mL were added to a 250 mL of three-neck flask after replacement repeatedly with  $H_2$ . The mixture was heated to  $40^\circ C$  and refluxed in hydrogen stream with stirring. About 25 minutes later, the reaction has been initiated; as a result, aluminum powder is activated to form an organic aluminum reagent intermediates and active aluminum.

One hour later, 3.5 g NaH and 30 mL of toluene (as the dispersant) were put into the flask. The mixture was heated to  $85^\circ C$  and refluxed with stirring for 6 h before it was cooled down to room temperature. After separation and crystallization, the gray powder was dried in vacuo at  $60^\circ C$  for 12 h.

The gray solid was dissolved in a mixed solvent of toluene and tetrahydrofuran, and then insoluble matter was filtered off. The solvent was removed from the filtrate under reducing atmosphere, and the resulting white solid was dried in vacuo at  $80^\circ C$  for 12 h.

**2.3. Characterization.** All powder X-ray diffraction experiments were performed on a Rigaku Ultima IV diffractometer equipped with a Cu-K $\alpha$  source operated at 40 kV, 44 mA, and 1.76 kW with the step size of  $5^\circ$  in the scanning range of the diffraction angle  $20^\circ \leq 2\theta \leq 80^\circ$  and a scintillation counter detector. The samples were confirmed by comparison with the appropriate pattern from the International Center for Diffraction Database (ICDD) crystallographic database. All Fourier transform infrared (FTIR) spectroscopic measurements were made on a Shimadzu model FTIR-8400S spectrometer equipped with an attenuated total reflectance (ATR) attachment. The sample morphologies were characterized with SEM on an Hitachi model Su-1500. Online Mass Spectrometry analysis was performed using PFEIFFER Omni Star.

### 3. Results and Discussion

**3.1. Infrared Spectroscopy Analysis.** The absorption peak of  $[AlH_4]^-$  corresponding to Al-H bond stretching was usually used to determine sodium aluminum hydride. As shown in Figures 1(a) and 1(b), there are Al-H bond characteristic peaks that appear in the vicinity of  $1660\text{ cm}^{-1}$  and  $710\text{ cm}^{-1}$ . Figure 1(c) is the intermediate from reaction started about an hour; there is a clear characteristic peak of aluminum alkyl in the vicinity of  $1250\text{ cm}^{-1}$ ,  $1040\text{ cm}^{-1}$ , and  $650\text{ cm}^{-1}$ . It indicates the formation of alkyl-aluminum. It can also be seen from the figure that the purity of the sample is improved

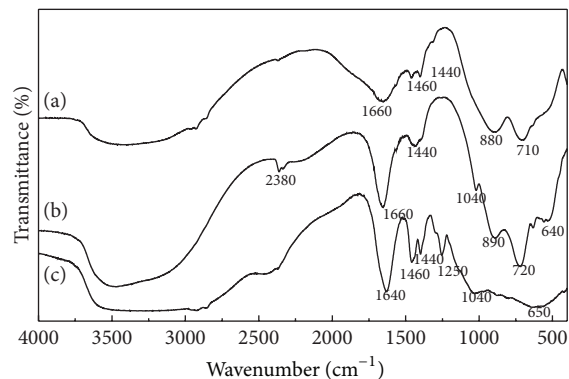


FIGURE 1: FTIR spectra of the sample: (a) sample after recrystallization, (b) sample after completion of the reaction, and (c) intermediate from reaction started about an hour.

TABLE 1: Analysis data of the sample elemental composition.

Element	Theoretical value		Actual measured value	
	Content (%)	Atomic ratio	Content (%)	Atomic ratio
Na	42.59	1.00	42.63	1.03
Al	50.00	1.00	49.74	0.99
H	7.41	4.00	7.36	4.06

after recrystallization, with a significant reduction of impurity peak. By comparing this is consistent with previous results reported in the literature [14, 15]. This indicates that the product has the presence of  $NaAlH_4$ .

**3.2. Elemental Analysis of Samples.** H elemental analysis was performed using Germany ELTRA ONH-2000 elemental analyzer. Al elemental analysis was performed using anti-titration according to GB/T 5121.13-2008. Metallic sodium content was measured by Prodigy Full Spectrum Direct Reading ICP emission spectrometer (Leeman Labs, US), and the sample analysis results are listed in Table 1. It can be seen that the actual measured value of these three elements is close to the theoretical value, and the contents of different element are approximately consistent with the theoretical values. The melting point of the sample is between  $182^\circ C$ – $185^\circ C$ . It has a melting process, it is a range, not a specific temperature point. In other words, it started to melt from  $182^\circ C$ , and melted completely at  $185^\circ C$ . Combining the results of the elemental analysis indicates that the molecular of our product is  $NaAlH_4$ .

**3.3. X-Ray Diffraction Analysis.** Figure 2 shows the diffractograms of the synthesized samples and the sample after recrystallization. The characteristic peaks of those samples are clearly discernible and consistent with the JCPDF index-card 22-1337 [16]. Based on this result as well as those of FTIR and elemental analysis, it can be conclude that the final product prepared by this method is  $NaAlH_4$ . It has a monoclinic crystal structure (cell parameters:  $a = b = 5.02\text{ \AA}$ ,  $c = 11.31\text{ \AA}$ ) and I41/a (88) space group. These results are consistent with other studies on the same  $NaAlH_4$  and

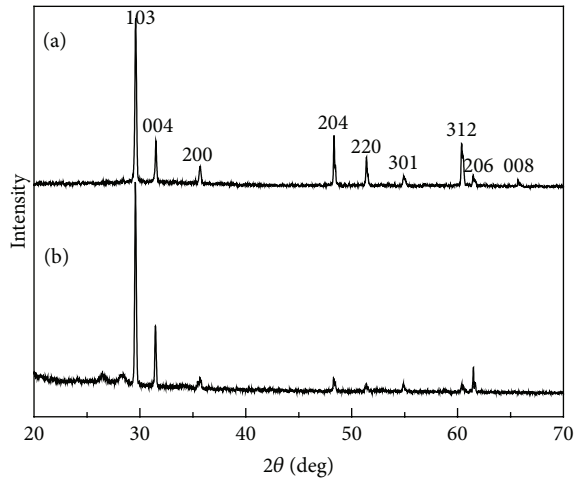
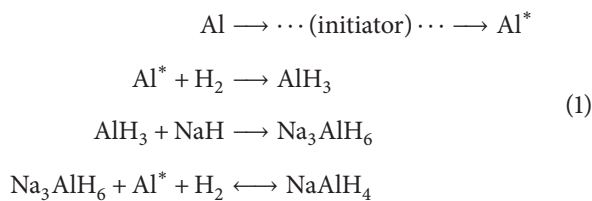


FIGURE 2: XRD patterns of (a) products after recrystallization and (b) products after completion of the reaction.

similar ones (despite being synthesized by different methods and at higher temperatures). It can also be seen from the figure that there are impurities present in the sample before recrystallization. In other words, the purity of the product is improved after recrystallization.

**3.4. Reaction Mechanism.** The reaction mechanism can be described as follows:



At first, aluminum powder is activated in the presence of initiator and the intermediate with a high activity can directly react with hydrogen to form aluminum hydride. The produced  $\text{AlH}_3$  then further react with NaH and hydrogen to form final product,  $\text{NaAlH}_4$ .

This is confirmed by FTIR and XRD as seen in Figures 1(c), 3, and 4. In Figure 1(c), there is a strong absorption peak at  $1640 \text{ cm}^{-1}$ , which can be attributed to the Al-H bond vibration absorption [17]. Because in the absence of sodium hydride, therefore it can not be  $[\text{AlH}_4]^-$  vibration peak, it should  $\text{AlH}_3$  vibration absorption.

To further confirm this reaction mechanism, we also ran some other experiments. Figures 3 and 1(c) show XRD and FTIR of the product without addition of sodium hydride. The results illustrate the generation of different crystal forms of aluminum hydride in the first reaction step. The intermediate obtained at a reaction time of 5 h was detected by XRD and the result is shown in Figure 4. It can be seen that the resulting intermediate contains multiple components including  $\text{Na}_3\text{AlH}_6$ ,  $\text{AlH}_3$ , NaH, and  $\text{NaAlH}_4$ . This result adds to and provides for our reaction mechanism [18].

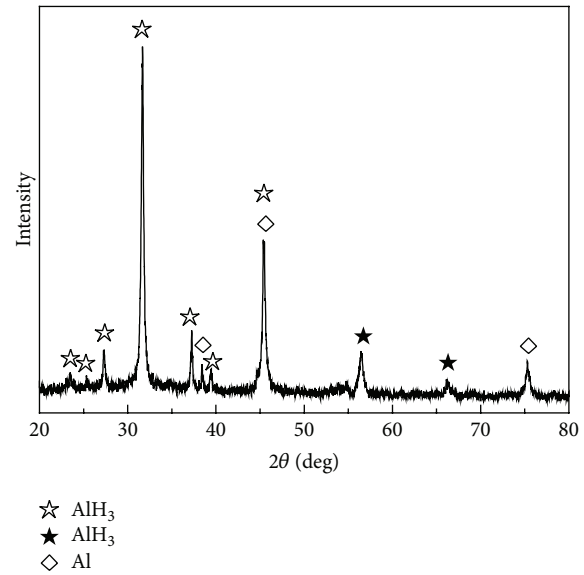


FIGURE 3: XRD patterns of mixture obtained after 1 h of reaction.

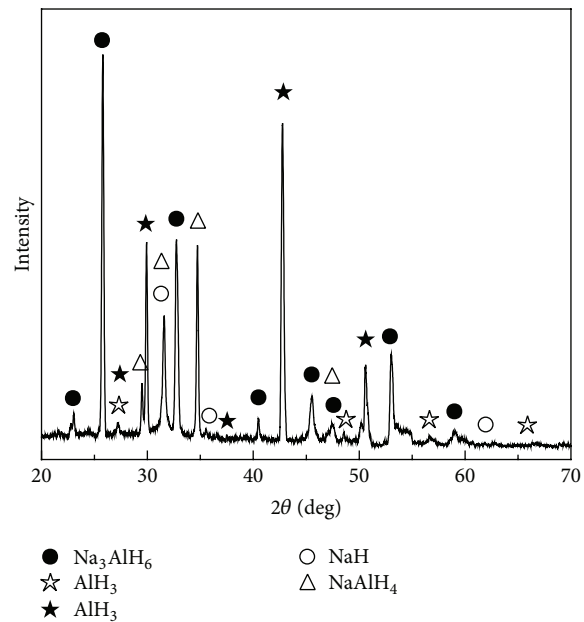


FIGURE 4: XRD patterns of mixture obtained after 5 h of reaction after adding NaH.

**3.5. Scanning Electron Microscopy Analysis.** Two scanning electron microscopy (SEM) photomicrographs of the sample surface are depicted in Figure 5. Figure 5(a) shows the microstructure of synthesized  $\text{NaAlH}_4$ , where plurality of smaller sized irregular particles and loose structure can be observed on the whole porous surface. This microstructure has large specific surface area; and it is beneficial to improve the capacity of hydrogen storage and release of materials [19]. The sample after recrystallization is shown in Figure 5(b); its surface is smooth but has a lot of voids there, which suggests that there is certain functional materials storage of

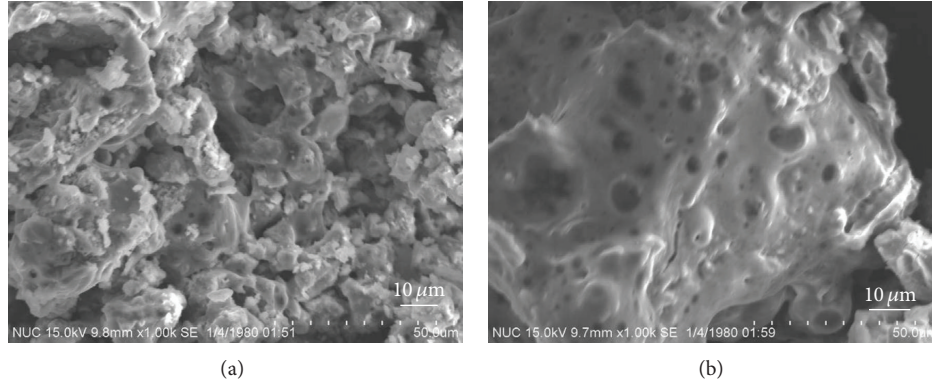
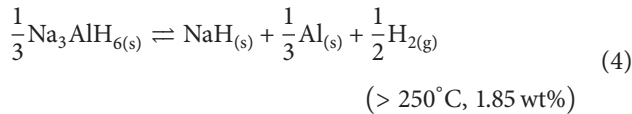
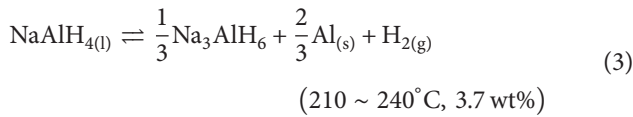


FIGURE 5: SEM micrographs of obtained  $\text{NaAlH}_4$  before its recrystallization (a) and that after recrystallization (b) for magnified 1000 times.

gas. Based on this phenomenon, compounds with different morphologies can be obtained using this method.

**3.6. Performance Analysis of Dehydrogenation.** According to the literature [20], the de/hydrogenation reactions of  $\text{NaAlH}_4$  take place in three steps as follows:



Online Mass Spectrometry is a gas collection device, in which acquisition gaseous substances are released during heating under the protection of  $\text{N}_2$ , so as to get its content. The heating rate of hydrogen online MS is  $5^\circ\text{C}$  per minute; the peak of the figure represents hydrogen release.

Figure 6 is the Online Mass Spectrometry of hydrogen from synthesized samples. It can be seen that hydrogen was released during the decomposition of the sample. This result showed that the synthesized sodium aluminum hydride has hydrogen storage capability. There are approximately 3.62 wt%  $\text{H}_2$  released at  $340^\circ\text{C}$  and 0.35 wt%  $\text{H}_2$  releasing at about  $100^\circ\text{C}$ , which can be attributed to the decomposition of remnant aluminum hydride [17] and influence of impurities. This shows that the stability to get  $\text{NaAlH}_4$  is not good.

Figure 7 shows the Online Mass Spectrometry of hydrogen from samples after recrystallization. By comparing Figures 6 and 7, there is only a hydrogen release peak at  $370^\circ\text{C}$  in Figure 7, and its content is about 3.87 wt%. This shows that the sample is more stable after recrystallization and has better purity.

It is concluded that sodium aluminum hydride obtained by this method has a hydrogen storage capacity from Online Mass Spectrometry and SEM. The hydrogen storage capacity is less than those reported in the literature by calculation. As the temperature increases, there will be a release of hydrogen;

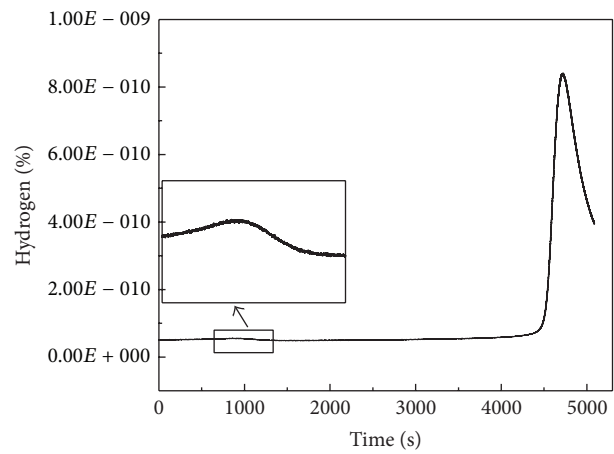


FIGURE 6: Online MS of hydrogen from synthesized  $\text{NaAlH}_4$ .

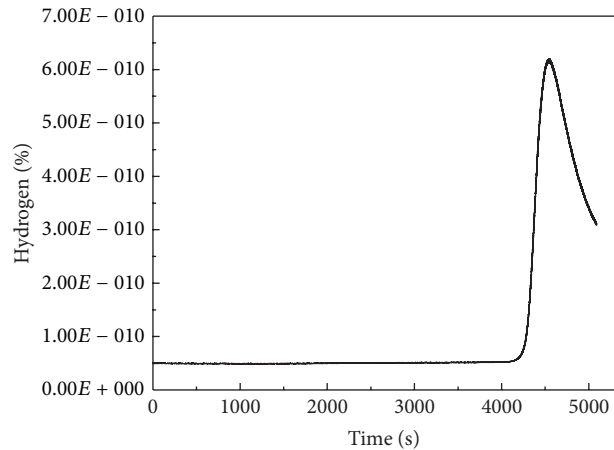


FIGURE 7: Online MS of hydrogen after recrystallization from synthesized  $\text{NaAlH}_4$ .

this also provides evidence for the stability. In summary, the sample has more stable and more complete polymorph after recrystallization.

## 4. Conclusions

From the above discussion, it can be concluded that  $\text{NaAlH}_4$  was successfully synthesized by a very effective method in this paper. Our preparation way has some advantages including low cost, mild reaction conditions, and high output rate. The synthesized  $\text{NaAlH}_4$  has hydrogen storage capacity and more moderate desorption conditions and better stability after recrystallization. All these advantages indicate that our process has potential application for the industrial production of  $\text{NaAlH}_4$ . This provides a strong guarantee of the research and development for other hydrogen storage materials.

## Conflict of Interests

The authors declare that there is no conflict of interests regarding the publication of this paper.

## Acknowledgments

The authors gratefully acknowledge the financial support of this work by the International Science & Technology Cooperation Program of China (no. 2011DFA51980) and Shanxi Science & Technology Cooperation Program of China (no. 2011DFA51980). Acknowledgement is made to the National Key Laboratory for Electronic Measurement Technology and Shanxi Polymer Composite Materials Engineering Research Center for the support of equipment and offering a variety of test equipment.

## References

- [1] X. Xiao, S. Wang, X. Fan et al., "Improved de/hydrogenation properties and favorable reaction mechanism of  $\text{CeH}_2 + \text{KH}$  co-doped sodium aluminum hydride," *International Journal of Hydrogen Energy*, vol. 39, no. 12, pp. 6577–6587, 2014.
- [2] K.-S. Lin, Y.-J. Mai, S.-R. Li, C.-W. Shu, and C.-H. Wang, "Characterization and hydrogen storage of surface-modified multiwalled carbon nanotubes for fuel cell application," *Journal of Nanomaterials*, vol. 2012, Article ID 939683, 13 pages, 2012.
- [3] K.-S. Lin, Y.-J. Mai, S.-W. Chiu, J.-H. Yang, and S. L. I. Chan, "Synthesis and characterization of metal hydride/carbon aerogel composites for hydrogen storage," *Journal of Nanomaterials*, vol. 2012, Article ID 201584, 9 pages, 2012.
- [4] L. E. Klebanoff and J. O. Keller, "Corrigendum to '5 years of hydrogen storage research in the U.S. DOE Metal Hydride Center of Excellence (MHCoe)' [Int J Hydrog Energy 38 (2013) 4533–4576]," *International Journal of Hydrogen Energy*, vol. 38, no. 19, 8022 pages, 2013.
- [5] H. M. Lee, S.-Y. Choi, and J.-Y. Yun, "Preparation of aluminum-organic nanocomposite materials via wet chemical process," *Advanced Powder Technology*, vol. 22, no. 5, pp. 608–612, 2011.
- [6] T. A. Semelsberger and K. P. Brooks, "Chemical hydrogen storage material property guidelines for automotive applications," *Journal of Power Sources*, vol. 279, pp. 593–609, 2015.
- [7] R. Bhattacharyya and S. Mohan, "Solid state storage of hydrogen and its isotopes: an engineering overview," *Renewable & Sustainable Energy Reviews*, vol. 41, pp. 872–883, 2015.
- [8] J. Huot, D. B. Ravnsbæk, J. Zhang, F. Cuevas, M. Latroche, and T. R. Jensen, "Mechanochemical synthesis of hydrogen storage materials," *Progress in Materials Science*, vol. 58, no. 1, pp. 30–75, 2013.
- [9] G. Lefèvre, "In situ Fourier-transform infrared spectroscopy studies of inorganic ions adsorption on metal oxides and hydroxides," *Advances in Colloid and Interface Science*, vol. 107, no. 2-3, pp. 109–123, 2004.
- [10] B. Hu, M. He, B. Chen, and L. Xia, "Liquid phase microextraction for the analysis of trace elements and their speciation," *Spectrochimica Acta Part B: Atomic Spectroscopy*, vol. 86, pp. 14–30, 2013.
- [11] E. David and J. Kopac, "Hydrolysis of aluminum dross material to achieve zero hazardous waste," *Journal of Hazardous Materials*, vol. 209-210, pp. 501–509, 2012.
- [12] R. Pedicini, B. Schiavo, P. Rispoli et al., "Progress in polymeric material for hydrogen storage application in middle conditions," *Energy*, vol. 64, pp. 607–614, 2014.
- [13] S. Veeraswamy, K. I. Reddy, R. V. Ragavan, K. T. Reddy, S. Yennam, and A. Jayashree, "An efficient one-step chemoselective reduction of alkyl ketones over aryl ketones in  $\beta$ -diketones using LiHMDS and lithium aluminium hydride," *Tetrahedron Letters*, vol. 53, no. 35, pp. 4651–4653, 2012.
- [14] E. M. A. Khalil, F. H. ElBatal, Y. M. Hamdy, H. M. Zidan, M. S. Aziz, and A. M. Abdelghany, "Infrared absorption spectra of transition metals-doped soda lime silica glasses," *Physica B: Condensed Matter*, vol. 405, no. 5, pp. 1294–1300, 2010.
- [15] V. D'Anna, A. Spyratou, M. Sharma, and H. Hagemann, "FT-IR spectra of inorganic borohydrides," *Spectrochimica Acta Part A: Molecular and Biomolecular Spectroscopy*, vol. 128, pp. 902–906, 2014.
- [16] T.-T. Chen, C.-H. Yang, and W.-T. Tsai, "In-situ synchrotron X-ray diffraction study on the dehydrogenation behavior of  $\text{NaAlH}_4$  modified by multi-walled carbon nanotubes," *International Journal of Hydrogen Energy*, vol. 37, no. 19, pp. 14285–14291, 2012.
- [17] B. Xu, J. Liu, and X. Wang, "Preparation and thermal properties of aluminum hydride polymorphs," *Vacuum*, vol. 99, pp. 127–134, 2014.
- [18] L.-Y. Han, X.-Z. Xiao, X.-L. Fan et al., "Enhanced dehydrogenation performances and mechanism of  $\text{LiBH}_4/\text{Mg}_{17}\text{Al}_{12}$ -hydride composite," *Transactions of Nonferrous Metals Society of China*, vol. 24, no. 1, pp. 152–157, 2014.
- [19] L. J. Murray, M. Dinc, and J. R. Long, "Hydrogen storage in metal-organic frameworks," *Chemical Society Reviews*, vol. 38, no. 5, pp. 1294–1314, 2009.
- [20] F. Sterpone, S. Bonella, and S. Meloni, "Early stage of the dehydrogenation of  $\text{NaAlH}_4$  by ab initio rare event simulations," *The Journal of Physical Chemistry C*, vol. 116, no. 37, pp. 19636–19643, 2012.

## Research Article

# Preparation and Microwave Absorbing Properties of an Electroless Ni-Co Coating on Multiwall Carbon Nanotubes Using $[\text{Ag}(\text{NH}_3)_2]^+$ as Activator

Qiao-ling Li, Xiao-yong He, Yue-qing Zhang, and Xiao-feng Yang

Department of Chemistry, School of Science, North University of China, Taiyuan 030051, China

Correspondence should be addressed to Qiao-ling Li; [qiaolingl@163.com](mailto:qiaolingl@163.com)

Received 16 December 2014; Accepted 17 April 2015

Academic Editor: Taeseup Song

Copyright © 2015 Qiao-ling Li et al. This is an open access article distributed under the Creative Commons Attribution License, which permits unrestricted use, distribution, and reproduction in any medium, provided the original work is properly cited.

Ni-Co-coated carbon nanotubes (CNTs) composites with different molar ratios of Ni/Co were synthesized using  $[\text{Ag}(\text{NH}_3)_2]^+$  as activator and  $\text{H}_2\text{PO}_2^-$  as reductant, thereby replacing the conventional noble metal Pd salt activator and  $\text{Sn}^{2+}$  reductant. Scanning electron microscopy, X-ray diffraction, and X-ray energy dispersive spectrometry analyses demonstrated that the CNTs were deposited with a dense, uniform Ni-Co coating. The possible mechanism of the electroless method was studied, which indicates that pure  $\text{Ag}^0$  acted as a nucleation site for subsequent Ni-Co-P deposition. Network vector analyzer measurements indicated that the composite with only Ni coated had an absorbing value of  $-12.6$  dB and the composite with a Ni/Co ratio of four had the maximum wave absorption ( $-15.6$  dB) and the widest absorption bandwidth (800 MHz,  $\text{RL} < -10$  dB), while the saturation magnetization (Ms) was  $4.28 \text{ emu}\cdot\text{g}^{-1}$  and the coercive force (Hc) was 31.33 Oe.

## 1. Introduction

Carbon nanotubes (CNTs), discovered by Iijima [1], have attracted considerable attention due to their perfect structure and outstanding mechanical, electrical properties [2–4]. However, their magnetic properties are not ideal, which limits their extensive application in electromagnetic energy dissipation field, especially in the microwave absorption field. Consequently, it is necessary to improve their magnetic and dielectric properties with electroless magnetic metal plating [5, 6] so as to make CNTs excellent microwave absorbing materials.

Electroless plating is a surface modification method, by which metallic ions were changed into metals under the catalytic activation of the substrate surface and are deposited on the substrate surface without an external current [7]. Considering the good conductivity, chemical stability, and unique one-dimensional structure of CNTs, they were chosen as the substrate of electroless plating. Besides, CNTs composites are light weight and high temperature resistant. In the case of a nonmetallic substrate, such as CNTs, the key to electroless plating lies in activating the substrate and

coating a catalytic metal layer on the substrate surface [8]. Palladium has been employed as an activator for many years [9]. Using  $\text{SnCl}_2\text{-PdCl}_2$  as sensitization-activation solution [10], the stannous ions adsorbed by the physical adsorption of the substrate surface reduce the palladium ions to metallic palladium seeds, which can then act as catalytic nuclei for subsequent metal electroless deposition [11]. The palladium activation method is costly [12] and has low efficiency and a risk of contamination.

In this paper, considering that Ag particles have strong oxidability [13, 14] and can also be used as catalysts of an electroless plating reaction [15, 16], we developed a low-cost and low-pollution palladium-free activation process: acidulated multiwalled carbon nanotubes (MWCNTs) were activated with silver ammonia solution and then the adsorbed silver ions were reduced to silver seeds by sodium hypophosphite solution. Silver seeds will catalyze succedent nickel-cobalt alloy deposition on the MWCNTs. The key work lies in the investigation of the effect of the molar ratio of nickel-cobalt on the magnetic properties and microwave absorbing properties of composites. Besides this, the electroless mechanism was studied to some extent.

TABLE 1: Composition of nickel-cobalt plating solution.

Compose	Chemicals	Content (g·L <sup>-1</sup> )
Main salt	NiSO <sub>4</sub> ·6H <sub>2</sub> O	4.5–18.2
Main salt	CoSO <sub>4</sub> ·7H <sub>2</sub> O	8.2–19.4
Reductant	NaH <sub>2</sub> PO <sub>2</sub>	18.2
Complexing agent	Na <sub>3</sub> C <sub>6</sub> H <sub>5</sub> O <sub>7</sub> ·H <sub>2</sub> O	41.3
Buffering agent	(NH <sub>4</sub> ) <sub>2</sub> SO <sub>4</sub>	23.1
Acidity	pH	9

## 2. Materials and Methods

**2.1. Pretreatment of MWCNTs.** MWCNTs (Nanoport Co., Ltd., Shenzhen, China) with 10–30 nm diameters, 5–15 μm length, and a purity higher than 98% were roasted in a muffle furnace at 500°C for 2 h; they were then stirred in a mixed acid solution of concentrated sulfuric and nitric acid (1:3 by volume) at 80°C for 2 h. Afterward, the MWCNTs were rinsed in distilled water several times until the pH value reached neutral and were then dried at 80°C for further use.

**2.2. Activation of Pretreated MWCNTs.** Silver ammonia solution was first prepared by dropping dilute aqua ammonia into 20 g/L silver nitrate solution until the solution changed from turbidity to clarity. Then, the pretreated MWCNTs were added to the silver ammonia solution, sonicated for 0.5 h, and stirred at 80°C for 0.5 h after adding 25 g/L sodium hypophosphite solution to the mixture just mentioned. Finally, the activated solution was filtered and the residue was rinsed in distilled water until the pH value reached neutral and was then dried at 70°C for 8 h for further use.

**2.3. Electroless Ni-Co Alloy Deposition on MWCNTs.** Figure 1 shows the procedure used for the preparation of Ni-Co plated MWCNTs; Table 1 shows the composition of the nickel-cobalt plating solution. NiSO<sub>4</sub>·6H<sub>2</sub>O, CoSO<sub>4</sub>·7H<sub>2</sub>O ( $n_{\text{Ni}} : n_{\text{Co}} = 4 : 1, 3 : 2, 1 : 1, 2 : 3$ ), Na<sub>3</sub>C<sub>6</sub>H<sub>5</sub>O<sub>7</sub>·H<sub>2</sub>O, and (NH<sub>4</sub>)<sub>2</sub>SO<sub>4</sub> were dissolved in distilled water of different volumes, respectively, orderly added to a certain quality of activated MWCNTs (the ratio of Ni-Co particles to MWCNTs was 9:1), and sonicated for 0.5 h; sodium hypophosphite solution was finally added, and ultrasonic treatment was continued for 20 min. Afterward, the mixture was stirred at a medium speed at 80°C for 1 h. During the entire reaction, the pH value was adjusted to 9 with aqua ammonia and sodium hypophosphite solution being added until the solution no longer bubbled. Finally, the solution was filtered and the residue was rinsed in distilled water until the pH value reached neutral and was then dried for 8 h at 80°C; samples were marked as A, B, C, and D. The Ni-MWCNTs composite was prepared in a similar manner and marked as E.

**2.4. Characterization.** The surface morphology and elemental composition of the coating were determined by scanning electron microscopy (SEM) and an X-ray energy dispersive spectrometer (EDS). The phase structure was analyzed by X-ray diffraction (XRD). The magnetic property was measured

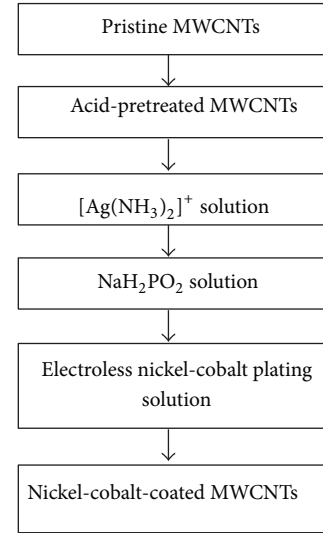


FIGURE 1: Procedure for preparation of nickel-cobalt-coated MWCNTs.

at room temperature using a vibration sample magnetometer (VSM) with a maximum field of 10 kOe. The absorbing property was detected by a Network Vector Analyzer.

## 3. Results and Discussion

**3.1. Morphology Analysis.** Figure 2 depicts the SEM micrographs of MWCNTs before and after electroless plating. The pristine MWCNTs are highly entangled (Figure 2(a)); the black dots on the surface of the MWCNTs were expected to be graphite, metallic catalyst particles, and amorphous carbons. After acid treatment, the black dots were completely removed; long MWCNTs were cut off; the caps of MWCNTs were opened and etched off (Figure 2(b)). The surface of the activated MWCNTs appeared to be coated with many uniform and white silver particles (Figure 2(c)), implying that the  $\text{Ag}(\text{NH}_3)_2^+$  activator can also form well-distributed active centers. Figure 2(d) was only the Ni-coated composite, which had a netty structure. As observed from the images of the Ni-Co-coated MWCNTs with a different molar ratio of nickel-cobalt, apparently, MWCNTs were completely covered with uniform and continuous alloy particles. Ni-Co grew into sphericity along active centers and formed metal nanofibers, which took carbon nanotubes as the core (Figures 2(e) and 2(f)). In particular, from Figure 2(g), we can see different radial nickel and cobalt atoms clusters getting together and forming a dense coating. Meanwhile, with the increase of Co content, the size of the Ni-Co particles gets bigger from 400 nm (Figure 2(e)) to 1 μm (Figure 2(g)).

**3.2. Schematic Procedure of Preparation of Nickel-Cobalt-Coated MWCNTs.** Figure 3 depicts the schematic procedure. In the process of electroless, the MWCNTs act as a one-dimensional template for Ni-Co deposition. At the same time, because of its outstanding conductivity, it can also enhance the property of composites. The whole nickel-cobalt

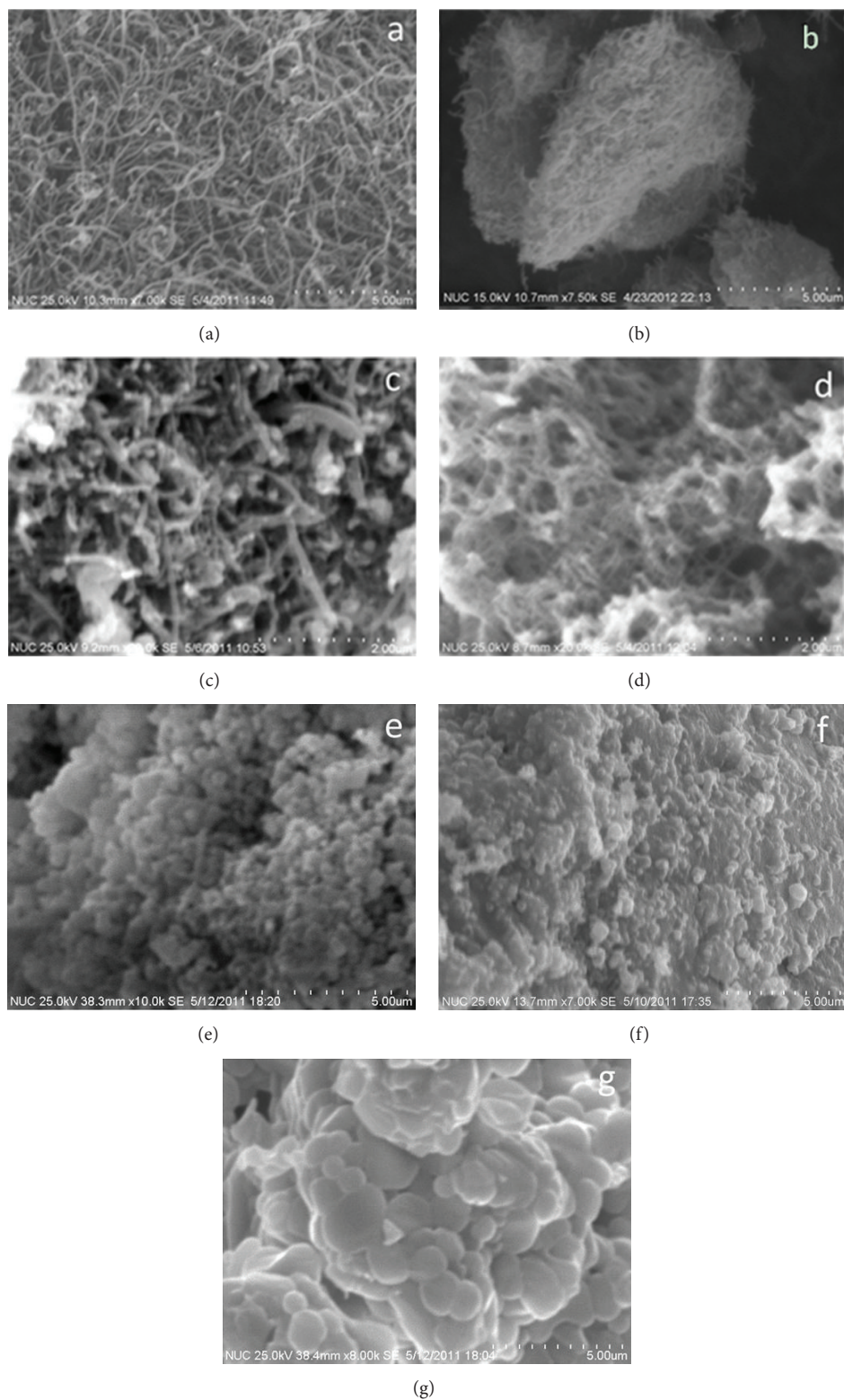


FIGURE 2: SEM micrographs of MWCNTs before and after coated (a) pristine MWCNTs; (b) acid-pretreated MWCNTs; (c) activated MWCNTs; (d) Ni-MWCNTs; (e) Ni<sub>8</sub>Co<sub>2</sub>-MWCNTs; (f) Ni<sub>5</sub>Co<sub>5</sub>-MWCNTs; (g) Ni<sub>4</sub>Co<sub>6</sub>-MWCNTs.

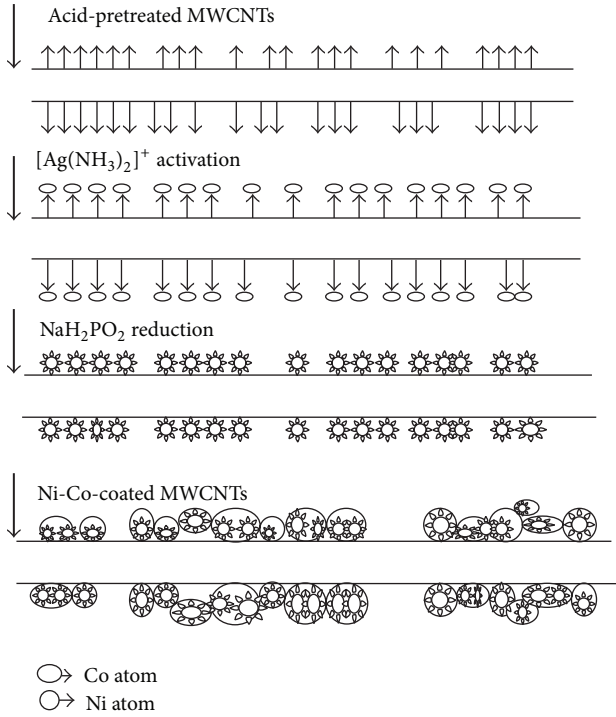
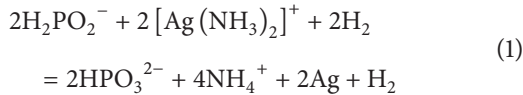


FIGURE 3: Schematic of electroless Ni-Co alloy-coated MWCNTs.

plating process consisted of four steps. After acid treatment, the caps of MWCNTs were etched off and the MWCNTs were activated with more oxidized functional groups, such as carboxylic groups and hydroxyl groups, which can improve the dispersion, water-solubility, and activity of MWCNTs in the electroless solution (step 1).

$\text{Ag}(\text{NH}_3)_2^+$  ions were adsorbed on the MWCNTs surface with considerable  $\text{OH}^-$  ions forming an  $\text{Ag}(\text{NH}_3)_2\text{OH}$  complex by an electrostatic interaction (step 2). Immersing MWCNTs into  $\text{NaH}_2\text{PO}_2$  solution,  $\text{H}_2\text{PO}_2^-$  will reduce the adsorbed  $\text{Ag}(\text{NH}_3)_2^+$  ions into Ag particles as active centers being uniformly distributed on the MWCNTs surface [17]. In alkaline condition, the standard electrode potential of  $\text{HPO}_3^{2-}/\text{H}_2\text{PO}_2^-$  couple is  $-1.57$  V, while  $\text{Ag}(\text{NH}_3)_2^+/\text{Ag}$  is  $+0.373$  V. The standard battery electromotive force of such electrode couples is positive value [ $\Delta E^\circ = +0.373$  V  $- (-1.57$  V)  $= 1.943$  V]; therefore, the reaction is spontaneous, and the equation is as follows (step 3):



Under the catalytic action of Ag, complex  $\text{Ni}^{2+}$  and  $\text{Co}^{2+}$  ions in the plating solution are changed into Ni and Co particles and deposited onto the surface by capturing electrons furnished by the reductant ( $\text{H}_2\text{PO}_2^-$ ) by the following reactions [18]:

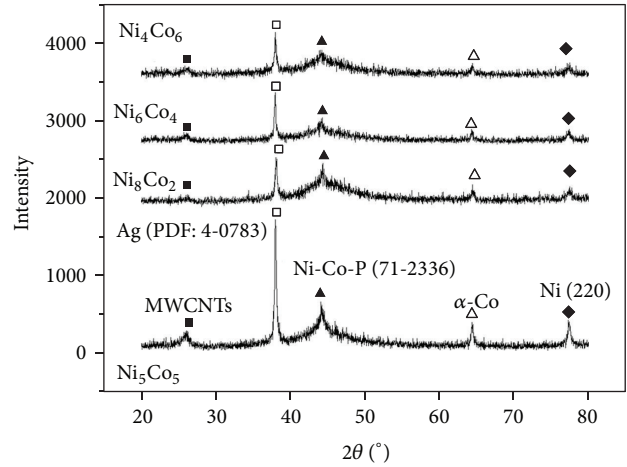
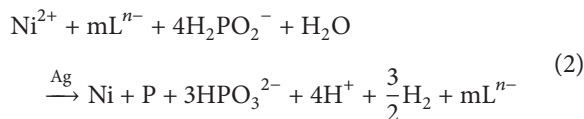
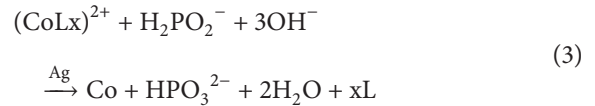
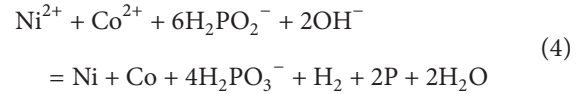


FIGURE 4: XRD patterns of different samples.



L stands for a complexing agent, and the overall reaction can be written as follows:



The deposited Ni and Co atoms then can act as self-catalysts for obtaining a well-developed Ni-Co coating. With the decrease in the  $\text{Ni}^{2+}$  and  $\text{Co}^{2+}$  ion concentration, fewer bubbles are released, implying that the reaction is gradually slowing down. In order to obtain a compact and continuous coating, we need to add an electroless solution and adjust the pH value constantly.

**3.3. X-Ray Diffraction Analysis and EDS Analysis.** Figure 4 depicts the XRD patterns of nickel-cobalt-coated MWCNTs composites without heat treatment. It was found that the molar ratio of nickel-cobalt influenced the intensity of only some peaks. A broad peak at about  $2\theta = 45^\circ$  was assigned to the Ni-Co-P amorphous diffraction peak, which indicated that the Ni-Co-P plating was amorphous under the electroless state. The amorphous peak was the most obvious and the sharpest when the molar ratio of nickel-cobalt was 1:1. Diffraction peaks at  $2\theta = 77.22^\circ$ ,  $64^\circ$ ,  $38.2^\circ$  were attributed to Ni (220),  $\alpha$ -Co, and Ag (111) (PDF: 4-0783) in each pattern. An intense Ag diffraction peak demonstrated the formation of many active centers on the surface of the MWCNTs, which were critical to the later electroless plating. Additionally, for the Ni-Co-MWCNTs composites, a diffraction peak assigned to the (002) plane of the MWCNTs at  $26.1^\circ$  has been less obvious, implying that the MWCNTs were completely coated by the Ni-Co alloy.

Figure 5 displays EDS spectra of the electroless MWCNTs, which mainly showed Ni and Co peaks. The element of Au plating on the surface can strengthen the

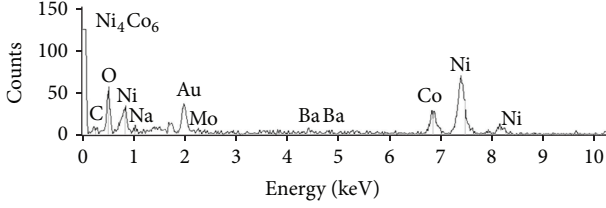


FIGURE 5: EDS spectra of Ni-Co alloy-coated MWCNTs.

reflectivity of the signal in the process of scanning. The contents of Ni and Co were 41.2 and 15.82 wt.%, which demonstrated that the main matter of coating was the Ni-Co alloy. The intense O peak indicated that the surface of the MWCNTs was sufficiently oxidized; the appearance of the weak C peak was attributed to a thin coating.

**3.4. Magnetic Property Analysis.** Figure 6 shows the hysteresis line of the Ni-Co-coated MWCNTs composites. Table 2 lists the main magnetic properties of different samples. As observed in the table, Ni-Co-coated MWCNTs had more excellent magnetic properties than pristine MWCNTs and Ni-Co alloy without MWCNTs. With an increase of Co content, saturation magnetization ( $M_s$ ) was gradually enhanced and coercive force ( $H_c$ ) was typically improved. Co is a densely hexagonal structure and has a great magnetic crystal anisotropic constant  $K$  and a magnetostrictive coefficient  $\lambda_s$ , which make the coercive force increase. In addition, the atomic magnetic moment of Co is larger than that of Ni; the increase in Co content is helpful in improving the saturation magnetization ( $M_s$ ) [19].

**3.5. Microwave Absorbing Analysis.** The Ni-Co-P-coated MWCNTs composite is a kind of microwave absorbing material which has both hysteresis losses and electric loss. The reflection loss can be defined by the loss tangent ( $\tan \delta$ ), which includes dielectric loss tangent and magnetic loss tangent [20]. Their relationship can be explained by the following formulas:

$$\begin{aligned} \tan \delta \epsilon_\gamma &= \frac{\epsilon_\gamma''}{\epsilon_\gamma'}, \\ \tan \delta \mu_\gamma &= \frac{\mu_\gamma''}{\mu_\gamma'}, \\ \tan \delta &= \tan \delta \epsilon_\gamma + \tan \delta \mu_\gamma = \frac{\epsilon_\gamma''}{\epsilon_\gamma'} + \frac{\mu_\gamma''}{\mu_\gamma'}. \end{aligned} \quad (5)$$

Here,  $\epsilon_\gamma$  and  $\mu_\gamma$  are the complex relative permittivity and complex relative permeability, respectively. Electromagnetic parameters ( $\epsilon_\gamma'$ ,  $\epsilon_\gamma''$ ,  $\mu_\gamma'$ , and  $\mu_\gamma''$ ) are the real part and imaginary part of relative permittivity and relative permeability, respectively. In this work, both the loss tangent and reflection loss are measured by the Network Vector Analyzer. The composite was mixed with paraffin in the mass ratio of 7 : 3; meanwhile, the absorbing layer thickness was 3 mm. As observed from

TABLE 2: The magnetic properties of different samples.

Sample	$H_c/Oe$	$M_s/emu \cdot g^{-1}$	$M_r/emu \cdot g^{-1}$
Ni-Co alloy without MWCNTs	11.09	3.21	0.27
Pristine MWCNTs	32.21	0.56	0.06
$Ni_8Co_2$	31.33	4.28	0.56
$Ni_6Co_4$	48.56	8.99	0.81
$Ni_5Co_5$	66.74	12.74	1.06
$Ni_4Co_6$	85.21	15.89	1.15

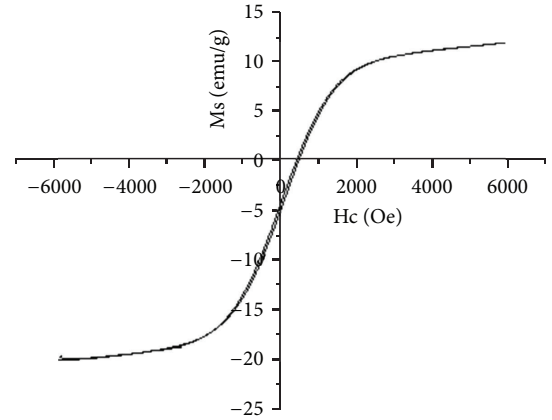


FIGURE 6: Hysteresis line of the composites.

Figures 7 and 8, the order of the dielectric loss tangent was  $A > C > E > D > B$ , while the magnetic loss tangent was  $B > A > D > C > E$ . As depicted in Figure 9, the reflection loss of sample A was the largest ( $-15.6$  db); next was that of the ordinal samples E ( $-12.6$  db), C ( $-9.8$  db), B ( $-9.6$  db), and D ( $-6$  db). The frequency range of the attenuation peak was 3000 MHz–5500 MHz; the bandwidth ( $RL < -5$  db) of sample E was the largest (1.8 GHz), with B (1.7 GHz), A (1.5 GHz), C (1.2 GHz), and D (0.8 GHz) successively; the bandwidth ( $RL < -10$  db) of samples A and E was 800 MHz and 400 MHz, respectively. Ni-Co-coated MWCNTs composites displayed stronger wideband microwave absorbing properties, and the possible reason was as follows: the surface of the MWCNTs consisted of coated metal nanoparticles, which possessed magnetism and microwave absorbing abilities of general nanoparticles. Coupling between the microwave field and internal magnetic field of the nanoparticles caused magnetic resonance absorption; magnetic particles were magnetized in an alternating magnetic field and produced a certain magnetic flux density, whose change produced magnetic induced electromotive force and eddy current, thus resulting in an eddy current loss. In addition, the magnetic lag effect also caused a part of electromagnetic energy loss.

## 4. Conclusions

The surface of acid-treated MWCNTs was coated with a dense and uniform Ni-Co plating by utilizing  $Ag(NH_3)_2^+$  as an activator replacing a conventional, costly, and polluttional Pd (II) activator. Results implied that coercive force ( $H_c$ )

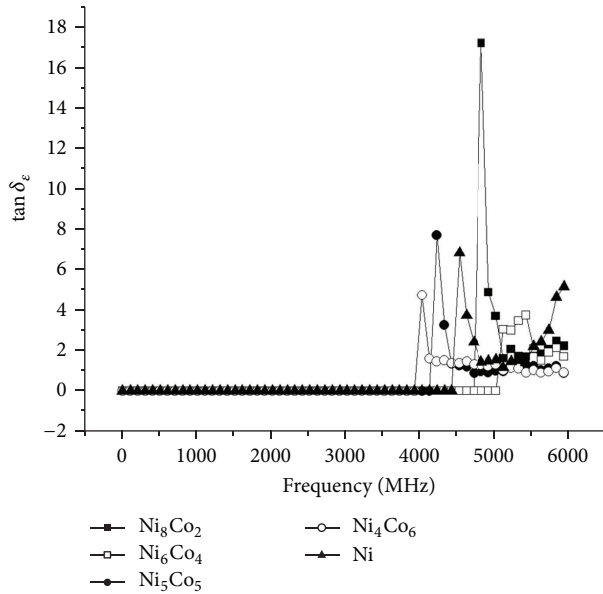


FIGURE 7: Dielectric loss tangent of different samples.

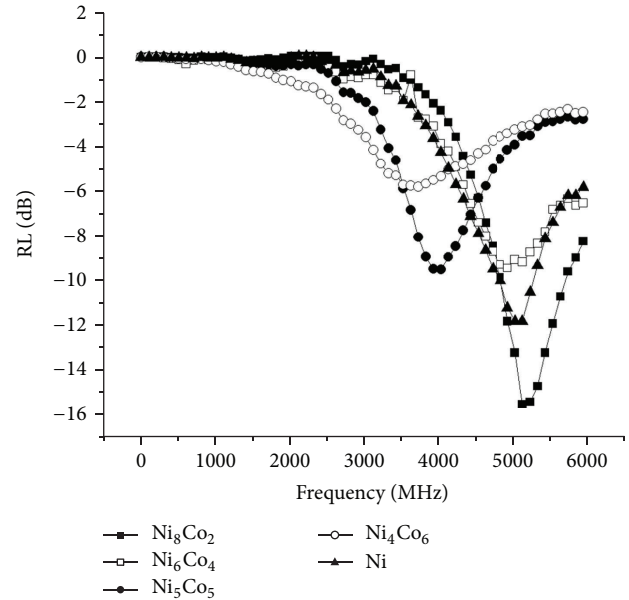


FIGURE 9: Reflection loss of different samples.

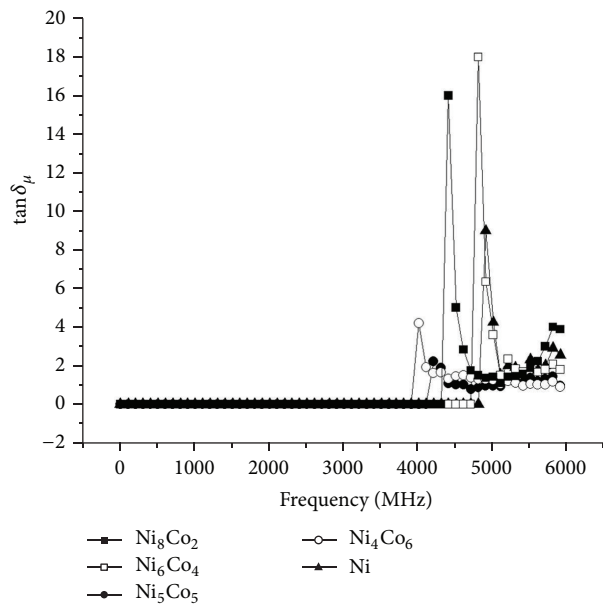


FIGURE 8: Magnetic loss tangent of different samples.

and saturation magnetization ( $M_s$ ) were gradually enhanced with the increase of Co content; the molar ratio of nickel-cobalt influenced the intensity of only some peaks. The  $\text{Ni}_8\text{Co}_2$  composite possessed the best microwave absorption ( $-15.6$  dB) in the lower frequency range (0–6000 MHz) owing to its better dielectric loss tangent and magnetic loss tangent and the frequency bandwidth ( $\text{RL} < -10$  dB) was also the largest (800 MHz). The electroless mechanism was studied to some extent, indicating that pure  $\text{Ag}^0$  acted as a nucleation site for subsequent Ni-Co-P deposition.

## Conflict of Interests

The authors declare that there is no conflict of interests regarding the publication of this paper.

## Acknowledgments

This work was supported by the National Natural Science Foundation of China (nos. 20871108 and 51272239), Youth Science Foundation of Shanxi Province (no. 2010021022-3), and the Scientific Research Foundation of the Higher Education Institutions of Shanxi Province, China (no. 2010115).

## References

- [1] S. Iijima, "Helical microtubules of graphitic carbon," *Nature*, vol. 354, no. 6348, pp. 56–58, 1991.
- [2] C. G. Hu, W. L. Wang, and W. Zhu, "Electrochemical investigation on carbon nanotube film with different pretreatments," *Acta Metallurgica Sinica (English Letters)*, vol. 16, no. 4, pp. 295–301, 2003.
- [3] J. W. Jiang and F. Peng, "Actuality and progress of application and research of Carbon Nanotubes," *Materials Science and Engineering Transaction*, vol. 21, no. 3, pp. 464–468, 2003.
- [4] H. Hiura, T. W. Ebbesen, J. Fujita, K. Tanigaki, and T. Takada, "Role of sp<sup>3</sup> defect structures in graphite and carbon nanotubes," *Nature*, vol. 367, no. 6459, pp. 148–151, 1994.
- [5] S. J. Tans, A. R. M. Verschueren, and C. Dekker, "Room-temperature transistor based on a single carbon nanotube," *Nature*, vol. 393, no. 6680, pp. 49–52, 1998.
- [6] C. Niu, E. K. Sichel, R. Hoch, D. Moy, and H. Tennent, "High power electrochemical capacitors based on carbon nanotube electrodes," *Applied Physics Letters*, vol. 70, no. 11, pp. 1480–1482, 1997.

- [7] Y. Zhao, Y.-J. Xue, H. Zheng, and Y.-X. Duan, "Electroless plating of Co-Fe on the surface of MWCNTs," *New Carbon Materials*, vol. 25, no. 1, pp. 65-70, 2010.
- [8] H. Liu, J. Li, and L. Wang, "Electroless nickel plating on APTHS modified wood veneer for EMI shielding," *Applied Surface Science*, vol. 257, no. 4, pp. 1325-1330, 2010.
- [9] P. K. Rohatgi, "Cast aluminium alloy composites containing copper-coated ground mica particles," *Journal of Materials Science*, vol. 16, no. 6, pp. 1599-1606, 1981.
- [10] T. J. O'Keefe, "Method for stripping metals in solvent extraction," U.S. Patent 5,228,903, 1993.
- [11] W. Sha, X. Wu, and K. G. Keong, *Electroless Copper and Nickel-Phosphorus Plating: Processing, Characterisation and Modeling*, Woodhead Publishing, Cambridge, UK, 2010.
- [12] J. Li, M. J. O'Keefe Matthew, and T. J. O'Keefe Thomas, "Activation of non-metallic substrates for metal deposition using organic solutions," *Surface and Coatings Technology*, vol. 205, no. 10, pp. 3134-3140, 2011.
- [13] D. Y. Zemlyanov, A. Nagy, and R. Schlögl, "The reaction of silver with  $\text{NO}/\text{O}_2$ ," *Applied Surface Science*, vol. 133, no. 3, pp. 171-183, 1998.
- [14] W. L. Dai, Y. Cao, L. P. Ren et al., "Ag-SiO<sub>2</sub>-Al<sub>2</sub>O<sub>3</sub> composite as highly active catalyst for the formation of formaldehyde from the partial oxidation of methanol," *Journal of Catalysis*, vol. 228, no. 1, pp. 80-91, 2004.
- [15] S. Shukla, S. Seal, Z. Rahaman, and K. Scammon, "Electroless copper coating of cenospheres using silver nitrate activator," *Materials Letters*, vol. 57, no. 1, pp. 151-156, 2002.
- [16] I. Lee, P. T. Hammond, and M. F. Rubner, "Selective electroless nickel plating of particle arrays on polyelectrolyte multilayers," *Chemistry of Materials*, vol. 15, no. 24, pp. 4583-4589, 2003.
- [17] Z. Aixiang, X. Weihao, and X. Jian, "Electroless Ni-Co-P coating of cenospheres using  $[\text{Ag}(\text{NH}_3)_2]^+$  activator," *Materials Letters*, vol. 59, no. 4, pp. 524-528, 2005.
- [18] X. Jiang and W. Shen, *The Fundamentals and Practice of Electroless Plating*, National Defence Industry Press, Beijing, China, 2000.
- [19] D. Cai, J. Gu, Z. Huang, and F. Kang, "Carbon nanotubes with nickel-cobalt alloy coating," *Journal of Materials Science and Engineering*, vol. 25, no. 5, pp. 713-714, 2007.
- [20] T. M. Meaz, S. M. Attia, and A. M. Abo El Ata, "Effect of tetravalent titanium ions substitution on the dielectric properties of Co-Zn ferrites," *Journal of Magnetism and Magnetic Materials*, vol. 257, no. 2-3, pp. 296-305, 2003.

## Research Article

# Fabrication of an Antireflective Nanodome Array with High Packing Density for Photovoltaic Applications

Jiseok Lim,<sup>1</sup> Sun-Mi Lee,<sup>2</sup> Ho-Young Jang,<sup>2</sup> and Seok-Min Kim<sup>2</sup>

<sup>1</sup>*School of Mechanical Engineering, Yeungnam University, Gyeongsan 712-749, Republic of Korea*

<sup>2</sup>*School of Mechanical Engineering, Chung-Ang University, Seoul 156-756, Republic of Korea*

Correspondence should be addressed to Seok-Min Kim; [smkim@cau.ac.kr](mailto:smkim@cau.ac.kr)

Received 22 May 2015; Revised 23 July 2015; Accepted 26 July 2015

Academic Editor: Xiaogang Han

Copyright © 2015 Jiseok Lim et al. This is an open access article distributed under the Creative Commons Attribution License, which permits unrestricted use, distribution, and reproduction in any medium, provided the original work is properly cited.

This paper describes a nanofabrication method for an antireflective nanodome array with high packing density. The master for the close packed nanodome array was fabricated by industrially well-established photolithography and physical vapor deposition processes to realize uniform and defect-free nanostructure in large area. The nanodome array was formed on the surface of a glass plate by a nanoimprinting process using the replicated mold from the master with the aim of reducing the Fresnel reflection of the glass surface. The replication fidelity was verified using scanning electron microscopy and the nanodome structured glass substrate showed ~3% increase in optical transmittance.

## 1. Introduction

Recently, the development of an antireflective surface to reduce the reflection that occurs at the interface between materials with different refractive indices had attracted research interest [1]. Antireflective surfaces have been applied to many applications, such as illumination, display, and imaging systems, as reflection can lead to performance issues in many optical and optoelectronic systems [2]. In particular, reflection is a very important issue for solar cell applications. Optical loss due to reflection at the optical interface of the solar cell is one of the most critical factors limiting the photovoltaic efficiency of solar cells [3]. To improve the conversion efficiency of solar cells, an antireflective surface is required.

Antireflection coatings (ARCs) made up of single- or multistacked layers with different refractive indices are widely used [4]. However, some of the limitations of these coating materials include optical bands and thermal mismatch between the film and substrate. As an alternative to ARCs, the use of antireflective nanostructures on optical interfaces has attracted intense interest [5]. The periodic subwavelength-patterned surface enables continuous changes in refractive index that remove the optical interface [6]. Considerable research efforts have sought to develop antireflective

nanopatterns on large optical surfaces for solar cell applications [7, 8].

Many studies evaluated the effect of the geometric shape of the nanostructure to the antireflection efficiency. Tapered shapes and pyramidal structures have been reported to be the most efficient design [9]. However, these nanostructure geometries have disadvantages in solar cell applications. To fabricate a sharp edge nanostructure on a large area at low cost is very challenging. Moreover, since the operation conditions of solar cell modules are relatively harsh, a linear tapered geometry can be easily damaged.

In this study, we propose an antireflective nanodome structure with high packing density and a cost-effective fabrication method using a nanoimprinting process. The nanoimprinting process is one of the most promising technologies for production of nanostructures at low cost [10, 11]. The most important element of the nanoimprinting process is a mold that has a negative shape of the final structure. Han et al. fabricated the mold for dome-shaped structured antireflection layer by polymer replication of electroformed master from the laser interference lithography [7] and Liu et al. fabricated the mold by electroforming of self-assembly nanosphere lithography [12]. The laser interference lithography and nanosphere lithography can be a promising

method to fabricate master pattern for the mold of dome-shaped antireflective nanostructure. However, this method has limitations to fabricate large area master pattern without any defects. In practical operation, it is difficult to fabricate uniform and defect-free dome-shaped nanostructure with more than 100 mm diameter size by the laser interference lithography or nanosphere lithography. In this study we fabricated replicated polymer mold from the dome-shaped master which was basically prepared by a photolithography and a physical vapor deposition process. The photolithography and physical vapor deposition process are industrially well-established techniques and can provide a large area uniform dome-shaped pattern (up to 300 mm diameter) without any defects. Finally, a nanodome array was replicated on a glass substrate using a UV imprinting process. As a result, the transmittance of the glass substrate was increased from 88-89% to 91-92% for a single-sided, patterned glass substrate in the spectral range of 350 to 850 nm.

## 2. Materials and Methods

A polymeric mold was fabricated using UV imprinting and physical e-beam evaporation processes, and then the antireflective nanodome-patterned structure was replicated on a glass substrate using the UV imprinting process. An overview of the fabrication procedures is presented in Figure 1.

A silicon master pattern with 500 nm pitch, 0.5 duty, and 100 nm grating height was fabricated via KrF scanner photolithography and reactive ion etching processes. A bottom antireflection coating (BARC) with a thickness of 58 nm was spin-coated on an 8-inch wafer and a photoresist was spin-coated with 580 nm thickness. Photolithography was conducted using a KrF step and repeat scanner (NSR-S203B, Nikon Co., Ltd., Japan), and the reactive ion etchings of the BARC layer and silicon substrate 110 nm in depth were performed using a poly etcher (TCP 9400DFM, Lam Research Co., Ltd.). The silicon master pattern was fabricated by the fab foundry service institute (National NanoFab Center, Daejeon, Korea). The fabricated silicon master wafer was subsequently treated with a self-assembled monolayer (SAM) coating to prevent adhesion of the cured polymer to the wafer. The SAM film was applied by dipping the wafer into a 2% solution of dimethyldichlorosilane dissolved in octamethylcyclotetrasilane (Repel-Silane ES, GE Healthcare Co., Ltd., USA). The fabricated silicon master was replicated using the UV imprinting process on polyester (PET) film (SH34, SKC Co., Ltd., Korea) to prepare the polymeric master. The UV imprinting processes were performed using a UV curable urethane acrylate based photopolymer (UP088, SK Chemicals Co., Ltd., Korea) with a refractive index of 1.52 and a UV curing system (2000 Flood, Dymax Co. Ltd., USA). Since the polymeric master has a cylindrical nanocavity structure, it was replicated once more to produce a nanopillar pattern array (Figures 1(a) and 1(b)). In order to form a nanodome structure, SiO<sub>2</sub> was deposited over the fabricated nanopillar pattern by e-beam evaporator (Modified SEE-7, Ultech Co., Ltd., Korea) with a deposition rate of 0.3 Å/s at a vacuum level of  $6 \times 10^{-6}$  Torr, as shown in Figure 1(c).

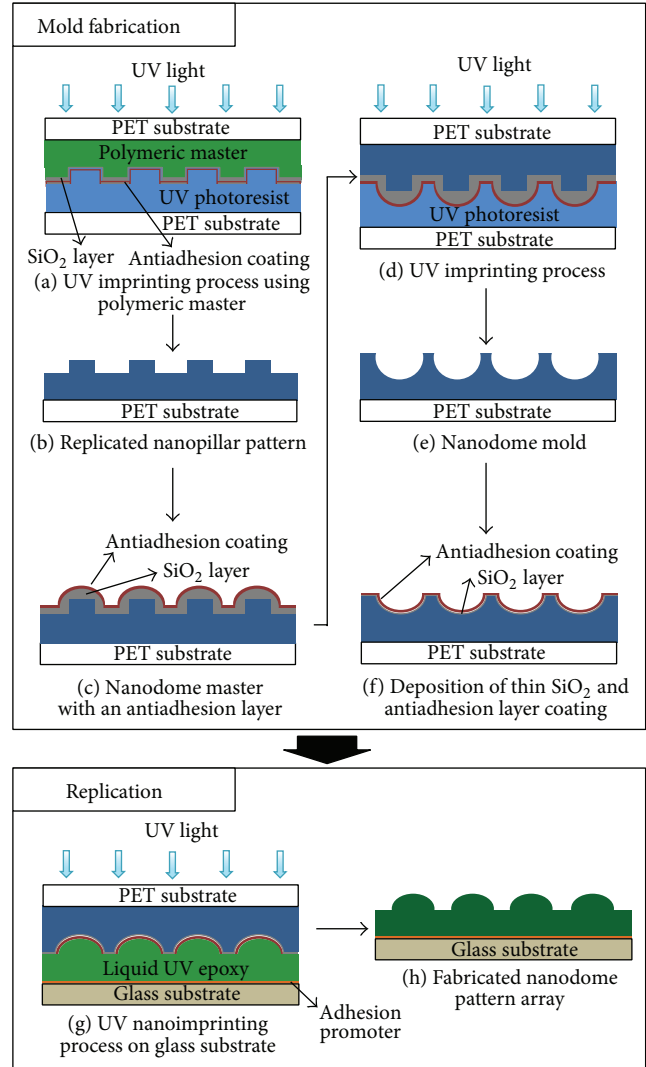


FIGURE 1: Schematic flow chart of nanodome pattern array fabrication.

The cylindrical pedestal structure evolves into a dome structure and the diameter of the dome structure increases with the deposition thickness of SiO<sub>2</sub> [13]. To evaluate the effect of the SiO<sub>2</sub> thickness on the geometric properties of the nanodome array, three different thicknesses of the SiO<sub>2</sub> layer (50, 100, and 150 nm) were tested. The fabricated nanodome structure was subsequently replicated by UV imprinting to form a polymer mold with a nanodome cavity array. Finally, the nanodome structure was fabricated by transferring the pattern of the mold to a glass slide substrate (Duran Group Co., Ltd., Germany) using UV imprinting. To improve the adhesion between the polymer and glass substrate, an adhesion promoter (ZAP-1020, Chemoptics Inc., Korea) was deposited on the glass substrate, which form an optically transparent amine monolayer on the glass substrate.

An optical grade urethane acrylate based photopolymer (UP088, SK Chemicals Co., Ltd., Korea) was used for the series of UV imprinting processes, and the UV imprinting processes were performed using a UV curing system

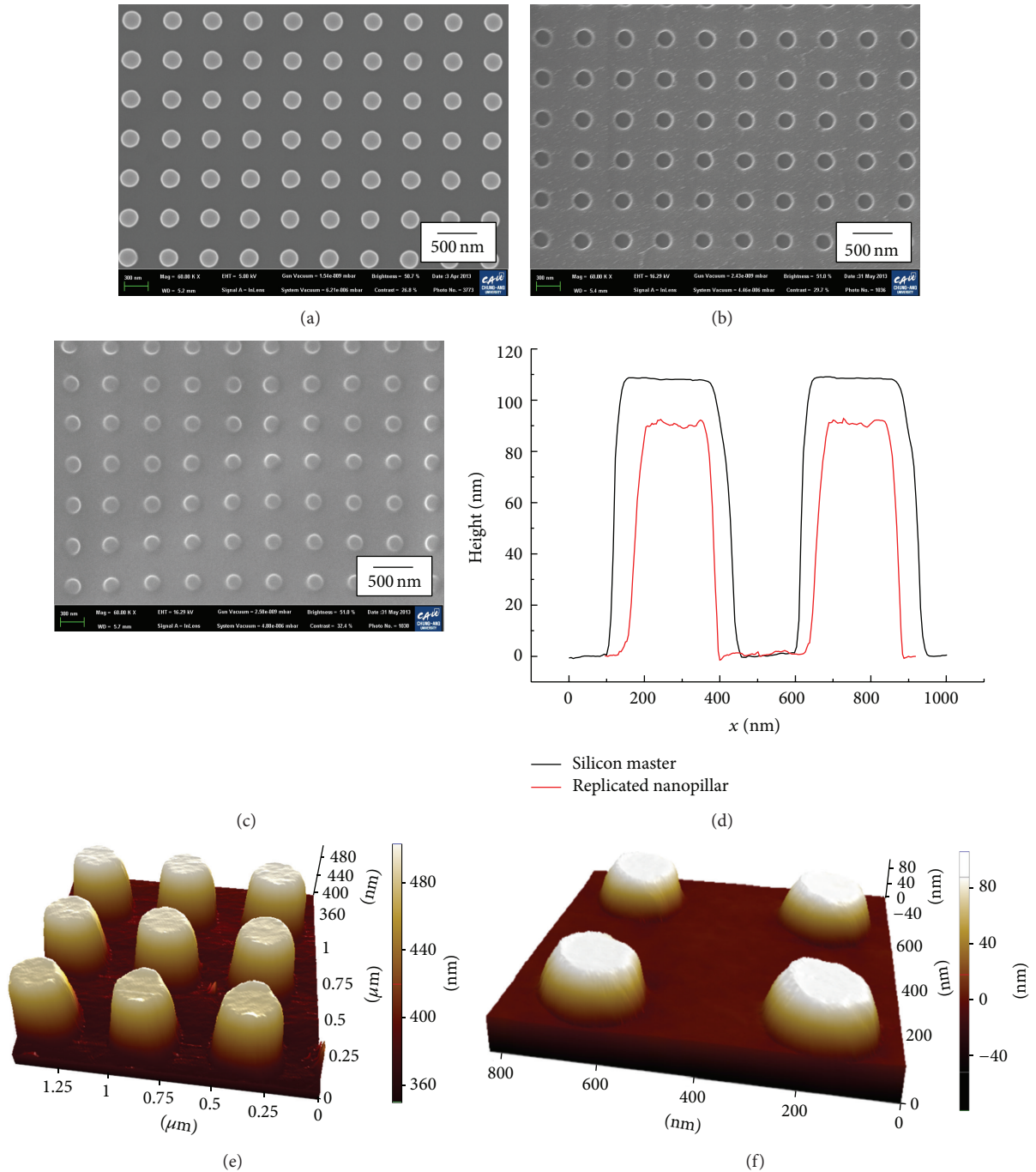


FIGURE 2: SEM of (a) silicon master, (b) polymeric master, and (c) replicated nanopillar pattern. (d) Profile comparison of the silicon master and replicated nanopillar and 3-dimensional surface profiles of (e) silicon master and (f) replicated nanopillar pattern.

(2000 Flood, Dymax). To prevent the replica adhering to the mold, a SAM coating was applied for each of the replication processes. Since a SAM treatment directly on the polymer surface can damage the polymeric structure, a thin film layer of 10 nm  $\text{SiO}_2$  was deposited on the surface of the polymeric replica by e-beam evaporation at  $6 \times 10^{-6}$  torr and a  $0.3 \text{ \AA/s}$  deposition rate, and it was subsequently dipped into a 2% solution of dimethyldichlorosilane dissolved in octamethylcyclotetrasilane (Repel-Silane ES, GE Healthcare

Co., Ltd., USA). After 20 minutes, the sample was rinsed with deionized (DI) water and dried at  $30^\circ\text{C}$ .

### 3. Results and Discussion

Figures 2(a)~2(c) show the scanning electron microscope (SEM) images of the silicon master, polymeric first replica of the silicon master, and the nanopillar pattern replicated from the polymeric master. A field emission-SEM (SIGMA, Carl

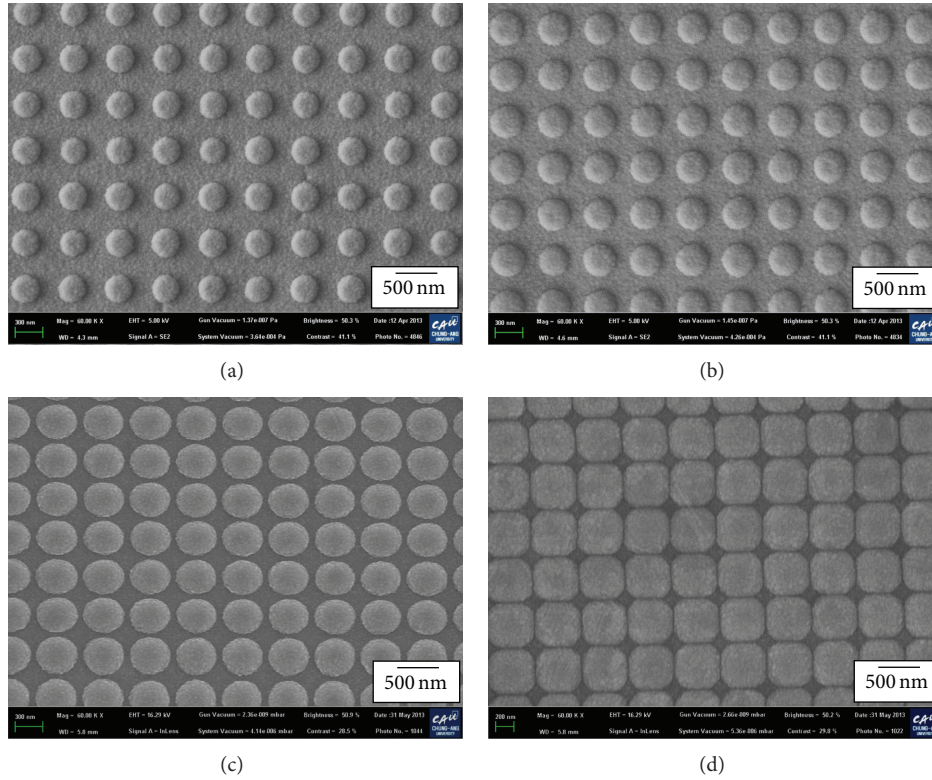


FIGURE 3: SEM images of the fabricated nanodome master with deposited  $\text{SiO}_2$  thicknesses of (a) 50, (b) 100, (c) 150, and (d) 200 nm; EHT of 5 kV was used for (a) and (b) and 16.29 kV was used for (c) and (d).

Zeiss Co., Ltd., Germany) was used for SEM measurement with an EHT of 5.00 kV (for Figure 2(a)) and an EHT of 16.29 kV (for Figures 2(b) and 2(c)). Figures 2(e) and 2(f) show the 3-dimensional surface profiles of the silicon master and the replicated nanopillar obtained by atomic force microscope (AFM) measurements. The AFM measurement was conducted by XE-100 (Park Systems Co., Ltd., Korea) with a noncontact scanning mode and a speed of 0.3 Hz using a noncontact AFM tip (PPP-NCHR-50, Park Systems Co., Ltd., Korea). Figure 2(d) shows the comparison of AFM measured cross-sectional surface profiles of the silicon master and the replicated nanopillar. According to Figure 2(d), the pattern sizes on the replica were slightly smaller than those on the silicon master wafer due to shrinkage of the imprinting material during polymerization and the thin film of  $\text{SiO}_2$  (thickness of 10 nm) deposited for SAM treatment.

Subsequently, the  $\text{SiO}_2$  deposition process was performed on the replicated nanopillar structure to form a dome-shaped structure with 4 different thicknesses (50, 100, 150, and 200 nm) using e-beam evaporation. Figure 3 shows the SEM images of the prepared nanodome master (Figure 1(c)). To evaluate the detailed geometrical properties of the nanodome master, the prepared nanodome samples were measured by AFM. Figure 4 shows the measured profiles of the nanodome master. For deposited  $\text{SiO}_2$  thicknesses of 0, 50, 100, and 150 nm, the diameters of the nanodome base were 246, 300, 353, and 436 nm, respectively (Figure 4). Since the pitch of the pattern was 500 nm, the separation distance of the nanodome

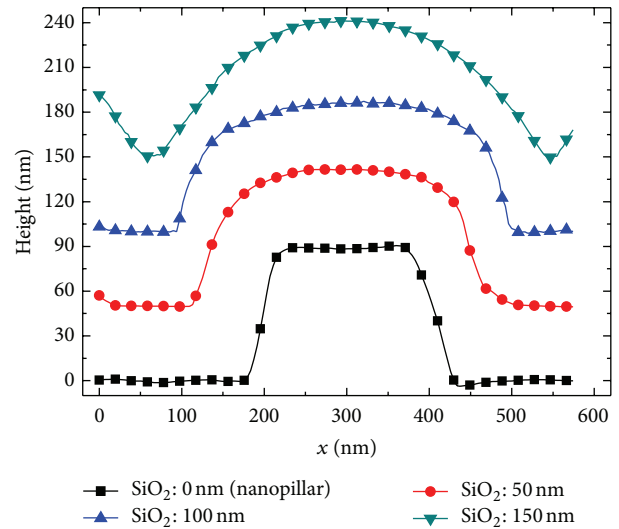


FIGURE 4: AFM of the nanodome master with different  $\text{SiO}_2$  deposition thicknesses.

decreased when the thickness of the  $\text{SiO}_2$  layer increased. As shown in Figure 3(d), when the separation distance is smaller than 0, the structures can evolve into a square shape, which can act as  $\text{SiO}_2$  thickness limitation for forming dome structures. Although the initial pillar pattern has a rectangular cross-sectional shape (Figure 4, black line), it is found

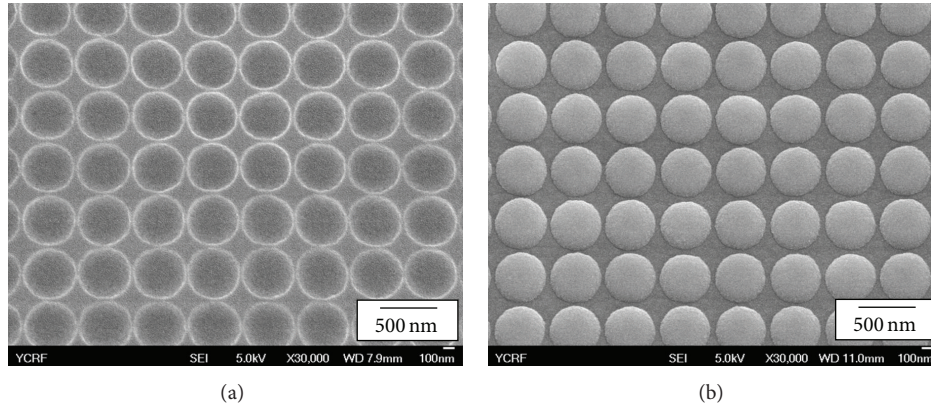


FIGURE 5: SEM images of (a) fabricated nanodome mold with a dome-shaped cavity array and (b) replicated polymeric nanodome on a glass substrate; EHV of 5 kV was used for both measurements.

that the edge of the pattern was rounded as increasing the deposition thickness of the  $\text{SiO}_2$ . At the  $\text{SiO}_2$  layer thickness of 150 nm, we can confirm that the cross-sectional profile of the structure was well matched with dome shape, which can provide gradual refractive index change and good antireflection characteristics. 150 nm was selected for the thickness of the  $\text{SiO}_2$  layer to ensure an improved dome shape.

The fabricated nanodome master was then replicated on a PET film to create a nanodome mold by the UV imprinting process. For the next UV imprinting process, the SAM was coated with the same manner as the previous replication processes with a polymeric mold. Figure 5(a) shows the prepared nanodome mold with a 10 nm  $\text{SiO}_2$  layer and SAM. The nanodome mold was employed to fabricate nanodomies on a glass substrate by the UV imprinting process. The adhesion promoter treatment was performed on the glass substrate. Figure 5(b) shows the fabricated nanodome array.

To evaluate the antireflective performance of the fabricated nanodome array, the transmission spectra through the sample were measured using a spectrophotometer (UV-670 UV-Vis, Jasco Inc., USA) in the wavelength range of 350 to 850 nm. Figure 6 shows the measured transmittance of the flat and nanodome featured glass substrates. While the flat glass substrate showed 88–89% transmittance in the visible range, the transmittance of the nanodome featured glass substrate increased to 91–92%. Since the antireflective nanodome structure was applied to only one side of the glass substrate, the transmittance can be improved up to ~95% when the developed structure is applied to both sides of the glass substrate, because additional antireflection effects can be obtained from the nanodome structured backside surface [7].

#### 4. Conclusions

In this paper, we demonstrated a fabrication method for antireflective nanodome patterns on a glass substrate. A series of UV imprinting processes were performed. First, a polymeric nanopillar array was fabricated by a UV replication process using a silicon nanomaster produced by KrF lithography and reactive ion etching processes. Subsequently,

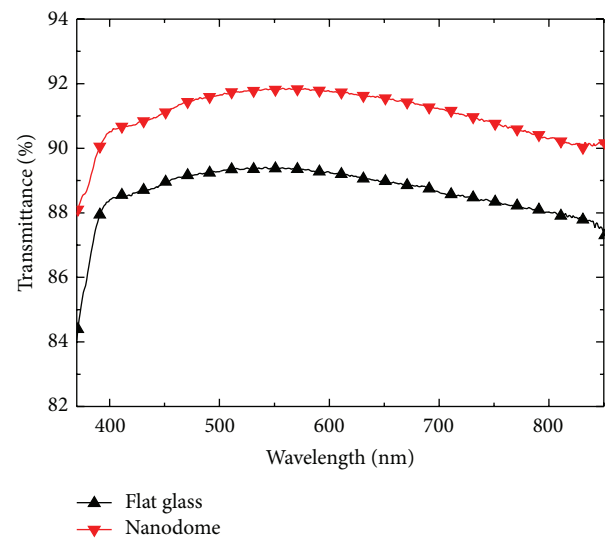


FIGURE 6: Transmittance of the flat and nanodome featured glass substrates.

a 150 nm  $\text{SiO}_2$  layer was deposited on the polymeric nanopillar array to form a nanodome master, and then it was replicated once more to create a nanodome mold. Finally, the antireflective nanodome structure was fabricated using the prepared mold. The SAM coating was applied for each of the replication processes. The dome shape was controlled by the thickness of the  $\text{SiO}_2$  layer. The optical transmittance of the fabricated sample was measured to evaluate the antireflective performance. The transmittance increased by approximately 3% compared to the bare glass substrate with a single-sided feature sample. Although we deposited  $\text{SiO}_2$  layer on the nanoimprinted pillar array to examine the effects of shape change while preserving the expensive silicon master pattern, the proposed nanodome master fabrication method by the deposition of  $\text{SiO}_2$  layer on the photolithographed silicon pillar array can be directly applied to the photolithographed silicon pillar array. We believe that the nanodome master fabrication process using photolithographed silicon pillar array and physical vapor

deposited SiO<sub>2</sub> layer can provide a uniform and defect-free nanodome master pattern in large area (up to 300 mm), because the photolithography and physical deposition processes are the industrially well-established techniques. This fabrication method can be used to create antireflective surfaces for various applications such as solar cells, illumination, and imaging optics.

### Conflict of Interests

The authors declare that there is no conflict of interests regarding the publication of this paper.

### Acknowledgments

This work was supported by the Human Resources Program in Energy Technology of the Korea Institute of Energy Technology Evaluation and Planning (KETEP) granted financial resource from the Ministry of Trade, Industry & Energy, Republic of Korea (no. 20134030200350) and was also supported by the Chung-Ang University Research Scholarship Grants in 2013.

### References

- [1] H. K. Raut, V. A. Ganesh, A. S. Nair, and S. Ramakrishna, "Anti-reflective coatings: a critical, in-depth review," *Energy & Environmental Science*, vol. 4, pp. 3779–3804, 2011.
- [2] S. Hong, B. Bae, K. Han, E. Hong, H. Lee, and K. Choi, "Imprinted moth-eye antireflection patterns on glass substrate," *Electronic Materials Letters*, vol. 5, no. 1, pp. 39–42, 2009.
- [3] J. W. Leem, D. H. Joo, and J. S. Yu, "Biomimetic parabola-shaped AZO subwavelength grating structures for efficient antireflection of Si-based solar cells," *Solar Energy Materials & Solar Cells*, vol. 95, no. 8, pp. 2221–2227, 2011.
- [4] K. M. A. Sobahan, Y. J. Park, J. J. Kim, and C. K. Hwangbo, "Nanostructured porous SiO<sub>2</sub> films for antireflection coatings," *Optics Communications*, vol. 284, no. 3, pp. 873–876, 2011.
- [5] M. Sun, A. Liang, Y. Zheng, G. S. Watson, and J. A. Watson, "A study of the anti-reflection efficiency of natural nano-arrays of varying sizes," *Bioinspiration & Biomimetics*, vol. 6, no. 2, Article ID 026003, 2011.
- [6] Y. M. Song, H. J. Choi, J. S. Yu, and Y. T. Lee, "Design of highly transparent glasses with broadband antireflective subwavelength structures," *Optics Express*, vol. 18, no. 12, pp. 13063–13071, 2010.
- [7] K. Han, J. Shin, and H. Lee, "Enhanced transmittance of glass plates for solar cells using nano-imprint lithography," *Solar Energy Materials & Solar Cells*, vol. 94, no. 3, pp. 583–587, 2010.
- [8] W. C. Luk, K. M. Yeung, K. C. Tam et al., "Enhanced conversion efficiency of polymeric photovoltaic cell by nanostructured antireflection coating," *Organic Electronics*, vol. 12, no. 4, pp. 557–561, 2011.
- [9] T. Søndergaard, J. Gadegaard, P. K. Kristensen, T. K. Jensen, T. G. Pedersen, and K. Pedersen, "Guidelines for 1D-periodic surface microstructures for antireflective lenses," *Optics Express*, vol. 18, no. 25, pp. 26245–26258, 2010.
- [10] S. Kim, W. Zhang, and B. T. Cunningham, "Coupling discrete metal nanoparticles to photonic crystal surface resonant modes and application to Raman spectroscopy," *Optics Express*, vol. 18, no. 5, pp. 4300–4309, 2010.
- [11] Y. Han, E. Byeon, J. Kim, and S. Kim, "A simulation model considering sidewall deposition for the precise prediction of the performance of label-free photonic-crystal biosensors," *Journal of Nano Science and Nano Technology*, vol. 12, no. 7, pp. 5429–5434, 2012.
- [12] S.-J. Liu and W.-A. Chen, "Nanofeatured anti-reflective films manufactured using hot roller imprinting and self-assembly nanosphere lithography," *Optics & Laser Technology*, vol. 48, pp. 226–234, 2013.
- [13] C. J. Choi, Z. Xu, H. Wu, G. L. Liu, and B. T. Cunningham, "Surface-enhanced Raman nanodomains," *Nanotechnology*, vol. 21, no. 41, Article ID 415301, 2010.

## Research Article

# Graphene-Tapered ZnO Nanorods Array as a Flexible Antireflection Layer

**Taeseup Song**

*School of Materials Science and Engineering, Yeungnam University, Gyeongsan 712-749, Republic of Korea*

Correspondence should be addressed to Taeseup Song; [tsong@yu.ac.kr](mailto:tsong@yu.ac.kr)

Received 21 May 2015; Revised 9 July 2015; Accepted 13 July 2015

Academic Editor: Xiaogang Han

Copyright © 2015 Taeseup Song. This is an open access article distributed under the Creative Commons Attribution License, which permits unrestricted use, distribution, and reproduction in any medium, provided the original work is properly cited.

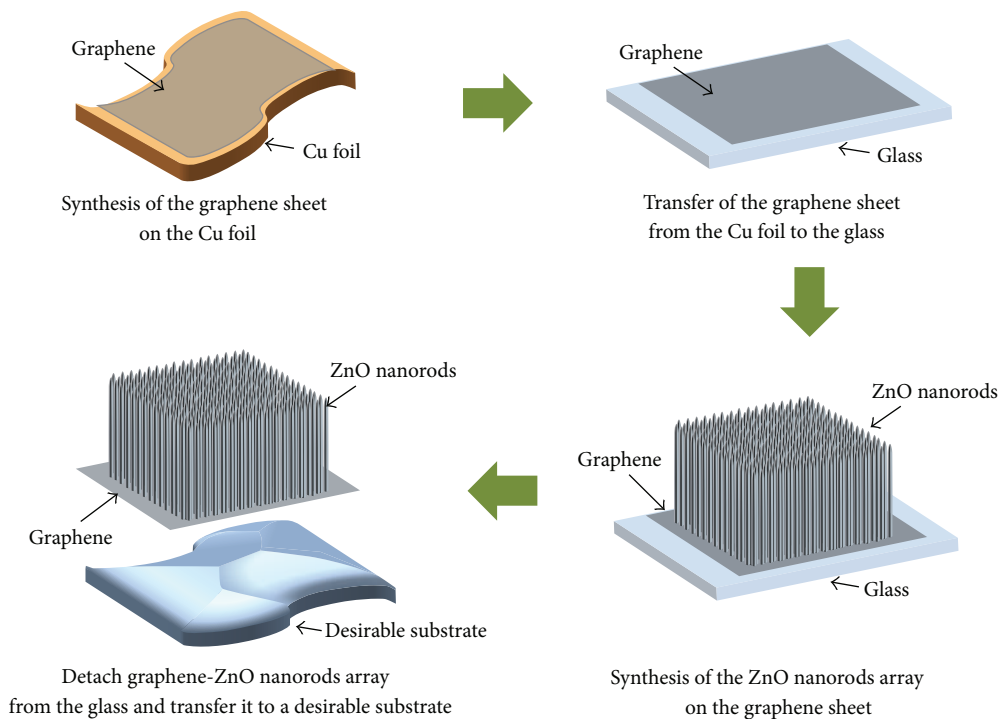
Flexible solar cells have drawn a great deal of attention due to their various advantages including deformable and wearable characteristics. In the solar cells, the antireflection layer plays an important role in the improvement in the conversion efficiency by increasing the light transmission and suppressing the Fresnel refraction. For the successful implantation of the antireflection layer into the flexible solar cells, the flexible mechanical property of the antireflection layer is also necessary. However, the study on flexible antireflection layer for the flexible solar cells or optoelectronics is still lacking. In this study, we report the graphene-tapered ZnO nanorods array as a flexible antireflection layer for the application in flexible solar cells. Flexible two-dimensional graphene sheet and the tapered morphology of ZnO nanorods enable conformal coverage on the flexible substrate with curved surface and significant improvements in antireflection properties, respectively.

## 1. Introduction

Flexible solar cells have drawn a great deal of attention in recent years due to their various advantages including lightweight, deformable, and wearable characteristics [1, 2]. Significant advances in both the performance and the processability have been achieved *via* engineering in active materials [3–5] and cell structures [6–8]. Antireflection layer is considered as an indispensable component in solar cells as it plays an important role in the improvement in the conversion efficiency of solar cells by increasing the light transmission and suppressing the Fresnel refraction of a material over a broad range of wavelengths [9–11]. Although many studies on flexible solar cells were carried out, the study on antireflection layer for the flexible solar cells or optoelectronics is still lacking. Recently, the transparent paper-based antireflection coating method was reported to improve the solar cells efficiency, which shows the possibility of utilizing it in the flexible solar cells [12–14]. However, further study should be carried out for its practical use.

Among various antireflection materials, ZnO, which is a semiconducting material with a wide-direct band gap of 3.37 eV, has been considered as a promising candidate owing

to its high transmittance and appropriate refractive index ( $n = 2$ , at a wave length of 600 nm) associated with that of air ( $n = 1$ ). In particular, ZnO nanorods array, with vertically aligned one-dimensional geometry, shows promise due to ability to form textured coating via anisotropic growth and its significant surface to volume ratio [15–17]. Chung et al. demonstrated that ZnO nanorods array enables the significant improvement in the light trapping and the reduction in Fresnel reflection resulting from the grading in the reflection index by avoiding the abrupt transition at the air/solar cells interface [18]. Furthermore, antireflection property of ZnO nanorods array could be further improved by engineering the morphology at the tip. Lee et al. demonstrated that tapering at the tip of ZnO nanorod leads to significant improvement in antireflection property by the elimination of interference fringes through roughening of the air-ZnO interface [19]. Graphene, a single-layered two-dimensional carbon sheet with a hexagonal packed lattice structure, has also received significant attention for the various applications including an active material for the electronic devices, a sacrificial template for the synthesis of 2D materials and due to its unique physicochemical properties. In particular, excellent mechanical properties of graphene sheet, the breaking



SCHEME 1: Schematic illustration of the fabrication process of the flexible graphene-ZnO nanorods array.

strength of  $42 \text{ N m}^{-1}$  and Young's modulus of  $1.0 \text{ TPa}$ , enables its practical use as a flexible and transparent electrode for various flexible devices [20]. Wang et al. demonstrated that the device thickness plays an important role on conformal contact between the flexible device and the desirable substrate [21]. Graphene could be the promising substrate for the fabrication of flexible antireflection layer based on ZnO nanorods array due to above mentioned advantages.

In this study, we report graphene-tapered ZnO nanorods array as a flexible antireflection layer for the flexible solar cells application. Flexible two-dimensional graphene sheet enables conformal coverage on the curved and bumpy surface even under highly bended condition. Our designed graphene-tapered ZnO nanorods array on the polydimethylsiloxane (PDMS) substrate exhibited robust antireflection properties after several bending experiences. We achieve robust and excellent antireflection properties on the bumpy surface by combining the advantages of the flexibility from the graphene sheet and significantly improved antireflection properties from tapered ZnO nanorods array.

## 2. Materials and Methods

The graphene sheet was synthesized on  $25 \mu\text{m}$  thick copper foil by chemical vapor deposition method at  $1,000^\circ\text{C}$  under a  $30\text{--}50 \text{ sccm}$  of  $\text{CH}_4$  for 30 min. The synthesis of graphene sheet is described elsewhere in detail [22]. ZnO thin film as a seed layer for the synthesis of ZnO nanorods was deposited on the graphene using radio frequency magnetron sputtering. The typical ZnO nanorods were synthesized using a hydrothermal method. ZnO seed layer coated

substrate was immersed into aqueous solution containing  $0.025 \text{ M}$  zinc nitrate hexahydrate (Sigma-Aldrich) and  $0.025 \text{ M}$  hexamethylenetetramine (Sigma-Aldrich) at  $80^\circ\text{C}$ . 1,3-Diaminopropane (Aldrich,  $190 \text{ mM}$ ) was added into the precursor solution to synthesize tapered ZnO nanorods. The typical and tapered ZnO nanorods grown on the graphene substrate were washed by deionized water. Detailed synthesis method for ZnO nanorods array is described elsewhere [19, 23]. The polydimethylsiloxane (PDMS, Sylgard 184, Dow Corning), with base to cross-linking agent with a mass ratio of  $10:1$ , was employed as a flexible substrate to evaluate the optical properties of graphene-ZnO nanorods array as an antireflection layer on the flexible substrate. As synthesized samples were characterized using a field emission scanning electron microscope (FE-SEM, S-4700, Hitachi, Hitachi City, Japan), X-ray diffraction (PANalytical X'Pert, Almelo, Netherlands), and optical microscope (Olympus U-TV 0.5XC2, Japan). Optical properties were evaluated using Varian Carry 5000 model UV-vis-NIR spectrophotometer.

## 3. Results and Discussion

Scheme 1 demonstrates the fabrication process of graphene-ZnO nanorods array. Graphene sheet is synthesized on the Cu foil using chemical vapor deposition method and then carefully transferred to the slide glass by selective etching of metal foil. Typical ZnO nanorods and tapered ZnO nanorods arrays were synthesized on the graphene sheet using hydrothermal method. (Please see the experimental part for detailed information). The graphene-ZnO nanorods

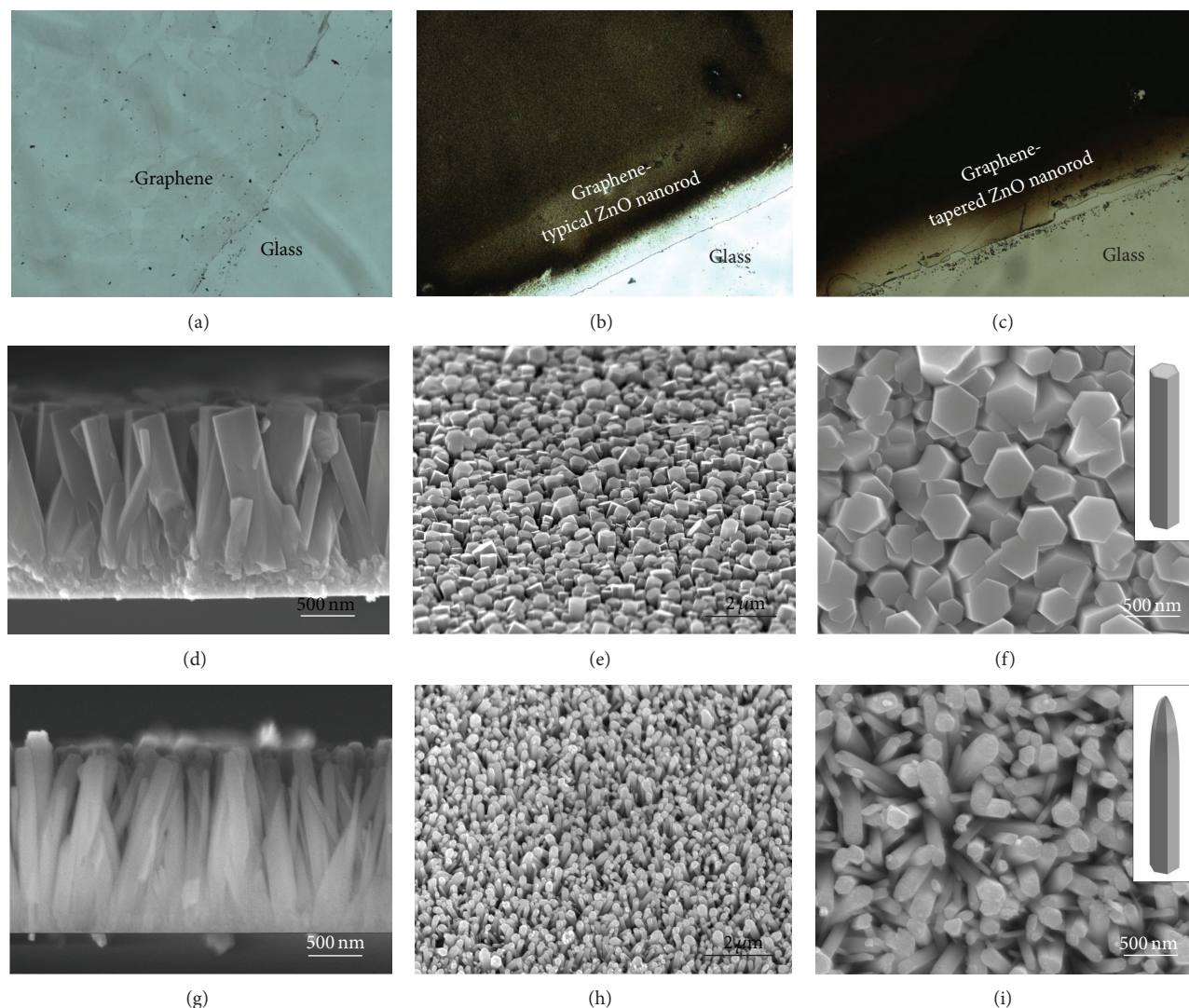


FIGURE 1: Photographs and SEM images of graphene (a), graphene-typical ZnO nanorods array ((b), (d)–(f)), and graphene-tapered ZnO nanorods array ((c), (g)–(i)). Cross-sectional SEM images ((d) and (g)), low magnification tilted view ((e) and (h)), and high magnification tilted view ((f) and (i)).

array was detached from the slide glass and then transferred to the desirable surface of the devices.

Figure 1 presents the photographs and scanning electron microscopy (SEM) images of the graphene sheet and ZnO nanorods arrays on the graphene sheet. As shown in Figure 1(a), graphene sheet was successfully transferred to the slide glass from the Cu foil. As shown in cross-sectional SEM images (Figures 1(d) and 1(g)), the length of typical ZnO nanorods and tapered ZnO nanorods grown on the graphene sheet is identical ( $\sim 2 \mu\text{m}$ ). The tilted SEM images show the vertically aligned geometry of both ZnO nanorods arrays. The flat top and tapered shape at the tip are clearly observed in typical ZnO nanorods and tapered ZnO nanorods, respectively, in high magnification SEM images. The insets in Figures 1(f) and 1(i) present schematic illustration of the morphologies of typical ZnO and tapered ZnO nanorods. The densities of both ZnO nanorods arrays

are about  $9 \times 10^8/\text{cm}^2$ . Typical ZnO nanorod and tapered ZnO nanorod have the diameters of 300 nm and 50 nm at the tip, respectively.

X-ray diffraction (XRD) analysis was carried out to study the crystallinity and orientations of typical ZnO nanorods and tapered ZnO nanorods arrays on the graphene sheet. In Figure 2(a) no noticeable difference between both ZnO nanorods arrays was observed in XRD result. Both ZnO nanorods arrays exhibit diffraction peaks at  $2\theta = 34.4^\circ$  and  $63.4^\circ$ , corresponding to the (002) and (103) planes of the hexagonal wurtzite ZnO phase. A strong peak at  $2\theta = 34.4^\circ$  indicates the preferred growth direction of ZnO phase with (002). Raman spectroscopy was employed to further investigate the structural characterizations of graphene sheet, graphene-typical ZnO nanorods array and graphene-tapered ZnO nanorods array. In Figure 2(b) the graphene sheet presents the typical Raman spectrum of one layer

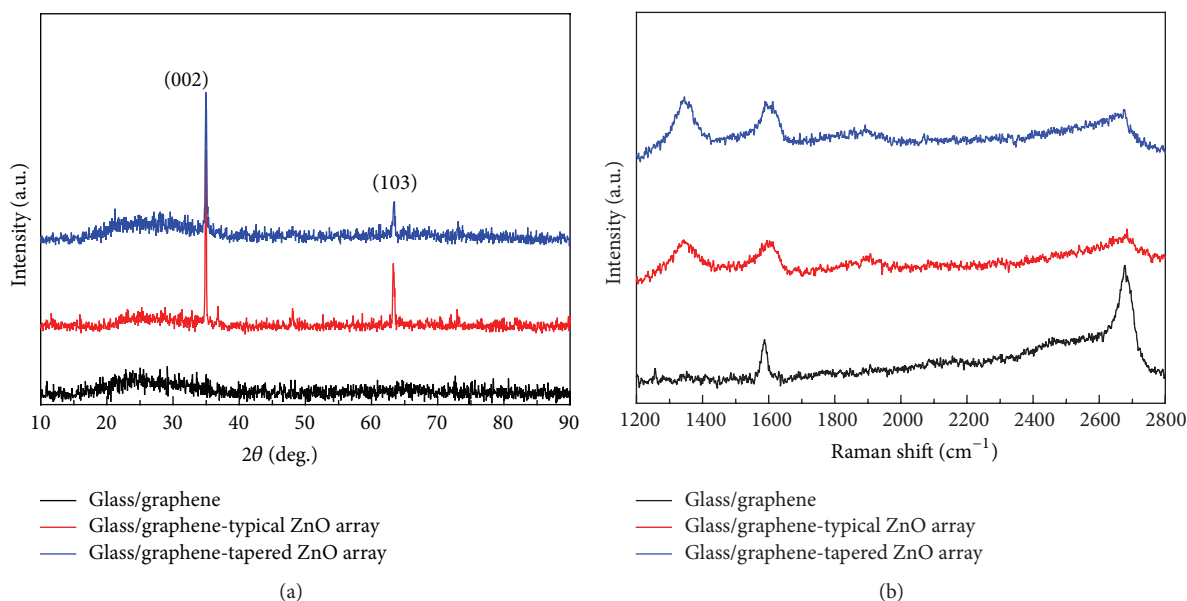


FIGURE 2: XRD (a) and Raman (b) data for graphene, graphene-typical ZnO nanorods array, and graphene-tapered ZnO nanorods array.

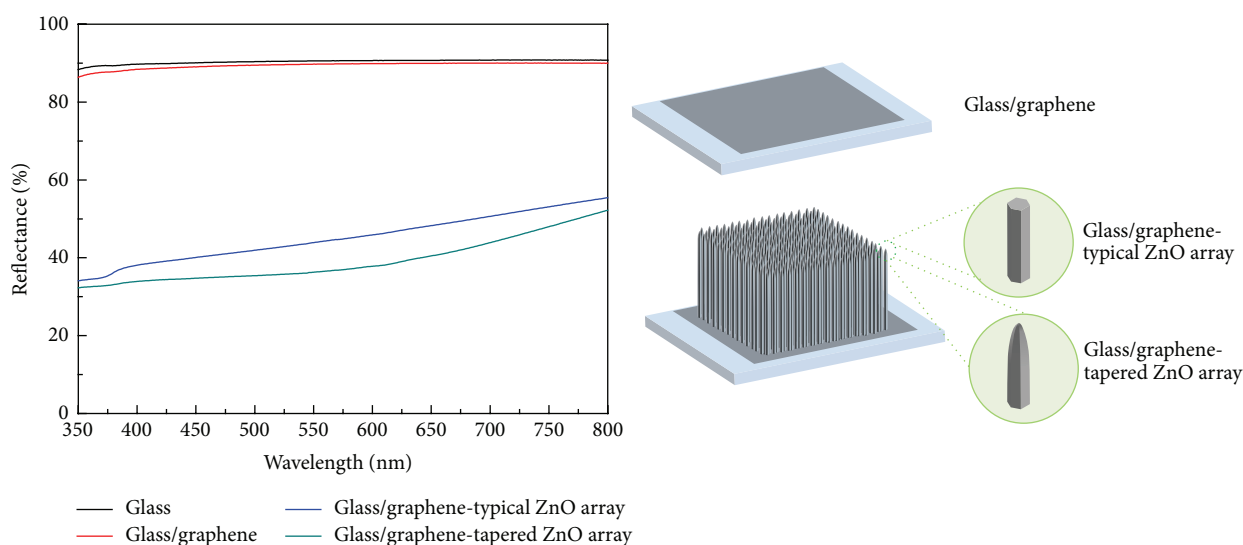


FIGURE 3: Reflectance spectra of glass/graphene, glass/graphene-typical ZnO array, and glass/graphene-tapered ZnO array.

graphene [22]. The new peak at  $1345\text{ cm}^{-1}$  assigned to D band was generated after ZnO nanorods growth regardless of their shape at the tip, which indicates a reduction of the average size of the  $\text{sp}^2$  domains and the generation of defects after ZnO nanorods growth [24–26]. We also carefully measured the Raman spectrum of the graphene-tapered ZnO nanorods arrays after their transfer from the glass to the flat and rough PDMS substrate. The results are exhibited in Figure S1, in Supplementary Material available online at <http://dx.doi.org/10.1155/2015/925863>, a noticeable difference in the spectra was not observed before/after the transfer of the graphene-tapered ZnO nanorods arrays, which indicates that the graphene layer was successfully transferred to the flat and rough PDMS substrate.

The reflectance spectra for graphene, graphene-ZnO nanorods, and graphene-tapered ZnO nanorods arrays on the glass were evaluated to determine their antireflection properties in the wave length range from 350 nm to 400 nm using the standard UV-vis spectrometer. In Figure 3, the reflectance of the bare glass was also measured for comparison. Graphene sheet does not provide any antireflection property on the glass. However, both graphene-ZnO nanorods and graphene-tapered ZnO nanorods arrays coated glass exhibited significantly low reflectance over a wide range of wavelengths compared to graphene coated glass, which results from the textured coating via anisotropic growth and appropriate refractive index [27, 28]. As expected, the tapered ZnO nanorods array coated glass shows further improved

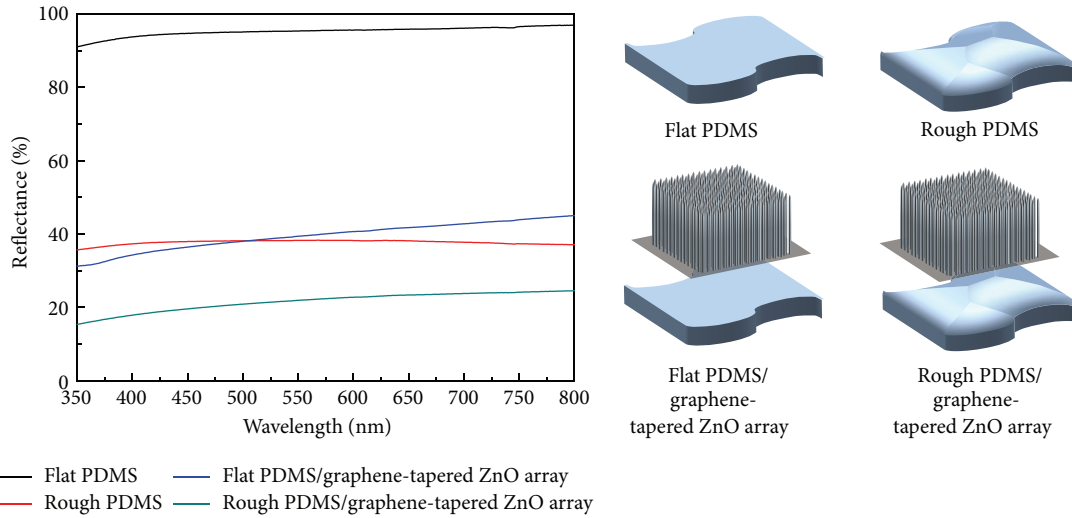


FIGURE 4: Reflectance spectra of flat PDMS, rough PDMS, flat PDMS/graphene-tapered ZnO array, and rough PDMS/graphene-tapered ZnO array.

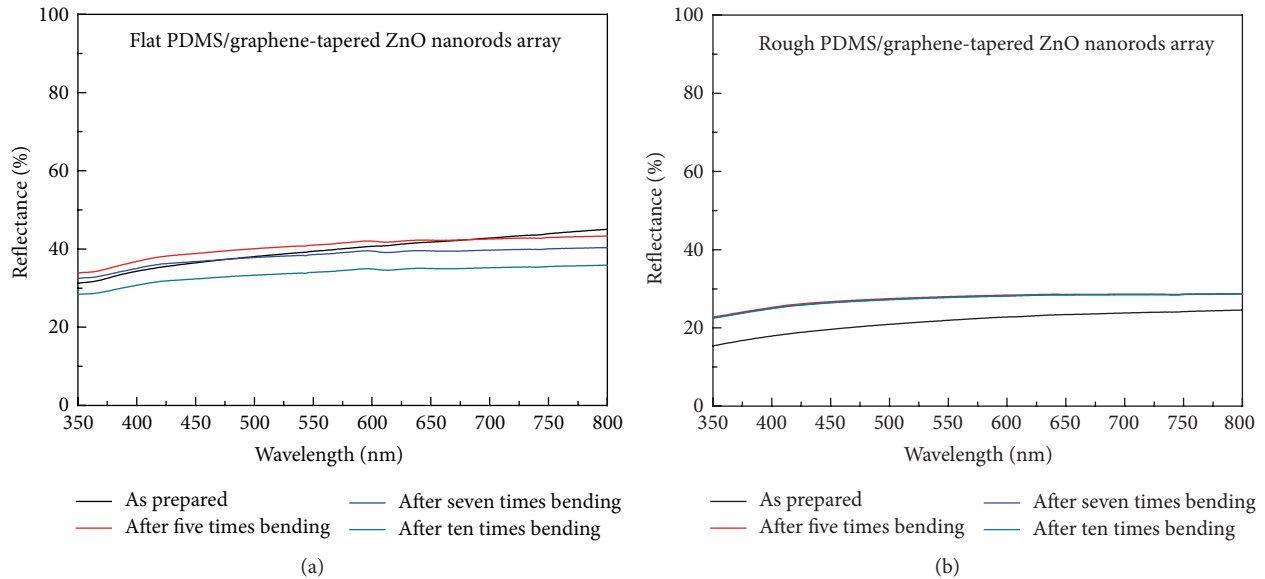


FIGURE 5: Reflectance spectra of flat (a) and rough (b) PDMS/graphene-tapered ZnO nanorods array as a function of the number of times being bended.

antireflection property, which is attributed to the elimination of interference fringes through roughening of the air-ZnO interface [19].

In order to study the antireflection properties of the graphene-tapered ZnO nanorods array on the flexible substrate with rough surface, two types of PDMS with flat surface and bumpy surface were prepared as a substrate for this study (Figure 4). The PDMS with rough surface exhibits much reduced reflectance compared to that of flat PDMS due to texturing effect. While the graphene-tapered ZnO nanorods array coated flat PDMS substrate presents comparable antireflection property with that of PDMS with rough surface, the graphene-tapered ZnO nanorods array coated PDMS with rough surface has the lowest reflectance, which indicates that

the graphene-tapered ZnO nanorods array was conformably transferred to the flexible substrate with the rough surface. The mechanical properties of the PDMS/graphene-tapered ZnO nanorods array were evaluated as a function of the number of times being bended (Figure 5). Both the flat and rough PDMS/graphene-tapered ZnO nanorods array exhibited robust antireflection properties even after several bending experiences without the degradation of its mechanical properties.

#### 4. Conclusion

In this study, we explored the antireflection properties of graphene-ZnO nanorods and graphene-tapered ZnO

nanorods arrays for the application in flexible solar cells. The graphene-tapered ZnO nanorods array shows excellent antireflection performance compared to that of the graphenotypical ZnO nanorods array. Furthermore, the graphene-tapered ZnO nanorods array is successfully transferred to the flexible substrate with the rough surface without degradation in mechanical and optical properties. Our design strategy for flexible antireflection layer could be extended to other optoelectronics.

## Conflict of Interests

The author declares that there is no conflict of interests regarding the publication of this paper.

## Acknowledgment

This work was supported by the 2015 Yeungnam University research grant (215A580031).

## References

- [1] V. Galstyan, A. Vomiero, I. Concina et al., "Vertically aligned TiO<sub>2</sub> nanotubes on plastic substrates for flexible solar cells," *Small*, vol. 7, no. 17, pp. 2437–2442, 2011.
- [2] Z. Y. Fan, H. Razavi, J.-W. Do et al., "Three-dimensional nanopillar-array photovoltaics on low-cost and flexible substrates," *Nature Materials*, vol. 8, no. 8, pp. 648–653, 2009.
- [3] Z. D. Li, Y. Zhou, C. X. Bao et al., "Vertically building Zn<sub>2</sub>SnO<sub>4</sub> nanowire arrays on stainless steel mesh toward fabrication of large-area, flexible dye-sensitized solar cells," *Nanoscale*, vol. 4, no. 11, pp. 3490–3494, 2012.
- [4] P. Docampo, J. M. Ball, M. Darwich, G. E. Eperon, and H. J. Snaith, "Efficient organometal trihalide perovskite planar-heterojunction solar cells on flexible polymer substrates," *Nature Communications*, vol. 4, article 2761, 2013.
- [5] S.-I. Na, S.-S. Kim, J. Jo, and D.-Y. Kim, "Efficient and flexible ITO-free organic solar cells using highly conductive polymer anodes," *Advanced Materials*, vol. 20, no. 21, pp. 4061–4067, 2008.
- [6] L. Hu, H. S. Kim, J.-Y. Lee, P. Peumans, and Y. Cui, "Scalable coating and properties of transparent, flexible, silver nanowire electrodes," *ACS Nano*, vol. 4, no. 5, pp. 2955–2963, 2010.
- [7] Z. K. Liu, J. H. Li, and F. Yan, "Package-free flexible organic solar cells with graphene top electrodes," *Advanced Materials*, vol. 25, no. 31, pp. 4296–4301, 2013.
- [8] C. Lungenschmied, G. Dennler, H. Neugebauer et al., "Flexible, long-lived, large-area, organic solar cells," *Solar Energy Materials and Solar Cells*, vol. 91, no. 5, pp. 379–384, 2007.
- [9] C.-J. Ting, F.-Y. Chang, C.-F. Chen, and C. P. Chou, "Fabrication of an antireflective polymer optical film with subwavelength structures using a roll-to-roll micro-replication process," *Journal of Micromechanics and Microengineering*, vol. 18, no. 7, Article ID 075001, 2008.
- [10] Z. N. Adamian, A. P. Hakhoyan, V. M. Aroutiounian, R. S. Barseghian, and K. Touryan, "Investigations of solar cells with porous silicon as antireflection layer," *Solar Energy Materials and Solar Cells*, vol. 64, no. 4, pp. 347–351, 2000.
- [11] Z. Z. Wu, J. Walsh, A. Nolte, L. Zhai, R. E. Cohen, and M. F. Rubner, "Deformable antireflection coatings from polymer and nanoparticle multilayers," *Advanced Materials*, vol. 18, no. 20, pp. 2699–2702, 2006.
- [12] D. Ha, J. Murray, Z. Q. Fang, L. B. Hu, and J. N. Munday, "Advanced broadband antireflection coatings based on cellulose microfiber paper," *IEEE Journal of Photovoltaics*, vol. 5, no. 2, pp. 577–583, 2015.
- [13] Z. Q. Fang, H. L. Zhu, Y. B. Yuan et al., "Novel nanostructured paper with ultrahigh transparency and ultrahigh haze for solar cells," *Nano Letters*, vol. 14, no. 2, pp. 765–773, 2014.
- [14] D. Ha, Z. Q. Fang, L. B. Hu, and J. N. Munday, "Paper-based anti-reflection coatings for photovoltaics," *Advanced Energy Materials*, vol. 4, no. 9, Article ID 1301804, 2014.
- [15] Y.-C. Chao, C.-Y. Chen, C.-A. Lin, Y.-A. Dai, and J.-H. He, "Antireflection effect of ZnO nanorod arrays," *Journal of Materials Chemistry*, vol. 20, no. 37, pp. 8134–8138, 2010.
- [16] L.-K. Yeh, K.-Y. Lai, G.-J. Lin et al., "Giant efficiency enhancement of GaAs solar cells with graded antireflection layers based on syringelike ZnO nanorod arrays," *Advanced Energy Materials*, vol. 1, no. 4, pp. 506–510, 2011.
- [17] M. K. Kim, D. K. Yi, and U. Paik, "Tunable, flexible antireflection layer of ZnO nanowires embedded in PDMS," *Langmuir*, vol. 26, no. 10, pp. 7552–7554, 2010.
- [18] R.-J. Chung, Z.-C. Lin, C.-A. Lin, and K.-Y. Lai, "Study of an antireflection surface constructed of controlled ZnO nanostructures," *Thin Solid Films*, vol. 570, pp. 504–509, 2014.
- [19] Y.-J. Lee, D. S. Ruby, D. W. Peters, B. B. McKenzie, and J. W. P. Hsu, "ZnO nanostructures as efficient antireflection layers in solar cells," *Nano Letters*, vol. 8, no. 5, pp. 1501–1505, 2008.
- [20] X. Huang, X. Y. Qi, F. Boey, and H. Zhang, "Graphene-based composites," *Chemical Society Reviews*, vol. 41, no. 2, pp. 666–686, 2012.
- [21] S. D. Wang, M. Li, J. Wu et al., "Mechanics of epidermal electronics," *Journal of Applied Mechanics*, vol. 79, no. 3, Article ID 031022, 2012.
- [22] X. S. Li, W. W. Cai, J. H. An et al., "Large-area synthesis of high-quality and uniform graphene films on copper foils," *Science*, vol. 324, no. 5932, pp. 1312–1314, 2009.
- [23] T. Song, J. L. Xia, J.-H. Lee et al., "Arrays of sealed silicon nanotubes as anodes for lithium ion batteries," *Nano Letters*, vol. 10, no. 5, pp. 1710–1716, 2010.
- [24] S. Z. Liu, H. Q. Sun, A. Suvorova, and S. B. Wang, "One-pot hydrothermal synthesis of ZnO-reduced graphene oxide composites using Zn powders for enhanced photocatalysis," *Chemical Engineering Journal*, vol. 229, pp. 533–539, 2013.
- [25] Q.-P. Luo, X.-Y. Yu, B.-X. Lei, H.-Y. Chen, D.-B. Kuang, and C.-Y. Su, "Reduced graphene oxide-hierarchical ZnO hollow sphere composites with enhanced photocurrent and photocatalytic activity," *The Journal of Physical Chemistry C*, vol. 116, no. 14, pp. 8111–8117, 2012.
- [26] A. Eckmann, A. Felten, A. Mishchenko et al., "Probing the nature of defects in graphene by Raman spectroscopy," *Nano Letters*, vol. 12, no. 8, pp. 3925–3930, 2012.
- [27] X. X. Pu, J. Liu, J. S. Liang et al., "Effective CdS/ZnO nanorod arrays as antireflection coatings for light trapping in c-Si solar cells," *RSC Advances*, vol. 4, no. 44, pp. 23149–23154, 2014.
- [28] S.-H. Baek, B.-Y. Noh, I.-K. Park, and J. H. Kim, "Fabrication and characterization of silicon wire solar cells having ZnO nanorod antireflection coating on Al-doped ZnO seed layer," *Nanoscale Research Letters*, vol. 7, article 29, 2012.

## Research Article

# Synthesis and Structural Characterization of Al<sub>2</sub>O<sub>3</sub>-Coated MoS<sub>2</sub> Spheres for Photocatalysis Applications

S. V. Prabhakar Vattikuti and Chan Byon

*School of Mechanical Engineering, Yeungnam University, Gyeongsan 712-749, Republic of Korea*

Correspondence should be addressed to Chan Byon; [cbyon@ynu.ac.kr](mailto:cbyon@ynu.ac.kr)

Received 8 April 2015; Revised 21 May 2015; Accepted 27 May 2015

Academic Editor: Junyou Yang

Copyright © 2015 S. V. P. Vattikuti and C. Byon. This is an open access article distributed under the Creative Commons Attribution License, which permits unrestricted use, distribution, and reproduction in any medium, provided the original work is properly cited.

This paper reports the synthesis of novel monodisperse Al<sub>2</sub>O<sub>3</sub>-coated molybdenum disulfide nanospheres (i.e., core-shell structures) using a one-step facile hydrothermal method. XPS analysis confirmed the purity and stable structure of the Al<sub>2</sub>O<sub>3</sub>-coated MoS<sub>2</sub> nanospheres. A possible growth mechanism of the core-shell structure is also reported, along with their influence on the photodegradation process of rhodamine B (RhB). The Al<sub>2</sub>O<sub>3</sub>-coated MoS<sub>2</sub> nanospheres demonstrate good photocatalytic activity and chemical stability compared to MoS<sub>2</sub> spheres. TG-DTA analysis provided insight into the decomposition process of the precursor solution and the stability of the nanoparticles. The enhanced photocatalytic activity makes the Al<sub>2</sub>O<sub>3</sub>-coated MoS<sub>2</sub> nanospheres a promising candidate as a photocatalyst that could be used in place of traditional Al<sub>2</sub>O<sub>3</sub>/MoS<sub>2</sub> photocatalyst for the removal of pollutants from waste water.

## 1. Introduction

Molybdenum disulfide (MoS<sub>2</sub>) is one of the important transition metal dichalcogenides (TMDs) with indirect band gap (1.23 eV) semiconductor characteristics [1]. Because of their outstanding properties like mechanical-to-electrochemical capabilities, MoS<sub>2</sub> is used in wide spectrum of applications in catalytic support materials [2, 3], solar cells [4], batteries [5], solid lubricants [6], and gas sensors [7]. These unique properties have attracted many researchers to design new synthesis approaches for uniform and well-controlled MoS<sub>2</sub> nanostructures. Synthesis methods include chemical vapor deposition [8], wetness impregnation method [9], hydrothermal methods [10], and solid state reaction [11]. These techniques have been used to prepare various morphologies of MoS<sub>2</sub>, like fullerene-like (IF) structures, nanoflowers, nanorods, nanosheets, nanoplates, and nanospheres.

In a recent report, Wang et al. demonstrated that carbon-decorated MoS<sub>2</sub> nanospheres have better cycling performance with good capacity as a Na-iron battery anode [12]. MoS<sub>2</sub> is clearly one of the most significantly and broadly used TMDs for transistors due to its favorable band gap

compared to graphene. In addition, MoS<sub>2</sub> is also a suitable candidate for photocatalytic materials. MoS<sub>2</sub> is an indirect narrow-band-gap semiconductor with good stability against photocorrosion in solution [13]. General issues with semiconductor catalysts in the conversion of solar energy to hydrogen are poor charge transport ability, slow kinetics for evolution reactions, poor stability, and the hydrophobic nature of the catalyst [14, 15]. On the other hand, individual MoS<sub>2</sub> catalyst has lower charge separation due to its poor crystallinity.

Despite previous efforts, there has been no material system that can simultaneously satisfy all the criteria for cost-effective photoelectrochemical hydrogen production, and new materials with new properties are needed. To overcome these problems, core-shell structures of MoS<sub>2</sub> coupled with another material with different activity are promising. Such structures could enable charge separation by gathering electrons and holes. The major parameters for the selection of shell materials are band alignment and small lattice mismatch between the core and shell materials [16]. There are very few studies that have focused on preparing MoS<sub>2</sub> nanosphere structures. Wu et al. [17] synthesized MoS<sub>2</sub> microspheres (with diameter up to 2 μm) using a solvothermal method

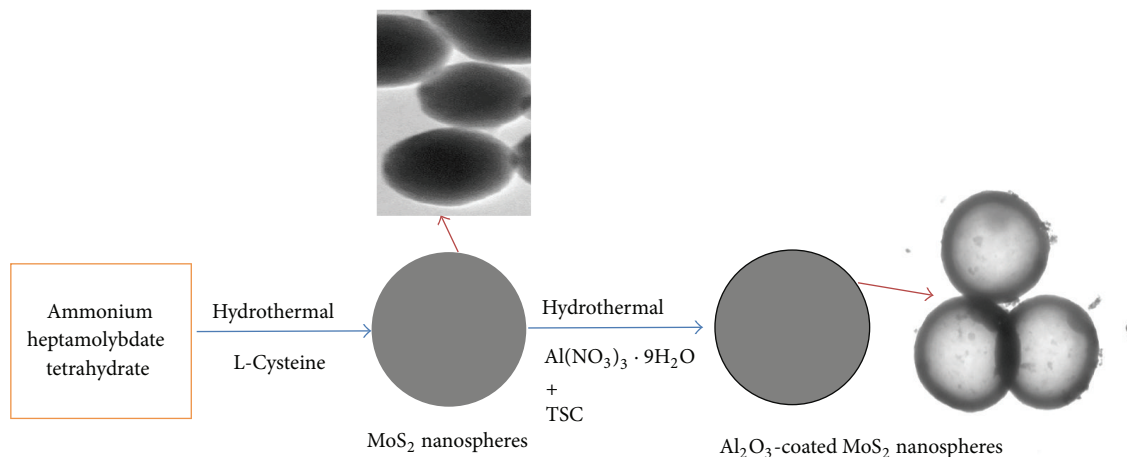


FIGURE 1: Schematic illustration of the methodology for the formation of Al<sub>2</sub>O<sub>3</sub>-coated MoS<sub>2</sub> nanospheres.

with the addition of SUDEI. Wu et al. [18] prepared MoS<sub>2</sub> nanospheres (with average diameter of 100 nm) using HCl as a surfactant. Park et al. [19] synthesized MoS<sub>2</sub> nanospheres with high capacity and cycle stability for lithium ion batteries using L-cysteine in a surfactant-assisted solvothermal route.

Common ways to synthesize core-shell structures are decorating the core particles with a surface coating [5] or shell formation using surface modification processes [20]. In this study, we report the influence of Al<sub>2</sub>O<sub>3</sub> as a shell material on the photocatalytic activity of MoS<sub>2</sub> nanosphere core-shell structures under UV light irradiation. We studied the variations of the activity and selectivity in the degradation of rhodamine B (RhB) using Al<sub>2</sub>O<sub>3</sub>-coated MoS<sub>2</sub> nanospheres as a catalyst.

## 2. Experimental Procedure

A schematic illustration of the methodology for the formation of Al<sub>2</sub>O<sub>3</sub>-coated MoS<sub>2</sub> nanospheres is shown in Figure 1. For the synthesis, 0.3 g of ammonium heptamolybdate tetrahydrate and 0.17 g of L-cysteine were dissolved in 30 mL of deionized water. This solution was stirred vigorously for 1 h at 80°C. The suspension was continuously stirred and refluxed near pH 1. Then, 1.2 mmol of Al(NO<sub>3</sub>)<sub>3</sub> · 9H<sub>2</sub>O and 0.3 mmol of trisodium citrate dehydrate (TSC) were added to the stirred solution and again stirred for 30 min at 80°C. Then, the solution was transferred to a Teflon-lined autoclave and heated at 230°C for 24 h. Finally, the resulting precipitates were collected by centrifugation and then the precipitates were washed three times with acetone and water. The obtained precipitates were dried at 250°C for 6 h and sintering at 450°C for 2 h.

The structural properties of the obtained precipitates were characterized by powder X-ray diffraction (XRD) with a Shimadzu Labx XRD 6100 using Cu-K $\alpha$  radiation ( $\lambda = 0.14056$  nm). The scan range was 10–80°, and the scan speed was 3 deg/min. The nanoparticles were analyzed with a transmission electron microscope (TEM, Hitachi H-7000) at 100 kV and a high-resolution TEM (HRTEM, Tecnai G<sup>2</sup> F 20

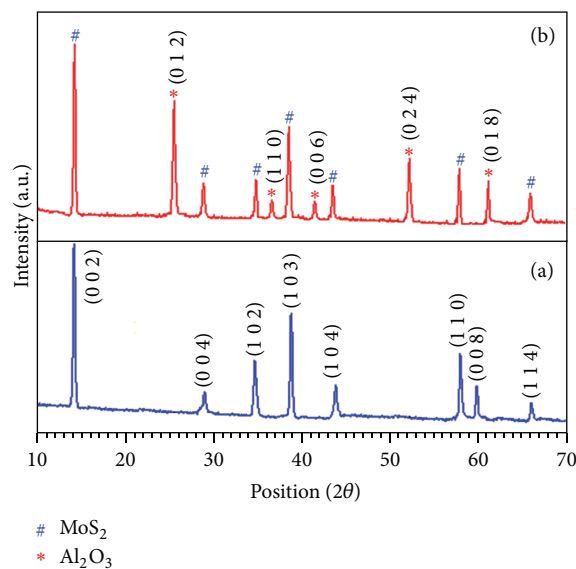


FIGURE 2: XRD pattern of MoS<sub>2</sub> nanospheres (curve (a)) and Al<sub>2</sub>O<sub>3</sub>-coated MoS<sub>2</sub> nanospheres (curve (b)).

S-Twin TEM) at an accelerating voltage of 210 kV. The optical properties of the nanoparticles were studied using UV-visible spectroscopy (Cary 5000 UV-Vis spectrophotometry). Thermogravimetric (TG) and differential thermal analysis (DTA) were carried out on a SDT Q600 thermogravimetric analyzer under N<sub>2</sub> flow at a rate of 30 cm<sup>3</sup>/min. The furnace temperature was increased from room temperature to 900°C at a heating rate of 10°C per minute. The purity of the final product was examined by X-ray photoelectron spectroscopy (XPS, Thermo Scientific K-alpha surface analysis instrument).

The photocatalytic experiments were carried out at the natural pH of the RhB organic pollutant solution. The photoreactor has a 150-W mercury lamp with a main emission wavelength of 254 nm as an internal light source, which is surrounded by a quartz vessel. The suspension includes

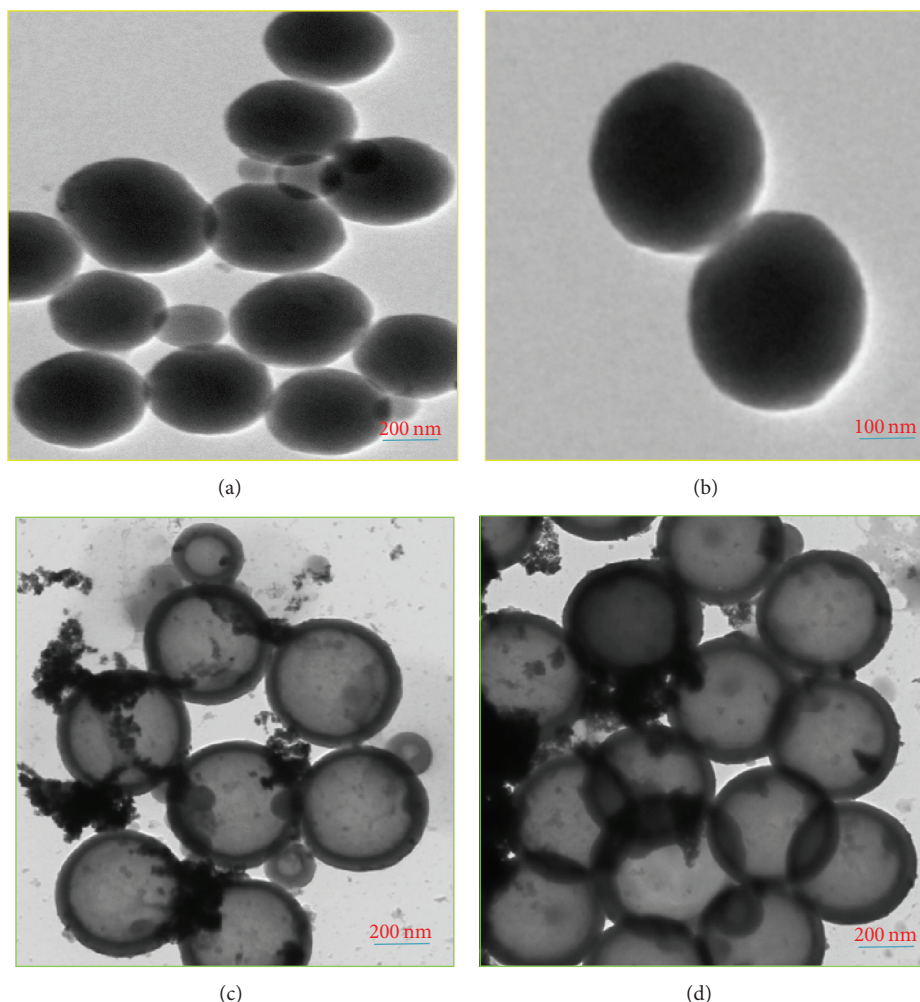


FIGURE 3: TEM images of ((a), (b)) MoS<sub>2</sub> nanospheres, ((c), (d)) Al<sub>2</sub>O<sub>3</sub>-coated MoS<sub>2</sub> nanospheres.

the Al<sub>2</sub>O<sub>3</sub>-decorated MoS<sub>2</sub> nanosphere catalyst and aqueous RhB (100 mL, 10 mg/L), which completely surrounds the light source. Before irradiation, the suspension was stirred in the dark for 30 min to obtain a good dispersion and to ensure adsorption-desorption equilibrium between the organic pollutant molecules and the catalyst. During light irradiation, the samples of the reaction solution were collected at given intervals and examined using an optical spectrophotometer.

### 3. Results and Discussions

The XRD patterns of MoS<sub>2</sub> nanospheres and Al<sub>2</sub>O<sub>3</sub>-coated MoS<sub>2</sub> nanospheres were shown in Figure 2. In case of MoS<sub>2</sub> sphere sample exhibits three well-resolved peaks which can be indexed as the 002, 103, and 110 reflections of the 2D hexagonal structure, which is matched with JCPDS number 77-1716. On the other hand, XRD pattern of Al<sub>2</sub>O<sub>3</sub>-coated MoS<sub>2</sub> sample exhibits hexagonal structure, whereas Al<sub>2</sub>O<sub>3</sub> layer is been crystallized, which is corresponding to JCPDS number 78-2426. The coexisting peaks of Al<sub>2</sub>O<sub>3</sub>-coated MoS<sub>2</sub> nanospheres corresponding to the 012, 110, 006, 024, and 018

crystal plane are ascribed to  $\gamma$ -Al<sub>2</sub>O<sub>3</sub> phase for the sintered samples at 450°C [21, 22]. The diffraction lines characteristics of MoS<sub>2</sub> and Al<sub>2</sub>O<sub>3</sub> and no other elemental peaks were detected.

The morphology of the MoS<sub>2</sub> nanospheres and Al<sub>2</sub>O<sub>3</sub>-coated MoS<sub>2</sub> nanospheres was examined using TEM, as shown in Figure 3. MoS<sub>2</sub> nanospheres were coated with Al<sub>2</sub>O<sub>3</sub> using Al(NO<sub>3</sub>)<sub>3</sub>·9H<sub>2</sub>O as a precursor via a hydrothermal method. For better understanding of the morphology of the composite, we initially tested the MoS<sub>2</sub> nanospheres without using Al precursors. The morphology of the MoS<sub>2</sub> materials reveal typical sphere-like morphology with several nanometers in diameter. On the other hand, the MoS<sub>2</sub> spheres obtained using Al precursors retained their spherical morphology with the formation of a uniform layer, forming a core-shell structure (Figures 3(c) and 3(d)). The average thickness of the Al<sub>2</sub>O<sub>3</sub> layer around the periphery of the MoS<sub>2</sub> is about 15 nm.

Further understanding of the structural and compositional characterizations of Al<sub>2</sub>O<sub>3</sub>-coated MoS<sub>2</sub> nanospheres was obtained using HRTEM. The HRTEM image of an edge

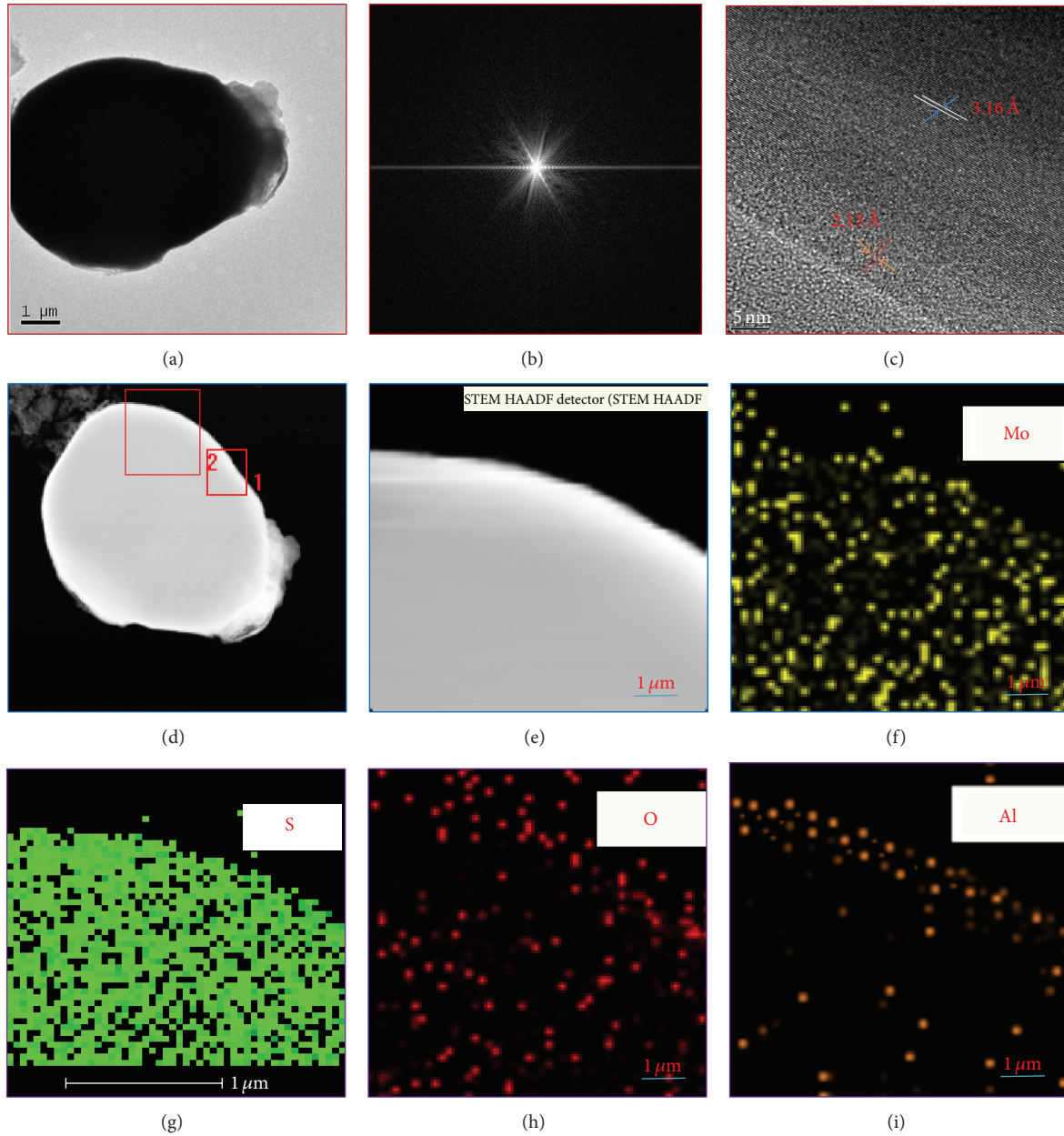


FIGURE 4: HR-TEM images ((a)–(e)) of  $\text{Al}_2\text{O}_3$ -coated  $\text{MoS}_2$  nanospheres, ((f)–(i)) HR-TEM elemental mapping images of  $\text{Al}_2\text{O}_3$ -coated  $\text{MoS}_2$  nanospheres.

portion of a core-shell sphere is shown in Figures 4(a)–4(d). The HRTEM image (Figure 4(a)) confirms that the  $\text{Al}_2\text{O}_3$  colloids are aggregated on the  $\text{MoS}_2$  nanospheres. The lattice fringes of the core-shell structure with lattice spacings of about 0.213 and 0.316 nm could be attributed to the (103) and (110) planes of 2H- $\text{MoS}_2$ , respectively. Figures 4(e)–4(i) show typical energy dispersive X-ray spectrometer (EDX) elemental mappings of the core-shell spheres of various elements in the core-shell structure, along with its TEM image. The Mo, S, Al, or O signals are predominantly distributed in the core and shell regions within the selected area, respectively. Figure 5 shows the EDX mapping of  $\text{Al}_2\text{O}_3$ -coated  $\text{MoS}_2$  nanospheres. There are no other traces observed.

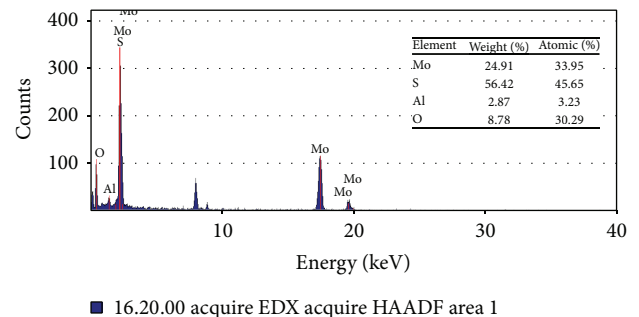


FIGURE 5: HR-TEM EDX data of  $\text{Al}_2\text{O}_3$ -coated  $\text{MoS}_2$  nanospheres.

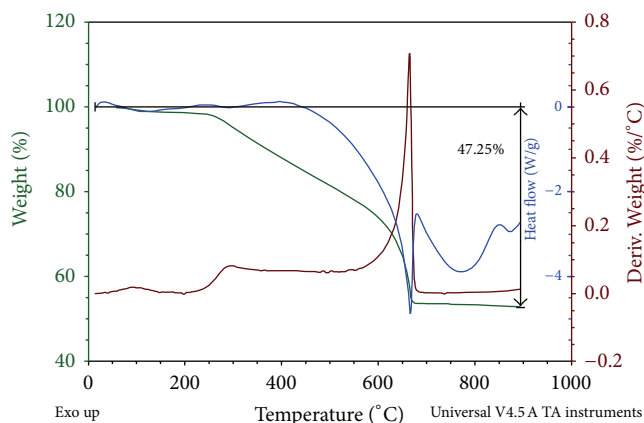


FIGURE 6: TG-DTA analysis of  $\text{Al}_2\text{O}_3$ -coated  $\text{MoS}_2$  nanospheres.

Thermogravimetric and differential thermal analysis (TG-DTA) was conducted to quantitatively determine the  $\text{Al}_2\text{O}_3$  content present in the  $\text{Al}_2\text{O}_3$ -coated  $\text{MoS}_2$  nanospheres, as shown in Figure 6. The initial weight loss below  $220^\circ\text{C}$  is ascribed to the evaporation of physically absorbed water from the product, whereas the weight loss between  $550$  and  $680^\circ\text{C}$  that occurred with an exothermic peak at  $650^\circ\text{C}$  could essentially be attributed to the decomposition and separation of the  $\text{Al}_2\text{O}_3$  layer. The  $\text{Al}_2\text{O}_3$  content was estimated to be approximately 47.25% by weight.

The electronic states of the metals and sulfur in the  $\text{Al}_2\text{O}_3$ -coated  $\text{MoS}_2$  nanospheres were tested using XPS, as shown in Figures 7(a)–7(e). The XPS survey spectra of the  $\text{Al}_2\text{O}_3$ -coated  $\text{MoS}_2$  nanospheres are shown in Figure 7(a). The  $\text{Al}2p$  XPS spectra were estimated for the  $\text{Al}_2\text{O}_3$ -coated  $\text{MoS}_2$  nanospheres to examine the chemical state of Al. The  $\text{Mo}3d$ ,  $\text{S}2p$ ,  $\text{Al}2p$ , and  $\text{O}1s$  peaks from the  $\text{Al}_2\text{O}_3$ -coated  $\text{MoS}_2$  sphere sample (Figures 7(b)–7(e)) show no presence of addition chemical states. The binding energy difference  $\Delta E$  between the  $\text{Al}2p$  and  $2s$  levels is  $53.34$  eV for the  $\text{Al}_2\text{O}_3$ -coated  $\text{MoS}_2$  nanospheres. The XPS results strongly indicate that Al species interacted with the  $\text{MoS}_2$  nanospheres and are preferentially formed in the  $\text{Al}_2\text{O}_3$ - $\text{MoS}_2$  composite using  $\text{Al}(\text{NO}_3)_3 \cdot 9\text{H}_2\text{O}$  as a precursor. The  $\text{Al}2p$  and  $\text{O}1s$  peaks were centered at  $74.45$  eV and  $532.36$  eV, as described elsewhere [23].

The  $\text{S}2p$  spectrum shows a supplementary peak at  $164.58$  eV coexisting with an  $\text{O}1s$  peak, which is ascribed to the oxidation of sulfur. The formation of covalent S-O bonding without breakage of the Mo-S bond is likely due to the oxidation state of sulfur. No S-O bond is observed in the  $\text{S}2s$  spectrum, which suggests that only the top surface of sulfur atoms of  $\text{MoS}_2$  are oxygen functionalized. This is good evidence that the  $\text{Al}_2\text{O}_3$  formed a bond with  $\text{MoS}_2$  nanospheres, resulting in the formation of the core-shell structure. The XPS binding energies  $\Delta E1$  ( $\text{Mo } 2p_{3/2} - \text{S } 2p_{3/2}$ ) and  $\Delta E2$  ( $\text{Mo } 3d_{5/2} - \text{S } 2p_{3/2}$ ) of the  $\text{Al}_2\text{O}_3$ -coated  $\text{MoS}_2$  nanospheres are  $70.3$  and  $67.09$  eV, respectively.

The UV-Vis spectrum of the synthesized  $\text{Al}_2\text{O}_3$ -coated  $\text{MoS}_2$  nanospheres is shown in Figure 8(a). The absorption edge at  $275$  nm could be attributed to the absorption of  $\text{Al}_2\text{O}_3$ - $\text{MoS}_2$  in the UV region. The absorption spectrum

shows two absorption edges at  $603$  and  $660$  nm. These are attributed to excitonic transitions of the Brillouin region at the  $K$  point, which is consistent with an earlier report [24]. The energy separation between the two absorption peaks (at  $603$  and  $660$  nm) is  $0.15$  eV due to the spin-orbit splitting at the  $K$  point at the surface of the valence band [24]. Moreover, there is weak absorbance in the visible region at a wavelength of  $425$  nm. The UV-absorption behavior of  $\text{MoS}_2$  strongly depends on its size due to quantum effects [25]. For example, the absorption edges of  $\text{MoS}_2$  nanoparticles with average diameters of about  $4.5$  and  $9$  nm have edges at  $470$  and  $700$  nm, respectively, in the visible light region [26]. In contrast, bulk  $\text{MoS}_2$  (with a band gap of  $1.23$  eV) has an absorption peak at around  $1040$  nm [25].  $\text{MoS}_2$ -based composites have diverse absorption edges with respect to their dimensional parameters [26].

The indirect band gap is estimated using the Tauc equation with optical absorption data for near the band edge [24]:  $(\alpha h\nu)^{1/2} = A(h\nu - E_g)$ . The band gaps ( $E_g$ ) are determined from extrapolation of a linear fit onto the  $x$ -axis. A plot of  $(\alpha h\nu)^{1/2}$  versus the photon energy ( $h\nu$ ) and the intercept of the tangent to the  $x$ -axis gives the band gap of the  $\text{Al}_2\text{O}_3$ -coated  $\text{MoS}_2$  nanospheres, as shown in Figure 8(b). The band gap energy of  $\text{Al}_2\text{O}_3$ -coated  $\text{MoS}_2$  nanospheres was found to be  $2.42$  eV.

Figure 9 shows the progressive changes of the UV-Vis absorption spectra of RhB solution in the presence of  $\text{Al}_2\text{O}_3$ -coated  $\text{MoS}_2$  nanosphere catalyst under UV light as a function of time. The strong absorption peak of the RhB solution at  $564$  nm gradually decreases from dark conditions to  $60$  min, and the color of the solution turns from pink to colorless at the end of the photodegradation process. Figure 10 shows the photodegradation efficiency of  $\text{MoS}_2$  nanospheres and  $\text{Al}_2\text{O}_3$ -coated  $\text{MoS}_2$  nanosphere catalysts under UV light in RhB solution. The results are shown as the relative concentration ( $C/C_0$ ) as a function of irradiation time, where  $C_0$  and  $C$  (mg/L) are the initial and final concentrations of the pollutant solution.

A blank experiment was carried out in the absence of photocatalyst for comparison, which showed no obvious change in the RhB concentration within  $60$  min. The introduction of  $\text{MoS}_2$  nanospheres and  $\text{Al}_2\text{O}_3$ -coated  $\text{MoS}_2$  nanosphere catalysts can greatly enhance the photocatalytic activity under UV light. Interestingly, the  $\text{Al}_2\text{O}_3$ -coated  $\text{MoS}_2$  nanosphere photocatalysts displayed much higher photodegradation performance than the  $\text{MoS}_2$  nanospheres, and more than  $97\%$  of the RhB was degraded within  $60$  min. The presence of  $\text{Al}_2\text{O}_3$ -coated  $\text{MoS}_2$  nanospheres plays a key role in the photocatalytic degradation process. The significant enhancement in photoactivity can be ascribed to the favorable van der Waals surfaces of the  $\text{Al}_2\text{O}_3$ -coated  $\text{MoS}_2$  nanospheres.

Figure 11 shows a kinetic plot of the photocatalytic degradation of RhB over time under UV light irradiation as  $\ln(C/C_0)$ . The removal efficiency of the  $\text{Al}_2\text{O}_3$ -coated  $\text{MoS}_2$  nanospheres was much faster than that of the  $\text{MoS}_2$  nanosphere catalyst. To understand the photostability and reusability of the photocatalyst, four successive recycling tests of the photocatalysts were done for the degradation of RhB under UV light, as shown in Figure 12. There were no

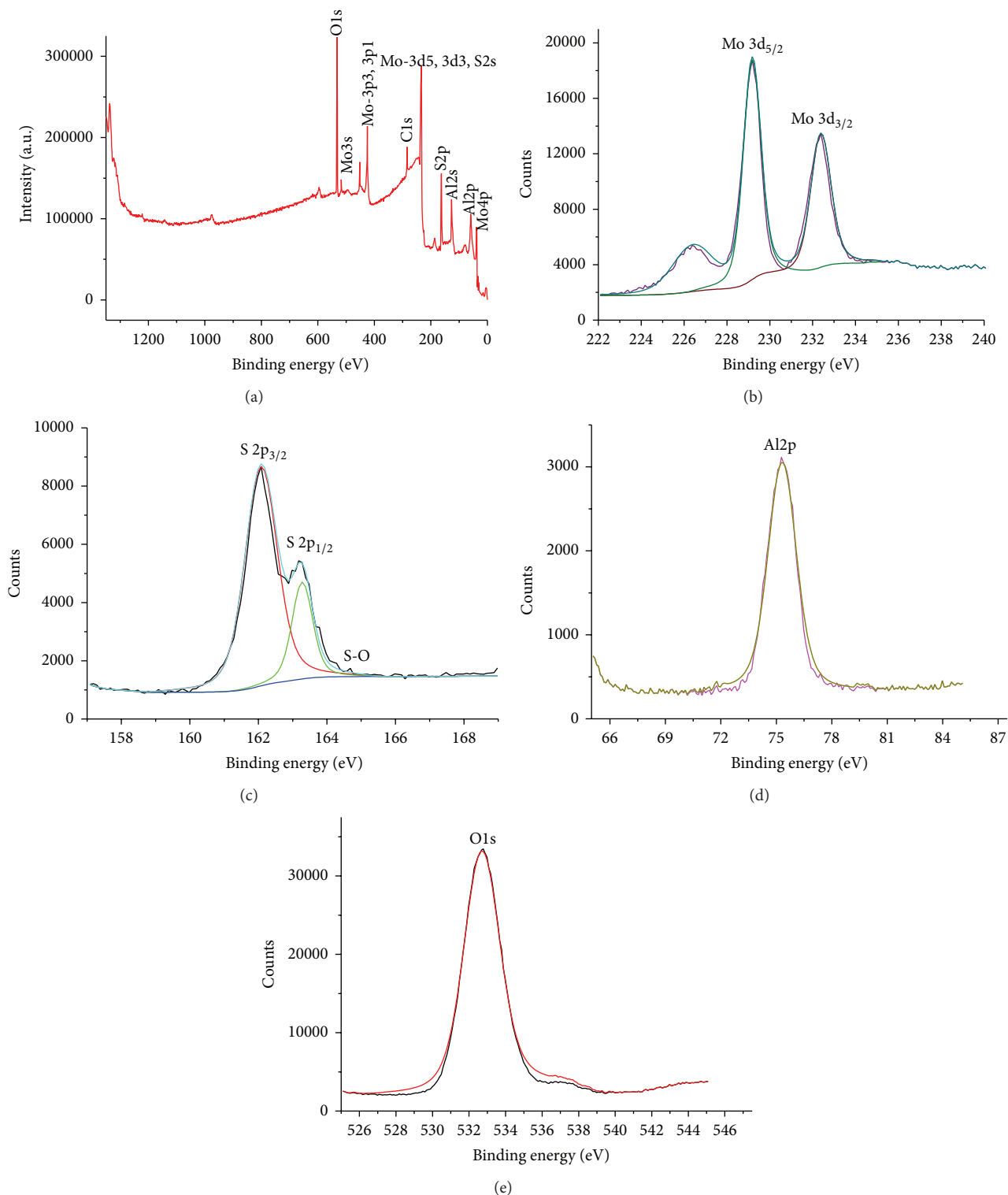


FIGURE 7: XPS data of  $\text{Al}_2\text{O}_3$ -coated  $\text{MoS}_2$  nanospheres: (a) survey spectrum, (b) Mo 3d, (c) S2p, (d) Al2p, and (e) O1s.

significant changes in photocatalytic activity, which shows the steadiness of the degradation efficiency of RhB solution. This result implies that the  $\text{Al}_2\text{O}_3$ -coated  $\text{MoS}_2$  nanosphere photocatalysts have high stability during the photocatalytic oxidation of the pollutant molecules and are reusable.

The catalytic activity increased with the  $\text{Al}_2\text{O}_3$ -coated  $\text{MoS}_2$  nanospheres. Figure 13 shows the RhB removal efficiency of the  $\text{Al}_2\text{O}_3$ -coated  $\text{MoS}_2$  photocatalytic nanospheres with 5 mg of catalyst and 50 mL of  $10 \text{ mgL}^{-1}$  RhB solution. The pollutant removal efficiency and the adsorption amount

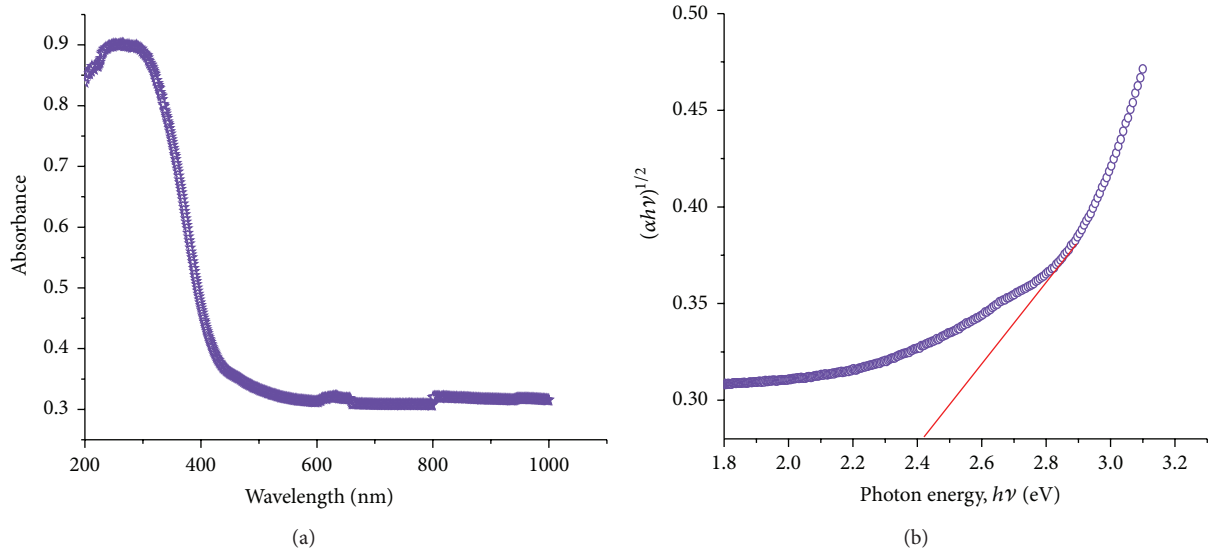


FIGURE 8: (a) UV-Vis light spectra of the  $\text{Al}_2\text{O}_3$ -coated  $\text{MoS}_2$  nanospheres, (b) Tauc plots of  $\text{Al}_2\text{O}_3$ -coated  $\text{MoS}_2$  nanospheres.

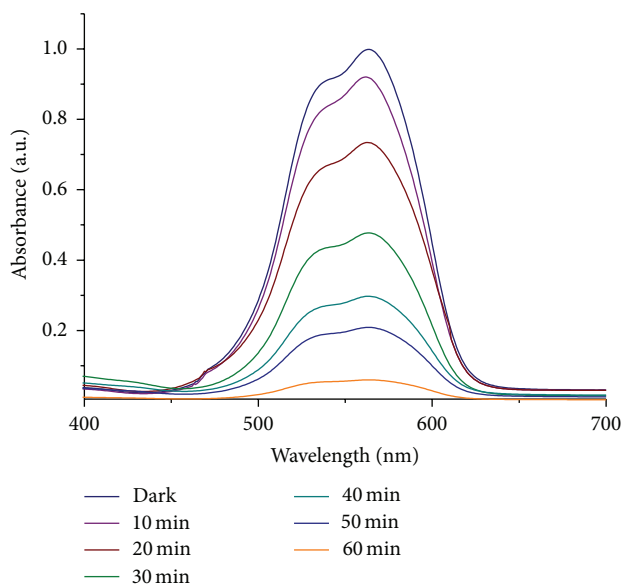


FIGURE 9: Time-dependent UV-Vis absorbance spectra of  $\text{Al}_2\text{O}_3$ -coated  $\text{MoS}_2$  nanospheres of the rhodamine B solution samples at different times.

at equilibrium ( $q_e$ ) were calculated using the following equation:

$$\text{Pollutant removal efficiency (PR\%)} = \frac{100(C_0 - C)}{C_0}, \quad (1)$$

where  $C_0$  and  $C$  (mg/L) are the initial and final concentrations of the pollutant, respectively,  $V$  is the volume of the pollutant solution, and  $m$  (g) is the mass of the catalyst. The  $\text{Al}_2\text{O}_3$ -coated  $\text{MoS}_2$  nanospheres exhibit high RhB removal efficiency (95%), in contrast to the (69%)  $\text{MoS}_2$  nanosphere sample. It is well known that catalytic ability increases with

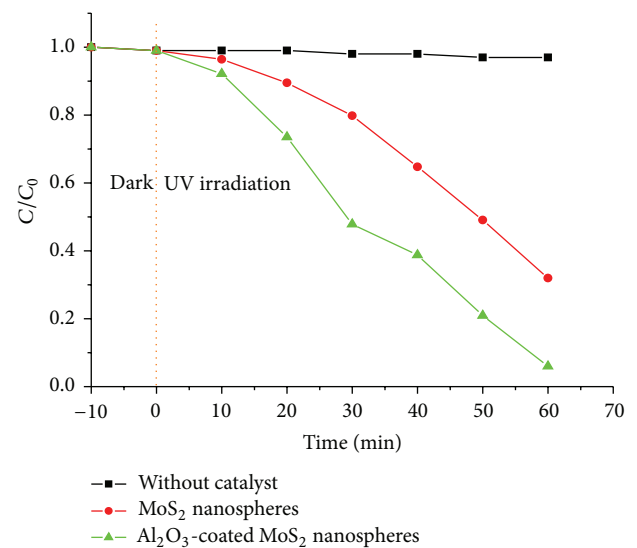


FIGURE 10: Photodegradation rate of the rhodamine B under UV light and light irradiation time for without catalyst,  $\text{MoS}_2$  nanospheres, and  $\text{Al}_2\text{O}_3$ -coated  $\text{MoS}_2$  nanospheres.

increasing content of the catalyst with respect to processing time and other environmental conditions like temperature and pH. In this work, the degradation rate of the RhB solution also increased with increasing catalyst content due to the small particle size and good dispersibility of the  $\text{Al}_2\text{O}_3$ -coated  $\text{MoS}_2$  nanoparticles, which facilitate electron migration between the catalyst and pollutant. The  $\text{Al}_2\text{O}_3$ -coated  $\text{MoS}_2$  nanospheres exhibit high catalytic activity due to the high dispersibility of the  $\text{Al}_2\text{O}_3$  coating around the  $\text{MoS}_2$  nanospheres, which secured more efficient charge transfer between the  $\text{MoS}_2$  and  $\text{Al}_2\text{O}_3$ .

The  $\text{MoS}_2$  behaves as the photoactive center, which is generating excited photoelectron pairs under UV irradiation,

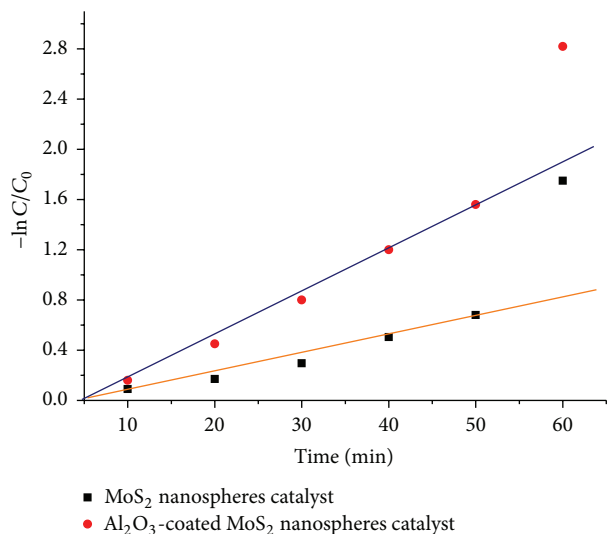


FIGURE 11: The kinetic plot of Al<sub>2</sub>O<sub>3</sub>-coated MoS<sub>2</sub> nanospheres photocatalytic degradation of rhodamine B under UV light irradiation.

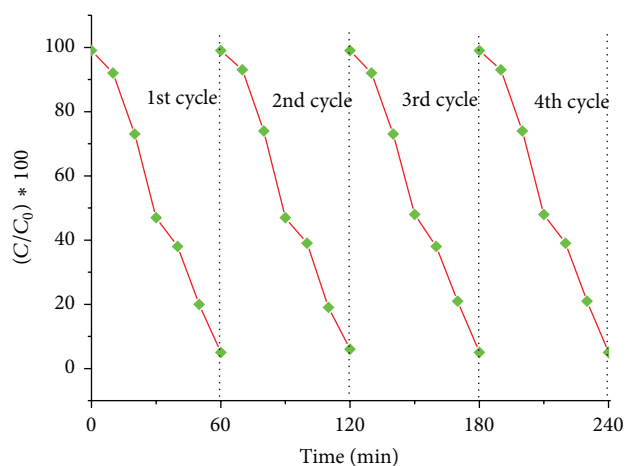


FIGURE 12: Recycling photocatalytic degradation of rhodamine B in the presence of Al<sub>2</sub>O<sub>3</sub>-coated MoS<sub>2</sub> nanospheres photocatalytic under UV light irradiation.

while the Al<sub>2</sub>O<sub>3</sub> provides better adsorption sites in the vicinity of the MoS<sub>2</sub>. The presence of insulating layers of Al<sub>2</sub>O<sub>3</sub> on the surface of MoS<sub>2</sub> nanospheres suppresses the unwanted charge recombination, thus enhancing the photocatalytic activity. The greater photocatalytic activity of Al<sub>2</sub>O<sub>3</sub>-coated MoS<sub>2</sub> nanospheres can be explained as follows. The HRTEM mapping results indicated that the periphery of the MoS<sub>2</sub> was covered with Al<sub>2</sub>O<sub>3</sub>. Under UV light irradiation, both MoS<sub>2</sub> and Al<sub>2</sub>O<sub>3</sub> are photoexcited, and holes and electrons form in the valance band and conduction band. The photogenerated holes and electrons are transferred within the valance and conduction bands of both the MoS<sub>2</sub> and Al<sub>2</sub>O<sub>3</sub> materials. This tendency helps to extend the charge carriers. The excited electrons and holes react with dissolved oxygen in the water or directly oxidize the pollutant molecules to form oxide

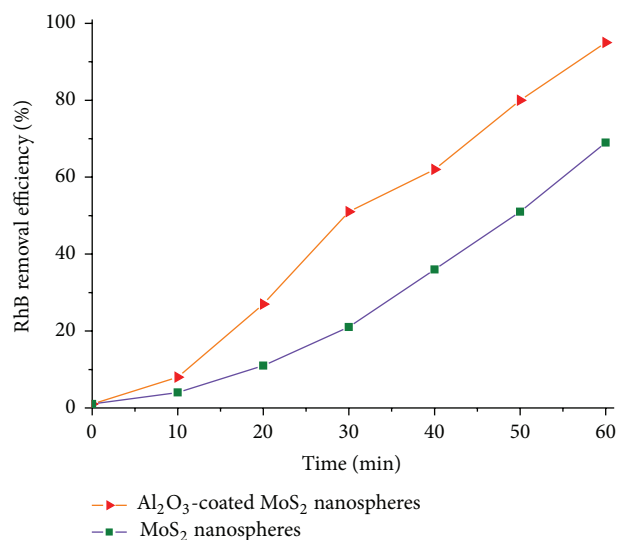


FIGURE 13: RhB removal efficiency of Al<sub>2</sub>O<sub>3</sub>-coated MoS<sub>2</sub> nanospheres photocatalytic, adsorption conditions: 5 mg catalyst, 50 mL 10 mgL<sup>-1</sup> RhB solution (conditions: 5 mg of catalyst and 50 mL of 10 mgL<sup>-1</sup> RhB solution).

radicals (O<sub>2</sub><sup>•-</sup>) and hydroxyl radicals (•OH), which are responsible for the degradation of RhB.

A possible mechanism for formation of MoS<sub>2</sub>@Al<sub>2</sub>O<sub>3</sub> core-shell structure is suggested involving MoS<sub>2</sub> spheres acting as a template for the formation of the coated nanospheres. Due to hydrothermal reactions between the metal-oxoanions and surfactant, cations form a composite phase at the surfactant/inorganic interfaces. Thus, nucleation domains were formed during the hydrothermal reaction between MoO<sub>4</sub><sup>2-</sup> and S<sup>2-</sup> and formed MoS<sub>2</sub> spheres. In this manner, the diameter of the nanospheres is no longer limited by the micelle dimensions. A spherical phase of MoS<sub>2</sub> is formed during hydrothermal treatment under the synthetic conditions, in which L-cysteine acts as a sulfur source to stabilize the spherical organization of Mo and S species. The Al species of the precursor solution can adsorb to the surface of MoS<sub>2</sub> spheres, and layer upon layer is formed by the electrostatic interaction. The TSC could be considered a crucial component for the growth mechanism of Al<sub>2</sub>O<sub>3</sub> coating because it acts as a capping agent for the formation of the coating surface on the MoS<sub>2</sub> nanospheres. The complete synthetic mechanism is expressed in Figure 1.

#### 4. Conclusions

Al<sub>2</sub>O<sub>3</sub>-coated MoS<sub>2</sub> nanospheres were successfully synthesized using a simple hydrothermal method. The Al<sub>2</sub>O<sub>3</sub> shell materials serve as additional electron sources that can significantly recover the electron conduction in MoS<sub>2</sub>, which favors the photodegradation of the pollutant. We revealed the appropriate selection of surfactants that could facilitate the adherence of Al species to the surfaces of the cores. Hydrothermally synthesized Al<sub>2</sub>O<sub>3</sub>-coated MoS<sub>2</sub> nanosphere catalysts show photocatalytic activity higher than that of the

MoS<sub>2</sub> nanosphere catalyst due to the enhanced crystallites with high metal content, which minimize the poisoning effect of sulfur by the chemisorption process.

### Conflict of Interests

The authors declare that there is no conflict of interests regarding the publication of this paper.

### Acknowledgments

This research was supported by the Basic Science Research Program through the National Research Foundation of Korea (NRF) and funded by the Ministry of Science, ICT, and Future Planning (2014R1A2A2A01007081).

### References

- [1] H. S. S. Ramakrishna Matte, A. Gomathi, A. K. Manna et al., "MoS<sub>2</sub> and WS<sub>2</sub> analogues of graphene," *Angewandte Chemie International Edition*, vol. 49, no. 24, pp. 4059–4062, 2010.
- [2] Y. Li, H. Wang, L. Xie, Y. Liang, G. Hong, and H. Dai, "MoS<sub>2</sub> nanoparticles grown on graphene: an advanced catalyst for the hydrogen evolution reaction," *Journal of the American Chemical Society*, vol. 133, no. 19, pp. 7296–7299, 2011.
- [3] J. J. Lee, H. Kim, and S. H. Moon, "Preparation of highly loaded, dispersed MoS<sub>2</sub>/Al<sub>2</sub>O<sub>3</sub> catalysts for the deep hydrodesulfurization of dibenzothiophenes," *Applied Catalysis B: Environmental*, vol. 41, no. 1–2, pp. 171–180, 2003.
- [4] D. Song, M. Li, Y. Jiang et al., "Facile fabrication of MoS<sub>2</sub>/PEDOT-PSS composites as low-cost and efficient counter electrodes for dye-sensitized solar cells," *Journal of Photochemistry and Photobiology A: Chemistry*, vol. 279, pp. 47–51, 2014.
- [5] C. Zhang, H. B. Wu, Z. Guo, and X. W. Lou, "Facile synthesis of carbon-coated MoS<sub>2</sub> nanorods with enhanced lithium storage properties," *Electrochemistry Communications*, vol. 20, pp. 7–10, 2012.
- [6] H.-H. Chien, K.-J. Ma, S. V. P. Vattikuti, C.-H. Kuo, C.-B. Huo, and C.-L. Chao, "Tribological behaviour of MoS<sub>2</sub>/Au coatings," *Thin Solid Films*, vol. 518, no. 24, pp. 7532–7534, 2010.
- [7] M. Donarelli, S. Prezioso, F. Perrozzi et al., "Response to NO<sub>2</sub> and other gases of resistive chemically exfoliated MoS<sub>2</sub>-based gas sensors," *Sensors and Actuators B: Chemical*, vol. 207, pp. 602–613, 2015.
- [8] Y. Shi, Y. Wang, J. I. Wong et al., "Self-assembly of hierarchical MoS<sub>x</sub>/CNT nanocomposites (2 < x < 3): towards high performance anode materials for lithium ion batteries," *Scientific Reports*, vol. 3, article 2169, 8 pages, 2013.
- [9] K. Hagiwara, T. Ebihara, N. Urasato, and T. Fujikawa, "Application of <sup>129</sup>Xe NMR to structural analysis of MoS<sub>2</sub> crystallites on Mo/Al<sub>2</sub>O<sub>3</sub> hydrodesulfurization catalyst," *Applied Catalysis A: General*, vol. 285, no. 1–2, pp. 132–138, 2005.
- [10] Y. Feldman, G. L. Frey, M. Homyonfer et al., "Bulk synthesis of inorganic fullerene-like MS<sub>2</sub> (M = Mo, W) from the respective trioxides and the reaction mechanism," *Journal of the American Chemical Society*, vol. 118, no. 23, pp. 5362–5367, 1996.
- [11] W. K. Hsu, B. H. Chang, Y. Q. Zhu et al., "An alternative route to molybdenum disulfide nanotubes," *Journal of the American Chemical Society*, vol. 122, no. 41, pp. 10155–10158, 2000.
- [12] J. Wang, C. Luo, T. Gao, A. Langrock, A. C. Mignerey, and C. Wang, "An advanced MoS<sub>2</sub>/carbon anode for high-performance sodium-ion batteries," *Small*, vol. 11, pp. 473–481, 2015.
- [13] R. Coehoorn, C. Haas, J. Dijkstra, C. J. F. Flipse, R. A. De Groot, and A. Wold, "Electronic structure of MoSe<sub>2</sub>, MoS<sub>2</sub>, and WSe<sub>2</sub>. I. Band-structure calculations and photoelectron spectroscopy," *Physical Review B*, vol. 35, no. 12, pp. 6195–6202, 1987.
- [14] J. A. Glasscock, P. R. F. Barnes, I. C. Plumb, and N. Savvides, "Formation of fractal-like structures driven by carbon nanotubes-based collapsed hollow capsules," *The Journal of Physical Chemistry C*, vol. 111, pp. 331–337, 2007.
- [15] O. Khaselev and J. A. Turner, "A monolithic photovoltaic-photoelectrochemical device for hydrogen production via water splitting," *Science*, vol. 280, no. 5362, pp. 425–427, 1998.
- [16] R. G. Chaudhuri and S. Paria, "Core/shell nanoparticles: classes, properties, synthesis mechanisms, characterization, and applications," *Chemical Reviews*, vol. 112, no. 4, pp. 2373–2433, 2012.
- [17] D. M. Wu, X. D. Zhou, X. Fu, H. Q. Shi, D. B. Wang, and Z. S. Hu, "Synthesis and characterization of molybdenum disulfide micro-sized solid spheres," *Journal of Materials Science*, vol. 41, no. 17, pp. 5682–5686, 2006.
- [18] Z. Wu, D. Wang, and A. Sun, "Surfactant-assisted fabrication of MoS<sub>2</sub> nanospheres," *Journal of Materials Science*, vol. 45, no. 1, pp. 182–187, 2010.
- [19] S.-K. Park, S.-H. Yu, S. Woo et al., "A facile and green strategy for the synthesis of MoS<sub>2</sub> nanospheres with excellent Li-ion storage properties," *CrystEngComm*, vol. 14, no. 24, pp. 8323–8325, 2012.
- [20] J. Li, P. Wu, Y. Ye et al., "Electronic structure of MoSe<sub>2</sub>, MoS<sub>2</sub>, and WSe<sub>2</sub>. I. Band-structure calculations and photoelectron spectroscopy," *CrystEngComm*, vol. 16, no. 4, pp. 517–521, 2014.
- [21] G. Paglia, C. E. Buckley, A. L. Rohl et al., "Boehmite derived  $\gamma$ -alumina system. I. structural evolution with temperature, with the identification and structural determination of a new transition phase,  $\gamma'$ -alumina," *Chemistry of Materials*, vol. 16, no. 2, pp. 220–236, 2004.
- [22] M. Trueba and S. P. Trasatti, " $\gamma$ -alumina as a support for catalysts: a review of fundamental aspects," *European Journal of Inorganic Chemistry*, vol. 2005, no. 17, pp. 3393–3403, 2005.
- [23] F. Lan, Z. Lai, R. Yan et al., "Epitaxial growth of single-crystalline monolayer MoS<sub>2</sub> by two-step method," *ECS Solid State Letters*, vol. 4, pp. 19–21, 2015.
- [24] R. Coehoorn, C. Haas, and R. A. de Groot, "Electronic structure of MoSe<sub>2</sub>, MoS<sub>2</sub>, and WSe<sub>2</sub>. II. The nature of the optical band gaps," *Physical Review B: Condensed Matter and Materials Physics*, vol. 35, no. 12, pp. 6203–6206, 1987.
- [25] K. K. Kam and B. A. Parkinson, "Detailed photocurrent spectroscopy of the semiconducting group VI transition metal dichalcogenides," *Journal of Physical Chemistry*, vol. 86, no. 4, pp. 463–467, 1982.
- [26] T. R. Thurston and J. P. Wilcoxon, "Photooxidation of organic chemicals catalyzed by nanoscale MoS<sub>2</sub>," *The Journal of Physical Chemistry B*, vol. 103, no. 1, pp. 11–17, 1999.

## Research Article

# Synthesis and Characterization of Molybdenum Disulfide Nanoflowers and Nanosheets: Nanotribology

S. V. Prabhakar Vattikuti and Chan Byon

*School of Mechanical Engineering, Yeungnam University, Gyeongsan 712-749, Republic of Korea*

Correspondence should be addressed to Chan Byon; [cbyon@ynu.ac.kr](mailto:cbyon@ynu.ac.kr)

Received 20 March 2015; Accepted 4 May 2015

Academic Editor: Xiaogang Han

Copyright © 2015 S. V. P. Vattikuti and C. Byon. This is an open access article distributed under the Creative Commons Attribution License, which permits unrestricted use, distribution, and reproduction in any medium, provided the original work is properly cited.

This paper reports the solvothermal synthesis of MoS<sub>2</sub> nanoflowers and nanosheets. The nanoflowers have a mean diameter of about 100 nm and were obtained using thioacetamide (C<sub>2</sub>H<sub>5</sub>NS) as a sulfur source. The few layered nanosheets were obtained using thiourea (CH<sub>4</sub>N<sub>2</sub>S) as a sulfur source. The obtained powders were characterized using powder X-ray diffraction (XRD), scanning electron microscopy (SEM) with energy dispersive spectroscopy (EDS), and transmission electron microscopy (TEM). The lubricating effect of MoS<sub>2</sub> nanoflowers and nanosheets were analyzed using four-ball test, the topography of the wear scar was analyzed using SEM, EDS, and 3D surface profilometry. The relationship between the tribological properties and morphology of the materials was determined. It is observed that the engine oil containing the MoS<sub>2</sub> nanomaterials penetrated more easily into the interface space, and it formed a continuous film on the interface surface. The tribological performance showed that the synthesized nanosheets had superior antiwear and friction-reducing properties as a lubrication additive compared with nanoflowers. Also, the wear scar of balls lubricated with nanoflowers revealed a larger diameter compared to nanosheets. In conclusion, nanosheets dispensed in oil have better tribological performance compared to nanoflowers oil in terms of capability to reduce friction.

## 1. Introduction

Two-dimensional (2D) and three-dimensional (3D) functional nanostructured materials have received great attention due to their inherent physicochemical properties, such as high specific surface-to-volume ratio, anisotropy, chemical inertness, photocorrosion resistance, and excellent tribological performance [1, 2]. Such materials are applicable in various fields, including lubricants, energy storage, field-effect transistors, and catalysis [1–4]. Novel lubricants containing nanoparticles could provide extended reliability and major energy savings in severe friction and wear conditions, which would impact industries related to sustainable engineering of heavy equipment and support energy self-reliance [5–10].

Tenne et al. discovered spherical fullerene-like nanoparticles of MoS<sub>2</sub> and WS<sub>2</sub> nanotubes in 1992 [11]. MX<sub>2</sub> (M = Mo, W and X = S, Se) are well known for their solid-lubrication properties. Molybdenum disulfide (MoS<sub>2</sub>) has a layered hexagonal crystal structure, which is mostly important for solid lubrication or as an additive for lubricating oils [12–14]. These materials offer low shear resistance to any applied shear

stress due to their layered structure with strong intralayer covalent bonds and weak interlayer van der Waals bonds, which decreases friction between interfaces [15].

These materials exist in numerous forms, such as fullerene-like nanoparticles, flake-like structures, and nanotubes [16, 17]. These materials are suitable for adding to lubrication fluids. MoS<sub>2</sub> nanoparticles perform very well in boundary-lubricated contact, particularly with steels [18–20]. However, the key parameters under different contact conditions with respect to morphology have yet to be determined. Lubricants mixed with nanoparticles are known to be the most effective approach to reducing the friction and wear at contact interfaces; however, the presence of solid particles may also lead to oil starvation for lubrication regimes [21].

Explaining the tribological performance of inorganic nanomaterials depends upon several mechanisms and effects: (a) rolling friction [22], (b) the inorganic nanoparticles acting as spacers to prevent direct contact between the asperities [23], and (c) third-body material transfer to form a thin lubricious film [24, 25]. However, the efficiency of the lubrication mechanism depends on various conditions and

intrinsic characteristics, including the morphology, crystal structure, shape, and size of the particular nanoparticles. For example, in the case of fullerene-like MoS<sub>2</sub> nanoparticles, different modes of deformation and destruction are exhibited when in contact with surfaces [18]. Kalin et al. demonstrated that the adhesion of thin MoS<sub>2</sub> nanosheets on a surface has four possible mechanisms: (i) exfoliation of individual nanotubes into nanosheets due to shear stress, (ii) nanosheet aggregation, (iii) nanotube deformation at the surface, and (iv) some nanotubes being damaged [26]. However, these mechanisms have been difficult to prove.

The main negative aspect of a nanofluid is sedimentation of the dispersed particles in the fluid due to poor compatibility between the dissimilar phases. This poses a problem of deteriorating the tribological properties of nanofluids [27, 28] due to small gaps between the asperities: the supply of nanoparticles to the contact is inadequate or interrupted at high contract loads in the boundary-lubricant regime [26]. It is believed that better lubrication is maintained only through the entrapment of multilayered or flake-like solid particles. Useful tribological properties have also been ascribed to their structure, such as chemical inertness and longevity. However, experimental confirmation of the tribological properties (and thus the lubrication mechanisms) of inorganic MoS<sub>2</sub> flake-like nanoparticles has remained limited.

Recently, various synthesis processes have been developed to prepare MoS<sub>2</sub> nanomaterials, including chemical vapor deposition (CVD), thermal reduction, high-temperature sulfurization, laser ablation, and sol-gel methods [27–35]. Using these approaches, different morphologies (fullerene-like, nanotube, nanosphere, and nanorods) have been tested and used in practical applications. However, the synthesis methods generally require complex technologies and harmful organic surfactants. The solvothermal method has attracted much interest due to its versatility and potential to fabricate nanoparticles for applications.

To the best of our knowledge, there have been limited reports using solvothermal methods to control the morphology and properties of MoS<sub>2</sub> nanomaterials with proper selection of the sulfur source. We report an optimized procedure for solvothermal synthesis of MoS<sub>2</sub> nanoflowers and nanosheets assembled with a few lamellar layers. Thioacetamide and thiourea were used as the respective sulfur sources. The aim of this work is to investigate the lubricating and antiwear behavior of the synthesized MoS<sub>2</sub> materials. The materials were tested under the same conditions in dispersion in engine oil and in the boundary lubrication regime. The tribofilm and wear debris were characterized to understand the lubrication mechanisms. In addition, the optical properties and band energies of these MoS<sub>2</sub> materials are reported.

## 2. Experimental Procedure

In order to obtain the optimal conditions for synthetic procedure, a series of trials were carried out. All the chemicals were used in this synthesis without further filtration. Figure 1 shows a schematic diagram of the synthesis procedure and formation of MoS<sub>2</sub> nanoflowers and nanosheets.

**2.1. Preparation of Nanoflowers.** To obtain the MoS<sub>2</sub> flower-like structure, ammonium heptamolybdate tetrahydrate ((NH<sub>4</sub>)<sub>6</sub>Mo<sub>7</sub>O<sub>24</sub>·4H<sub>2</sub>O), citric acid (C<sub>6</sub>H<sub>8</sub>O<sub>7</sub>), and thioacetamide (C<sub>2</sub>H<sub>5</sub>NS) were used as the starting materials and the sulfur source. The synthesis methodology was performed with an optimized molar ratio of Mo to citric acid of 1:2. Starting, 1.4 g of ammonium heptamolybdate tetrahydrate and 0.61 g of citric acid were dissolved in distilled water under magnetic stirring and kept at 130°C on a hot plate for 25 min. The suspension was continuously stirred and refluxed with a final pH of 4. Then, 2.36 mL of thioacetamide in water was added dropwise to the solution. Finally, the precipitate solution was placed in a Teflon-lined stainless-steel autoclave.

**2.2. Preparation of Nanosheets.** The ammonium heptamolybdate tetrahydrate, citric acid, and thiourea (CH<sub>4</sub>N<sub>2</sub>S) were used as the starting materials and the sulfur source to obtain the MoS<sub>2</sub> sheet-like structure. Starting, 1.3 g of ammonium heptamolybdate and 0.49 g of citric acid were dissolved in distilled water under magnetic stirring and kept at 90°C on a hot plate for 25 min. The ammonia water is added to suspension solution with continuous stirring to adjust the pH at 4. Then, 1.27 g of thiourea in water was added dropwise to the solution with continuous stirring on a hot plate for 5 min. Finally, suspension solution was transferred into a 40 mL Teflon autoclave.

For both samples, the autoclave was maintained at 160°C for 10 h. The reactor was cooled to room temperature; the obtained black precipitates were collected by centrifugation and then filtered and washed three times with distilled water and ethanol. The obtained powders were finally dried under vacuum at 140°C for 8 h.

**2.3. Lubricants Preparation.** Experiments were performed using Durasyn-170 oil (polyalphaolefin (PAO)), which is a typical synthetic oil for automotive applications that has a density of 277 kg/m<sup>3</sup> at 15°C. The experiments were carried out with the base oil and with base oil containing 0.05, 0.1, 0.5, and 1 wt% of nanoflowers and nanosheets additives. A relatively various concentration of synthesized MoS<sub>2</sub> materials was used to determine the effect of morphology on the tribological performance. The suspensions of oil and nanoadditives were thoroughly mixed with a magnetic stirrer for 3 hours. The MoS<sub>2</sub> materials were added to the base oil and mixed with hexane, and stability measurement was done using a dynamic light scattering system (Nano ZS (ZEN 3600)). The kinematic viscosity of the oils was observed using an Ultra Programmable Rheometer as per ASTM standards.

**2.4. Tribological Tests.** The coefficient of friction and wear scar of all samples were studied using a four-ball tribometer. The four-ball test machine is used to estimate the wear preventive characteristics of the lubricant. The test force was kept constant at 40 Kgf, and 1000 rpm was applied for 60 minutes at 75°C. Steel balls with a 12.5 mm diameter and hardness of HRC 65 were used. The scar diameter of ball serves as a characteristic of the lubricant. In dissipative systems, extreme pressure at contacts is a major issue, depending on

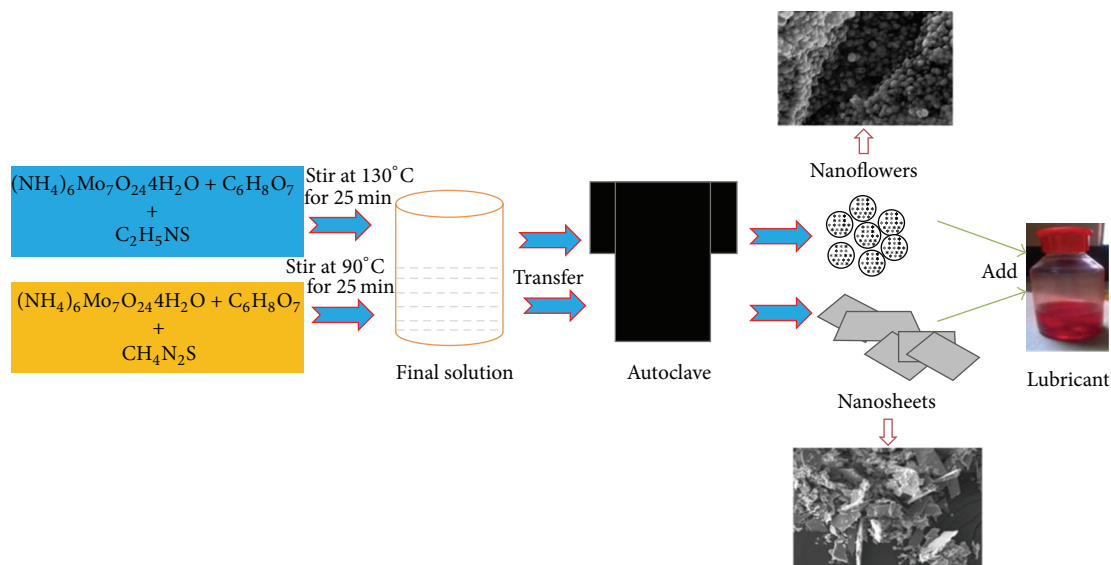


FIGURE 1: Schematic diagram of the formation of MoS<sub>2</sub> nanoflowers and nanosheets.

the potential applications, which is why we selected the four-ball tribometer for these studies.

The crystalline structure of the samples was estimated using powder X-ray diffraction (XRD) using a Shimadzu Labx XRD 6100 with Cu-K $\alpha$  radiation ( $\lambda = 0.14056$  nm). The morphologies of the samples were observed by scanning electron microscopy (SEM) on a Shimadzu Corporation Superscan SSX-550 SEM-EDS. Transmission electron microscope (TEM) analysis of the samples was carried out with a Hitachi H-7000 of 100 KV. The phase purity was estimated using a Fourier transform infrared spectroscope (FTIR) (Avatar 370) with a spectral range of 400–4000 cm<sup>-1</sup>. Thermogravimetry analysis was done using a DTG-60/60H TG/differential thermal analyzer under an argon gas at 900°C at a heating rate of 9°C per minute. The topography of the wear scar was studied by SEM and 3D surface profilometer. The chemical composition of the tribofilm formed on the worn surfaces of the upper ball was examined using EDS mapping.

### 3. Results and Discussion

The powder X-ray diffraction (XRD) studies were carried out to analyze the crystal structure of the MoS<sub>2</sub> nanoparticles as a function of the processing conditions as shown in Figure 2. Both samples exhibit the crystallite nature of MoS<sub>2</sub> materials with an XRD pattern indexed at 14°, 32°, 39.5°, and 58° corresponding to the (002), (100), (103), and (110) crystal planes of the MoS<sub>2</sub> structure, consistent with the corresponding standard card (JCPDS card number 371492). No impurity peaks or other phases were observed.

SEM images (Figures 3(a) and 3(b)) show that the sample obtained with C<sub>2</sub>H<sub>5</sub>NS as the sulfur source comprises uniform MoS<sub>2</sub> nanoflowers with an average size of 100 nm. The nanoflowers are well defined and rounded with a large amount of agglomeration of open-ended structure. It is

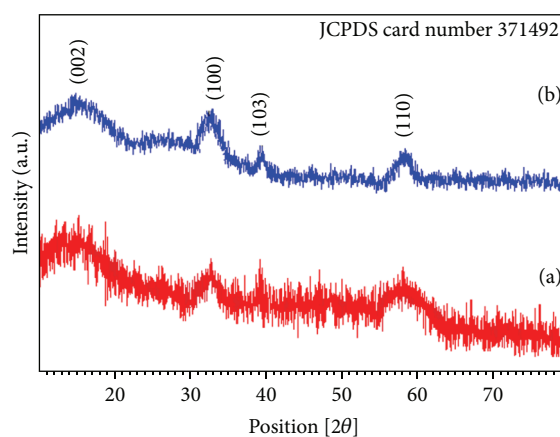


FIGURE 2: XRD patterns of MoS<sub>2</sub>: (a) nanoflowers and (b) nanosheets.

believed that this open-ended structure would offer more effective triboactive mechanisms for easy distribution on the interfacing surfaces. Interestingly, the sample obtained using thiourea as the sulfur source formed multilayer nanosheets of a size of a few nanometers, as shown in Figures 3(c) and 3(d) with different magnifications.

TEM images of the nanoflowers are shown with different magnifications in Figures 4(a), 4(b), and 4(c). The images show that the nanoflowers are rounded and loosely connected to each other with a narrow size distribution and regular spherical structure, which is in good agreement with the SEM results. This means that the nanoflowers have well-defined shape and are uniform in both morphology and particle size distribution. Figures 4(d), 4(e), and 4(f) show the structures of the nanosheets with different magnifications. The edge lengths of the nanosheets are controllable at the nanometer scale, typically from 40 nm to a few tens of nanometers, and their thickness is 10 to 50 nm.

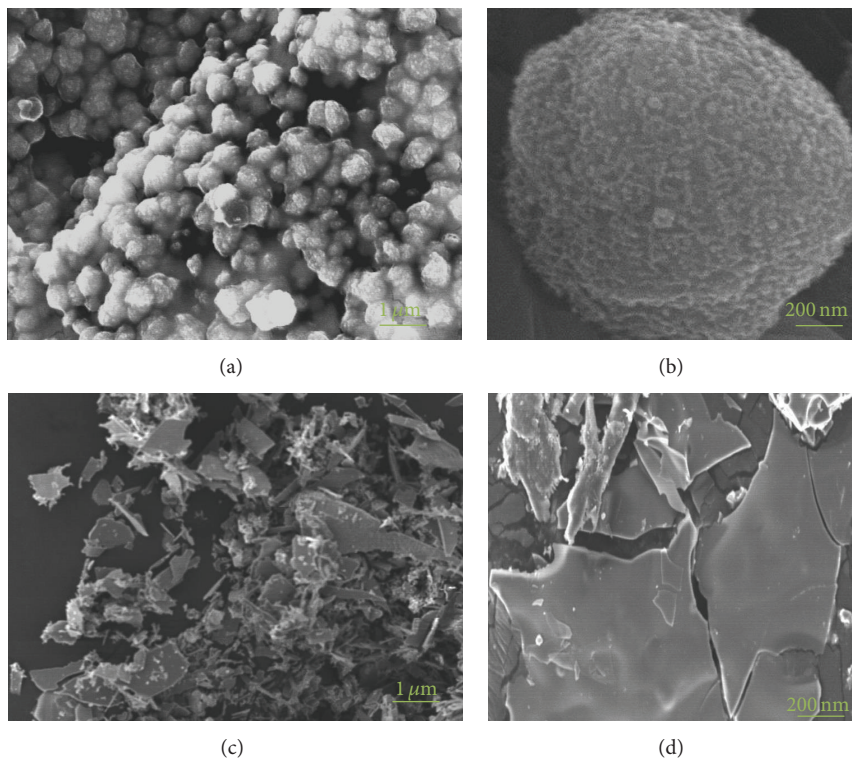


FIGURE 3: SEM images of MoS<sub>2</sub>: ((a) and (b)) nanoflowers and ((c) and (d)) nanosheets.

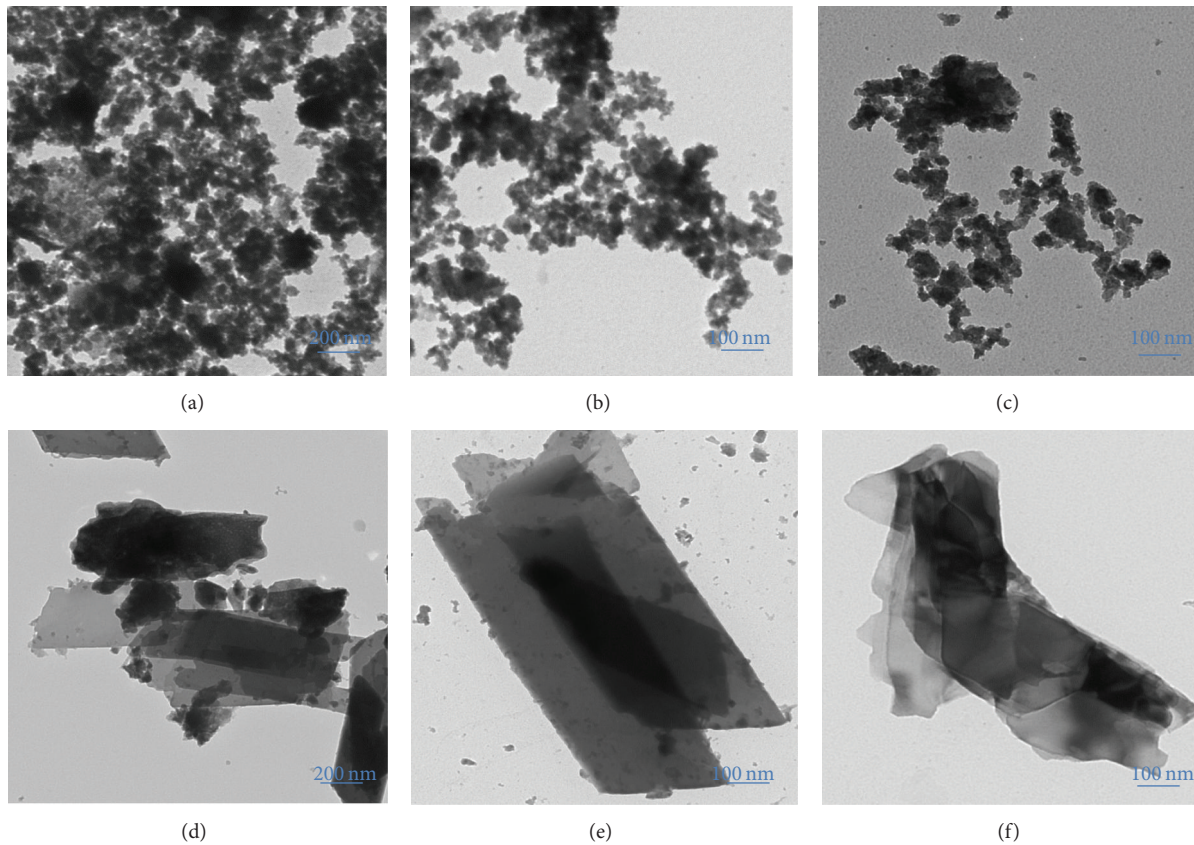


FIGURE 4: TEM images of MoS<sub>2</sub>: ((a), (b), and (c)) nanoflowers and ((d), (e), and (f)) nanosheets.

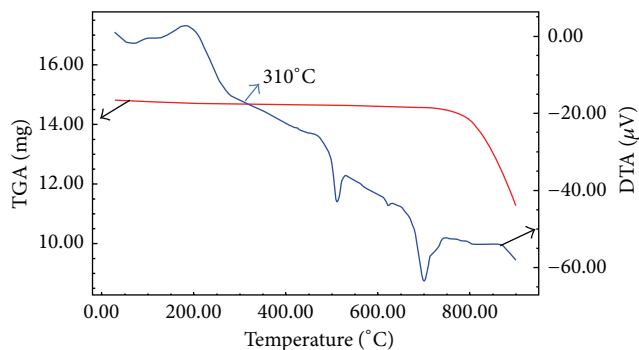


FIGURE 5: TG-DTA curves of MoS<sub>2</sub> nanosheets.

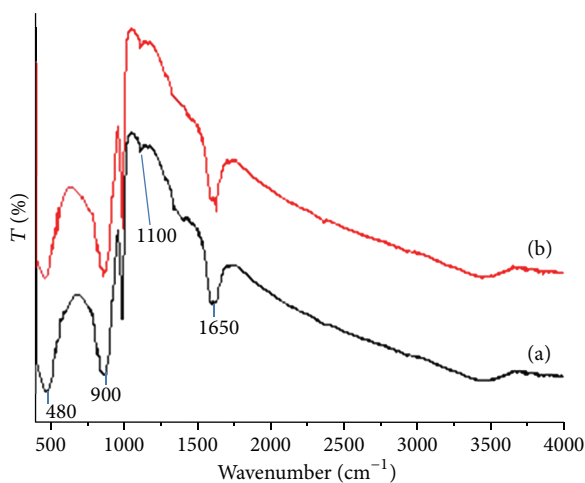


FIGURE 6: FT-IR spectra of MoS<sub>2</sub>: (a) nanoflowers and (b) nanosheets.

TG-DTA curves of the MoS<sub>2</sub> nanosheets are shown in Figure 5. The nanosheets display 5% weight loss occurring above 730°C when heating to 900°C throughout the analysis. This can be attributed to dehydroxylation of the material, which is favorable for recrystallization and growth of the nanosheets. The prominent exothermic peaks at 495°C and 700°C correspond to the decomposition of surfactants and the sheet crystallization phase. As a result, the decomposition of physisorbed solvent occurred during the preparation using heat-assisted magnetic stirring. Furthermore, there is a possibility that recrystallization could occur above 800°C, which reflects the stable state.

FT-IR spectra of the nanoflowers and nanosheets are shown in Figures 6(a) and 6(b). There are broad absorption bands at 480 cm<sup>-1</sup>, 900 cm<sup>-1</sup>, 1100 cm<sup>-1</sup>, and 1650 cm<sup>-1</sup> for both samples. The band at 480 cm<sup>-1</sup> is due to the Mo-S bond, and that at 900 cm<sup>-1</sup> is due to the S-S bond [36]. The absorption band between 1100 cm<sup>-1</sup> and 1650 cm<sup>-1</sup> is ascribed to the stretching vibrations of the hydroxyl group and Mo-O vibrations [36]. The absorption band at 3500 cm<sup>-1</sup> formed by the stretching vibration of hydroxyls vanished in the nanosheet sample, which was confirmed by the TG-DTA curve (Figure 5).

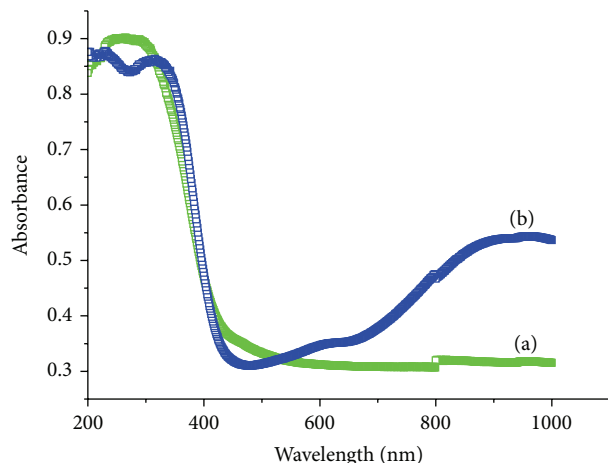


FIGURE 7: UV-Vis spectra of MoS<sub>2</sub>: (a) nanoflowers and (b) nanosheets.

The UV-Vis optical absorption spectra were recorded at room temperature in the wavelength region of 250–750 nm, as shown in Figures 7(a) and 7(b). The nanoflowers and nanosheets have strong absorption in the visible-light region. However, the absorption of the nanosheets compared to nanoflowers is stronger due to the higher light harvesting behavior of nanosheets with active edge sites. The absorption bands appeared at 340 and 610 nm, which are attributed to the direct excitonic transition at the *K* and *M* point of the Brillouin zone [37]. The indirect band gap was calculated by the Tauc equation using the optical absorption data near the band edge [38, 39]:

$$(\alpha h\nu)^{1/2} = A(h\nu - E_g), \quad (1)$$

where  $\alpha$  is the absorbance,  $h\nu$  is the incident photon energy, and  $A$  is a constant. The band gaps ( $E_g$ ) are determined by linear fit extrapolation onto the  $x$ -axis. A plot of  $(\alpha h\nu)^{1/2}$  versus photon energy ( $h\nu$ ) gives the band energies of the nanoflowers and nanosheets by the intercept of the tangent to the  $x$ -axis, as shown in Figures 8(a) and 8(b). The band energies of the MoS<sub>2</sub> nanoflowers and nanosheets were estimated to be 2.72 and 2.83 eV, respectively, which are fairly close to earlier reports [37, 40].

The agglomeration and stability of nanomaterials are quantified based on the zeta potential absolute value, which designates the static repellency of nanomaterials dispersed in oil, as shown in Figure 9. The maximum zeta potential absolute value of the nanoflowers and nanosheets in oil was obtained at 0.1 wt%, which is ascribed to the optimum concentration with maximum stability of the nanosheets in the base oil. The bigger value designates improved dispersion of the nanomaterials in the base oil. If the absolute value of zeta potential is higher than 30 mV, then the nanofluid becomes stable [41]. For nanoflowers and nanosheets dispersed oils, the absolute values of zeta potential are 32 and 34 mV, respectively. Thus, the stability of both oils is indicated to be good. In the case of nanosheets dispersed oil, the zeta potential of 0.6 wt % concentration is shown to be smaller than 1 wt% due

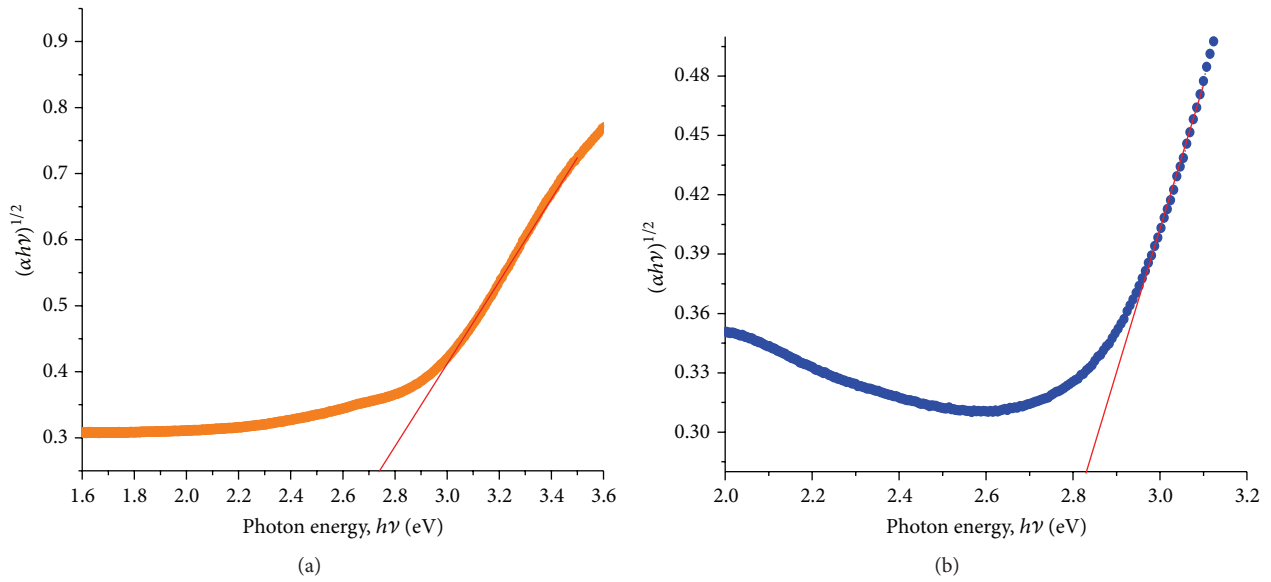


FIGURE 8: Tauc plots of MoS<sub>2</sub>: (a) nanoflowers and (b) nanosheets.

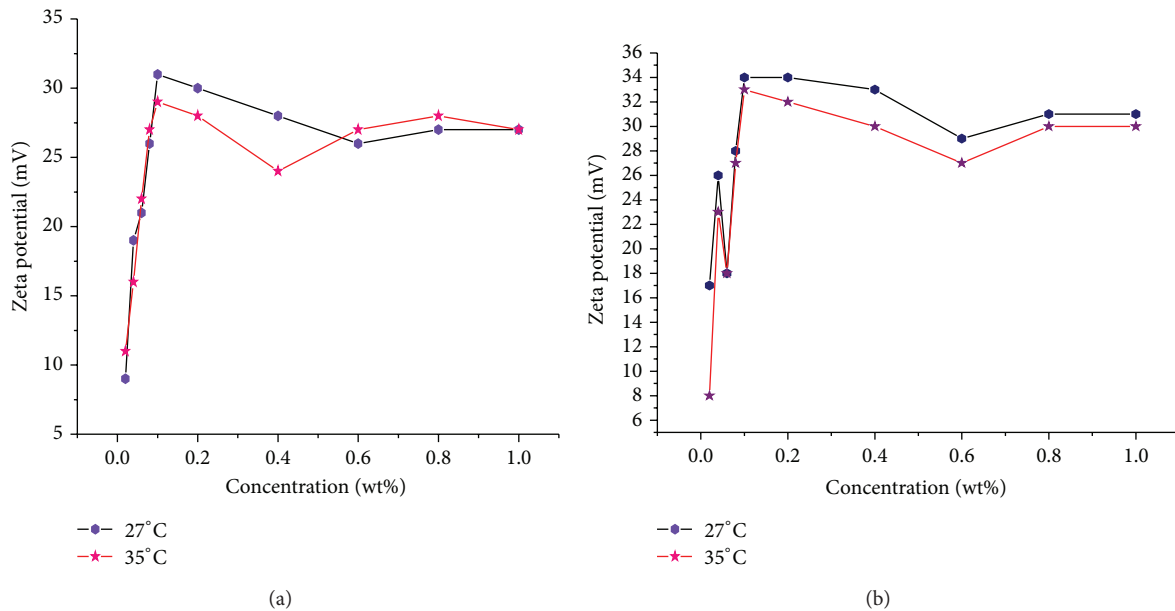


FIGURE 9: Variation of zeta potential with MoS<sub>2</sub> (a) nanoflowers and (b) nanosheets for different concentration at 27°C and 35°C.

to low pH value of the oil. Therefore, the zeta potential is related with corresponding pH of the nanoparticles dispersed oils. The dispersion nature of nanoadditives in oils depends on process parameters such as the type, concentration (wt% of nanoparticles), and nature of the base oil and temperature. Figure 10 shows the viscosity of the base oil and oils with 0.1 wt% of nanoflowers and nanosheets added was estimated in the temperature range of room temperature to 120°C. In all cases, the viscosity of lubricant decreases with increasing temperature. In addition, the viscosity increases by 20% for oil with nanoflowers and nanosheets added compared to the base oil at the elevated temperature, and no significant change

of viscosity was observed with the different morphologies of these nanomaterials.

Figure 11 shows the friction coefficient as a function of time with different concentrations of nanoflowers and nanosheets in oil. This data was obtained using a four-ball test with a 40 Kgf load and a speed of 1000 rpm for 60 minutes. The friction coefficient of the pure base oil without any additives increases with the applied load. Furthermore, the friction coefficient of the base oil containing nanoflowers or nanosheets is always lower than that of the pure base oil. On the other hand, the base oil containing nanosheets exhibits a lower friction coefficient than that with nanoflowers.

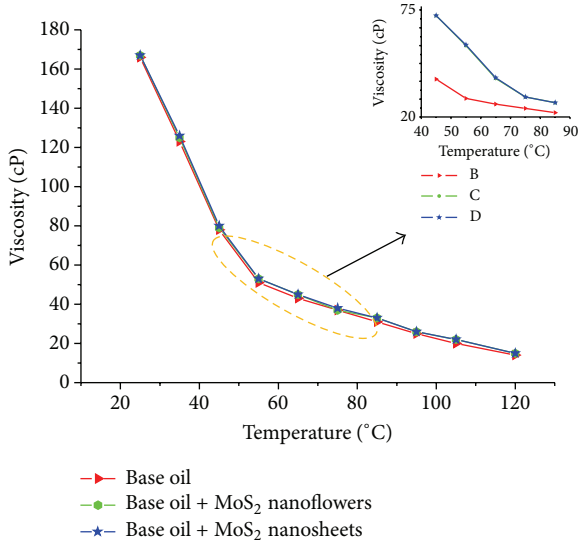


FIGURE 10: Variation of viscosity with respect to temperature.

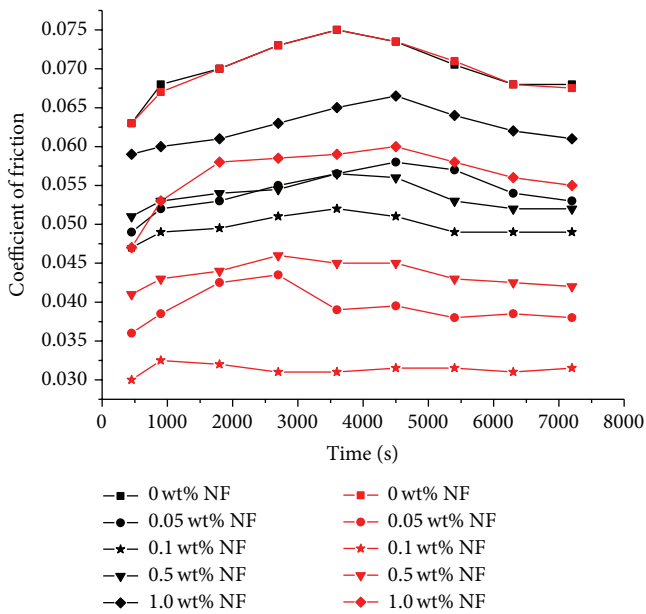


FIGURE 11: Friction coefficient curves of different concentrations of MoS<sub>2</sub> nanoflowers (black color line) and nanosheets (red color line) with respect to time.

This is due to the slippage of nanosheets at asperities and deformation into individual nanosheets to form a tribofilm at the interfaces, which reduces the coefficient of friction. The friction coefficient ( $\mu$ ) is equal to  $T\sqrt{6}/3Wr$ , where  $T$  is the frictional torque in kg mm,  $W$  is the normal load in kg, and  $r$  is the distance between the center of the interface on the lower balls and the axis of rotation [42, 43].

To evaluate the wear-resistance tribological properties of the MoS<sub>2</sub> nanomaterials, a noncontact universal surface profilometer was used to measure the wear scar and debris of the balls. Figure 12 shows the micrographs of worn

surfaces produced after the 1 h tests with lubrication using the nanoflowers and nanosheets. Negligible wear scar for the steel balls was observed during these experiments for oil containing 0.1 wt% nanoflowers and nanosheets. There is a clean film on the surface of the steel balls, and in the case of nanosheets dispersed in oil, the tested balls have greater film formation than the nanoflower oil. The base oil with nanosheets is easily adherent and causes plastic deformation due to the contact pressure. The formation of tribofilm containing nanosheets supports reducing the friction due to slippage of the individual layers of nanosheets.

Interestingly, the average surface roughness ( $R_a$ ) value of the nanoflowers and nanosheets dispersed in oils remained constant as a function of the normal load.  $R_a$  of the wear scars of the nanoflower and nanosheet oils were low: approximately 85.3 and 54.2 nm, respectively, as shown in Figure 12. The results suggest some fracture occurs due to adhesive wear upon continuous sliding friction under the applied load. This proves that the base oils with nanoflowers and nanosheets have better antiwear capability than the pure base oil. MoS<sub>2</sub> nanomaterials can easily react and form an abrasion-resistant protective film at contact interfaces due to high surface energy with many dangling bonds [16]. A firm boundary lubrication effect between the friction pairs occurs when protective tribofilms formed. This may yield a good ability to resist the shear failure due to fine lubricity. The friction coefficient thus declines distinctly, and the surface quality of the contact elements improves greatly, as shown in Figures 12(a) and 12(b).

SEM micrographs (Figures 13(a), 13(b), and 13(c)) show the wear scars of the base oil with and without nanoflowers or nanosheets. The rubbed surface was lubricated by the base oil and had many wide and deep ruts compared to the nanoflowers and nanosheets oils. We believe that the many regular nanosheets penetrate more easily into the interface with the lubricant than the nanoflowers. The nanosheets could form a continuous film on the rubbing surfaces due to strong adherence to contacts and enhance the tribological properties. The nanoflowers are so small that they can easily go into worn areas under compressive stress and perturb the hydrodynamic regime. Because of this, a higher coefficient of friction was obtained for nanoflowers rather than nanosheets, which is in good agreement with Figure 11.

The presence and formation of a tribofilm on the worn surface were examined with EDS for base oil containing 0.1 wt% nanoflowers and nanosheets, as shown in Figures 13(d), 13(e), and 13(f). Mo-S signals detected on the worn surface indicate that the MoS<sub>2</sub> nanomaterials settle and fill the furrows on the worn surface, although the Mo-S signal is much weaker than the Fe signal on the ball surface. Moreover, the surface scratches and the furrows became vanished. Both the friction coefficient and the wear scar diameter were minimal. In both cases (i.e., nanoflowers and nanosheets), the surface edges were slightly ragged and obscured by metal particles at normal loads greater than 40 Kgf. As a result, worn surfaces revealed abrasive wear and no severe adhesive wear was noticed.

The superior friction reduction and antiwear behavior of MoS<sub>2</sub> nanoflowers and nanosheets dispersed in oil compared

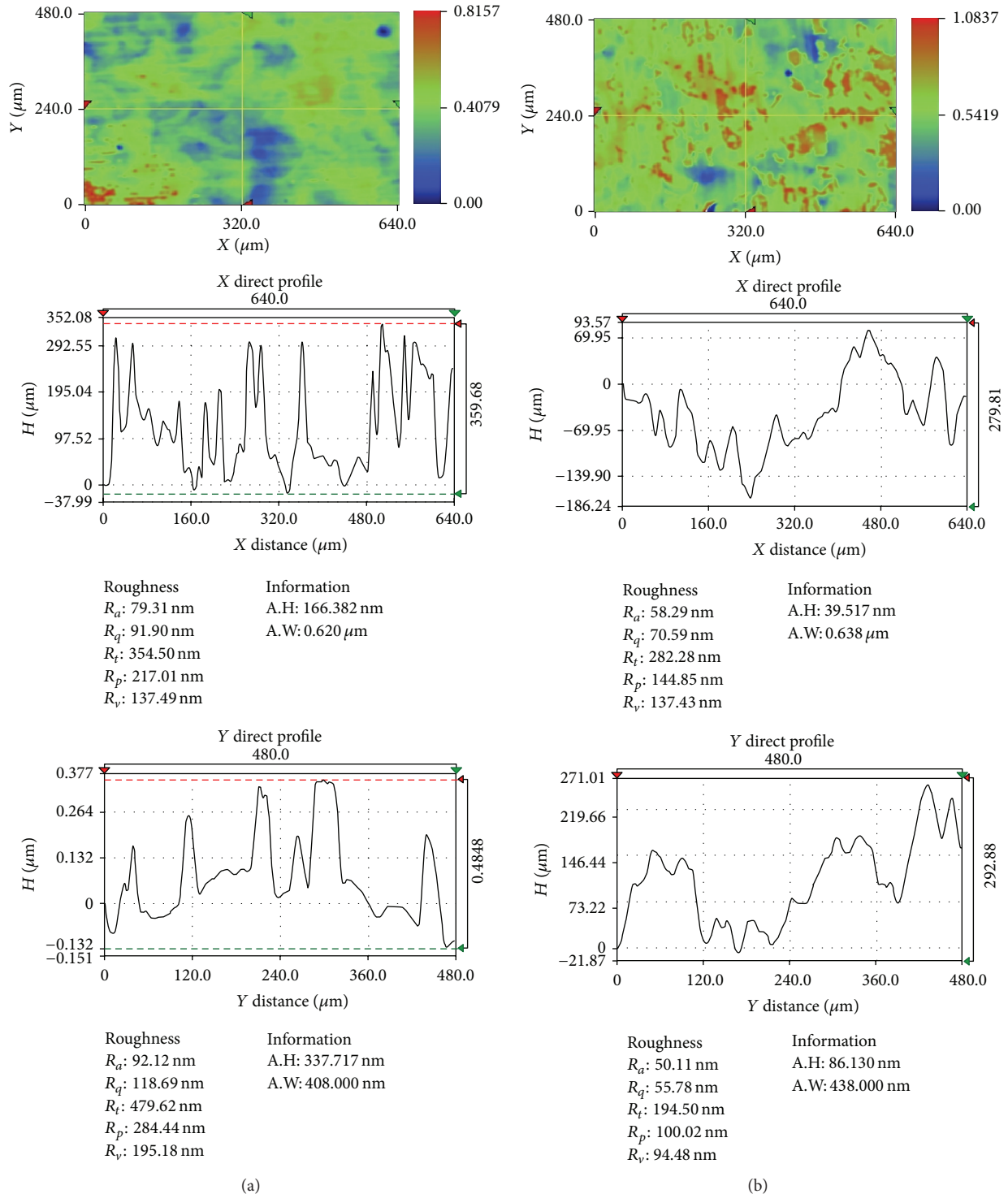


FIGURE 12: Noncontact optical profile testing apparatus images of wear scar at 1000 rpm under 40 Kgf loads for 1 h: (a) base oil with MoS<sub>2</sub> nanoflowers and (b) base oil with 1.0 wt% MoS<sub>2</sub> nanosheets.

to pristine oil are attributed to development of tribofilms between the contact interfaces [10, 12, 13, 20]. The wear mechanism of MoS<sub>2</sub> nanosheets is ascribed to separation of interlayers into individual layers due to weaker van der Waals or Coulombic repulsive interaction at contact pressure

[13, 25, 26]. This mechanism helps to form a tribofilm and adhere at counter parts, enhancing the tribological properties which are confirmed with 3D topography results (Figure 12). The tribological properties with dispersion of MoS<sub>2</sub> additives in oil are improved. The worn surface of the upper ball

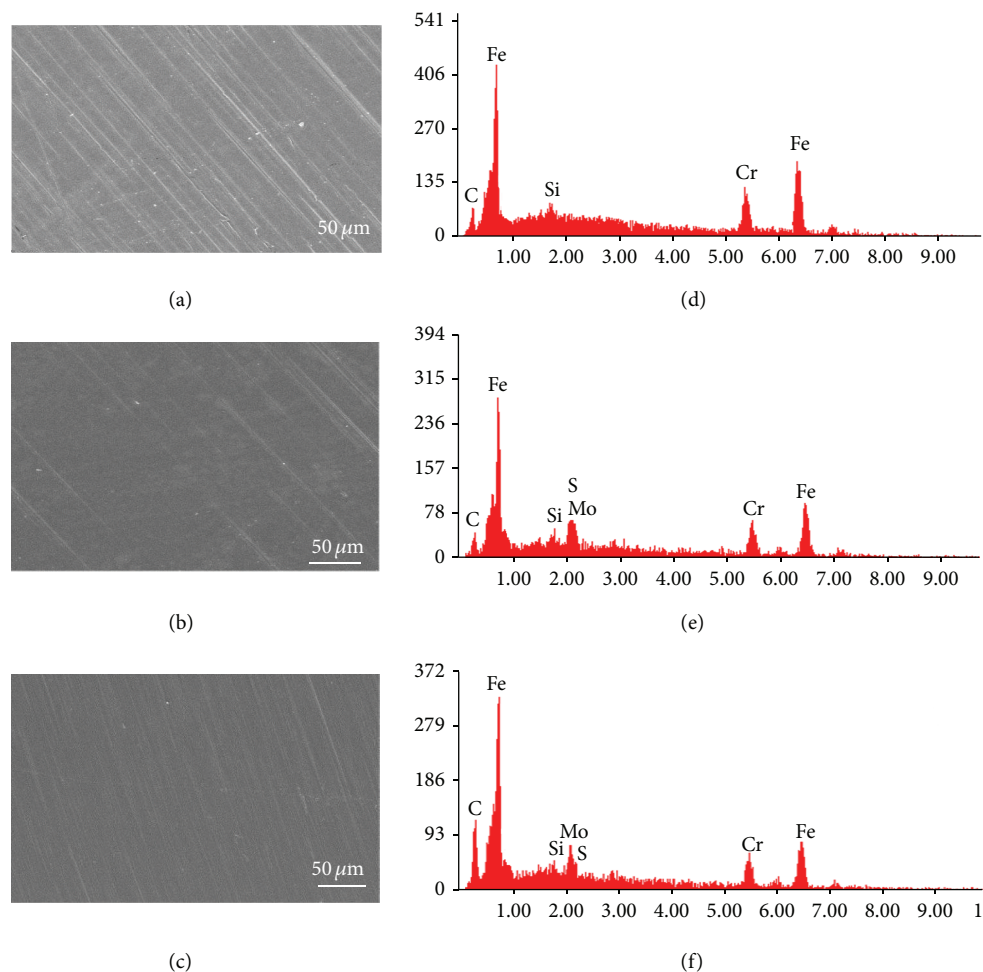


FIGURE 13: Wear scar of upper ball on contacted surface with different conditions: (a) base oil, (b) base oil with 0.1 wt% MoS<sub>2</sub> nanoflowers, and (c) base oil with 0.1 wt% MoS<sub>2</sub> nanosheets. (d), (e), and (f) represent EDS spectra of (a), (b), and (c) conditions, respectively.

showed metal-to-metal contact at interfaces. Therefore, the nanosheets could reduce the coefficient of friction, since the metal-to-metal contact is smaller than when nanoflowers were used. Presumably, these results indicated that the nanosheets are more suitable and helped the lubricant to adsorb onto the metal surface very well, which reduced the friction.

#### 4. Conclusions

We report the solvothermal synthesis of MoS<sub>2</sub> nanoflowers and nanosheets using thioacetamide and thiourea as sulfur source, respectively. The method presented enables large-scale production of unique and controllable morphologies by suitable selection of the surfactant. The effects and nature of morphology on the tribological properties have been presented. Substantial friction and wear reduction was achieved in boundary lubrication, and the beneficial effects are attributed to the nanosheets rather than nanoflowers when added to the lubricant oil. The results revealed tribological effect of engine oil without additive and presence of nanoflowers and nanosheets.

From the friction tests, the performance of lubricating oil using these synthesized MoS<sub>2</sub> materials as additives is investigated using the four-ball test and results show that the optimal additive concentration of nanoflowers and nanosheets is 0.1 wt%. The friction test results revealed that the average friction coefficient was two times lower for the nanosheets than for the nanoflowers. It was concluded that the significant improvement in tribological properties of oil with nanoflowers and nanosheets additives was due to the beneficial tribofilm transferred on the contact surfaces when particles entered the wear regime as evident from SEM and EDS studies.

The surface roughness analyses reveal that the roughness of the friction surface is reduced and the surface gets smoother when MoS<sub>2</sub> materials at optimum concentration level are added to the lubricants. It was also concluded that, as the benefits of exfoliation mechanism, the nanoflowers and nanosheets act as reservoir of low friction layers which cover the interface surfaces with a thickness of a few monolayers. Therefore, nanoflowers and nanosheets used as lubricating oil additives exhibit wear reduction characteristics. The unique mechanical and tribological properties indicate that the MoS<sub>2</sub>

nanosheets are a promising material for autolocomotive applications and help to contribute to successful commercialization of hybrid lubricants.

### Conflict of Interests

The authors declare that there is no conflict of interests regarding the publication of this paper.

### Acknowledgments

This research was supported by the Basic Science Research Program through the National Research Foundation of Korea (NRF) and funded by the Ministry of Science, ICT, and Future Planning (2014R1A2A2A01007081).

### References

- [1] Z. Yu, L. Tetard, L. Zhai, and J. Thomas, "Supercapacitor electrode materials: nanostructures from 0 to 3 dimensions," *Energy & Environmental Science*, vol. 8, no. 3, pp. 702–730, 2015.
- [2] X.-R. Wang, Y. Shi, and R. Zhang, "Field-effect transistors based on two-dimensional materials for logic applications," *Chinese Physics B*, vol. 22, no. 9, Article ID 098505, 2013.
- [3] W. E. Buhro and V. L. Colvin, "Semiconductor nanocrystals: shape matters," *Nature Materials*, vol. 2, pp. 138–139, 2003.
- [4] Y. Jung, J. Shen, and J. J. Cha, "Surface effects on electronic transport of 2D chalcogenide thin films and nanostructures," *Nano Convergence*, vol. 1, article 18, 8 pages, 2014.
- [5] C. Tan and H. Zhang, "Two-dimensional transition metal dichalcogenide nanosheet-based composites," *Chemical Society Reviews*, vol. 44, no. 9, pp. 2713–2731, 2015.
- [6] K. P. Rao and C. L. Xie, "A comparative study on the performance of boric acid with several conventional lubricants in metal forming processes," *Tribology International*, vol. 39, no. 7, pp. 663–668, 2006.
- [7] J. Luo, M. H. Zhu, Y. D. Wang, J. F. Zheng, and J. L. Mo, "Study on rotational fretting wear of bonded MoS<sub>2</sub> solid lubricant coating prepared on medium carbon steel," *Tribology International*, vol. 44, no. 11, pp. 1565–1570, 2011.
- [8] F. A. Deorsola, N. Russo, G. A. Blengini, and D. Fino, "Synthesis, characterization and environmental assessment of nanosized MoS<sub>2</sub> particles for lubricants applications," *Chemical Engineering Journal*, vol. 195–196, pp. 1–6, 2012.
- [9] I. Efeoglu, Ö. Baran, F. Yetim, and S. Altıntaş, "Tribological characteristics of MoS<sub>2</sub>-Nb solid lubricant film in different tribo-test conditions," *Surface and Coatings Technology*, vol. 203, no. 5–7, pp. 766–770, 2008.
- [10] I. Lahouij, B. Vacher, J.-M. Martin, and F. Dassenoy, "IF-MoS<sub>2</sub> based lubricants: influence of size, shape and crystal structure," *Wear*, vol. 296, pp. 558–567, 2012.
- [11] R. Tenne, L. Margulis, M. Genut, and G. Hodes, "Polyhedral and cylindrical structures of WS<sub>2</sub>," *Nature*, vol. 360, pp. 444–446, 1992.
- [12] R. R. Sahoo and S. K. Biswas, "Effect of layered MoS<sub>2</sub> nanoparticles on the frictional behavior and microstructure of lubricating greases," *Tribology Letters*, vol. 53, no. 1, pp. 157–171, 2014.
- [13] G. Zhu, J. Sun, B. Wang, and Y. Wang, "Study on tribological properties of the rolling fluid containing nano-MoS<sub>2</sub> for cold rolling of steel strip," *China Petroleum Processing and Petrochemical Technology*, vol. 13, no. 1, pp. 64–69, 2011.
- [14] M. Praveena, V. Jayaram, and S. K. Biswas, "Friction between a steel ball and a steel flat lubricated by MoS<sub>2</sub> particles suspended in hexadecane at 150 °C," *Industrial and Engineering Chemistry Research*, vol. 51, no. 38, pp. 12321–12328, 2012.
- [15] J. Kogovšek, M. Remškar, and M. Kalin, "Lubrication of DLC-coated surfaces with MoS<sub>2</sub> nanotubes in all lubrication regimes: surface roughness and running-in effects," *Wear*, vol. 303, no. 1–2, pp. 361–370, 2013.
- [16] Y. Feldman, E. Wasserman, D. J. Srolovitz, and R. Tenne, "High-rate, gas-phase growth of MoS<sub>2</sub> nested inorganic fullerenes and nanotubes," *Science*, vol. 267, no. 5195, pp. 222–225, 1995.
- [17] L. Margulis, G. Salitra, R. Tenne, and M. Talianker, "Nested fullerene-like structures," *Nature*, vol. 365, no. 6442, pp. 113–114, 1993.
- [18] L. Rapoport, Y. Feldman, M. Homyonfer et al., "Inorganic fullerene-like material as additives to lubricants: structure-function relationship," *Wear*, vol. 225–229, pp. 975–982, 1999.
- [19] R. Greenberg, G. Halperin, I. Etsion, and R. Tenne, "The effect of WS<sub>2</sub> nanoparticles on friction reduction in various lubrication regimes," *Tribology Letters*, vol. 17, no. 2, pp. 179–186, 2004.
- [20] J. Tannous, F. Dassenoy, I. Lahouij et al., "Understanding the tribochemical mechanisms of IF-MoS<sub>2</sub> nanoparticles under boundary lubrication," *Tribology Letters*, vol. 41, no. 1, pp. 55–64, 2011.
- [21] P. Rabaso, F. Ville, F. Dassenoy, J. M. Martin, and M. Diaby, "Tribological behaviour of fullerene-like MoS<sub>2</sub> nanoparticles for different lubrication regimes in the presence of dispersants," in *Proceedings of the 40th Leeds-Lyon Symposium on Tribology & Tribochemistry Forum*, Lyon, France, September 2013.
- [22] L. Rapoport, Y. Bilik, Y. Feldman, M. Homyonfer, S. R. Cohen, and R. Tenne, "Hollow nanoparticles of WS<sub>2</sub> as potential solid-state lubricants," *Nature*, vol. 387, no. 6635, pp. 791–793, 1997.
- [23] L. Cizaire, B. Vacher, T. le Mogne et al., "Mechanisms of ultra-low friction by hollow inorganic fullerene-like MoS<sub>2</sub> nanoparticles," *Surface and Coatings Technology*, vol. 160, no. 2–3, pp. 282–287, 2002.
- [24] L. Joly-Pottuz, F. Dassenoy, M. Belin, B. Vacher, J. M. Martin, and N. Fleischer, "Ultralow-friction and wear properties of IF-WS<sub>2</sub> under boundary lubrication," *Tribology Letters*, vol. 18, no. 4, pp. 477–485, 2005.
- [25] R. Rosentsveig, A. Gorodnev, N. Feuerstein et al., "Fullerene-like MoS<sub>2</sub> nanoparticles and their tribological behavior," *Tribology Letters*, vol. 36, no. 2, pp. 175–182, 2009.
- [26] M. Kalin, J. Kogovšek, and M. Remškar, "Mechanisms and improvements in the friction and wear behavior using MoS<sub>2</sub> nanotubes as potential oil additives," *Wear*, vol. 280–281, pp. 36–45, 2012.
- [27] A. Moshkovith, V. Perfiliev, A. Verdyan et al., "Sedimentation of IF-WS<sub>2</sub> aggregates and a reproducibility of the tribological data," *Tribology International*, vol. 40, no. 1, pp. 117–124, 2007.
- [28] A. Moshkovith, V. Perfiliev, I. Lapsker, N. Fleischer, R. Tenne, and L. Rapoport, "Friction of fullerene-like WS<sub>2</sub> nanoparticles: effect of agglomeration," *Tribology Letters*, vol. 24, no. 3, pp. 225–228, 2006.
- [29] M. Chhowalla and G. A. J. Amaratunga, "Thin films of fullerene-like MoS<sub>2</sub> nanoparticles with ultra-low friction and wear," *Nature*, vol. 407, no. 6801, pp. 164–167, 2000.
- [30] X. L. Li and Y. D. Li, "Formation of MoS<sub>2</sub> inorganic fullerenes (IFs) by the reaction of MoO<sub>3</sub> nanobelts and S," *Chemistry—A European Journal*, vol. 9, no. 12, pp. 2726–2731, 2003.

- [31] H. Tang, C. Li, X. Yang, C. Mo, K. Cao, and F. Yan, "Synthesis and tribological properties of NbSe<sub>3</sub> nanofibers and NbSe<sub>2</sub> microsheets," *Crystal Research and Technology*, vol. 46, no. 4, pp. 400–404, 2011.
- [32] L. Rapoport, N. Fleischer, and R. Tenne, "Applications of WS<sub>2</sub> (MoS<sub>2</sub>) inorganic nanotubes and fullerene-like nanoparticles for solid lubrication and for structural nanocomposites," *Journal of Materials Chemistry*, vol. 15, no. 18, pp. 1782–1788, 2005.
- [33] I. Uzcanga, I. Bezverkhy, P. Afanasiev, C. Scott, and M. Vrinat, "Sonochemical preparation of MoS<sub>2</sub> in aqueous solution: replication of the cavitation bubbles in an inorganic material morphology," *Chemistry of Materials*, vol. 17, no. 14, pp. 3575–3577, 2005.
- [34] G. Santillo, F. A. Deorsola, S. Bensaid, N. Russo, and D. Fino, "Sonochemical preparation of MoS<sub>2</sub> in aqueous solution: replication of the cavitation bubbles in an inorganic material morphology," *Chemical Engineering Journal*, vol. 207–208, no. 1, pp. 322–328, 2012.
- [35] H. Akram, C. Mateos-Pedrero, E. Gallegos-Suárez, A. Guerrero-Ruiz, T. Chafik, and I. Rodríguez-Ramos, "Effect of electrolytes nature and concentration on the morphology and structure of MoS<sub>2</sub> nanomaterials prepared using one-pot solvothermal method," *Applied Surface Science*, vol. 307, pp. 319–326, 2014.
- [36] G. Nagaraju, C. N. Tharamani, G. T. Chandrappa, and J. Livage, "Hydrothermal synthesis of amorphous MoS<sub>2</sub> nanofiber bundles via acidification of ammonium heptamolybdate tetrahydrate," *Nanoscale Research Letters*, vol. 2, no. 9, pp. 461–468, 2007.
- [37] E. P. Nguyen, B. J. Carey, T. Daeneke et al., "Investigation of two-solvent grinding-assisted liquid phase exfoliation of layered MoS<sub>2</sub>," *Chemistry of Materials*, vol. 27, no. 1, pp. 53–59, 2015.
- [38] S. K. Bhar, N. Mukherjee, S. K. Maji, B. Adhikary, and A. Mondal, "Synthesis of nanocrystalline iron oxide ultrathin films by thermal decomposition of iron nitropruside: structural and optical properties," *Materials Research Bulletin*, vol. 45, no. 12, pp. 1948–1953, 2010.
- [39] L. Diamandescu, F. Vasiliu, D. Tarabasanu-Mihaila et al., "Structural and photocatalytic properties of iron- and europium-doped TiO<sub>2</sub> nanoparticles obtained under hydrothermal conditions," *Materials Chemistry and Physics*, vol. 112, no. 1, pp. 146–153, 2008.
- [40] M. Zhong, Z. Wei, X. Meng, F. Wu, and J. Li, "From MoS<sub>2</sub> microspheres to  $\alpha$ -MoO<sub>3</sub> nanoplates: growth mechanism and photocatalytic activities," *European Journal of Inorganic Chemistry*, no. 20, pp. 3245–3251, 2014.
- [41] J.-H. Lee, K. S. Hwang, S. P. Jang et al., "Effective viscosities and thermal conductivities of aqueous nanofluids containing low volume concentrations of Al<sub>2</sub>O<sub>3</sub> nanoparticles," *International Journal of Heat and Mass Transfer*, vol. 51, no. 11–12, pp. 2651–2656, 2008.
- [42] T. C. Ing, A. K. Mohammed Rafiq, Y. Azli, and S. Syahrullail, "The effect of temperature on the tribological behavior of RBD palm stearin," *Tribology Transactions*, vol. 55, no. 5, pp. 539–548, 2012.
- [43] J. M. Thorp, "Four-ball assessment of deep drawing oils," *Wear*, vol. 33, no. 1, pp. 93–108, 1975.

## Review Article

# Preparation and Application of Fluorescent Carbon Dots

**Jun Zuo, Tao Jiang, Xiaojing Zhao, Xiaohong Xiong, Saijin Xiao, and Zhiqiang Zhu**

*Jiangxi Key Laboratory for Mass Spectrometry and Instrumentation, East China Institute of Technology, Nanchang 330013, China*

Correspondence should be addressed to Zhiqiang Zhu; [zhiqiangz@iccas.ac.cn](mailto:zhiqiangz@iccas.ac.cn)

Received 20 May 2015; Accepted 21 June 2015

Academic Editor: Xiaogang Han

Copyright © 2015 Jun Zuo et al. This is an open access article distributed under the Creative Commons Attribution License, which permits unrestricted use, distribution, and reproduction in any medium, provided the original work is properly cited.

Fluorescent carbon dots (CDs) are a novel type of fluorescent nanomaterials, which not only possess the specific quantum confinement effects of nanomaterials due to the small size of nanomaterials, but also have good biocompatibility and high fluorescence. Meanwhile, fluorescence CDs overcome the shortcomings of high toxicity of traditional nanomaterials. Moreover, the preparation procedure of fluorescent CDs is simple and easy. Therefore, fluorescent CDs have great potential applied in photocatalysis, biochemical sensing, bioimaging, drug delivery, and other related areas. In this paper, recent hot researches on fluorescent CDs are reviewed and some problems in the progress of fluorescent CDs are also summarized. At last, a future outlook in this direction is presented.

## 1. Introduction

Nanotechnology is one of the most important technologies in 21st century. Currently, nanotechnology has been widely applied in numerous fields, such as biomedical and chemical analysis. In recent years, fluorescent nanomaterials have garnered much interest as potential competitors to traditional fluorescent dye probe and developed quite rapidly due to the extensive demand of fluorescent probe in chemical sensing, biological monitoring, and other related fields. Compared with the traditional fluorescent dye, fluorescent nanomaterials have quantum size effect and the unique effects of nanomaterials, which can overcome many shortcomings of the latter, such as the low stability, weak fluorescence intensity, and fast photobleaching. Therefore, fluorescent nanomaterials have been applied widely in the physical, biological, and chemistry as well as other related fields [1]. Among many kinds of nanoparticles, semiconductor quantum dots have become the focus of attention due to their unique electronic and luminescent properties [2–4]. However, semiconductor quantum dots usually contain heavy metals, which are general great toxic and limit their further applications in the field of biomedicine [5–7]. Thereby, the development of new nontoxic heavy metal-contained nanomaterials is one of the current trends.

In 2004, Xu et al. [8] discovered accidentally this kind of carbon nanoparticles with fluorescent properties for the first time when they separated single-walled carbon nanotubes using gel electrophoresis from carbon soot produced by arc discharge. Based on this study, in 2006, Sun et al. [9] synthesised fluorescent carbon nanoparticles with diameter less than 10 nm and named them carbon dots (CDs). The discovery of CDs has gathered to widespread concern of scientific researchers; in particular, their low toxicity and stable chemical properties make them become powerful candidates for new types of fluorescent probe and overcome the common drawbacks of previous fluorescent probes. In addition, fluorescent CDs possess rather strong ability to bind with other organic and inorganic molecules due to their abundant surface groups, so that fluorescent CDs can be manipulated via a series of controllable chemical treatments and satisfied the demands in the photocatalytic, biochemical, and chemical sensing, bioimaging, and drug carrier. Currently, the researches of fluorescent CDs mainly focus on two aspects; one is developing rapid, simple preparation method of fluorescent CDs, and the other is expanding the application field. This paper reviews the recent progress in these two aspects and especially discusses the advantages of fluorescent CDs applied in these new scientific fields.

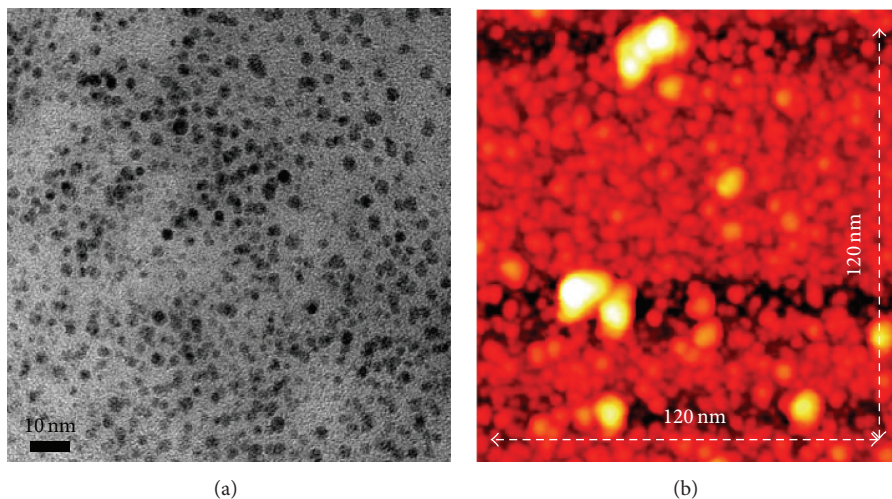


FIGURE 1: (a) HR-TEM image, (b) AFM image (reproduced with permission from [11]).

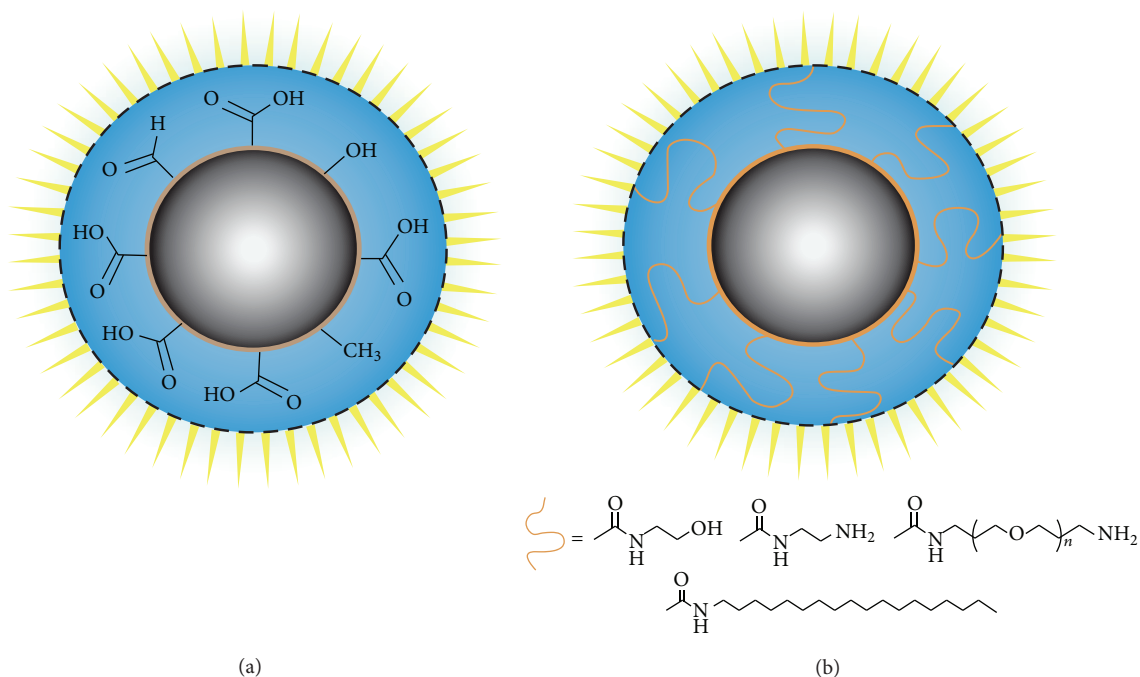


FIGURE 2: Depiction of Cdots (a) after surface oxidation treatment and (b) after functionalization with surface passivation reagents (reproduced with permission from [12]).

## 2. Structures and Properties of CDs

Generally, CDs are nearly spherical nanocrystals with the diameter less than 10 nm and comprising few molecules or atoms of nanoclusters (Figure 1) [10, 11]. Compared with those larger particles like quantum dots, the size of carbon particles is generally only a few nanometers, and molecular weight is also only a few thousand to tens of thousands. Generally, there exist a large amount of -OH and -COOH and -NH<sub>2</sub> and other groups on CDs surfaces (Figure 2) [9], which endow CDs with good water solubility and polymerization

ability with various inorganic, organic, or biologically active substances.

**2.1. The Optical Properties of CDs.** CDs have strong absorption in the ultraviolet region, which can also extend to visible region [12]. After modification of some passivating agents, the absorption spectral region may be red shift continuously [13]. The luminescence properties of CDs are mainly the photoluminescence and electrochemical luminescence, in which photoluminescence is the most prominent

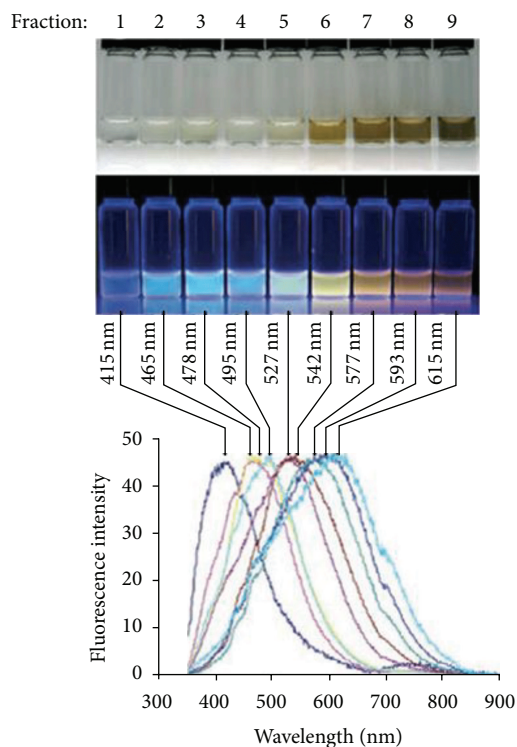


FIGURE 3: Optical characterization of the purified CNPs. Optical images illuminated under white (top) and UV light (312 nm, center). Bottom: fluorescence emission spectra (excitation at 315 nm) of the corresponding CNP solutions. The maximum emission wavelengths are indicated above the spectra (reproduced with permission from [14]).

performance. As an important role in almost all areas of fluorescent nanomaterials, the excellent optical properties of CDs mainly include high fluorescence stability, nonblinking, tunable excitation, and emission wavelengths (Figure 3) [14–17]. However, the emitting mechanisms of CDs are still not clear, only keeping the phenomenon levels. The in-depth quantum interpretation needs to be established. Some researchers speculated that the emitting mechanisms of CDs involve quantum confinement effect, stabilizing surface trap, or exciton recombination radiation [18].

**2.2. Biocompatibility and Low Toxicity of CDs.** Since carbon element is the skeleton of all living body, full carbon nanomaterials have a lower toxicity compared with other nanomaterials; simultaneously, the particle size of CDs is smaller and then more convenient to enter the cell in vivo, which makes CDs have great potential application in the biological fields. In addition, the surface of CDs contains a lot of functional groups, so that the surface of CDs can be modified with organic, inorganic, polymer, and other substances endowing different functional properties.

### 3. Preparation of CDs

In recent decade, there is great progress in the preparation process of CDs, not only simplifying the manufacturing

process, but also optimizing the luminescence properties of the CDs. Basically, self-preparation processes from the bottom-up and the top-down approaches are two main categories. Since the top-down approach is through cutting, oxidation, the larger carbon cluster structure is cleaved into small carbon nanoparticles resulting in CDs with smaller particle diameter. On the contrary, the bottom-up approach is based on series of chemical reactions of small molecule precursors to form nanoscale CDs.

**3.1. Top-Down Approach.** Top-down preparations of fluorescence CDs are the early preparation approaches, including arc-discharge method [8, 19], electrochemical oxidation [20–23], and laser ablation [24, 25]. In 2004, Xu et al. [8] firstly separated accidentally fluorescent nanoparticle from the products when they prepared the single-walled carbon nanotubes by arc discharge. They also introduced nitril onto the fluorescent CDs by arc discharging fuming nitric acid, improving the hydrophilicity of nanomaterials. After that, NaOH solution (pH = 8.4) was used to extract the precipitate to give a black suspension and obtained three groups of fluorescent carbon nanoparticles with different molecular weights after further electrophoretic separation. These three groups of fluorescent carbon nanoparticles emit blue green, yellow, and orange fluorescence, respectively, wherein the fluorescence quantum yield of yellow phosphor carbon nanomaterials can reach 1.6%. Subsequently, Sun et al. pioneered in synthesis of fluorescent CDs by means of laser ablation [26].

Zhou and his coworkers [22] used electrochemical methods for preparing fluorescent CDs. They used multiwalled carbon nanotubes as the working electrode grown in carbon membrane by means of chemical vapor deposition (CVD) method and the cycle voltage to obtain the CDs with blue fluorescence. The particle size of CDs produced in their method is 2.8 nm, and the fluorescence quantum yield is about 6.4%. Subsequently, some research group obtained CDs by means of the same method only replacing the solution with aqueous solution and electrochemical oxidation of graphite rods shock. The fluorescence quantum yield is about 1.2% [20, 23]. In order to further improve the efficiency of the electrochemical method for preparing CDs, the researchers prepared the fluorescent CDs by using ionic liquid assisted electrochemical exfoliation of graphite electrodes. Using the ionic liquid solvent to replace the traditional solution can play a dual role of dissolving and catalysis, in which the reaction rate can be improved several times. Furthermore, by adjusting the ratio of the ionic liquid and water, the fluorescence emission wavelengths of CDs can be adjusted [21]. However, the fluorescence quantum yield of the CDs prepared in electrochemical methods is not high and needs further improvement.

Compared with the multistep preparation method of CDs, one-step reaction processes not only simplify the preparation procedure and the prepared CDs also with better fluorescent properties, but also can obtain CDs with different fluorescent properties by choosing different organic reaction solution. For example, Hu et al. [27] combined laser ablation

and surface passivation merger in one-step reaction, with the polyethylene solution under laser radiation for 4 h, to get a black suspension. After separating the black suspension, they obtained fluorescence CDs with particle size about 3.2 nm, and the quantum yield is 12.2%, which significantly improved the fluorescence quantum yield of CDs.

**3.2. Bottom-Up Approach.** Bottom-up approaches are based on the polymerization reaction for small molecules to the formation of nanoscale CDs. This strategy includes hydrothermal method [14, 28–33], microwave-assisted pyrolysis method [34–38], ultrasonic method [39], acid dehydration method [40], and pyrolysis method [41, 42]. Among them, the most widely used are the hydrothermal method and microwave-assisted pyrolysis method, which can be realized by the one-step method for preparing fluorescent CDs.

In 2007, Liu and coworkers [14] first prepared CDs by hydrothermal methods. They mixed candle ash as the carbon source with nitric acid through heat reflux and generated a black homogeneous solution and then purified through a series of centrifugation, dialysis, gel electrophoresis, and other processes to obtain fluorescent CDs with different particle sizes. They found that the emission wavelengths of fluorescent CDs depend on the particle sizes even under the same excitation light ( $\lambda_{\text{ex}}$ , 315 nm); the emission wavelength is gradually red shift with the increasing of the particle size, which reflects fully an optical character of fluorescent CDs, named elementary excitations and multiemission. In the past two years, a lot of reports are about the researches of preparing CDs through hydrothermal method using different carbon sources, and the fluorescence quantum yield of CDs has been greatly increased. For instance, Gao and so forth [32] chose C60 as the carbon source and CTAB as passivator to prepared CDs with high fluorescence quantum yield up to 60%. Even more, the fluorescent CDs prepared in their method possess the distinctive property of aggregation induced enhanced emission, which is different from the common reports in the literatures.

Zhu et al. [35] developed a simple microwave method to synthesize the new type of CDs. With carbohydrate as a carbon source and PEG200 as both solvent and coating agent, the reaction system gradually changed from colorless to dark brown solution when under 500 W microwave power radiation for 2–10 min, and the product was diluted with water to obtain fluorescent CDs. In this method, the particle size and the quantum yields of fluorescent CDs depended on the reaction time. Wang et al. [36] created a “green,” “fast,” “economy” CDs synthesis method by means of microwave method. They first burn eggshell into ashes, then mixed the ashes with NaOH aqueous solution, and treated the solution via microwave radiation for five minutes to get CDs. This method is quite simple; the raw materials are cheap and available, and the consuming time is very short; the fluorescence quantum yield of CDs reaches to 14%. Chandra et al. [37] used sucrose as a carbon source and promote the synthesis of fluorescent CDs in phosphoric acid environment by microwave radiation. The reaction time is just 3 minutes and 40 seconds, and the prepared CDs are shining bright

green fluorescence. Yang et al. [38] created a rapid synthesis method of amino modified CDs using chitosan as a carbon source under mild conditions and applied them to human lung adenocarcinoma A549 cells imaging.

## 4. Fluorescent Applications Carbon Dots

**4.1. Photocatalysis.** With the rising demand for low-carbon society, how to utilize full advantage of solar energy and other clean energies becomes an important issue. The appearance of photocatalytic technology caused the research of photocatalytic technology boom, involving solar energy, photovoltaic cells, self-cleaning materials, and environmental pollution control and many other related fields. However, the traditional photocatalytic materials such as  $\text{TiO}_2$  and ZnO generally with absorption range in ultraviolet light, visible light cannot be taken as full advantage and have been greatly restricted in practical applications. Thus preparing nanomaterials with high stability and high visible light composite catalyst activity is of great significance in solving environmental problems and energy issues.

Cao et al. [43] prepared CDs through acid reflux dehydration method and modified the CDs with PEG1500, to obtain the CDs with surface coated metal gold or platinum cluster coated via liquid phase method. In this reaction system, the CDs play the role of electron donor and can restore gold salts or platinum salts ( $\text{HAuCl}_4$  or  $\text{H}_2\text{PtCl}_6$ ), so that the corresponding sites of metal on the CDs surface form CDs/Au composite. The gold-coated CDs were placed in a wide room with abundant carbon dioxide pass and kept at room temperature until they reach saturation. With visible light (425–720 nm) irradiation for five hours, the carbon dioxide can be restored to formic acid. Meanwhile, gold-coated or platinum-coated CDs can be used in the reduced reaction of water to give hydrogen.

Zhang et al. [44] prepared CDs by electrochemical method, in which the  $\text{CH}_3\text{COOAg}$  and PVP were dissolved in prepared CDs solution, and dropping  $\text{Na}_2\text{HPO}_4$  solution to prepared CDs/ $\text{Ag}_3\text{SO}_4$  composite catalyst. Meanwhile,  $\text{CH}_3\text{COOAg}$  and PVP were dissolved in prepared CDs solution in sunlight reflux with dropping  $\text{Na}_2\text{HPO}_4$  solution to obtain CDs/Ag/ $\text{Ag}_3\text{SO}_4$  composite catalyst. Both these two catalysts were used in the degradation reactions of methylene blue under visible light radiation. Their experimental results showed that the photocatalytic ability of CDs/Ag/ $\text{Ag}_3\text{SO}_4$  is 5.5 times larger than that of CDs/ $\text{Ag}_3\text{SO}_4$ . In addition, the structure of CDs/Ag/ $\text{Ag}_3\text{SO}_4$  is more stable in the catalytic process; when repeating the photocatalytic experiments, the catalytic efficiency has almost no change.

As one of the most common photocatalysts,  $\text{TiO}_2$  has been widely used in the decomposition of organic pollution and  $\text{H}_2\text{O}$  to generate  $\text{H}_2$  [45]. However, due to the quite large gap between the conduction band and the energy band of  $\text{TiO}_2$ ,  $\text{TiO}_2$  has only absorbed peak in very short wavelength ultraviolet. Thus visible light is the useless energy for  $\text{TiO}_2$ . In order to improve the photocatalytic properties of  $\text{TiO}_2$ , the researchers have done a lot of efforts and found that the composite of  $\text{TiO}_2$  nanoparticles and carbon dots can

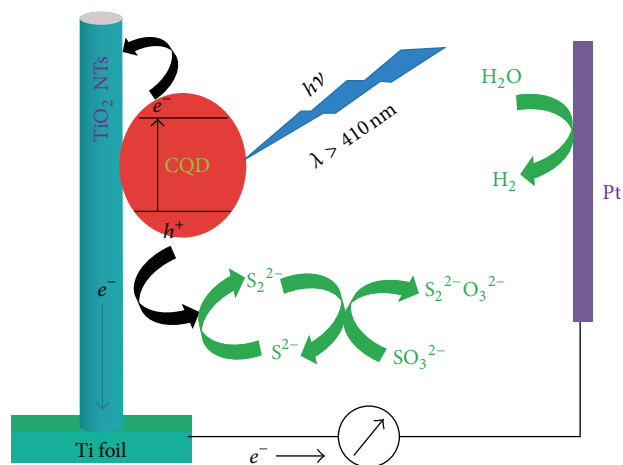


FIGURE 4: Illustration of the sensitization mechanism of CQDs (reproduced with permission from [46]).

effectively broaden the range of the optical response of the composite structure and increase the utilization of solar energy and transformation. For instance, Zhang et al. [46] used CQDs-TiO<sub>2</sub> composites as catalyst successfully to get H<sub>2</sub> (Figure 4) from the water decomposition under visible light irradiation, wherein the introduction of CQDs obviously broadens the light response range of TiO<sub>2</sub>. Subsequently, based on the upconversion property of the CQDs and the synergistic effect between the CdSe quantum dots and CQDs, the CdSe quantum dots were served to modify the TiO<sub>2</sub>-CQD nanocomposites, and the photocatalytic efficiency was greatly improved [47]. Although photocatalytic technology still stays in the laboratory level and it is difficult to spread into everyday life, the photocatalytic technology as a new pollution control technology is huge potential in the utilization of new means of solar energy and is promising in future exploring.

#### 4.2. Luminescent Device

**4.2.1. LED Device.** Guo et al. [48] synthesized a series of multicolor CQDs by the thermolysis of epoxy group containing polystyrene microspheres (Figure 5). CQDs produced under 200, 300, and 400°C could emit blue, orange, and white fluorescence with the excitation of single wavelength ultraviolet, respectively, and the fluorescent quantum yield is 47%. With the excellent properties, those CQDs could be used as the above-mentioned three color LED devices. Wang et al. [49] used citric acid as carbon source to synthesize new CQDs in octadecene coupled with 1-cetylamine as surface passivator. The max quantum yield of these CQDs made white light emitting devices reach 0.083% under the irritation of 5 Ma/cm<sup>2</sup> ampere density.

**4.2.2. Macrostructure Material.** Zhang et al. [50] used electrochemistry corrosion of graphite electrode to produce the new types of CQDs. Upon the addition of CQDs on glass surface with the concentration of 1.3 mg/mL, the CQDs thin film was obtained after being dried. The oxygen contained group at

the CQDs surface determined its sensitivity of humidity and the conductivity of CQDs was in direct proportion to the relative humidity. Because of the high specific surface area and excellent stability of the CQDs thin film, it is suitable for gas sensing.

Fan et al. [51] employed electrodeposition to prepare CQDs by electrolyzing of graphite rods in SiO<sub>2</sub> nanosphere matrix. After dissolving the nanosphere matrix by HF, two-dimensional and three-dimensional mesh structure CQDs were obtained (Figure 6). This unique structure has high absorbability for particular application. The nano-Au contained mesh structure of CQDs could be used as probes for high sensitivity detection. Furthermore, the surface Raman scattering of nano-Au contained mesh structure CQDs can gain 8 to 11 times of signal intensity comparing with the widely used SERS materials.

**4.3. Chemical Sensing.** Fluorescent carbon dots, due to their excellent optical properties, chemical stability, and good solubility in water, in the field of chemical sensing under great attention, are widely used in metal ion detection, anion detection, small organic molecules, and biomolecules detection. Like the semiconductor quantum dots, CQDs by the interaction with the analyte can change the efficiency of recombination between the surfaces of the electron-hole pairs, which occurred in the fluorescence enhancement and quenching treatment to achieve quantitative or qualitative analysis of the measured object.

**4.3.1. Metal Ion Probe.** Carbon dots as a new fluorescent probe in solution are easily quenched efficiently by electron acceptor and thus can effectively detect metal ions in solution and determine the concentration of metal ions in a certain concentration range, to achieve the trace analysis of metal ions.

Hg<sup>2+</sup> is one of the most toxic heavy metal ions in environment, has received the attention of scientific researchers. Currently, based on CQDs as sensor, scientists have developed a variety of methods to detect Hg<sup>2+</sup> [52–55]. Lu et al. [52] prepared a new type of CQDs from grapefruit peel through hydrothermal method. As the Hg<sup>2+</sup> can effectively quench the fluorescence of CQDs, a new method for the detection of Hg<sup>2+</sup> was developed, the detection limit of 0.23 nM, and this method has been successfully applied to the detection of Hg<sup>2+</sup> in the river. Liu et al. [53] obtained CQDs with excellent fluorescent stability by the polyethylene glycol (PEG) refluxed with NaOH; taking these CQDs as a sensor can specifically detect Hg<sup>2+</sup> in solution and the detection limit reaches 1 fM (Figures 7 and 8). This test method successfully detected Hg<sup>2+</sup> in the rivers, lakes, and tap water samples and the sensitivity is very high. Zhang and Chen [54] used vitamin B as carbon and nitrogen sources and prepared a high fluorescence yield and nitrogen-rich fluorescence CQDs by hydrothermal method. It was found that Hg<sup>2+</sup> can be able to bind specifically with these CQDs, the use of this fluorescent probe to establish a new method for label-free detection of Hg<sup>2+</sup>, the detection limit of 0.23 nM. In addition to the detection of Hg<sup>2+</sup>, scientists have

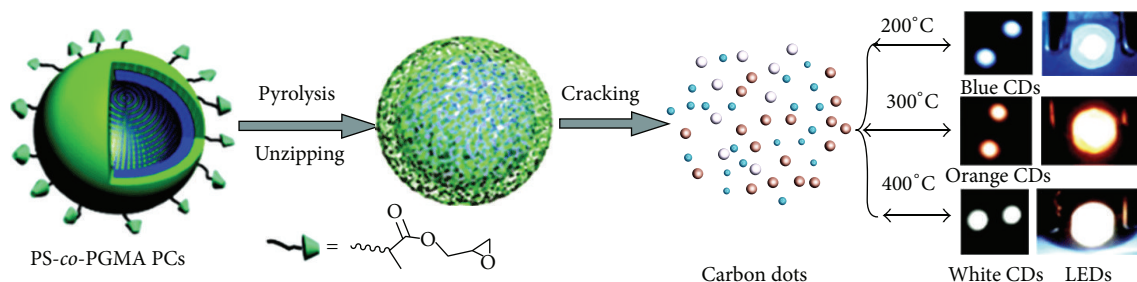


FIGURE 5: Schematic representation of the formation of carbon dots from the pyrolysis of photonic crystals (reproduced with permission from [48]).

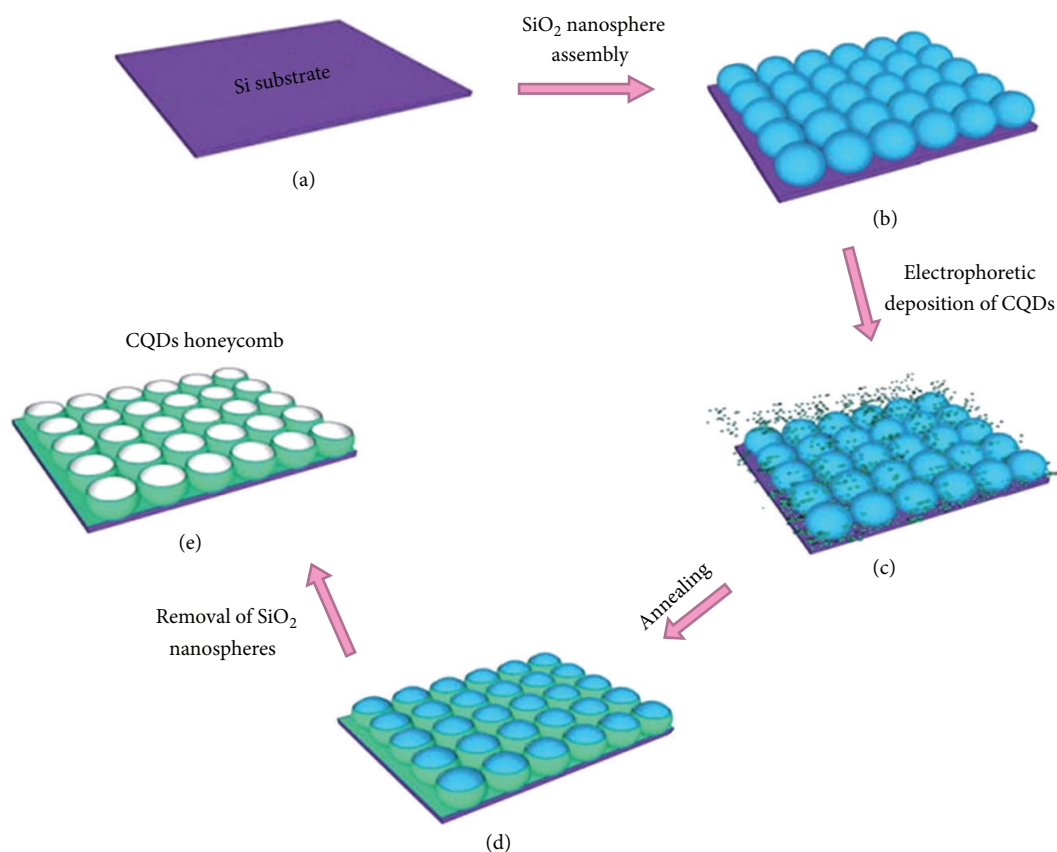


FIGURE 6: A scheme of the fabrication process for the formation of a 2D honeycomb structure of CDs (reproduced with permission from [51]).

also developed a variety of methods to detect  $\text{Cu}^{2+}$  [56, 57],  $\text{Fe}^{3+}$  [58, 59],  $\text{Pb}^{2+}$  [60], and  $\text{Ag}^+$  [61]. Because of the rich type of carbon sources, scientists will synthesize more excellent properties of CDs for the detection of heavy metal ions in environment.

**4.3.2. Anions and Small Molecule Detection.** During the metal ion sensor development, scientists expand the CDs probe used in detection of anions and small molecular. Unlike heavy metal ions detected fluorescence quenching mechanism CDs, anionic or small molecules generally by restoring fluorescence of the quenched CDs to achieve the purpose of detection.

Zong et al. [42] selected spherical mesoporous silica as nanoreactor, added to the solution of citric acid and three other inorganic salts ( $\text{NaCl}$ ,  $\text{LiCl}$ , and  $\text{KNO}_3$ ) and ultrasound to obtain CDs. The study found that the CDs can bond with  $\text{Cu}^{2+}$  specificity and quench the fluorescence of CDs. While adding L-cysteine in the solution of  $\text{CDs-Cu}^{2+}$ ,  $\text{Cu}^{2+}$  could be released from the surface of the CDs, thereby recovering the fluorescence of CDs. With these chemical sensors, which successfully detected  $\text{Cu}^{2+}$  and L-cysteine, two substances, the detection limit was  $2.3 \times 10^{-8}$  mol/L and  $3.4 \times 10^{-10}$  mol/L, respectively (Figure 9). Du et al. [62] take the same way, take I replacing the  $\text{Hg}^{2+}$  bound with CDs, successfully detected the iodide in aqueous solution.

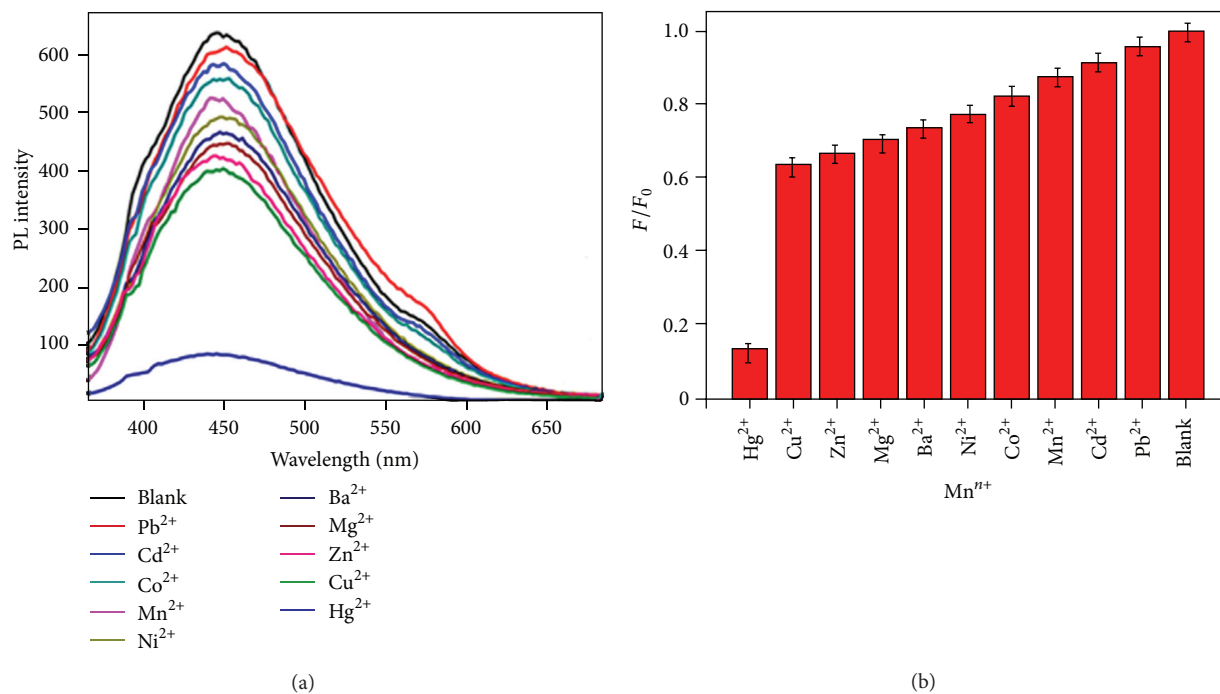


FIGURE 7: (a, b) PL spectra and the different PL intensity ratio ( $F/F_0$ ) of the FCDs solution with various metal ions (at the same metal ions concentration of 1 mM).

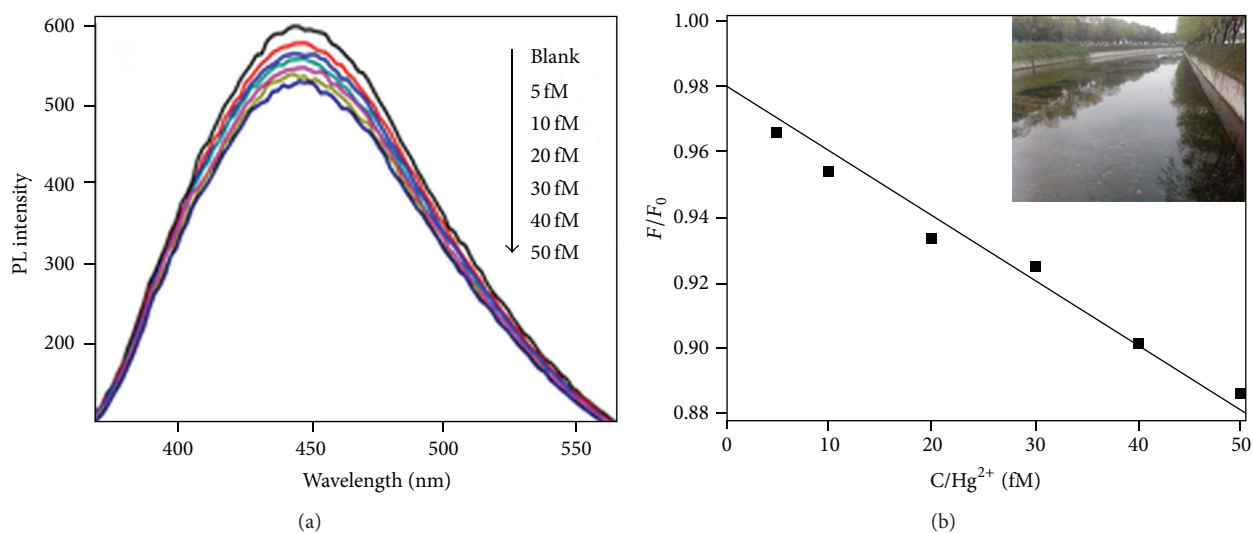


FIGURE 8: (a, b) PL spectra and the different PL intensity ratio ( $F/F_0$ ) of the FCDs with various  $\text{Hg}^{2+}$  ions concentrations in the range of 0–50 fM in river water (reproduced with permission from [53]).

**4.4. Biosensor.** In 2011, researchers first achieved the detection of DNA; Bai and other studies [63] have found that methylene blue can effectively quench the fluorescence of CDs; then they joined ct-DNA in solution; the fluorescence of the solution was found to be restored. Based on this phenomenon, a new fluorescent sensor for DNA detection was designed; the detection limit was  $1.0 \times 10^{-6}$  mol/L with the linear ranging from  $3.0 \times 10^{-6}$  mol/L to  $8.0 \times 10^{-5}$  mol/L.

Xu et al. [64] described aptamer-functionalized CDs as a sensor for protein detection. Since the thrombin has two different combine sites, the presence of thrombin could induce the CDs and aptamer to form a sandwich structure (Figure 10). The sensor shows high specificity and sensitivity towards thrombin. The detection limit of this sensor reaches 1 nmol, which is improved compared with the other reported fluorescence-based thrombin detection assays.

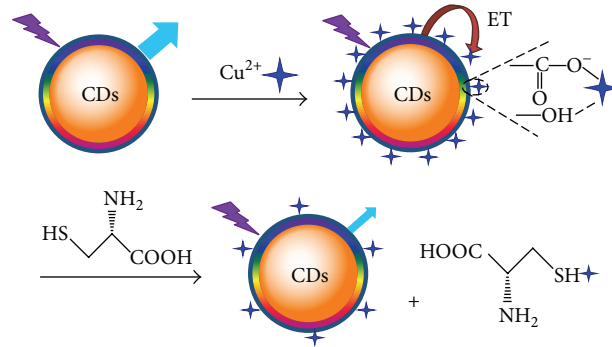


FIGURE 9: Carbon dots detection mechanism  $\text{Cu}^{2+}$  and cysteine (reproduced with permission from [42]).

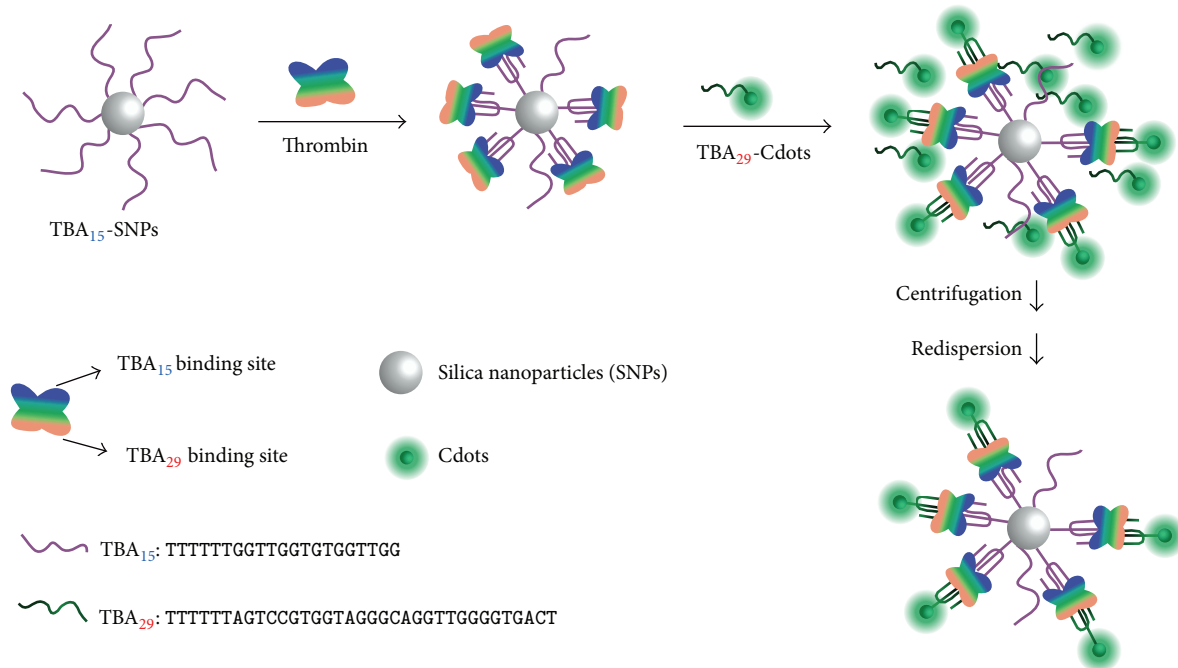


FIGURE 10: Schematic illustration of the sandwich-based thrombin detection principle using the carbon dots (reproduced with permission from [64]).

**4.5. Bioimaging.** We have already learned that the fluorescent CDs possess great advantages comparing with the traditional semiconductor quantum dots, including their outstanding optical properties and stable chemical properties; moreover, CDs are environmentally friendly and low toxicity nanomaterials. These characteristics make it possible that CDs replace semiconductor quantum dots in biological imaging [65].

Sun's team is the first research group that applied fluorescent CDs in bioimaging. They cultured MCF-7 cells vaccination in medium containing CDs for 2 h; fluorescent microscope was used to observe the fluorescence of cells; it was found that the fluorescence area is mainly concentrating in the cell membrane and cytoplasm [9]. Then Wang et al. [66] used vitamin B as precursor synthesized low toxicity and good biocompatibility fluorescent CDs via hydrothermal method and successfully applied it in U87 cell imaging. The U87 cells were seeded in the medium containing CDs for

cultured 2 h; with a focus fluorescence microscope, it was found that only cell membrane and cytoplasm emit bright fluorescence, while the nucleus has not been invaded by CDs [61].

Zhang et al. [67] used lactose as a carbon source and 3-hydroxymethyl amino methane as carbon surface passivation agent to get high light, low toxicity fluorescent CDs via hydrothermal method. The study shows that the fluorescent intensity of the fluorescent carbon dots in the environment is not affected by the change of fluorescence intensity and the fluorescence intensity is still not affected by the salt solution and these CDs were successfully applied in HeLa cell imaging (Figure 11).

Yang et al. [24] take the purified CDs injected into female DBA/1 mice body by three ways of subcutaneous injection, intradermal injection, and intravenous injection and get successful in vivo imaging under light irradiation of 470 nm

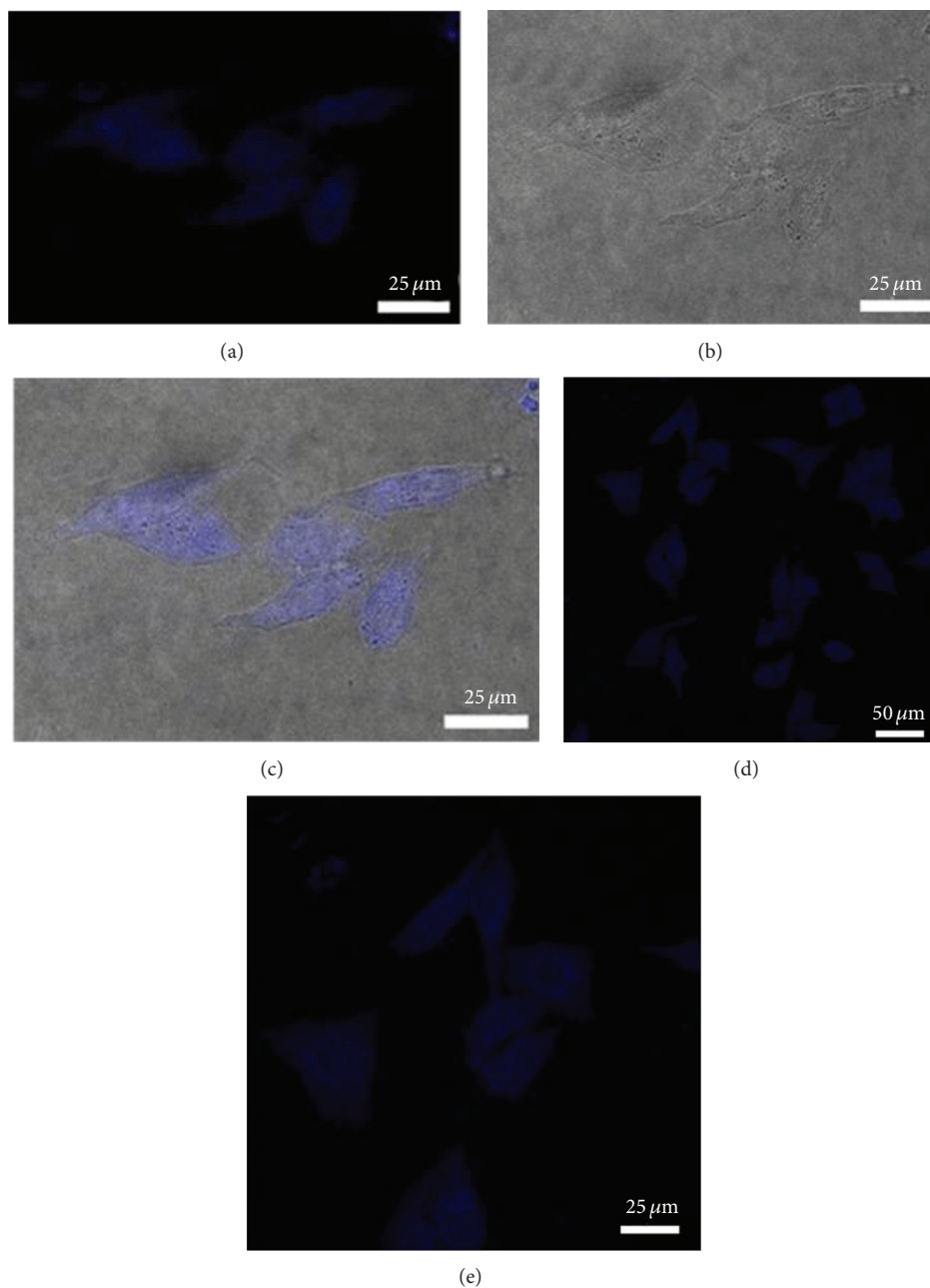


FIGURE 11: (a, d, e) Confocal fluorescence image ( $\lambda_{\text{ex}}$ : 405 nm); (b) bright-field microphotograph of HeLa cells incubated with  $200 \mu\text{g mL}^{-1}$  of CDs for 4 h and (c) overlay image of (a) and (b) (reproduced with permission from [67]).

and 545 nm. They found that CDs subcutaneously injected into the mice of the forelimb would migrate along the forearm to the axillary lymph nodes, while CDs of intravenous injection in the systemic circulation concentrated at the bladder area. They also found that the urine can be detected with fluorescence after 3 h by injection. 4 h later, the fluorescent CDs can exist mainly at the kidney of mice and slightly at liver through dissection. They speculated that polyethylene glycol could reduce the effective surface of CDs on the affinity to protein and makes CDs more difficult in uptake by the liver comparing with the previous nanoparticles and nanotubes.

Goh et al. [68] take advantage of the properties that CDs can combine with hyaluronic acid (HA) homologues and applied the composite of hyaluronic acid homologues and CDs (HA-CDs) successfully to hyaluronic acid imaging in vitro. They injected HA-CDs into mice through subcutaneous injection and observed the fluorescence on the mouse skin, validating the feasibility of HA-CDs imaging in vivo. Subsequently, they injected HA-CDs by means of intravenous injection manner into mice; after 4 h they get the distribution of HA in the liver, kidney, and spleen of the mice through the fluorescence microscope (Figure 12).

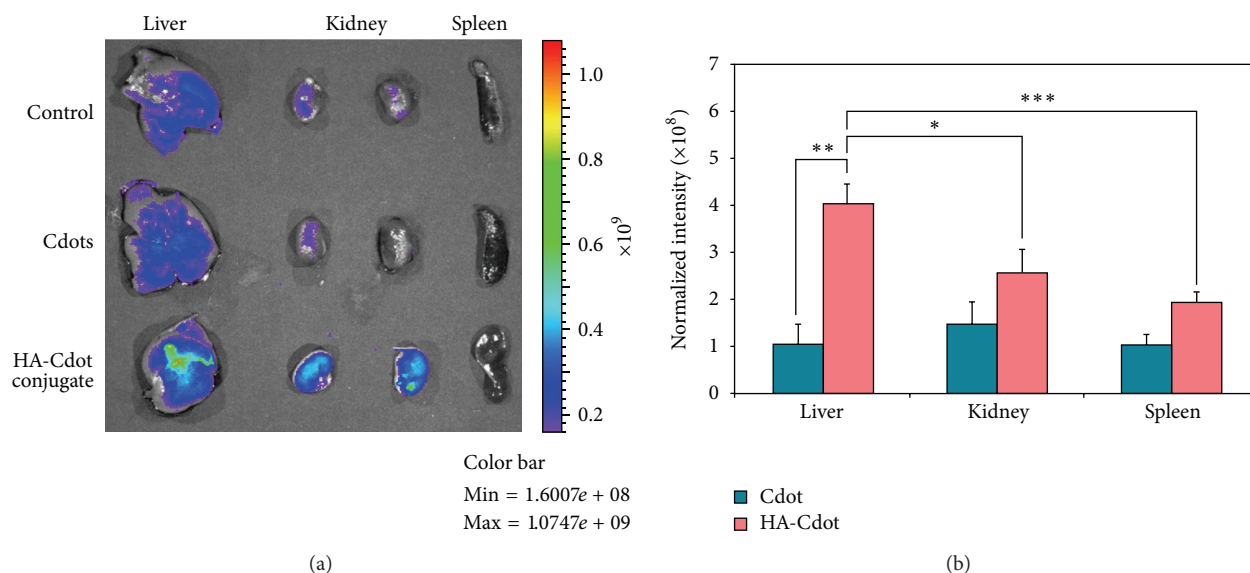


FIGURE 12: (a) Fluorescence image of dissected livers, kidney, and spleens 4 h after tail-vein injection of Cdots or HA-Cdots conjugates. (b) Quantitative fluorescence analysis of Cdots and HA-Cdots conjugated in the dissected organs (\* $P < 0.05$ , \*\* $P < 0.005$ , and \*\*\* $P < 0.001$ ) (reproduced with permission from [68]).

**4.6. Drug Delivery.** Traditional drug carrier does not have the observability and traceability; thus the researches that applied fluorescent nanomaterial to the drug carrier are expected to solve these problems. Due to its low toxicity, excellent biocompatibility, and modifiable surface function groups, CDs have become a hot spot of drug delivery research.

Lai et al. [69] employed glycerol as the carbon source and prepared CDs by pyrolysis. After that, they modified the CDs via PEG and controlled the particle size through mesoporous nanoparticles to obtain uniform and excellent optical properties of CDs (CDs @ mSiO<sub>2</sub>-PEG). The CDs @ mSiO<sub>2</sub>-PEG can be used as an anticancer drug doxorubicin (DOX) carrier and the release rate of DOX was studied in HeLa cells. The results showed that CDs and DOX in the cytoplasm and nucleus emitted blue fluorescence and red fluorescence, respectively. According to the proportions of the two fluorescent colors, this method can achieve a pharmaceutical carrier and observability traceability by in situ monitoring of DOX in cells release rate.

Zheng et al. [70] combined amino groups on CDs surface with oxaliplatin through the chemical coupling reaction, with the two substances incorporating as one. The modified CDs can enter into the interior of cancer cells via endocytosis. Due to the rapid changes in the internal environment of the cancer cells, the drug can be released from the surface of the CDs. The results showed that by monitoring CDs fluorescence signal in cancer cells they can fully understand the distribution of oxaliplatin in cancer cases, which will provide great help for doctors to grasp the exact time and dose drug injection.

## 5. Summary

As a new category of nanomaterials, fluorescent nanomaterials have outstanding optical properties, good biocompatibility, and surface functional division of regulatory and other characteristics; thus they have been studied extensively in photocatalysis, biochemical analysis, bioimaging, drug delivery, and other areas and show great potential and are promising in these fields. However, as a budding member of the family of carbon nanomaterials, the application ranges of fluorescent CDs should still be further improved and make sufficient use of surface rich functional groups on CDs, broadening their composite structural applications in various fields. Although fluorescence CDs realized the great-leap-forward from in vitro imaging to in vivo imaging, the emission fluorescence of most of CDs is distributed in ultraviolet region or short wavelength visible region, which limits the optical imaging in life body for deep tissue. In addition, almost all of life organisms will produce autofluorescence under short wavelength UV and visible light radiation, which often interfere seriously with the visual effects. Therefore, the development of fluorescent CDs in near-infrared region is urgently needed in the future. Moreover, the current researches on in vivo imaging merely stay in the experimental stage for small animals; further progress for the live animal imaging needs to be promoted. The optimization of preparation process of fluorescent CDs and the development of green, convenient, and low-cost methods for preparing CDs with fine physical, optical properties both can be addressed further.

In a word, CDs are novel fluorescent nanomaterials with outstanding fluorescence properties. They have numerous

excellent applications in a variety of fields involving chemical and biological sensing, biological imaging, drug delivery, and photocatalysis, which are greatly promising for the future development.

## Conflict of Interests

The authors declare that there is no conflict of interests regarding the publication of this paper.

## Acknowledgments

This work was financially supported by the National Natural Science Foundation of China (no. 2120501) and the National Ministry of Science and Technology of China, the National Science and Technology Support Program of China (2011YQ14015009). The authors are grateful for the support of 2011 collaborative innovation center in mass spectrometry science and instrumentation, East China Institute of Technology.

## References

- [1] U. Resch-Genger, M. Grabolle, S. Cavaliere-Jaricot, R. Nitschke, and T. Nann, "Quantum dots versus organic dyes as fluorescent labels," *Nature Methods*, vol. 5, no. 9, pp. 763–775, 2008.
- [2] A. R. Clapp, T. Pons, I. L. Medintz et al., "Two-photon excitation of quantum-dot-based fluorescence resonance energy transfer and its applications," *Advanced Materials*, vol. 19, no. 15, pp. 1921–1926, 2007.
- [3] C. E. Probst, P. Zrazhevskiy, V. Bagalkot, and X. Gao, "Quantum dots as a platform for nanoparticle drug delivery vehicle design," *Advanced Drug Delivery Reviews*, vol. 65, no. 5, pp. 703–718, 2013.
- [4] H. J. Li, X. Wei, Y. Q. Xu et al., "Determination of aspirin using functionalized cadmium-tellurium quantum dots as a fluorescence probe," *Analytical Letters*, vol. 48, no. 7, pp. 1117–1127, 2015.
- [5] D. R. Larson, W. R. Zipfel, R. M. Williams et al., "Water-soluble quantum dots for multiphoton fluorescence imaging *in vivo*," *Science*, vol. 300, no. 5624, pp. 1434–1436, 2003.
- [6] R. Liu, D. Wu, S. Liu, K. Koynov, W. Knoll, and Q. Li, "An aqueous route to multicolor photoluminescent carbon dots using silica spheres as carriers," *Angewandte Chemie*, vol. 48, no. 25, pp. 4598–4601, 2009.
- [7] J. Geys, A. Nemmar, E. Verbeken et al., "Acute toxicity and prothrombotic effects of quantum dots: impact of surface charge," *Environmental Health Perspectives*, vol. 116, no. 12, pp. 1607–1613, 2008.
- [8] X. Xu, R. Ray, Y. Gu et al., "Electrophoretic analysis and purification of fluorescent single-walled carbon nanotube fragments," *Journal of the American Chemical Society*, vol. 126, no. 40, pp. 12736–12737, 2004.
- [9] L. Cao, X. Wang, M. J. Meziani et al., "Carbon dots for multiphoton bioimaging," *Journal of the American Chemical Society*, vol. 129, no. 37, pp. 11318–11319, 2007.
- [10] H. Zhang, Y. Chen, M. Liang et al., "Solid-phase synthesis of highly fluorescent nitrogen-doped carbon dots for sensitive and selective probing ferric ions in living cells," *Analytical Chemistry*, vol. 86, no. 19, pp. 9846–9852, 2014.
- [11] S. Y. Park, H. U. Lee, E. S. Park et al., "Photoluminescent green carbon nanodots from food-waste-derived sources: large-scale synthesis, properties, and biomedical applications," *ACS Applied Materials & Interfaces*, vol. 6, no. 5, pp. 3365–3370, 2014.
- [12] S.-L. Hu, K.-Y. Niu, J. Sun, J. Yang, N.-Q. Zhao, and X.-W. Du, "One-step synthesis of fluorescent carbon nanoparticles by laser irradiation," *Journal of Materials Chemistry*, vol. 19, no. 4, pp. 484–488, 2009.
- [13] H. Peng and J. Travas-Sejdic, "Simple aqueous solution route to luminescent carbogenic dots from carbohydrates," *Chemistry of Materials*, vol. 21, no. 23, pp. 5563–5565, 2009.
- [14] H. Liu, T. Ye, and C. Mao, "Fluorescent carbon nanoparticles derived from candle soot," *Angewandte Chemie International Edition*, vol. 46, no. 34, pp. 6473–6475, 2007.
- [15] X. Jia, J. Li, and E. Wang, "One-pot green synthesis of optically pH-sensitive carbon dots with upconversion luminescence," *Nanoscale*, vol. 4, no. 18, pp. 5572–5575, 2012.
- [16] L. Wang, S.-J. Zhu, H.-Y. Wang et al., "Common origin of green luminescence in carbon nanodots and graphene quantum dots," *ACS Nano*, vol. 8, no. 3, pp. 2541–2547, 2014.
- [17] K. Wang, Z. Gao, G. Gao et al., "Systematic safety evaluation on photoluminescent carbon dots," *Nanoscale Research Letters*, vol. 8, no. 1, pp. 1–9, 2013.
- [18] H. Li, Z. Kang, Y. Liu, and S.-T. Lee, "Carbon nanodots: synthesis, properties and applications," *Journal of Materials Chemistry*, vol. 22, no. 46, pp. 24230–24253, 2012.
- [19] H. Jiang, F. Chen, M. G. Lagally, and F. S. Denes, "New strategy for synthesis and functionalization of carbon nanoparticles," *Langmuir*, vol. 26, no. 3, pp. 1991–1995, 2010.
- [20] L. Zheng, Y. Chi, Y. Dong, J. Lin, and B. Wang, "Electrochemiluminescence of water-soluble carbon nanocrystals released electrochemically from graphite," *Journal of the American Chemical Society*, vol. 131, no. 13, pp. 4564–4565, 2009.
- [21] J. Lu, J.-X. Yang, J. Wang, A. Lim, S. Wang, and K. P. Loh, "One-pot synthesis of fluorescent carbon nanoribbons, nanoparticles, and graphene by the exfoliation of graphite in ionic liquids," *ACS Nano*, vol. 3, no. 8, pp. 2367–2375, 2009.
- [22] J. Zhou, C. Booker, R. Li et al., "An electrochemical avenue to blue luminescent nanocrystals from multiwalled carbon nanotubes (MWCNTs)," *Journal of the American Chemical Society*, vol. 129, no. 4, pp. 744–745, 2007.
- [23] Q.-L. Zhao, Z.-L. Zhang, B.-H. Huang, J. Peng, M. Zhang, and D.-W. Pang, "Facile preparation of low cytotoxicity fluorescent carbon nanocrystals by electrooxidation of graphite," *Chemical Communications*, no. 41, pp. 5116–5118, 2008.
- [24] S.-T. Yang, L. Cao, P. G. Luo et al., "Carbon dots for optical imaging *in vivo*," *Journal of the American Chemical Society*, vol. 131, no. 32, pp. 11308–11309, 2009.
- [25] H. M. R. Gonçalves, A. J. Duarte, and J. C. G. Esteves da Silva, "Optical fiber sensor for Hg(II) based on carbon dots," *Biosensors & Bioelectronics*, vol. 26, no. 4, pp. 1302–1306, 2010.
- [26] Y.-P. Sun, B. Zhou, Y. Lin et al., "Quantum-sized carbon dots for bright and colorful photoluminescence," *Journal of the American Chemical Society*, vol. 128, no. 24, pp. 7756–7757, 2006.
- [27] S. Hu, J. Liu, J. Yang, Y. Wang, and S. Cao, "Laser synthesis and size tailor of carbon quantum dots," *Journal of Nanoparticle Research*, vol. 13, no. 12, pp. 7247–7252, 2011.
- [28] C.-I. Wang, A. P. Periasamy, and H.-T. Chang, "Photoluminescent C-dots@RGO probe for sensitive and selective detection of acetylcholine," *Analytical Chemistry*, vol. 85, no. 6, pp. 3263–3270, 2013.

- [29] Z. Qian, X. Shan, L. Chai, J. Ma, J. Chen, and H. Feng, "Si-doped carbon quantum dots: a facile and general preparation strategy, bioimaging application, and multifunctional sensor," *ACS Applied Materials & Interfaces*, vol. 6, no. 9, pp. 6797–6805, 2014.
- [30] Y. Xu, X.-H. Jia, X.-B. Yin, X.-W. He, and Y.-K. Zhang, "Carbon quantum dot stabilized gadolinium nanoprobe prepared via a one-pot hydrothermal approach for magnetic resonance and fluorescence dual-modality bioimaging," *Analytical Chemistry*, vol. 86, no. 24, pp. 12122–12129, 2014.
- [31] H. Dong, A. Kuzmanoski, D. M. Gößl, R. Popescu, D. Gerthsen, and C. Feldmann, "Polyol-mediated C-dot formation showing efficient  $Tb^{3+}/Eu^{3+}$  emission," *Chemical Communications*, vol. 50, no. 56, pp. 7503–7506, 2014.
- [32] M. X. Gao, C. F. Liu, Z. L. Wu et al., "A surfactant-assisted redox hydrothermal route to prepare highly photoluminescent carbon quantum dots with aggregation-induced emission enhancement properties," *Chemical Communications*, vol. 49, no. 73, pp. 8015–8017, 2013.
- [33] S. C. Ray, A. Saha, N. R. Jana, and R. Sarkar, "Fluorescent carbon nanoparticles: synthesis, characterization, and bioimaging application," *Journal of Physical Chemistry C*, vol. 113, no. 43, pp. 18546–18551, 2009.
- [34] Y. Tang, Y. Su, N. Yang, L. Zhang, and Y. Lv, "Carbon nitride quantum dots: a novel chemiluminescence system for selective detection of free chlorine in water," *Analytical Chemistry*, vol. 86, no. 9, pp. 4528–4535, 2014.
- [35] H. Zhu, X. Wang, Y. Li, Z. Wang, F. Yang, and X. Yang, "Microwave synthesis of fluorescent carbon nanoparticles with electrochemiluminescence properties," *Chemical Communications*, no. 34, pp. 5118–5120, 2009.
- [36] Q. Wang, X. Liu, L. Zhang, and Y. Lv, "Microwave-assisted synthesis of carbon nanodots through an eggshell membrane and their fluorescent application," *The Analyst*, vol. 137, no. 22, pp. 5392–5397, 2012.
- [37] S. Chandra, P. Das, S. Bag, D. Laha, and P. Pramanik, "Synthesis, functionalization and bioimaging applications of highly fluorescent carbon nanoparticles," *Nanoscale*, vol. 3, no. 4, pp. 1533–1540, 2011.
- [38] Y. Yang, J. Cui, M. Zheng et al., "One-step synthesis of amino-functionalized fluorescent carbon nanoparticles by hydrothermal carbonization of chitosan," *Chemical Communications*, vol. 48, no. 3, pp. 380–382, 2012.
- [39] G. Oza, K. Oza, S. Pandey et al., "A green route towards highly photoluminescent and cytocompatible carbon dot synthesis and its separation using sucrose density gradient centrifugation," *Journal of Fluorescence*, vol. 25, no. 1, pp. 9–14, 2015.
- [40] G. E. Lecroy, S. K. Sonkar, F. Yang et al., "Toward structurally defined carbon dots as ultracompact fluorescent probes," *ACS Nano*, vol. 8, no. 5, pp. 4522–4529, 2014.
- [41] A. B. Bourlinos, A. Stassinopoulos, D. Anglos, R. Zboril, M. Karakassides, and E. P. Giannelis, "Surface functionalized carbogenic quantum dots," *Small*, vol. 4, no. 4, pp. 455–458, 2008.
- [42] J. Zong, X. Yang, A. Trinchì et al., "Carbon dots as fluorescent probes for 'off-on' detection of  $Cu^{2+}$  and l-cysteine in aqueous solution," *Biosensors & Bioelectronics*, vol. 51, pp. 330–335, 2014.
- [43] L. Cao, S. Sahu, P. Anilkumar et al., "Carbon nanoparticles as visible-light photocatalysts for efficient  $CO_2$  conversion and beyond," *Journal of the American Chemical Society*, vol. 133, no. 13, pp. 4754–4757, 2011.
- [44] H. Zhang, H. Ming, S. Lian et al., " $Fe_2O_3$ /carbon quantum dots complex photocatalysts and their enhanced photocatalytic activity under visible light," *Dalton Transactions*, vol. 40, no. 41, pp. 10822–10825, 2011.
- [45] X. Chen and S. S. Mao, "Titanium dioxide nanomaterials: synthesis, properties, modifications and applications," *Chemical Reviews*, vol. 107, no. 7, pp. 2891–2959, 2007.
- [46] X. Zhang, F. Wang, H. Huang et al., "Carbon quantum dot sensitized  $TiO_2$  nanotube arrays for photoelectrochemical hydrogen generation under visible light," *Nanoscale*, vol. 5, no. 6, pp. 2274–2278, 2013.
- [47] X. Zhang, H. Huang, J. Liu, Y. Liu, and Z. Kang, "Carbon quantum dots serving as spectral converters through broadband upconversion of near-infrared photons for photoelectrochemical hydrogen generation," *Journal of Materials Chemistry A*, vol. 1, no. 38, pp. 11529–11533, 2013.
- [48] X. Guo, C.-F. Wang, Z.-Y. Yu, L. Chen, and S. Chen, "Facile access to versatile fluorescent carbon dots toward light-emitting diodes," *Chemical Communications*, vol. 48, no. 21, pp. 2692–2694, 2012.
- [49] F. Wang, Y.-H. Chen, C.-Y. Liu, and D.-G. Ma, "White light-emitting devices based on carbon dots' electroluminescence," *Chemical Communications*, vol. 47, no. 12, pp. 3502–3504, 2011.
- [50] X. Zhang, H. Ming, R. Liu et al., "Highly sensitive humidity sensing properties of carbon quantum dots films," *Materials Research Bulletin*, vol. 48, no. 2, pp. 790–794, 2013.
- [51] Y. Fan, H. Cheng, C. Zhou et al., "Honeycomb architecture of carbon quantum dots: a new efficient substrate to support gold for stronger SERS," *Nanoscale*, vol. 4, no. 5, pp. 1776–1781, 2012.
- [52] W. Lu, X. Qin, S. Liu et al., "Economical, green synthesis of fluorescent carbon nanoparticles and their use as probes for sensitive and selective detection of mercury(II) ions," *Analytical Chemistry*, vol. 84, no. 12, pp. 5351–5357, 2012.
- [53] R. H. Liu, H. T. Li, W. Q. Kong et al., "Ultra-sensitive and selective  $Hg^{2+}$  detection based on fluorescent carbon dots," *Materials Research Bulletin*, vol. 48, no. 7, pp. 2529–2534, 2013.
- [54] R. Zhang and W. Chen, "Nitrogen-doped carbon quantum dots: facile synthesis and application as a 'turn-off' fluorescent probe for detection of  $Hg^{2+}$  ions," *Biosensors & Bioelectronics*, vol. 55, pp. 83–90, 2014.
- [55] X. Cui, L. Zhu, J. Wu et al., "A fluorescent biosensor based on carbon dots-labeled oligodeoxyribonucleotide and graphene oxide for mercury (II) detection," *Biosensors & Bioelectronics*, vol. 63, pp. 506–512, 2015.
- [56] A. Salinas-Castillo, M. Ariza-Avidad, C. Pritz et al., "Carbon dots for copper detection with down and upconversion fluorescent properties as excitation sources," *Chemical Communications*, vol. 49, no. 11, pp. 1103–1105, 2013.
- [57] M. Vedamalai, A. P. Periasamy, C.-W. Wang et al., "Carbon nanodots prepared from o-phenylenediamine for sensing of  $Cu^{2+}$  ions in cells," *Nanoscale*, vol. 6, no. 21, pp. 13119–13125, 2014.
- [58] Y.-L. Zhang, L. Wang, H.-C. Zhang et al., "Graphitic carbon quantum dots as a fluorescent sensing platform for highly efficient detection of  $Fe^{3+}$  ions," *RSC Advances*, vol. 3, no. 11, pp. 3733–3738, 2013.
- [59] K. Qu, J. Wang, J. Ren, and X. Qu, "Carbon dots prepared by hydrothermal treatment of dopamine as an effective fluorescent sensing platform for the label-free detection of iron(III) ions and dopamine," *Chemistry A*, vol. 19, no. 22, pp. 7243–7249, 2013.
- [60] S. S. Wee, Y. H. Ng, and S. M. Ng, "Synthesis of fluorescent carbon dots via simple acid hydrolysis of bovine serum albumin

- and its potential as sensitive sensing probe for lead (II) ions,” *Talanta*, vol. 116, pp. 71–76, 2013.
- [61] Z. Qian, J. Ma, X. Shan, H. Feng, L. Shao, and J. Chen, “Highly luminescent N-doped carbon quantum dots as an effective multifunctional fluorescence sensing platform,” *Chemistry—A European Journal*, vol. 20, no. 8, pp. 2254–2263, 2014.
- [62] F. K. Du, F. Zeng, Y. H. Ming, and S. Wu, “Carbon dots-based fluorescent probes for sensitive and selective detection of iodide,” *Microchimica Acta*, vol. 180, no. 5-6, pp. 453–460, 2013.
- [63] W. Bai, H. Zheng, Y. Long, X. Mao, M. Gao, and L. Zhang, “A carbon dots-based fluorescence turn-on method for DNA determination,” *Analytical Sciences*, vol. 27, no. 3, pp. 243–246, 2011.
- [64] B. Xu, C. Zhao, W. Wei et al., “Aptamer carbon nanodot sandwich used for fluorescent detection of protein,” *The Analyst*, vol. 137, no. 23, pp. 5483–5486, 2012.
- [65] V. N. Mehta, S. Jha, and S. K. Kailasa, “One-pot green synthesis of carbon dots by using *Saccharum officinarum* juice for fluorescent imaging of bacteria (*Escherichia coli*) and yeast (*Saccharomyces cerevisiae*) cells,” *Materials Science & Engineering C*, vol. 38, no. 1, pp. 20–27, 2014.
- [66] L. Wang, Y. Yin, A. Jain, and H. Susan Zhou, “Aqueous phase synthesis of highly luminescent, nitrogen-doped carbon dots and their application as bioimaging agents,” *Langmuir*, vol. 30, no. 47, pp. 14270–14275, 2014.
- [67] Y.-Y. Zhang, M. Wu, Y.-Q. Wang, X.-W. He, W.-Y. Li, and X.-Z. Feng, “A new hydrothermal refluxing route to strong fluorescent carbon dots and its application as fluorescent imaging agent,” *Talanta*, vol. 117, pp. 196–202, 2013.
- [68] E. J. Goh, K. S. Kim, Y. R. Kim et al., “Bioimaging of hyaluronic acid derivatives using nanosized carbon dots,” *Biomacromolecules*, vol. 13, no. 8, pp. 2554–2561, 2012.
- [69] C.-W. Lai, Y.-H. Hsiao, Y.-K. Peng, and P.-T. Chou, “Facile synthesis of highly emissive carbon dots from pyrolysis of glycerol; gram scale production of carbon dots/mSiO<sub>2</sub> for cell imaging and drug release,” *Journal of Materials Chemistry*, vol. 22, no. 29, pp. 14403–14409, 2012.
- [70] M. Zheng, S. Liu, J. Li et al., “Integrating oxaliplatin with highly luminescent carbon dots: an unprecedented theranostic agent for personalized medicine,” *Advanced Materials*, vol. 26, no. 21, pp. 3554–3560, 2014.

## Review Article

# A Review on Fault Mechanism and Diagnosis Approach for Li-Ion Batteries

Chao Wu,<sup>1,2</sup> Chunbo Zhu,<sup>1</sup> Yunwang Ge,<sup>2</sup> and Yongping Zhao<sup>1</sup>

<sup>1</sup>*School of Electrical Engineering and Automation, Harbin Institute of Technology, Harbin 150001, China*

<sup>2</sup>*Department of Electrical Engineering, Luoyang Institute of Science and Technology, Luoyang 471023, China*

Correspondence should be addressed to Chao Wu; [shiningi@163.com](mailto:shiningi@163.com)

Received 8 January 2015; Accepted 4 March 2015

Academic Editor: Jiayu Wan

Copyright © 2015 Chao Wu et al. This is an open access article distributed under the Creative Commons Attribution License, which permits unrestricted use, distribution, and reproduction in any medium, provided the original work is properly cited.

Li-ion battery has attracted more and more attention as it is a promising storage device which has long service life, higher energy, and power density. However, battery ageing always occurs during operation and leads to performance degradation and system fault which not only causes inconvenience, but also risks serious consequences such as thermal runaway or even explosion. This paper reviews recent research and development of ageing mechanisms of Li-ion batteries to understand the origins and symptoms of Li-ion battery faults. Common ageing factors are covered with their effects and consequences. Through ageing tests, relationship between performance and ageing factors, as well as cross-dependence among factors can be quantified. Summary of recent research about fault diagnosis technology for Li-ion batteries is concluded with their cons and pros. The suggestions on novel fault diagnosis approach and remaining challenges are provided at the end of this paper.

## 1. Introduction

These years, Li-ion battery has been commercialized widely for the advantages such as long service life, high energy density, and environmental protection. It is considered as the most promising energy storage device in EV (electrical vehicle) field, which has gradually taken increasing rate in all vehicles sold. Along with the development of EV and Li-ion battery industry, BMS (battery management system) technology made rapid progress [1]. Basic BMS should provide the following functions [2]: (1) data acquisition, (2) SOC (state of charge), SOH (state of health) and SOF (state of health) estimation, (3) charge control, (4) equalization, and (5) thermal management. All these techniques were reported and reviewed frequently during the last twenty years [3, 4]. However little attention has been paid to fault diagnosis technology for Li-ion batteries until several issues and accidents related to batteries occurred during recent years: batteries of laptops from Panasonic, Dell, and Sony were successively recalled for fire hazards; Tesla Model S EV had 5 fire accidents in last 6 months totally related to batteries; BYD electrical taxi caught a fire during charging process. All these events brought the safety issue of Li-ion batteries to public concern.

Although Li-ion batteries are known as long-service devices, their lives depend greatly on environmental condition and operation mode. Conditions such as elevated temperature and overcharging/overdischarging will shorten service life, so it is necessary for users to understand the ageing mechanism and detect faults before terrible accidents occur.

Faults of Li-ion batteries usually come from ageing process or abuse operation. Usually, the concept SOH is used for description of current status of health or remaining life [5]. However, it is not sufficient to describe one cell with only one variable, especially for diagnosis system. More information should be provided such as operation history and real-time variation to foresee further performance, and this is important for echelon use of Li-ion batteries [6, 7].

Fault diagnosis technology has been developed and applied in industrial applications in recent years with advanced models, algorithms and ideas. However, different from mechanical or pure electrical system, Li-ion battery is much more complex due to its electrochemical property. Hysteresis and inconsistency among cells make it even harder to directly extract the fault symptoms. Therefore fault diagnosis for Li-ion batteries requires completely understanding

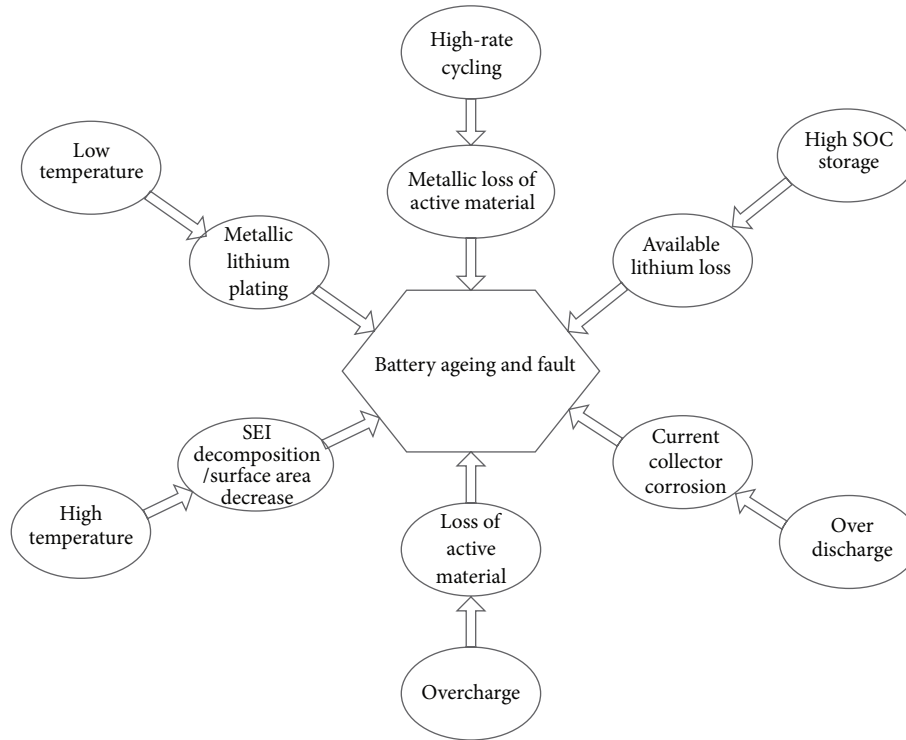


FIGURE 1: Causes for battery ageing at anode and their effects.

their ageing mechanism and certain advanced diagnosis technology.

This review intends to summarize recent achievements in fault diagnosis for Li-ion batteries, including the ageing mechanism, tests, and diagnosis methods. Subsequent sections of this paper are arranged as follows. Section 2 introduces the basic ageing mechanism of Li-ion batteries in electrochemical point of view. With the mechanism, accelerated tests are represented, trying to quantify performance degradation with one or more ageing factors. This content will be arranged in Section 3. After that, recent researches on fault diagnosis for Li-ion batteries are reviewed and compared in Section 4. Finally conclusion is drawn and we suggest a novel diagnosis method for batteries with reference of this review.

## 2. Ageing Mechanism

Battery ageing, usually in form of capacity fade and resistance growth, perhaps as well as available power fade, is one of the most challenging issues for system safety. Life prediction and fault diagnosis technologies require a good understanding of this process [8–10]. The main ageing causes for Li-ion batteries are decomposition of SEI (Solid Electrolyte Interphase), deposition at anode [11, 12], metal dissolution from anode [13, 14], loss of active material [15] and lithium plating [16]. Since the degradation mechanisms from the positive and negative electrodes may be different, we will discuss the mechanism in view of electrode degradation.

**2.1. Ageing at Anode.** In this paper, only the most popular anode material graphite is discussed. Many researchers

regarded the electrochemical changes at the electrode/electrolyte as the main cause for anode ageing [17, 18]. Decomposition products, which are caused by reductive electrolyte decomposition at the electrode/electrolyte interface, build up the so called “SEI” that covers the electrode’s surface during the first few cycles. SEI is stable and has a rather slowly ageing process unless the battery operates at improper conditions such as elevated temperature or heavy cycles. High temperature accelerates SEI breakdown or dissolution and results in an increased degradation rate [19]. In case of overcharge or high SOC storage, gas from graphite exfoliation induces crack of SEI and loss of active area [20], while low temperature may lower lithium ion diffusion. In this case, SEI is covered by lithium plating and safety issue may occur due to metallic lithium plating and lithium dendrite growth. Other origins of anode ageing such as changes of active material, changes of composite electrode, and contact loss [21] will not be discussed in detail here. The factors of battery ageing occurring at anode and their main effects are summarized in Figure 1. Notice that these factors are not isolated and the relationships cannot be discussed separately. For example, both high-rate discharge and low temperature may limit ion diffusion while both high temperature and overcharge perform an additive energy directly into batteries. This content will be discussed in Section 3 with corresponding test procedure and quantitative research.

**2.2. Ageing at Cathode.** Bourlot et al. reported that there was no evident change of the cathode morphology, for all levels of battery utilization. The author quantified the ratio of active Li/metal at anode and active lithium in

wt% at cathode. For aged batteries, more active lithium at cathode was observed with low-rate discharge to 0.5 V compared with fresh batteries. The author attributed this to limitation of anode, which was the main effect of ageing mechanism [22]. Although the changes at cathode seem to have less influences on battery ageing than those at anode [23], the influence indeed exists. SEI also forms at the interface [24], and it experiences the same process of growing, ageing, and decomposition. The ageing originates from SEI decomposition, changes of composite electrode and chemical decomposition, and dissolution reaction and differs according to the composition of cathode as well. The most popular chemistries in current production are  $\text{LiCoO}_2$ ,  $\text{LiMn}_2\text{O}_4$ , and  $\text{LiFePO}_4$ . These cathode materials have their advantages and disadvantages. For example,  $\text{LiFePO}_4$  is attractive because of its high stability, low cost, and high compatibility with environment. Major disadvantages lie on its low electrical conductivities and slow diffusion rates of Li-ions. Conductive additives may be an available approach to overcome their own drawbacks. Carbon nanotube has been proven to be the most effective one in improving the electrochemical performance and guaranteeing the safety of the composite cathode.

### 3. Ageing Test and Analysis

In previous section, we attributed battery ageing to external factors such as improper temperature, overcharge/overdischarge, high voltage storage, and even the load profile. Efforts have been made to characterize the relationship between them. However, all these factors affect battery in different manner. Moreover, cross-dependence among factors makes it more difficult to quantify the ageing behavior. Thus, environmental factors and their consequences were deeply studied. Following subsections give a brief review for the ageing tests and relationship between the factors and performance of aged batteries.

**3.1. Performance during Cycle and Storage.** Many researches on normal operation for Li-ion batteries were reported to understand the performance degradation during cycling and storage [25]. Bloom et al. [26] tried to find the mathematical relationship between external conditions and performance degradation, in form of power fade and ASI (area specific impedance) increase. The author changed temperature and SOC during calendar tests while temperature and  $\Delta\text{SOC}$  during cycle tests. All test data were fit into the equation, trying to build a life prediction model:

$$Q = A \exp\left(\frac{-E_a}{RT}\right) t^z, \text{ where} \quad (1)$$

$Q$  is the evaluated parameter, ASI or power.

In calendar test the fitted  $z$  stayed around 1/2 (varying from 0.46–0.61), following Arrhenius kinetics [27] so the ageing was considered due to SEI layer growth. However, during high SOC cycle ( $\Delta\text{SOC} = 6\%$ ),  $z$  dropped to 1/10, which indicated that more complex reaction occurred. Service lives of Li-ion batteries in different conditions were predicated with the fitted equation.

### 3.2. Performance at Extreme Environment

**3.2.1. Overcharge.** More researches were carried out to evaluate one single factor, especially the extreme condition, on ageing. Because external energy is directly added into batteries, overcharge is considered as one of the most serious problems resulting in thermal runaway. Author in [28, 29] constructed “soft” overcharge strategy for a detailed study on overcharge. Irreversible changes could be observed at 150% overcharge and distraction of anode and cathode at 200% overdischarge, both of which induce irreversible loss of active material. Through examining the surface of recovered separator, author believed thermal runaway caused by overdischarge might result from microshorting initiated by growth penetrating through separator and accelerated side reactions at anode.

**3.2.2. Overdischarge.** Overdischarge barely induces thermal runaway directly. However, overdischarged cells experience irreversible capacity loss and changes of thermal stability, which may impact tolerance to abuse condition and increase the potential of safety issues. In order to verify the explanation in [30] about overdischarge, a series of overdischarge tests at 0.0–2.0 V were carried out in [31]. Irreversible capacity loss was observed differently according to its discharge cutoff voltage, and overdischarged cells represented an accelerated ageing trend under normal cycles. Furthermore, overdischarge to 0 V made an even worse condition where the behavior became unpredictable. After examining the separator, copper was found at the anode side, which indicated the possible cause of copper dissolution from collector.

**3.2.3. Abnormal Temperature.** Although Arrhenius theory is usually used for description of ageing, especially the effect of temperature, it may not be appropriate for all range of temperatures. Wide-ranged temperature tests show that the predominant ageing mechanism at low temperature is plating of metallic lithium at the anodes due to the slow ion diffusion, which is deduced from the measurement of negative polarization versus  $\text{Li}/\text{Li}^+$  with reference electrode. In this case, delivered energy and efficiency are lower, considering 60% at  $-20^\circ\text{C}$  compared with nearly 100% at room temperature [32], and it is difficult to charge a normal battery under  $-25^\circ\text{C}$ . On the contrary, high temperature accelerated degradation of cathode and SEI growth at anode, resulting in the capacity fade. The degradation of performance usually exhibits two different slopes with inflexion at about  $25^\circ\text{C}$ . Ramadass et al. [33] gave the full representation and explanation of performance for Li-ion batteries at  $25^\circ\text{C}$ ,  $45^\circ\text{C}$ ,  $50^\circ\text{C}$ , and  $55^\circ\text{C}$ , whose results are listed in Table 1. From the table, the capacity loss is higher when battery suffers higher temperature. After 800 cycles, the cells at  $25^\circ\text{C}$  and  $45^\circ\text{C}$  lost about 31% and 36% of their initial capacity, while cell at  $50^\circ\text{C}$  lost more than 60% capacity after 600 cycles and cell at  $55^\circ\text{C}$  lost 70% after 500 cycles. The author attributed the loss to ohmic loss, secondary active material loss, and primary active material loss and quantified their contributions, respectively.

Even higher temperature (above  $65^\circ\text{C}$ ) cycle was tested. Capacity loss of 22% during 29 cycles was observed, which

TABLE 1: Capacity loss at different temperatures.

	25°C	45°C	50°C	55°C
150 cyc	107	125	141	168
300 cyc	182	209	427	481
800 cyc	539	643	1074 (600)	1255 (490)

was attributed to positive electrode bind and composition changes in SEI [34].

**3.2.4. High-Rate Cycling.** Charging/discharging rate is an important factor especially for power applications. High-rate discharge usually means short period for Li-ion transfer. In this case ions are not fully deintercalated which results in capacity loss and lithium dendrite. Moreover, high rate current forms higher power consumption across the same internal resistor and accelerates the internal temperature increase. Side reactions will be enhanced so that loss of active material will result in battery degradation. So there is always a capacity fade and accelerated ageing when suffering high-rate discharge. The capacity fade at different rate was quantified in [35, 36] and deep researches were carried out to understand the relationship between current profiles and internal behaviors. In [37], different charging protocol was proposed to achieve a fast charging strategy with minimized degradation cost. Same approach was applied to discharging case, which showed that the driving mode had great influence on battery life [38, 39].

The high-rate related problem may be relieved through advanced nanotechnology. Carbon nanotube, as a unique 1D additive material for Li-ion batteries, not only increases contact area with electrolyte, but also reduces the transport path for ions and improves the insertion/removal rate. In this case, capacity loss originating from high-rate cycling is reduced.

**3.2.5. Interactions.** More and more researches have been focused on interactions among different ageing factors, because in real application, for example, EV or HEV, all these factors mentioned above always occur simultaneously. The temperature varies with climate and thermal management; load profile lies on the driving mode [40], and voltages of individual cells depend on the balancing protocol. Complex situation accelerates the performance degradation and makes the diagnosis ever harder. Li [41] took into account the following factors: ambient temperature, discharge rate, discharge cut-off voltage, charge rate, and charge cut-off voltage for battery ageing and tried to verify the coupling between these factors. However, the result seemed not satisfactory. The author in [42] also committed to find the coupling of cycling rate and low temperature. Moreover, he suggested that aged Li-ion batteries could only be deployable in second-life applications only if their ageing history was known and appropriate tests were necessary. All these facts invoke further efforts on research about the ageing mechanism and relationship between performance degradation and related factors.

## 4. Fault Diagnosis Methods for Li-Ion Batteries

When a fault occurs, some variables in this system (direct or indirect) represent different behaviors from the ordinary case. Diagnosis system extracts the fault information from the difference and deals with the fault in time. Fault diagnosis is a critical topic which has been widely applied in mechanical, aerostatic, electrical, and military fields [43]. Main processes for fault diagnosis consist of fault feather extraction, fault isolation, and estimation as well as fault evaluation and decision. According to the principle of diagnosis methods, they can be classified as model based method and nonmodel based method. Classification of diagnosis technology can be found in Figure 2 [44].

**4.1. Model Based Method.** Through the difference between prior information from model and measured information from diagnosed object, residual signal is obtained and processed for fault information. This is the main principle of model based method which can be divided into state estimation and parameter estimation. There are essentially four types of common models: mathematical models, electrochemical models, equivalent circuit models, and experimental models. Each model has its own emphasis, for example, mathematical models are based on stochastic approaches or empirical equations; electrochemical models characterize internal kinetics and thermal behaviors while equivalent circuit models represent external response. Here we focus on equivalent circuit model for its clear physical meaning of parameters and less computation taken. One of the most common models is displayed in Figure 3, where  $R_0$ : Electrolyte Resistance,  $C_{dl}$ : Double Layer Capacity,  $R_{ct}$ : Charge Transfer Resistance, and  $Z_w$ : Warburg Impedance. These parameters change according to the state of the cell and can be good indicators for battery ageing [45].

Author in [46] simplified Randles equivalent circuit model of Li-ion batteries and extracted interested parameters through impedance spectrum. After overcharge and discharge cycling tests, the effects of cycles on the parameters were summarized to form rule base and update proposed model. Finally fuzzy logic was applied to diagnose the overcharge and overdischarge fault during battery operation. The similar idea appeared in [47]. The author also performed a series of overcharge and overdischarge cycles and constructed models for normal operation and fault operation with Kalman filter. MMAE (multiple model adaptive estimation) was adopted for comparison of results from each model with actual result. Fault information was given in form of possibility. More fault modes can be solved through model based method if the fault pattern is known, for example, in [48], author tried to locate contact resistor fault.

### 4.2. Nonmodel Based Method

**4.2.1. Signal Processing Based Method.** The simplest idea of signal processing based method sets a threshold, if the target signal or its changing rate exceeds the threshold, a fault will be located. The work of [49] sets the upper and lower thresholds

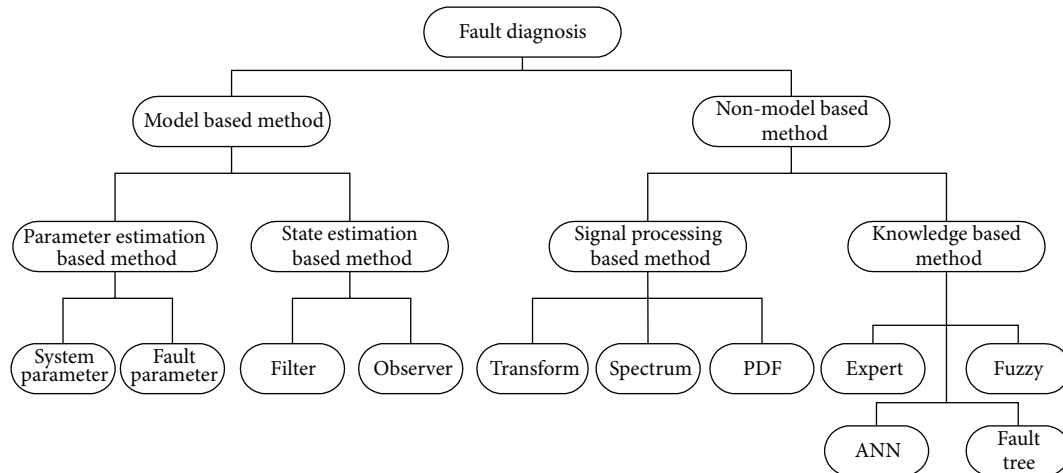


FIGURE 2: Typical classification of diagnosis technology.

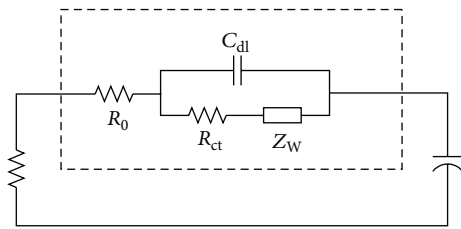


FIGURE 3: Randles Equivalent Circuit Model.

directly with the average value and average standard error. Individual parameters were monitored in real time to see if their values fell into permitted range.

However direct diagnosis method may be not suitable for complicated target whose fault symptom cannot be easily accessed. In this case the fault may be related to the amplitude, phase, frequency, or correlation of output signals. For instance, power spectrum will be affected by localized corrosion of rotating bearing. In this case analysis such as spectrum analysis, ARMA (autoregressive moving average), wavelet transform, and PDF (possibility distribution function) are the better ways to extract fault symptoms.

EIS (electrochemical impedance spectroscopy) is a powerful tool for battery analysis, and it provides abundant electrochemical information about different aging mechanism. However, it requires special equipment such as electrochemical station which limits its online applications. The author in [50] proposed an online impedance spectroscopy method of fault diagnosis for Li-ion batteries. Through applying a slight signal during charging and discharging cycles, frequency spectrum of current and voltage were obtained through DFT, with which impedance spectroscopy of target battery was calculated without any professional equipment or off-line requirement.

Wavelet transform has been widely applied in fault diagnosis for mechanical and electrical system, but barely adopted for that of Li-ion batteries. In [51], the author selected dB3 and scale 5 as wavelet function, and took the

5th level of approximation and detail as indicators of battery degradation. Wavelet process could be treated as signal decomposition through low-pass and high-pass filters so that the detailed information of operation profile at different frequency range were achieved. Finally a novel definition of SOH was given. The principle of wavelet transform is shown in Figure 5.

Other powerful signal processing tools such as impulse response [52], PDF [53], sliding mode observer [54] and support vector machine and relevance vector machine [55, 56] were applied in fault diagnosis for Li-ion batteries and made certain progress.

**4.2.2. Knowledge Based Method.** Knowledge based method has been developing rapidly these years and achieved great success in fault diagnosis with progress in artificial intelligence and expert system. By means of established historical database or expert experience, knowledge based method overcomes the dependence on accurate model and the requirement for huge computations. According to its diagnosis principle, it can be classified as follows:

- (a) expert system;
- (b) fuzzy logic;
- (c) fault tree analysis;
- (d) ANN (artificial neural network);
- (e) information fusion technology.

As declared above, expert system induces the expert experience and heuristic knowledge to solve certain kind of problem. Usually it consists of knowledge base and inference engine as well as knowledge acquisition module and interpretation interface. In fault diagnosis expert system, fault feature of battery was analyzed according to huge amount of data, committed to construct an open knowledge database which connected the fault with symptoms [57]. After an intelligent and independent inference engine was constructed, the system showed effectiveness on battery fault

diagnosis. Another expert system was also implemented in [58], unlike [57] the author applied the fuzzy logic and chose proper membership function to define the symptoms and faults, as well as a fuzzy relationship matrix to connect both domains. Rule database was achieved through experience, and fault membership could be calculated which determined the health status in form of DOF (degree of failure). Similar expert system could be seen also in [59] with diagnosis object of Li-ion batteries.

Not only the faults of batteries but also the faults from the whole battery management system attract researchers' attention. The accuracy of fault diagnosis system depends on the data acquisition element, so it's necessary for BMS to determine if the received data is reliable. Hu et al. [60] focused on temperature sensor failure during operation. The author adopted residual sensor and data fusion technology, and selected the optimal input to guarantee the system free from temperature sensor failure. Same technique may be available for voltage and current acquisition.

*4.2.3. Comparison of Diagnosis System.* All these introduced diagnosis methods for Li-ion batteries have made certain progress to improve the safety problem, but they still have limitations in real application, respectively. Model based method achieves a perfect performance towards linear system diagnosis, but diagnosis for nonlinear system remains a key problem in research field. Li-ion batteries, as a fully nonlinear electrochemical system, may not be solved with linear approach, so nonlinear theory, adaptive observer, and qualitative methods such as EKF (extended Kalman filter) have been adopted to improve the performance of model based method for quasinonlinear system. Besides, compromise between robustness and sensitivity of diagnosis system is another issue to be considered [61].

Signal processing based method avoids the difficulty in system modeling, which is simpler and has better dynamic performance. However, it has some difficulties on dealing with the early faults and fault location. Calculation requirement depends greatly on applied technology, but is always larger compared with model based method.

Knowledge based method suits well in case of complicated and nonlinear system. It takes experience and knowledge into consideration, which is a promising diagnosis method due to its artificial intelligence. On the contrary, training process or rule establishment is time consuming and has great influence on diagnosis accuracy. So there is still a long road ahead before its real application.

*4.2.4. Module Diagnosis.* Batteries need to be assembled into packs to provide enough capacity or power for consumer electronics and EV, so fault diagnosis towards module should be more meaningful [62–64]. However, due to the complexity of battery electrochemical characteristic and inhomogeneity among individual cells, researches on module diagnosis have been reported only in recent few years and are still developing. After a bridge between individual cells and battery pack was constructed, [65] constructed the model for individual cell and three cells were connected in series to form a string.

Parameter estimation of the “small module” was carried out in form of matrix.

System integration of battery pack is an important issue for system safety. Cells as well as contact condition and other assembly, will influence the system performance simultaneously. This problem was introduced in [66]. After acceleration test and continuous discharging test, the fault of individual cell occurred. The author not only provided a way to identify faulty cell in battery module, but also demonstrated the imbalances phenomena resulting from unequal current path in highly paralleled strips due to contact resistance. He suggested that careful module design and balancing strategy are necessary.

In this section, we demonstrate cons and pros of the common used diagnosis methods for Li-ion batteries and the difficulties for module diagnosis, with expectation for an accurate and practical diagnosis system in real applications. As we all know, Li-ion batteries are a complex electrochemical system which may not be sufficiently characterized by equivalent circuit model. And hardware limitation may not be adequate for huge computation or entire database storage. A hybrid approach may be the best solution if we merge the ideas together.

## 5. Conclusion

Faults of Li-ion batteries usually result from ageing process or abuse operation in form of internal impedance increment, power fade and capacity degradation [67]. This paper reviewed the battery ageing mechanisms with the purpose to connect external fault symptom with internal electrochemical property of Li-ion batteries. Main ageing factors such as overcharge/overdischarge, elevated temperature were analyzed to explain their relationship with ageing process and performance of Li-ion batteries. With good understanding of the fault origins and their symptoms summarized, fault diagnosis system could be realized.

Model based and non-model based approaches in fault diagnosis technology have been introduced, with their cons and pros. Model based can perform perfect diagnosis if the system model is known, especially the system is linear. When the system is complex and nonlinear, signal processing may be necessary to extract fault symptoms from real-time data with cost of huge computation. Knowledge based method can also be considered if historical database or expert system has been established. However, this establishment process may be time consuming. A hybrid approach may be wise to gain all the advantages of the method above. For example, equivalent circuit model is used for explanation of ageing process, whose ageing parameters are extracted through signal processing methods [68]. With reference of data from database and inference from expert system, ageing and fault diagnosis will be achieved (see Figure 4).

Therefore, safety issue for Li-ion batteries system is still a challenge due to the complexity of battery system. It requires further researches on (1) deep understanding of ageing mechanism and estimation method; (2) advanced manufacture technology for Li-ion batteries such as nanotubes and

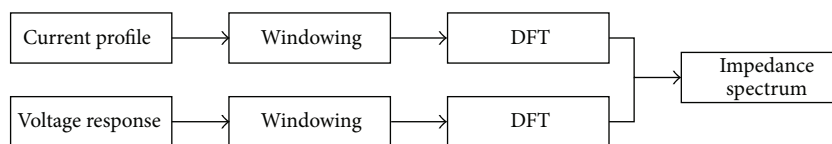


FIGURE 4: Signal processing method for impedance spectroscopy.

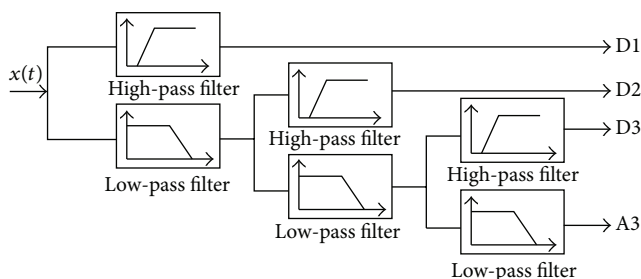


FIGURE 5: Block diagram of wavelet transform.

nanowalls to improve performance; and (3) accurate and reliable fault diagnosis approach merging the advantages of the method mentioned above.

### Additional Points

A review of ageing mechanism of Li-ion batteries and diagnosis method for it is provided, covering the classic and newest researches in this field. The diagnosis methods are compared for establishment of a novel approach. The challenges for battery diagnosis are discussed.

### Conflict of Interests

The authors declare no conflict of interests.

### Authors' Contribution

Chao Wu reviewed the ageing mechanism of Li-ion batteries as well as diagnosis methods. Professor Chunbo Zhu made the contribution to establishment of the novel approach and discussion on challenges for battery diagnosis. Other authors provided the classic and newest researches in related field.

### Acknowledgment

This research was supported by the Research and Development of Application Technology Plan Project in Heilongjiang Province of China (GA13A202) and the Science and Technology Project of State Grid Corporation of China.

### References

- [1] M. Bowkett, K. Thanapalan, T. Stockley, M. Hathway, and J. Williams, "Design and implementation of an optimal battery management system for hybrid electric vehicles," in *Proceedings of the 19th International Conference on Automation and Computing (ICAC '13)*, pp. 212–216, London, UK, September 2013.
- [2] H. F. Dai, X. L. Zhang, X. Z. Wei, Z. Sun, J. Wang, and F. Hu, "Cell-BMS validation with a hardware-in-the-loop simulation of lithium-ion battery cells for electric vehicles," *International Journal of Electrical Power and Energy Systems*, vol. 52, no. 1, pp. 174–184, 2013.
- [3] W. Waag, S. Käbitz, and D. U. Sauer, "Experimental investigation of the lithium-ion battery impedance characteristic at various conditions and aging states and its influence on the application," *Applied Energy*, vol. 102, pp. 885–897, 2013.
- [4] S. M. Rezvanianiani, Z. Liu, Y. Chen, and J. Lee, "Review and recent advances in battery health monitoring and prognostics technologies for electric vehicle (EV) safety and mobility," *Journal of Power Sources*, vol. 256, pp. 110–124, 2014.
- [5] Y. Xing, E. W. M. Ma, K.-L. Tsui, and M. Pecht, "An ensemble model for predicting the remaining useful performance of lithium-ion batteries," *Microelectronics Reliability*, vol. 53, no. 6, pp. 811–820, 2013.
- [6] Q. Miao, L. Xie, H. J. Cui, W. Liang, and M. Pecht, "Remaining useful life prediction of lithium-ion battery with unscented particle filter technique," *Microelectronics Reliability*, vol. 53, no. 6, pp. 805–810, 2013.
- [7] G. Jin, D. E. Matthews, and Z. Zhou, "A Bayesian framework for on-line degradation assessment and residual life prediction of secondary batteries in spacecraft," *Reliability Engineering and System Safety*, vol. 113, no. 1, pp. 7–20, 2013.
- [8] V. Yufit, P. Shearing, R. W. Hamilton, P. D. Lee, M. Wu, and N. P. Brandon, "Investigation of lithium-ion polymer battery cell failure using X-ray computed tomography," *Electrochemistry Communications*, vol. 13, no. 6, pp. 608–610, 2011.
- [9] C. Marino, J. Fullenwarth, L. Monconduit, and B. Lestriez, "Diagnostic of the failure mechanism in NiSb<sub>2</sub> electrode for Li battery through analysis of its polarization on galvanostatic cycling," *Electrochimica Acta*, vol. 78, pp. 177–182, 2012.
- [10] X. D. Liu, C. Z. Chen, Y. Y. Zhao, and B. Jia, "A review on the synthesis of manganese oxide nanomaterials and their applications on lithium-ion batteries," *Journal of Nanomaterials*, vol. 2013, Article ID 736375, 7 pages, 2013.
- [11] A. Blyr, C. Sigala, G. Amatucci, D. Guyomard, Y. Chabre, and J.-M. Tarascon, "Self-discharge of LiMn<sub>2</sub>O<sub>4</sub>/C Li-ion cells in their discharged state: understanding by means of three-electrode measurements," *Journal of the Electrochemical Society*, vol. 145, no. 1, pp. 194–209, 1998.
- [12] Z. P. Wang, G. W. Xie, and L. J. Gao, "Electrochemical characterization of Li<sub>4</sub>Ti<sub>5</sub>O<sub>12</sub>/C anode material prepared by starch-sol-assisted rheological phase method for Li-ion battery," *Journal of Nanomaterials*, vol. 2012, Article ID 876197, 7 pages, 2012.
- [13] J. M. Tarascon, W. R. McKinnon, F. Coowar, T. N. Bowmer, G. Amatucci, and D. Guyomard, "Synthesis conditions and oxygen stoichiometry effects on Li insertion into the spinel LiMn<sub>2</sub>O<sub>4</sub>," *Journal of the Electrochemical Society*, vol. 141, no. 6, pp. 1421–1431, 1994.

- [14] J. Park, J. H. Seo, G. Plett, W. Lu, and A. M. Sastry, "Numerical simulation of the effect of the dissolution of  $\text{LiMn}_2\text{O}_4$  particles on Li-Ion battery performance," *Electrochemical and Solid-State Letters*, vol. 14, no. 2, pp. A14–A18, 2011.
- [15] J. Christensen and J. Newman, "Cyclable lithium and capacity loss in li-ion cells," *Journal of the Electrochemical Society*, vol. 152, no. 4, pp. A818–A829, 2005.
- [16] H.-P. Lin, D. Chua, M. Salomon et al., "Low-temperature behavior of Li-ion cells," *Electrochemical and Solid-State Letters*, vol. 4, no. 6, pp. 71–73, 2001.
- [17] D. Aurbach, E. Zinigrad, Y. Cohen, and H. Teller, "A short review of failure mechanisms of lithium metal and lithiated graphite anodes in liquid electrolyte solutions," *Solid State Ionics*, vol. 148, no. 3-4, pp. 405–416, 2002.
- [18] D. Aurbach, M. D. Levi, E. Levi et al., "Common electroanalytical behavior of Li intercalation processes into graphite and transition metal oxides," *Journal of the Electrochemical Society*, vol. 145, no. 9, pp. 3024–3034, 1998.
- [19] M. N. Richard and J. R. Dahn, "Accelerating rate calorimetry study on the thermal stability of lithium intercalated graphite in electrolyte. I. Experimental," *Journal of the Electrochemical Society*, vol. 146, no. 6, pp. 2068–2077, 1999.
- [20] T. Abe, H. Fukuda, Y. Iriyama, and Z. Ogumi, "Solvated Li-ion transfer at interface between graphite and electrolyte," *Journal of the Electrochemical Society*, vol. 151, no. 8, pp. A1120–A1123, 2004.
- [21] Y. Wang, X. Guo, S. Greenbaum, J. Liu, and K. Amine, "Solid electrolyte interphase formation on lithium-ion electrodes. A  $7\text{Li}$  nuclear magnetic resonance study," *Electrochemical and Solid-State Letters*, vol. 4, no. 6, pp. A68–A70, 2001.
- [22] S. Bourlot, P. Blanchard, and S. Robert, "Investigation of aging mechanisms of high power Li-ion cells used for hybrid electric vehicles," *Journal of Power Sources*, vol. 196, no. 16, pp. 6841–6846, 2011.
- [23] P. Liu, J. Wang, J. Hicks-Garner et al., "Aging Mechanisms of  $\text{LiFePO}_4$  batteries deduced by electrochemical and structural analyses," *Journal of the Electrochemical Society*, vol. 157, no. 4, pp. A499–A507, 2010.
- [24] K. Edström, T. Gustafsson, and J. O. Thomas, "The cathode-electrolyte interface in the Li-ion battery," *Electrochimica Acta*, vol. 50, no. 2-3, pp. 397–403, 2004.
- [25] N. Khare, U. Banasthali, Jaipur, and R. Govil, "A battery storage system for fault tolerance," in *Proceedings of the 29th International Telecommunications Energy Conference*, Rome, Italy, September–October 2007.
- [26] I. Bloom, B. W. Cole, J. J. Sohn et al., "An accelerated calendar and cycle life study of Li-ion cells," *Journal of Power Sources*, vol. 101, no. 2, pp. 238–247, 2001.
- [27] B. Y. Liaw, E. P. Roth, R. G. Jungst, G. Nagasubramanian, H. L. Case, and D. H. Doughty, "Correlation of Arrhenius behaviors in power and capacity fades with cell impedance and heat generation in cylindrical lithium-ion cells," *Journal of Power Sources*, vol. 119-121, pp. 874–886, 2003.
- [28] D. Belov and M.-H. Yang, "Failure mechanism of Li-ion battery at overcharge conditions," *Journal of Solid State Electrochemistry*, vol. 12, no. 7-8, pp. 885–894, 2008.
- [29] D. Belov and M. H. Yang, "Investigation of the kinetic mechanism in overcharge process for Li-ion battery," *Solid State Ionics*, vol. 179, no. 27–32, pp. 1816–1821, 2008.
- [30] M. Zhao, H. D. Dewald, F. R. Lemke, and R. J. Staniewicz, "Electrochemical stability of graphite-coated copper in lithium-ion battery electrolytes," *Journal of the Electrochemical Society*, vol. 147, no. 11, pp. 3983–3988, 2000.
- [31] H. Maleki and J. N. Howard, "Effects of overdischarge on performance and thermal stability of a Li-ion cell," *Journal of Power Sources*, vol. 160, no. 2, pp. 1395–1402, 2006.
- [32] H.-P. Lin, D. Chua, M. Salomon et al., "Low-temperature behavior of Li-ion cells," *Electrochemical and Solid-State Letters*, vol. 4, no. 6, pp. 71–73, 2001.
- [33] P. Ramadass, B. Haran, R. White, and B. N. Popov, "Capacity fade of Sony 18650 cells cycled at elevated temperatures: part II. Capacity fade analysis," *Journal of Power Sources*, vol. 112, no. 2, pp. 614–620, 2002.
- [34] D. P. Abraham, E. M. Reynolds, P. L. Schultz, A. N. Jansen, and D. W. Dees, "Temperature dependence of capacity and impedance data from fresh and aged high-power lithium-ion cells," *Journal of the Electrochemical Society*, vol. 153, no. 8, pp. A1610–A1616, 2006.
- [35] M. Zackrisson, L. Avellán, and J. Orlenius, "Life cycle assessment of lithium-ion batteries for plug-in hybrid electric vehicles—critical issues," *Journal of Cleaner Production*, vol. 18, no. 15, pp. 1517–1529, 2010.
- [36] X. B. Han, M. G. Ouyang, L. G. Lu, and J. Q. Li, "Cycle life of commercial lithium-ion batteries with lithium titanium oxide anodes in electric vehicles," *Energies*, vol. 7, no. 8, pp. 4895–4909, 2014.
- [37] B. Lunz, Z. Yan, J. B. Gerschler, and D. U. Sauer, "Influence of plug-in hybrid electric vehicle charging strategies on charging and battery degradation costs," *Energy Policy*, vol. 46, pp. 511–519, 2012.
- [38] Z. G. Yang and S. P. Wang, "High cycling performance cathode material: interconnected  $\text{LiFePO}_4$ /Carbon nanoparticles fabricated by sol-gel method," *Journal of Nanomaterials*, vol. 2014, Article ID 801562, 7 pages, 2014.
- [39] J. C. Arrebola, A. Caballero, L. Hernán, and J. Morales, "Improving the performance of lithium-ion batteries by using spinel nanoparticles," *Journal of Nanomaterials*, vol. 2008, Article ID 659397, 10 pages, 2008.
- [40] M. Ecker, J. B. Gerschler, J. Vogel et al., "Development of a lifetime prediction model for lithium-ion batteries based on extended accelerated aging test data," *Journal of Power Sources*, vol. 215, pp. 248–257, 2012.
- [41] Z. Li, *Characterization research of  $\text{LiFePO}_4$  batteries for application on pure electric vehicles [Ph.D. thesis]*, Tsinghua University, Beijing, China, 2011.
- [42] Y. M. Zhang and J. Jiang, "Issues on integration of fault diagnosis and reconfigurable control in active fault-tolerant control systems," in *Proceedings of the 6th IFAC Symposium on Fault Detection, Supervision and Safety of Technical Processes (SAFEPROCESS '06)*, pp. 1437–1448, Beijing, China, September 2006.
- [43] N. Williard, W. He, M. Osterman, and M. Pecht, "Reliability and failure analysis of Lithium Ion batteries for electronic systems," in *Proceedings of the 13th International Conference on Electronic Packaging Technology and High Density Packaging (ICEPT-HDP '12)*, pp. 1051–1055, Guilin, China, August 2012.
- [44] C. H. Hu and H. L. Xu, *Design and Analysis of Fault-Tolerant Control and Fault Diagnosis for Control System*, National Defense Industry Press, Beijing, China, 2008.
- [45] Z. W. He, M. Y. Gao, C. S. Wang, L. Y. Wang, and Y. Liu, "Adaptive state of charge estimation for Li-ion batteries based

- on an unscented kalman filter with an enhanced battery model,” *Energies*, vol. 6, no. 8, pp. 4134–4151, 2013.
- [46] T. C. Kaypmaz and R. N. Tuncay, “An advanced cell model for diagnosing faults in operation of Li-ion polymer batteries,” in *Proceedings of the 7th IEEE Vehicle Power and Propulsion Conference (VPPC '11)*, pp. 1–5, Chicago, Ill, USA, September 2011.
- [47] A. Singh, A. Izadian, and S. Anwar, “Fault diagnosis of Li-Ion batteries using multiple-model adaptive estimation,” in *Proceedings of the 39th Annual Conference of the IEEE Industrial Electronics Society (IECON '13)*, pp. 3524–3529, November 2013.
- [48] S. A. Gadsden and S. R. Habibi, “Model-based fault detection of a battery system in a hybrid electric vehicle,” in *Proceedings of the 7th IEEE Vehicle Power and Propulsion Conference (VPPC '11)*, pp. 1–6, IEEE, Chicago, Ill, USA, September 2011.
- [49] J.-C. Hwang, J.-C. Chen, J.-S. Pan, and Y.-C. Huang, “Measurement method for online battery early faults precaution in uninterrupted power supply system,” *IET Electric Power Applications*, vol. 5, no. 3, pp. 267–274, 2011.
- [50] U. Tröltzsch, O. Kanoun, and H. R. Tränkler, “Characterizing aging effects of lithium ion batteries by impedance spectroscopy,” *Electrochimica Acta*, vol. 51, no. 8-9, pp. 1664–1672, 2006.
- [51] J. Kim and B. H. Cho, “An innovative approach for characteristic analysis and state-of-health diagnosis for a Li-ion cell based on the discrete wavelet transform,” *Journal of Power Sources*, vol. 260, pp. 115–130, 2014.
- [52] A. Banaei and B. Fahimi, “Real time condition monitoring in Li-ion batteries via battery impulse response,” in *Proceedings of the IEEE Vehicle Power and Propulsion Conference (VPPC '10)*, pp. 1–6, Lille, France, September 2010.
- [53] T. A. Moebes, “Lithium battery analysis: probability of failure assessment using logistic regression,” in *Proceedings of the Annual Reliability and Maintainability Symposium (RAMS '11)*, 5, p. 1, Vista, Fla, USA, January 2011.
- [54] D. Kim, K. H. Koo, J. J. Jeong, T. D. Goh, and S. W. Kim, “Second-order discrete-time sliding mode observer for state of charge determination based on a dynamic resistance Li-ion battery model,” *Energies*, vol. 6, no. 10, pp. 5538–5551, 2013.
- [55] A. Widodo, M.-C. Shim, W. Caesarendra, and B.-S. Yang, “Intelligent prognostics for battery health monitoring based on sample entropy,” *Expert Systems with Applications*, vol. 38, no. 9, pp. 11763–11769, 2011.
- [56] J. I. Park, S. H. Baek, M. K. Jeong, and S. J. Bae, “Dual features functional support vector machines for fault detection of rechargeable batteries,” *IEEE Transactions on Systems, Man and Cybernetics Part C: Applications and Reviews*, vol. 39, no. 4, pp. 480–485, 2009.
- [57] X. J. Liu, *Research and application of intelligent battery fault diagnosis system [M.S. dissertation]*, Beijing University of Posts and Telecommunications, Beijing, China, 2010.
- [58] W. J. Liu, *Research and implementation of failure diagnosis expert system for battery pack [M.S. thesis]*, Hunan University, Hunan, China, 2005.
- [59] J. R. Wu, *Design of remote monitoring system and study on fault diagnosis method for electric vehicle [M.S. thesis]*, Jilin University, Jilin, China, 2011.
- [60] C. H. Hu, R. He, R. C. Wang, and J. B. Yu, “Fault prediction and fault-tolerant of lithium-ion batteries temperature failure for electric vehicle,” in *Proceedings of the 3rd International Conference on Digital Manufacturing and Automation (ICDMA '12)*, pp. 410–413, Guilin, China, August 2012.
- [61] B. Wu, G. J. Offer, V. Yufit, D. A. Howey, and N. P. Brandon, “Fault analysis in battery module design for electric and hybrid vehicles,” in *Proceedings of the 6th IET International Conference on Power Electronics, Machines and Drives (PEMD '12)*, pp. 1–6, IET, Bristol, UK, March 2012.
- [62] J. López, R. Navarro, J. M. Gallego, F. Parres, and S. Ferrándiz, “Failure analysis of automotive battery parts,” *Engineering Failure Analysis*, vol. 16, no. 7, pp. 2217–2223, 2009.
- [63] Z. Q. Chen, F. Lin, C. S. Wang, Y. L. Wang, and M. Xu, “Active diagnosability of discrete event systems and its application to battery fault diagnosis,” *IEEE Transactions on Control Systems Technology*, vol. 22, no. 5, pp. 1892–1898, 2014.
- [64] L. Ahmadi, M. Fowler, S. B. Young, R. A. Fraser, B. Gaffney, and S. B. Walker, “Energy efficiency of Li-ion battery packs re-used in stationary power applications,” *Sustainable Energy Technologies and Assessments*, vol. 8, pp. 9–17, 2014.
- [65] W. Chen, W.-T. Chen, M. Saif, M.-F. Li, and H. Wu, “Simultaneous fault isolation and estimation of lithium-ion batteries via synthesized design of Luenberger and learning observers,” *IEEE Transactions on Control Systems Technology*, vol. 22, no. 1, pp. 290–298, 2014.
- [66] S. Buller, M. Thele, R. W. A. A. de Doncker, and E. Karden, “Impedance-based simulation models of supercapacitors and lithium-ion batteries for power electronic applications,” *IEEE Transactions on Industry Applications*, vol. 41, no. 3, pp. 742–747, 2005.
- [67] D. Mukoyama, T. Momma, H. Nara, and T. Osaka, “Electrochemical impedance analysis on degradation of commercially available lithium ion battery during chargedischarge cycling,” *Chemistry Letters*, vol. 41, no. 4, pp. 444–446, 2012.
- [68] D. Andre, A. Nuhic, T. Soczka-Guth, and D. U. Sauer, “Comparative study of a structured neural network and an extended Kalman filter for state of health determination of lithium-ion batteries in hybrid electricvehicles,” *Engineering Applications of Artificial Intelligence*, vol. 26, no. 3, pp. 951–961, 2013.

## Research Article

# Study of the Electroless Deposition of Ni for Betavoltaic Battery Using PN Junction without Seed Layer

Jin Joo Kim,<sup>1</sup> Young Rang Uhm,<sup>1</sup> Byoung Gun Choi,<sup>2</sup> and Kwang Jae Son<sup>1</sup>

<sup>1</sup>Radioisotope Research Division, Korea Atomic Energy Research Institute, 989-111 Daedeokdaero, Yuseong-gu, Daejeon 305-353, Republic of Korea

<sup>2</sup>Human Interface SoC Research Section, Electronics and Telecommunications Research Institute, 218 Gajeong-ro, Yuseong-gu, Daejeon 305-700, Republic of Korea

Correspondence should be addressed to Young Rang Uhm; [uyrang@kaeri.re.kr](mailto:uyrang@kaeri.re.kr)

Received 19 May 2015; Revised 30 June 2015; Accepted 30 June 2015

Academic Editor: Xiaogang Han

Copyright © 2015 Jin Joo Kim et al. This is an open access article distributed under the Creative Commons Attribution License, which permits unrestricted use, distribution, and reproduction in any medium, provided the original work is properly cited.

The method and conditions of Ni plating were optimized to maximize the output of a betavoltaic battery using radioactive <sup>63</sup>Ni. The difference of the short circuit currents between the pre- and postdeposition of <sup>63</sup>Ni on the PN junction was 90 nA at the *I-V* characteristics. It is suspected that the beta rays emitted from <sup>63</sup>Ni did not deeply penetrate into the PN junction due to a Ni seed layer with a thickness of 500 Å. To increase the penetration of the beta rays, electroless Ni plating was carried out on the PN junction without a seed layer. To establish the electroless coating conditions for <sup>63</sup>Ni, nonradioactive Ni was deposited onto a Si wafer without flaws on the surface. This process can be applied for electroless Ni plating on a PN junction semiconductor using radioactive <sup>63</sup>Ni in further studies.

## 1. Introduction

A betavoltaic battery that converts the decay energy of beta- ( $\beta^-$ ) emitting radioisotopes into electricity is characterized by specialized properties such as a long service life and being free of maintenance [1]. The origin of nuclear batteries using beta-particle was the pacemaker related to pacing industry in 1973. These devices offered young patients the possibility of having a single pacemaker implant that could last their whole life. The  $\beta^-$ -cell for pacemaker had promethium (<sup>147</sup>Pm) sandwiched between semiconductor wafers. The impact of the  $\beta^-$ -particles on PN junction causes a forward bias in the semiconductor similar to the behavior of photovoltaic cell. The  $\beta^-$ -cell had an open circuit voltage of 4.7 V and a short circuit current of 115  $\mu$ A. However, it has a half-life of 2.6 years, at most. So, nuclear pacemakers were displaced by devices powered by lithium cells in mid-1980, due to longevity of lithium-powered batteries with approximately 10 years. The important factor affecting the performance of a betavoltaic battery is a radioisotope used as a power source. <sup>63</sup>Ni is pure beta-emitter with a low energy spectrum of  $E_{\text{avg}} = 17.4$  keV and

significantly long half-life of 100.1 years and thus is widely used as the power source of betavoltaic batteries. Tritium (<sup>3</sup>H) has shorter half-life (12.3 years) than those of <sup>63</sup>Ni. However, this isotope has enough longevity, the same as lithium-powered batteries. The beta spectrum of <sup>63</sup>Ni is below the radiation damage threshold (approximately 200 keV for Si) of semiconductors such as Si and SiC. Also, <sup>63</sup>Ni is easier to handle than other beta-particles such as <sup>3</sup>H, <sup>90</sup>Sr, and <sup>147</sup>Pm because of its low energy spectrum and solid-metal form. For this reason, it is suitable for the power source of a betavoltaic battery to be within the nano- to microwatt range [2–4]. There are several methods for the formation of a Ni deposit onto a substrate such as electroplating, electroless plating [5, 6], and chemical vapor deposition (CVD). Among them, the electroplating process is most commonly used for Ni deposition when using <sup>63</sup>Ni as a power source for a battery. The Ni seed layer on a semiconductor is necessary for the deposition of Ni during electroplating, but it can cause a decrease of electric efficiency of the battery because it absorbs beta rays emitted from <sup>63</sup>Ni and causes a self-shielding effect of the beta rays. In order to prevent the self-shielding and improve

TABLE 1: The composition of the bath for electroless Ni plating.

Bath composition	Concentration
$\text{NiSO}_4 \cdot 6\text{H}_2\text{O}$	0.10 M
$\text{NaH}_2\text{PO}_3 \cdot \text{H}_2\text{O}$	0.23 M
$\text{Na}_3\text{C}_6\text{H}_5\text{O}_7 \cdot 2\text{H}_2\text{O}$	0.07 M
$\text{NaC}_2\text{H}_3\text{O}_2$	0.06 M
$\text{Pb}(\text{CH}_3\text{COO})_2 \cdot 2\text{H}_2\text{O}$	0.004 mM
Deposition condition	Value
Temperature	75°C
pH	10

the electrical efficiency of a betavoltaic battery, electroless Ni plating that can be carried out without a seed layer was performed in this study.

Electroless plating is a process for the deposition of metals, such as nickel, onto a substrate via a catalyzed chemical reduction of metal ions at the surface of the substrate without the use of an electric current. Unlike electroplating, an electroless plating process has some advantages such as a thickness uniformity and independence of the electrical properties of the substrate [7, 8]. In addition, it is possible to form a Ni deposit directly on a substrate without a Ni seed layer when using electroless plating, which can solve the problem in which beta rays emitted from radioactive  $^{63}\text{Ni}$  are absorbed on the seed layer.

The aim of this work is to optimize the method and conditions of Ni plating to maximize the electrical efficiency of a betavoltaic battery using radioactive  $^{63}\text{Ni}$ . In this study, a betavoltaic battery using  $^{63}\text{Ni}$  coated on a PN junction semiconductor was fabricated and the  $I$ - $V$  characteristics were measured using Probe Station. In addition, an electroless Ni plating process using nonradioactive Ni was established to minimize the decrease in electric efficiency. This process can be applied for electroless plating on a PN junction semiconductor using radioactive  $^{63}\text{Ni}$ .

## 2. Experimental Technique

**2.1.  $^{63}\text{Ni}$  Electroplating and Measurement of  $I$ - $V$  Characteristics.** The process of electroplating using radioactive  $^{63}\text{Ni}$  in a hot cell (Bank-2, HANARO research reactor in KAERI) was carried out using a two-step process: the preparation of an ionic solution including  $^{63}\text{Ni}$  and electroplating on the PN junction semiconductor as a substrate. The spacing of the PN junction semiconductor was 5  $\mu\text{m}$ , and the specific radioactivity of electroplated  $^{63}\text{Ni}$  was estimated to be about 2.5 mCi. To perform electroplating  $^{63}\text{Ni}$  on the PN junction, the minimum thickness of the seed layer should be 500 Å, for a semiconductor fully covered with metal. The  $I$ - $V$  characteristics of a  $^{63}\text{Ni}$ -coated semiconductor were investigated using Probe Station of the Precision Source/Measure Unit, B2911A.

**2.2. Electroless Ni Plating on Si Wafer.** Table 1 shows the composition and operating conditions of an electroless Ni plating bath. The solution for electroless Ni plating was made up of

0.1 M nickel sulfate, 0.23 M sodium hypophosphite, 0.07 M sodium citrate, 0.06 M sodium acetate, and 4 nM lead acetate used as stabilizer. Nickel sulfate is the main salt, sodium hypophosphite is a reducing agent, and sodium citrate and sodium acetate are used as a complexing agent. The pH value of the plating solution was adjusted to 10 with the addition of NaOH, and the bath is heated to a temperature of 75°C. Si wafers with dimensions of 5 × 5 mm<sup>2</sup> were used as the substrates. Prior to electroless Ni plating, the wafers were dipped in an HCl solution (10%) for 40 s and washed with distilled water. The cleaned Si wafers were put into a plating beaker for 20 min without any pretreatment, activation, or sensitization. The Ni-coated Si wafers obtained by the electroless plating were cleaned with distilled water and dried for 1 h at 90°C in a vacuum.

The surface morphology of the Ni deposits was observed using field emission scanning electron microscopy (FE-SEM) of JSM-7100F, and the composition and content of deposited Ni was analyzed by X-ray diffraction (XRD). XRD investigations were carried out using a Philips X'Pert-Pro instrument operated at 40 kV and 30 mA with CuK $\alpha$  radiation ( $\lambda = 1.5418 \text{ \AA}$ ) at a scanning rate of 2°/min.

## 3. Results and Discussion

To evaluate the PN junction prepared by the Electronic Telecommunications Research Institute (ETRI), the electron beam induced current technique has been employed to experimentally simulate the beta emission of  $^{63}\text{Ni}$  and to estimate the total device current [9]. The open circuit voltage was found to be 0.29 V. The short circuit currents were 3.3 A. The power output was found to be 66.5 W/cm<sup>2</sup>. From the e-beam illumination test, we confirmed the good operation of the PN absorber. Figure 1 shows the performance characteristics of the  $^{63}\text{Ni}$ -coated PN junction semiconductor with a Ni seed layer with a thickness of 500 Å. A prototype of the electroplating  $^{63}\text{Ni}$  was carried out in a glove box in a hot cell (Bank-2, HANARO Reactor in KAERI). The specific radioactivity of the electroplated Ni including  $^{63}\text{Ni}$  was estimated to be about 2.5 mCi. The nominal specific activity was measured by a portable activity meter (PAM 1704). The  $I$ - $V$  curves of both dark and deposited  $^{63}\text{Ni}$  show almost the same values. The difference between the predeposition (dark) and deposited  $^{63}\text{Ni}$  can be obtained through a magnification of the  $I$ - $V$  curve [4]. The difference of the short circuit current ( $I_{sc}$ ) between the predeposition and postdeposition of  $^{63}\text{Ni}$  with a thickness of about 3  $\mu\text{m}$  was found to be 90 nA. The output power was found to be 8.0 pW (picowatt) at an open circuit voltage ( $V_{oc}$ ) of 0.08 mV. The performance of betavoltaic battery prepared by Ulmen et al. was achieved as 2.5 pW of maximum power output at a voltage of 0.4 mV using 4 mCi of  $^{63}\text{Ni}$ . [4]. Recently, the maximum performance was achieved at 5~500 nW of stack structure (package) prepared by Widetronix Co. [10]. We obtained a relatively enhanced power output at a single cell, though the specific radioactivity was a lower value than those of other groups. From the  $I$ - $V$  characteristics analysis, we confirmed that there are no large differences in the power output between pre- and postdeposition, though

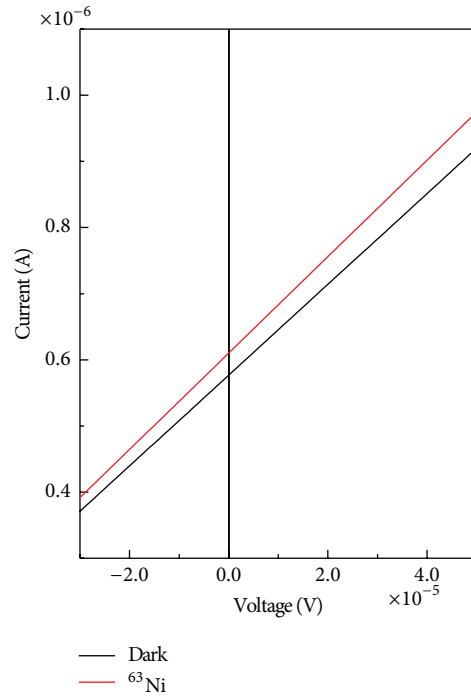


FIGURE 1:  $I$ - $V$  characteristics for  $^{63}\text{Ni}$ -coated PN junction semiconductor.

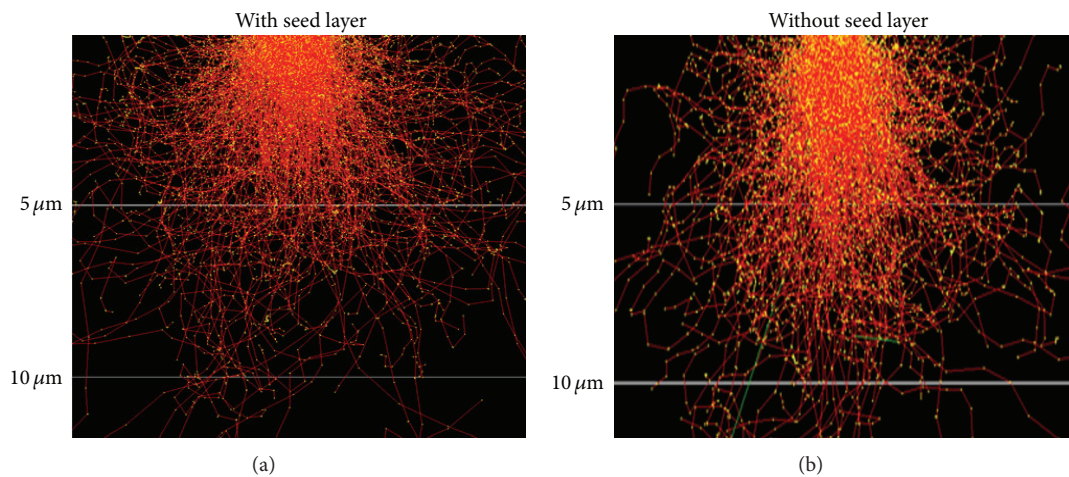


FIGURE 2: Energy absorption in silicon (a) with and (b) without seed layer as a function of  $^{63}\text{Ni}$  thickness.

the power output is increased as compared with other research groups. This is thought to be due to beta rays emitted from  $^{63}\text{Ni}$  not penetrating the Ni seed layer because of the self-shielding of the beta rays.

The penetration depth of the particles in the silicon device was reported in a Katz-Penfold range equation [11]. This equation considers only the density of the materials and energy of the particles. This effectively determines the depth of the depletion region required. We modeled the energy deposition as a function of the depth in the silicon with/without a seed layer using the Monte Carlo code. The self-shielding effect at the seed layer of the radioisotope layer was also investigated. Figure 2 shows the results of the relative energy deposition

as a function of thickness for the deposit layer of  $^{63}\text{Ni}$  on a Si wafer (a) with a seed layer and (b) without a seed layer. Energy absorption in silicon with a seed layer as a function of  $^{63}\text{Ni}$  thickness was decreased compared with those without a seed layer.

To prevent the self-shielding, which causes a decrease in the output of the betavoltaic battery, electroless Ni plating that can be carried out without the Ni seed layer was performed. The reaction temperature was changed from 50 to 80°C. The reaction was inactive at and below 70°C. The coating layer was delaminated at and above a reaction temperature of 80°C because of a tremendous massive reduction. A large amount of colloids and precipitation was observed at a high reaction

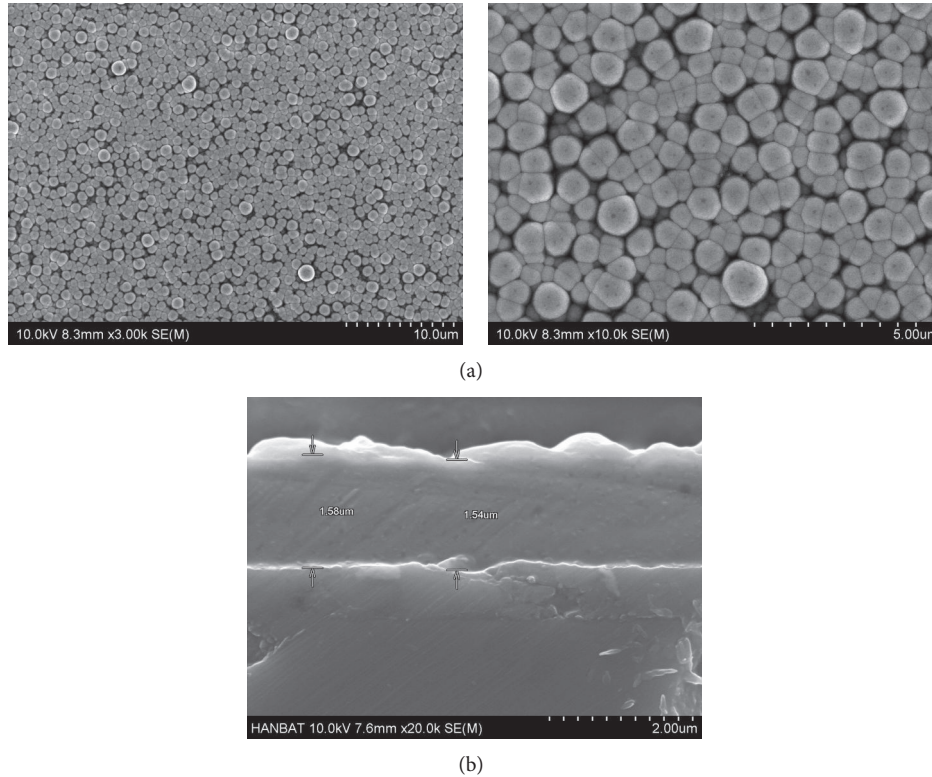


FIGURE 3: (a) Surface morphology of the Ni deposits on Si wafers and (b) SEM images for thickness of the Ni-coated Si wafers.

temperature of above  $80^{\circ}\text{C}$ . The coating layer was formed at a pH between 9 and 11. The pH and reaction temperature of the solution were determined at pH 10 and  $75^{\circ}\text{C}$ , respectively. Lead acetate was added to the solution as a stabilizer. The adhesion strength between substrate and coating layer was enhanced, as the stabilizer prevents overabundance of reduction on the substrate. The reaction was inactive, though the stabilizer was added above 0.004 mM in the solution. Figures 3(a) and 3(b) present SEM images of Ni deposits after 20 min of electroless plating. As shown in Figure 3, well-distributed spherical particles are spread on the Si wafer under a condition of  $75^{\circ}\text{C}$  at pH 10. The Ni deposits were uniformly and continuously formed, and there were no flaws on the surface. If the temperature of the plating solution is too high, many more hydrogen bubbles were generated, and thus the coating layer was peeled from the Si wafer because of an unstable surface formation. Figure 3(b) shows the SEM images for thickness of the Ni-coated Si wafers. The thickness of the Ni deposit is about  $1.5\ \mu\text{m}$  after 20 min of electroless plating. The agglomeration of Ni particles is observed on the surface layer.

Figure 4 shows the results of XRD for the deposited Ni on a Si wafer under the plating condition of  $75^{\circ}\text{C}$  at pH 10. XRD patterns were observed showing that the crystal structure of the Ni deposits is pure FCC (face-centered cubic) Ni. Five characteristic peaks at around  $2\theta$  are  $44.5^{\circ}$ ,  $51.8^{\circ}$ ,  $76.4^{\circ}$ ,  $93^{\circ}$ , and  $98.5^{\circ}$ , which is consistent with the (111), (200), (220), (311), and (222) lattice plane diffractions of Ni crystals, respectively, which are definitely observed for the Ni particles. Crystal

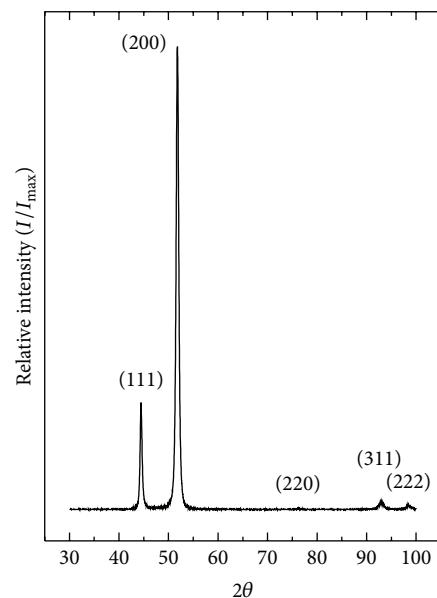


FIGURE 4: XRD patterns of the Ni deposits on Si wafers.

orientations of the films were estimated by the high degree (200) in the XRD patterns, as shown in Figure 4. The main peak of the bulk Ni is presented generally at (111). However, the plane orientation was formed, because of the thin thickness of the coating layer [12].

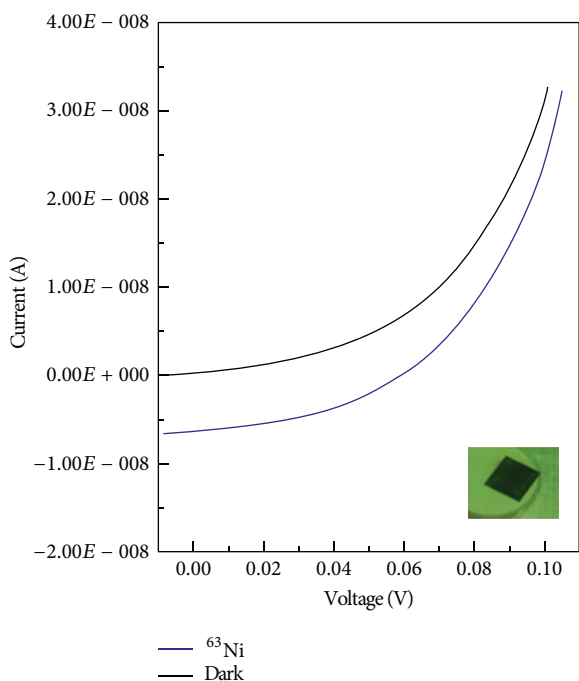


FIGURE 5:  $I$ - $V$  characteristics for  $^{63}\text{Ni}$  on PN junction semiconductor and prepared beta source of  $^{63}\text{Ni}$  by electroless plating.

This process can be applied for electroless plating on a PN junction semiconductor using radioactive  $^{63}\text{Ni}$ . The solution for electroless plating using  $^{63}\text{Ni}$  is made up of radioactive Ni sulfate dissolved in a sulfuric acid solution. The whole process will be performed in a hot cell in Bank-2, the HANARO reactor in KAERI. An investigation of the surface morphology, component of the deposits, and  $I$ - $V$  characteristic of the PN junction semiconductor coated with radioactive  $^{63}\text{Ni}$  will be carried out in further studies. However, we could prepare a beta source of  $^{63}\text{Ni}$  on substrate with the nominal specific radioactivity on the surface of 0.45 mCi. Figure 5 includes a photograph of the prepared beta source. We attached prepared beta source on the PN junction without seed layer using vacuum. The difference of the short circuit current ( $I_{sc}$ ) between the predeposition and postdeposition of  $^{63}\text{Ni}$  was found to be 6.6 nA. The output power was found to be 0.29 nW at an open circuit voltage of 0.044 V. The power output of a single cell was significantly enhanced compared with previously prepared single cell with seed layer.

#### 4. Conclusion

Radioactive  $^{63}\text{Ni}$  was coated onto a PN junction semiconductor with a Ni seed layer of 500 Å and the performance characteristics of this semiconductor were measured. There are no significant differences of the short circuit current ( $I_{sc}$ ) between pre- and postdeposition. This is suspected to be due to the self-shielding of beta rays on a Ni seed layer. Thus, electroless Ni plating that can be carried out without the seed layer was performed using nonradioactive Ni. We confirmed that the Ni deposits were well coated onto a Si wafer using

SEM and XRD studies. The coating condition was determined by the optimum temperature, pH, and amount of stabilization. In a further study, the process for electroless Ni plating on a PN junction semiconductor using radioactive  $^{63}\text{Ni}$  will be optimized. Also, the power output was significantly increased, as the seed layer on the PN junction was removed.

#### Conflict of Interests

The authors declare that there is no conflict of interests regarding the publication of this paper.

#### Acknowledgment

This work is supported by the National Strategic R&D Program for Industrial Technology (10043868), funded by the Ministry of Trade, Industry and Energy (MOTIE).

#### References

- [1] G. Wang, R. Hu, H. Wei et al., "The effect of temperature changes on electrical performance of the betavoltaic cell," *Applied Radiation and Isotopes*, vol. 68, no. 12, pp. 2214–2217, 2010.
- [2] A. Thomas, "Nuclear batteries: types and possible uses," *Nuclearonics*, vol. 13, pp. 129–133, 1995.
- [3] M. Petek, J. S. Wike, B. P. Phillips, and C. A. Sampson, "Plating nickel-63 on copper coupons," Tech. Rep. ORNL/TM-10989, 1989.
- [4] B. Ulmen, P. D. Desai, S. Moghaddam, G. H. Miley, and R. I. Masel, "Development of diode junction nuclear battery using  $^{63}\text{Ni}$ ," *Journal of Radioanalytical and Nuclear Chemistry*, vol. 282, no. 2, pp. 601–604, 2009.
- [5] M. V. Sullivan and J. H. Eigler, "Electroless nickel plating for making ohmic contacts to silicon," *Journal of the Electrochemical Society*, vol. 104, no. 4, pp. 226–230, 1957.
- [6] H. Iwasa, M. Yokozawa, and I. Teramoto, "Electroless nickel plating on silicon," *Journal of the Electrochemical Society*, vol. 115, no. 5, pp. 485–488, 1968.
- [7] G. O. Mallory and J. B. Hajdu, *Electroless Plating: Fundamentals and Applications*, Noyes Publishing; William Andrew Publishing, New York, NY, USA, 1990.
- [8] P. Suresh, A. K. Shukla, and N. Munichandraiah, "Capacity stabilization of layered  $\text{Li}_{0.9}\text{Mn}_{0.9}\text{Ni}_{0.1}\text{O}_2$  cathode material by employing ZnO coating," *Materials Letters*, vol. 59, no. 8–9, pp. 953–958, 2005.
- [9] Y. R. Uhm, K. J. Son, K. Y. Park, B. G. Choi, and J. S. Lee, "The effect of Ni seed layer for electroplating  $^{63}\text{Ni}$  in radioisotope battery," in *Proceedings of the 2nd International Congress on Energy Efficiency and Energy Related Materials*, Springer, Oludeniz, Turkey, October 2014.
- [10] Widetronix, <http://www.widetronix.com>.
- [11] L. Katz and A. S. Penfold, "Range-energy relations for electrons and the determination of beta-ray end-point energies by absorption," *Reviews of Modern Physics*, vol. 24, no. 1, pp. 28–44, 1952.
- [12] Y. R. Uhm, K. Y. Park, and S. J. Choi, "The effects of current density and saccharin addition on the grain size of electroplated nickel," *Research on Chemical Intermediates*, vol. 41, no. 7, pp. 4141–4149, 2015.

## Research Article

# Enhanced Photovoltaic Properties of the Solar Cells Based on Cosensitization of CdS and Hydrogenation

Hongcai He, Kui Yang, Shuangshuang Ren, Tao Liu, and Ning Wang

State Key Laboratory of Electronic Thin Films and Integrated Devices and School of Microelectronics and Solid-State Electronics, University of Electronic Science and Technology of China, Chengdu 610054, China

Correspondence should be addressed to Ning Wang; [ning.wang@uestc.edu.cn](mailto:ning.wang@uestc.edu.cn)

Received 4 May 2015; Accepted 21 May 2015

Academic Editor: Xiaogang Han

Copyright © 2015 Hongcai He et al. This is an open access article distributed under the Creative Commons Attribution License, which permits unrestricted use, distribution, and reproduction in any medium, provided the original work is properly cited.

The hydrogenated TiO<sub>2</sub> porous nanocrystalline film is modified with CdS quantum dots by successive ionic layer adsorption and reaction (SILAR) method to prepare the cosensitized TiO<sub>2</sub> solar cells by CdS quantum dots and hydrogenation. The structure and topography of the composite photoanode film were confirmed by X-ray diffraction and scanning electron microscopy. With deposited CdS nanoparticles, UV absorption spectra of H:TiO<sub>2</sub> photoanode film indicated a considerably enhanced absorption in the visible region. The cosensitized TiO<sub>2</sub> solar cell by CdS quantum dots and hydrogenation presents much better photovoltaic properties than either CdS sensitized TiO<sub>2</sub> solar cells or hydrogenated TiO<sub>2</sub> solar cells, which displays enhanced photovoltaic performance with power conversion efficiency ( $\eta$ ) of 1.99% ( $J_{sc} = 6.26 \text{ mA cm}^{-2}$ ,  $V_{oc} = 0.65 \text{ V}$ , and  $FF = 0.49$ ) under full one-sun illumination. The reason for the enhanced photovoltaic performance of the novel cosensitized solar cell is primarily explained by studying the Nyquist spectrums, IPCE spectra, dark current, and photovoltaic performances.

## 1. Introduction

Photoelectrochemical solar cells based on TiO<sub>2</sub> nanocrystalline films sensitized with organic dyes have been studied intensely for the past 20 years as a potential promising low-cost alternative to traditional solid-state solar cells. Semiconductor nanocrystals with narrow band gap such as CdS, CdSe, PbS, and InP were also demonstrated as efficient sensitizers in the spectral range from the visible to mid infrared with advantages such as low-cost fabrication, good stability, multiple exciton generation, and the tunability of optical properties and electronic structure by changing the size of nanocrystals [1, 2]. The photoelectrochemical cells with semiconductor nanocrystals as sensitizers also were called quantum dot sensitized solar cells (QDSSCs) [1]. Among the common semiconductors, CdS is one of the most commonly used inorganic sensitizers [3] due to its optical properties and narrowed band gap adjusted by the particle size [4] and better UV stability [5] and it has reduced dark current [6]. However, the efficiencies of CdS sensitized TiO<sub>2</sub> solar cells have still stayed low up to now. It has been extensively studied how to enhance their photovoltaic efficiency. One common effective

method is cosensitization of more than one kind of quantum dots with different band gap. CdS and CdSe quantum dots cosensitized nanocrystalline TiO<sub>2</sub> is one of the most common cosensitization structures with a power conversion efficiency of more than 3% [7, 8].

The other alternative method is to modify TiO<sub>2</sub>. In order to improve the photoelectric properties of TiO<sub>2</sub> under sunlight, some metal or nonmetal impurities [9, 10] were added to generate donor or acceptor states in the band gap and to modulate energy band structure [11]. Recently, the hydrogenated TiO<sub>2</sub> has attracted extensive attention. Chen et al. [12] demonstrated that the hydrogenated TiO<sub>2</sub> nanocrystal enhanced solar absorption by introducing disorder in the surface layers of nanophase TiO<sub>2</sub>, and Wang et al. [13] reported hydrogen treatment was a simple and effective strategy to fundamentally improve the photoelectrochemical performance of TiO<sub>2</sub> nanowires for water splitting. Our previous work reported the self-sensitized effect of hydrogenated TiO<sub>2</sub> film which led to enhanced photovoltaic properties in the solar cell with hydrogenated TiO<sub>2</sub> as photoanode without adding any dye [14].

If a photoanode was prepared by depositing CdS quantum dots on the surface of hydrogenated TiO<sub>2</sub> film, the self-sensitized effect of hydrogenated TiO<sub>2</sub> film would work together with quantum dots sensitization, which should also be a kind of cosensitization to be a promising method to enhance the photovoltaic properties of quantum dot sensitized solar cells. In this work, hydrogenated TiO<sub>2</sub> films were fabricated on fluorine-doped tin oxide (FTO) glasses by screen printing and annealing under the specific temperature and time; then CdS quantum dots were attached to the surface of hydrogenated TiO<sub>2</sub> by successive ionic layer adsorption and reaction (SILAR) method. Structural characterization, photoelectrochemical properties, and photovoltaic performances were investigated and discussed. The cosensitized TiO<sub>2</sub> solar cells by CdS quantum dots and hydrogenation present much better photovoltaic properties than either CdS sensitized TiO<sub>2</sub> solar cells or hydrogenated TiO<sub>2</sub> solar cells. The reason for the enhanced photovoltaic performance of the novel cosensitized inorganic solar cell was also explained in detail.

## 2. Experimental

**2.1. Preparation of Hydrogenated TiO<sub>2</sub> Films and CdS Quantum Dots.** Hydrogenated TiO<sub>2</sub> (H:TiO<sub>2</sub>) films were prepared on fluorine-doped tin oxide (FTO) glasses with an area of 0.16 cm<sup>2</sup> via the same processing as reported previously [14]. Then CdS quantum dots were attached to the surface of hydrogenated TiO<sub>2</sub> by successive ionic layer adsorption and reaction (SILAR) method [15, 16]. In brief, 0.1 M Cd(NO<sub>3</sub>)<sub>2</sub> in methanol was used as the cation source and 0.1 M Na<sub>2</sub>S in 1 : 1 methanol and water as the anion source. The H:TiO<sub>2</sub> films with FTO substrates were successively dipped into the cation source and anion source for 5 min each. Following each dip, the films were rinsed for 1 min or more using pure ethanol to remove excess precursor, and the electrode was dried for 10 min before the next dipping. This dip cycle was repeated several times to obtain desirable CdS quantum dots on the surface of the H:TiO<sub>2</sub> films as photoanodes. According to the preliminary experimented research on the effect of SILAR cycles for CdS quantum dots, an optimized SILAR cycle was determined as 9 cycles. For comparison, the H:TiO<sub>2</sub> films without any quantum dots and TiO<sub>2</sub> films with CdS quantum dots were also fabricated as photoanodes.

**2.2. Assembly of Solar Cells.** To assemble solar cells, the mixed solution of water and methanol with volume ratio of 3 : 7 consisting of 0.2 M KCl, 0.5 M Na<sub>2</sub>S, and 2.0 M S was used as polysulfide electrolyte. The photoanode, a platinized counter electrode, and the polysulfide electrolyte were sealed together with a hot-melt polymer film (Surllyn 1702-25, DuPont) to constitute a sandwich-like solar cell to measure photoelectrochemical properties. The active area of the cell is 0.16 cm<sup>2</sup>.

**2.3. Testing Device and Characterization Method.** The crystal structure of TiO<sub>2</sub> films was characterized by an X-ray

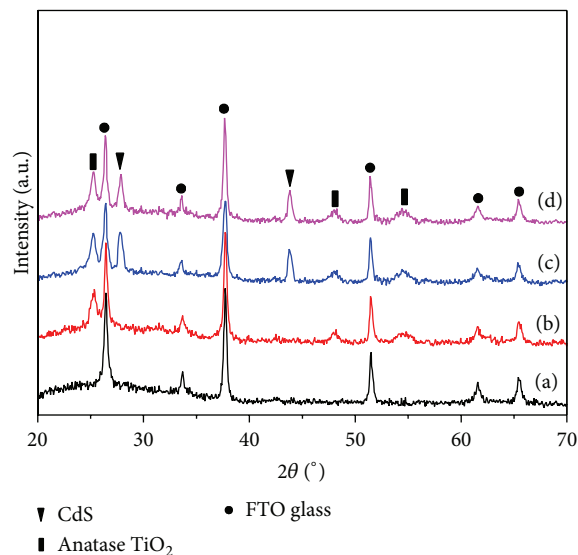


FIGURE 1: X-ray diffraction patterns of (a) FTO glass substrates; (b) H:TiO<sub>2</sub> films; (c) CdS sensitized TiO<sub>2</sub> films; (d) CdS sensitized H:TiO<sub>2</sub> films.

diffraction (XRD; X' Pert Pro MPD) with Cu K $\alpha$ 1 radiation ( $\lambda = 0.154$  nm) and the film surface morphology was observed by SEM (INSPECT F, FEI Company). Ultraviolet-visible absorption spectra were measured by Shimadzu UV2100 Spectrophotometer. In order to measure photovoltaic performance of the solar cells, simulated sunlight (AM 1.5 G) was irradiated using a solar simulator with a Xe lamp (calibrated with a standard Si-based solar cell), and the current-voltage ( $I$ - $V$ ) curve was recorded by a CHI-660 electrochemical workstation. The photocurrent density ( $J_{sc}$ ), open-circuit voltage ( $V_{oc}$ ), fill factor (FF), and corresponding photoenergy conversion efficiency ( $\eta$ ) were calculated from the obtained  $I$ - $V$  curves. The incident photon to current conversion efficiencies (IPCE) spectra were obtained by Newport QE-PV-SI. Electrochemical impedance spectroscopy (EIS) was also measured at the CHI-660 electrochemical workstation with sinusoidal perturbations of 10 mV at frequencies from 0.01 Hz to 10 kHz with zero bias potential.

## 3. Results and Discussion

**3.1. Characterization of TiO<sub>2</sub> Films Cosensitized by CdS and Hydrogenation.** X-ray diffraction patterns of the H:TiO<sub>2</sub> film, CdS/TiO<sub>2</sub> film, and CdS/H:TiO<sub>2</sub> film are shown in Figure 1. TiO<sub>2</sub> in all the films is in the anatase phase, the same as reported in our previous work [14]. With the successive ionic layer adsorption in 9 cycles, the peaks at 27.9° and 43.8° corresponding to (100) and (110) planes of CdS quantum dots, respectively, can be observed in the patterns of CdS sensitized TiO<sub>2</sub> and H:TiO<sub>2</sub> films as shown in Figures 1(c) and 1(d), respectively. No obvious difference is observed between the XRD patterns of the CdS sensitized TiO<sub>2</sub> films with or without hydrogenation. Figure 2 shows SEM surface morphology of pure H:TiO<sub>2</sub> film and CdS/H:TiO<sub>2</sub> film. The

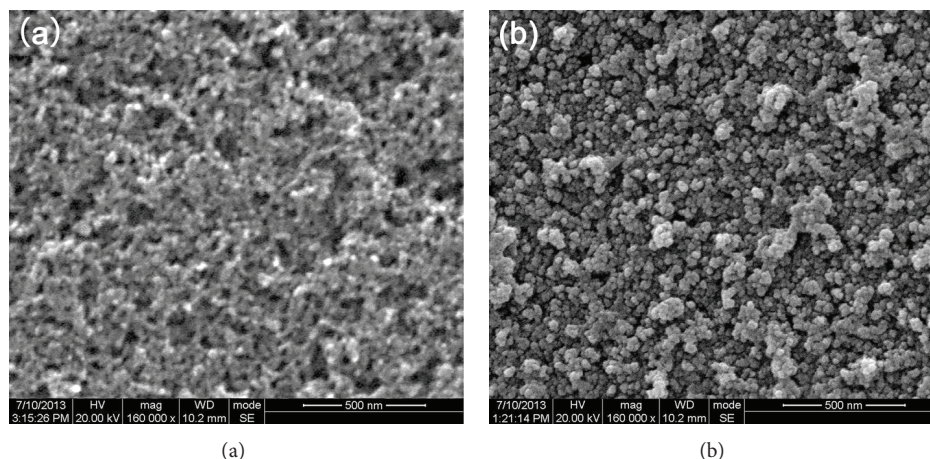


FIGURE 2: SEM surface morphology of (a) pure H:TiO<sub>2</sub> film and (b) CdS/H:TiO<sub>2</sub> film.

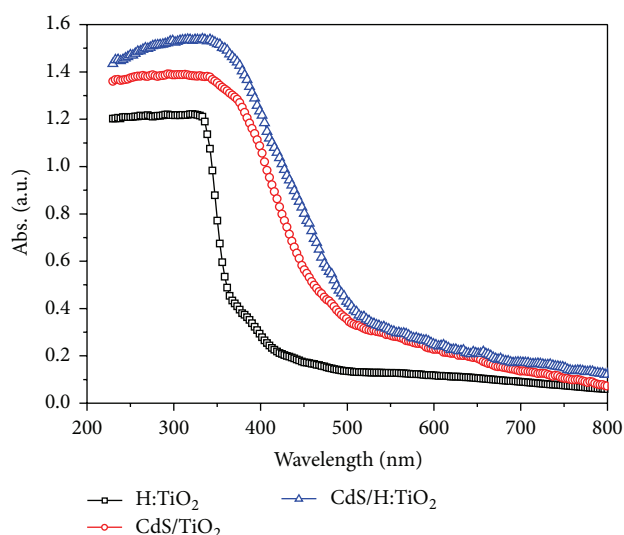


FIGURE 3: UV-visible absorption spectra of the H:TiO<sub>2</sub> film, the CdS sensitized TiO<sub>2</sub> film, and the CdS sensitized H:TiO<sub>2</sub> film.

H:TiO<sub>2</sub> film is typical porous nanocrystals as in Figure 2(a), while the CdS/H:TiO<sub>2</sub> film displays dense-packing CdS quantum dots with the grain size of about 25 nm according to Figure 2(b).

**3.2. Absorption of TiO<sub>2</sub> Films Cosensitized by CdS and Hydrogenation.** The UV-visible absorption spectra of H:TiO<sub>2</sub> film, CdS/TiO<sub>2</sub> film, and CdS/H:TiO<sub>2</sub> film are showed in Figure 3. It has been demonstrated that hydrogenation treatment can improve light absorption of TiO<sub>2</sub> due to the generated dangling bonds and disordered surface layers on the surface of TiO<sub>2</sub> nanophase [12]. Compared with the H:TiO<sub>2</sub> film with a band gap of about 3.10 eV, the CdS/TiO<sub>2</sub> film has a much stronger absorption in the range of 300~800 nm in that CdS has a much smaller band gap (2.25 eV in bulk) than H:TiO<sub>2</sub> [17]. When CdS quantum dots are deposited on the surface of the H:TiO<sub>2</sub> films, the obtained CdS/H:TiO<sub>2</sub> film combines

the advantages of both hydrogenation treatment and CdS quantum dots and thus reveals the strongest absorption as shown in Figure 3.

**3.3. Impedance Spectra of the Solar Cells Based on Cosenitization of CdS and Hydrogenation.** In order to analyze the internal electron transport process of solar cells, the electrical impedance spectra (EIS) for the sensitized solar cells based on CdS/H:TiO<sub>2</sub>, CdS/TiO<sub>2</sub>, and H:TiO<sub>2</sub> are shown in Figure 4(a), and Figure 4(b) shows the relevant equivalent-circuit model. Similar to a typical DSSC system [18, 19],  $R_{ct1}$  and CPE1 represent the electron transfer resistance and interfacial capacitance at the interface between counter electrode and electrolyte, respectively.  $R_{ct2}$  and CPE2 are electron transport resistance and interfacial capacitance at the interface between electrolyte and photoanode, respectively.  $R_s$  is ohmic series connection resistance of the whole cell.  $Z_N$  is the electrolyte Nernst diffusion impedance. Theoretically, the solar cell impedance spectroscopy has three semicircles representing high-, middle-, and low-frequency features, associated with  $R_{ct1}$  and CPE1,  $R_{ct2}$  and CPE2, and  $Z_N$ , respectively [20]. In Figure 4(a), the largest semicircle at middle-frequency almost covers the other two, which is attributed to carrier transportation and recombination at photoanode/electrolyte interfaces. The fitted values of  $R_{ct2}$  are 18  $\Omega$ , 32  $\Omega$ , and 56  $\Omega$  for the solar cells with photoanode of CdS/H:TiO<sub>2</sub>, CdS/TiO<sub>2</sub>, and H:TiO<sub>2</sub>, respectively. According to our previous work, hydrogenation treatment of TiO<sub>2</sub> can reduce  $R_{ct2}$  because the band gap is narrowed down and meanwhile the oxygen vacancy density increases. The loading of CdS nanoparticles on pure TiO<sub>2</sub> also decreases  $R_{ct2}$  of the CdS/TiO<sub>2</sub>/electrolyte interfaces significantly. For the CdS/H:TiO<sub>2</sub> photoanode, both of hydrogenation self-sensitization and CdS sensitization work together and result in the lowest  $R_{ct2}$ . The lower  $R_{ct2}$  reflects quicker electrons transport at the interface between electrolyte and photoanode, which implies that smaller probability of interface recombination occurs at the photoanode/electrolyte interface.

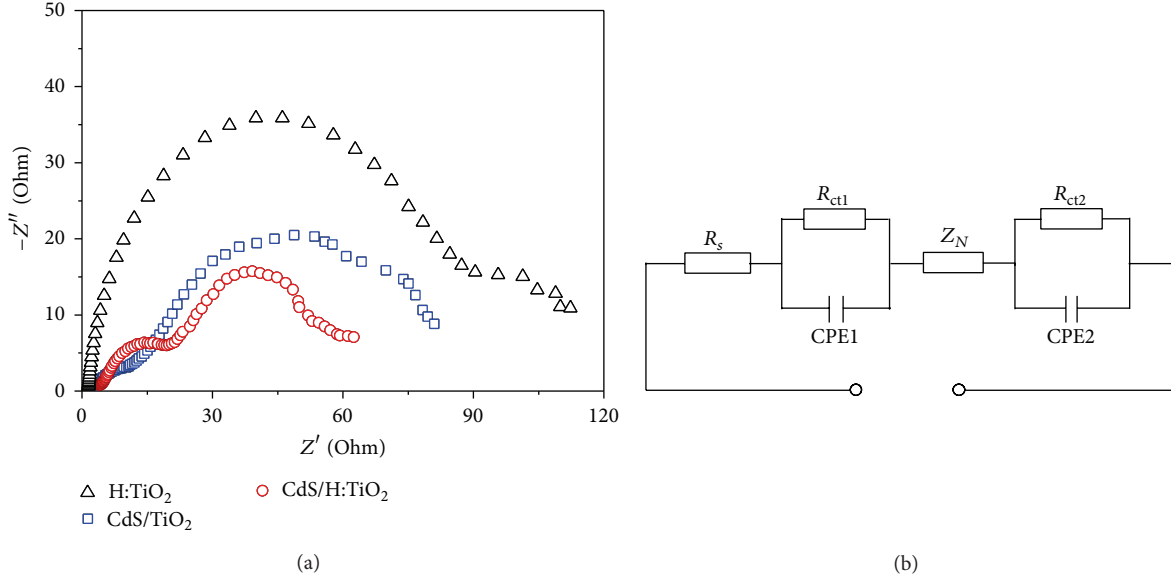


FIGURE 4: (a) Electrochemical impedance spectra of the solar cells with different photoanodes; (b) the corresponding equivalent circuit.

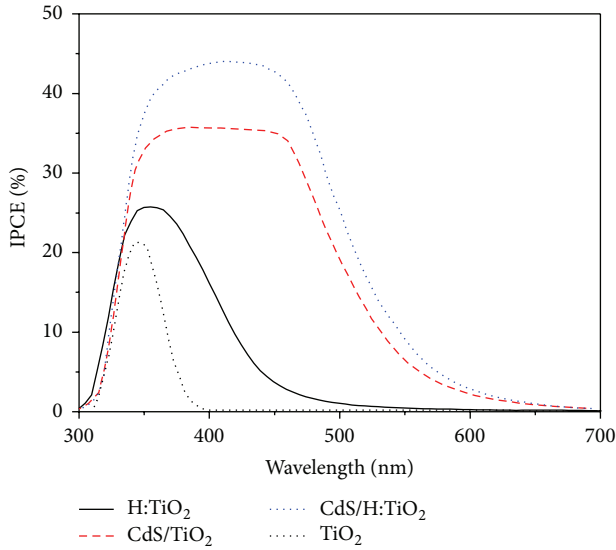


FIGURE 5: IPCE spectra of the solar cells with different photoanodes.

**3.4. Photovoltaic Performances of the Solar Cells Based on Cosensitization of CdS and Hydrogenation.** The incident photon to current conversion efficiencies (IPCE) spectra of the solar cells with different photoanodes are shown in Figure 5. The IPCE can be expressed as [21]

$$\text{IPCE}(\lambda) = \eta_{\text{LHE}} \eta_{\text{inj}} \eta_{\text{cc}}, \quad (1)$$

where  $\eta_{\text{LHE}}$  is the light harvesting efficiency,  $\eta_{\text{inj}}$  is the electron injection yield, and  $\eta_{\text{cc}}$  is the charge collection efficiency. It can be seen that the profile of IPCE plot corresponds well with the UV-vis absorption spectra in Figure 3. The IPCE of  $\text{TiO}_2$  nanocrystal film without any sensitizer is low in the UV region and negligible in the visible region. The  $\text{H:TiO}_2$

TABLE 1: The photovoltaic performances of the solar cells with different photoanodes.

Photoanodes	$J_{\text{sc}}$ ( $\text{mA cm}^{-2}$ )	$V_{\text{oc}}$ (V)	FF	$\eta$ (%)
$\text{H:TiO}_2$	0.14	0.28	0.38	0.015
$\text{CdS/TiO}_2$	4.68	0.56	0.42	1.10
$\text{CdS/H:TiO}_2$	6.26	0.65	0.49	1.99

solar cell exhibits stronger IPCE. The hydrogenated  $\text{TiO}_2$  increases oxygen vacancy density and has much more trap states near the conduction band, leading to the enhancement of the absorption as reported in our previous work [14]. The absorption enhancement implies the increase of the light harvesting efficiency, which increases the IPCE value according to the above formula. Significantly enhanced IPCE can be observed in the CdS sensitized solar cells, which can be attributed to the fact that CdS quantum dots have much higher absorption coefficients of  $10^5$  to  $10^6 \text{ M}^{-1} \text{ cm}^{-1}$  above the band gap energy [22]. The  $\text{CdS/H:TiO}_2$  solar cell exhibits the strongest IPCE due to the cosensitization of CdS and self-sensitization of hydrogenated  $\text{TiO}_2$ . The maximum IPCE of the  $\text{CdS/H:TiO}_2$  solar cell can reach 41.7% using a polysulfide electrolyte, suggesting that the cosensitization of CdS and hydrogenation has the potential to enhance the photoelectric properties.

Figure 6 shows the illuminated and dark  $J$ - $V$  characteristics of the solar cells with different photoanodes, and the photovoltaic performances of them are listed in Table 1. The self-sensitization effect of  $\text{H:TiO}_2$  photoanode with polysulfide electrolyte is very weak, exactly as our previous results of  $\text{H:TiO}_2$  photoanode with the  $\text{I}^-/\text{I}_3^-$  electrolyte. The  $\text{CdS/TiO}_2$  QDSSC also displays the ordinary photovoltaic performance as others' work with an energy conversion efficiency of 1.1%. Compared with the other two solar cells, the  $\text{CdS/H:TiO}_2$  solar cell, which is cosensitized by CdS and

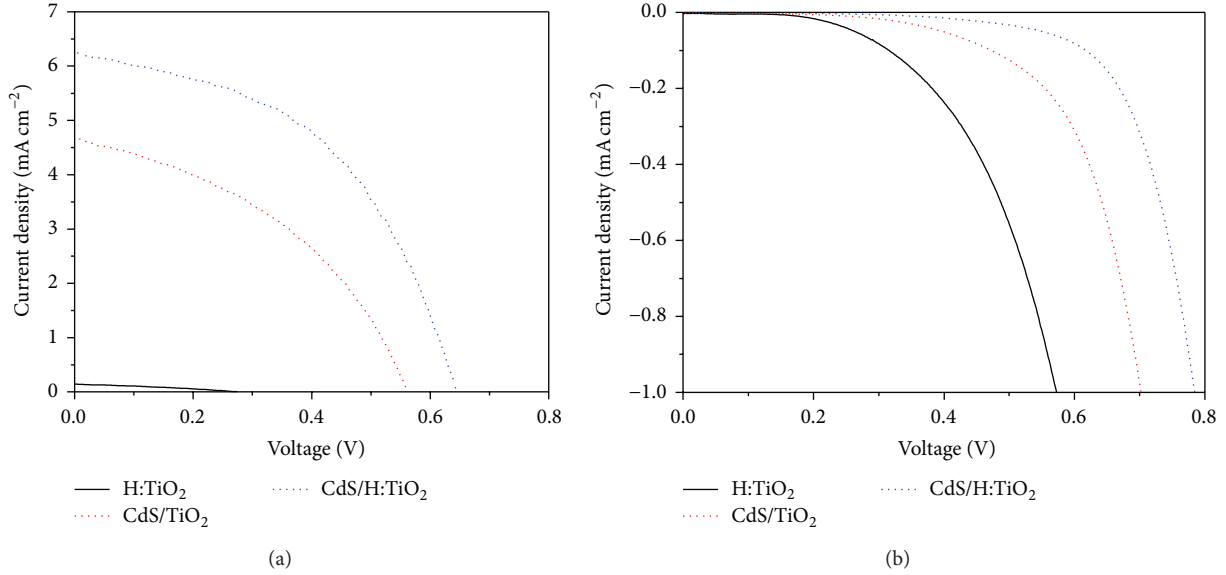


FIGURE 6: The  $J$ - $V$  characteristics of the solar cells with different photoanodes (a) under simulated AM 1.5 solar spectrum irradiation at  $100 \text{ mW cm}^{-2}$  and (b) in the dark.

hydrogenation, exhibits enhanced photovoltaic characteristics with short circuit current density ( $J_{sc}$ ) of  $6.26 \text{ mA/cm}^2$ , open-circuit voltage ( $V_{oc}$ ) of  $0.65 \text{ V}$ , fill factor (FF) of  $0.49$ , and power conversion efficiency ( $\eta$ ) of  $1.99\%$ .

The enhancement of  $J_{sc}$  can be explained by the equation:  $J_{sc} = J_{inj} - J_{rec}$ , where  $J_{inj}$  and  $J_{rec}$  are the electron injection current density and the recombination current density [23]. The stronger absorption at the UV-vis (as shown in Figure 3) and the higher IPCE (as shown in Figure 5) of CdS/H:TiO<sub>2</sub> hold out the potential of increasing  $J_{inj}$  and consequently enhancing the photoelectric effect. On the other hand, the recombination current is derived from the interface recombination mostly caused by the reduction reaction with the electron in the conduction band of TiO<sub>2</sub> and  $S_n^{2-}$  in the electrolyte, which would form the dark currents and reduce photovoltaic performance of solar cells. As shown in Figure 6(b), the dark current density of the solar cell with CdS/H:TiO<sub>2</sub> photoanode is obviously lower than that of the CdS/TiO<sub>2</sub> or H:TiO<sub>2</sub> solar cell, which should be attributed to lower  $R_{ct2}$  of the CdS/H:TiO<sub>2</sub> solar cell than that of the other two solar cells. The enhanced  $J_{inj}$  and the suppressed dark current density of the CdS/H:TiO<sub>2</sub> solar cell lead to the enhancement of the  $J_{sc}$ .

Under constant illumination, the solar cell reaches a photostationary situation, and  $V_{oc}$  corresponds to the increase of the quasi-Fermi level of the semiconductor ( $E_{Fn}$ ) with respect to the dark value ( $E_{F0}$ ), which equals the electrolyte redox energy ( $E_{F0} = E_{redox}$ ).  $V_{oc}$  can be determined by the following equation [24]:

$$V_{oc} = \frac{E_{Fn} - E_{redox}}{e} = \frac{k_B T}{e} \ln \left( \frac{n}{n_0} \right), \quad (2)$$

where  $e$  is the positive elementary charge;  $k_B T$  is the thermal energy;  $n$  is the electron concentration in conduction band of the semiconductor photoanode under illumination;  $n_0$  is

the electron concentration in the dark condition. Here,  $n$  and  $n_0$  can be characterized by IPCE and dark current density, respectively. The stronger IPCE as shown in Figure 5 implies the higher  $n$  of the CdS/H:TiO<sub>2</sub> solar cell than the H:TiO<sub>2</sub> solar cell and the CdS/TiO<sub>2</sub> solar cell, while the lower dark current density as shown in Figure 6(b) manifests the lower  $n_0$  of the CdS/H:TiO<sub>2</sub> solar cell than the other two solar cells. As a result, the higher  $n$  and the lower  $n_0$  lead to the improvement of  $V_{oc}$  for the CdS/H:TiO<sub>2</sub> solar cell as shown in Figure 6(a).

## 4. Conclusions

In summary, a cosensitized TiO<sub>2</sub> photoanode by CdS quantum dots sensitization and self-sensitization of hydrogenated TiO<sub>2</sub> film was achieved by depositing CdS quantum dots on the surface of hydrogenated TiO<sub>2</sub> film. By comparing solar cells with different photoanodes of H:TiO<sub>2</sub>, CdS/TiO<sub>2</sub>, and CdS/H:TiO<sub>2</sub>, the cosensitization effect by CdS and hydrogenation in the CdS/H:TiO<sub>2</sub> solar cell enhanced photovoltaic performance with power conversion efficiency ( $\eta$ ) of  $1.99\%$ , which was increased by more than  $80\%$  compared with CdS/TiO<sub>2</sub> solar cells. The cosensitization effect combined the quantum dots sensitization and self-sensitization of hydrogenated TiO<sub>2</sub> films and caused larger extension absorption in the visible light range, quicker electrons transport, smaller probability of interface recombination, and consequently better photovoltaic performance. This study will give some useful enlightenment to the development of novel inorganic low-cost solar cells.

## Conflict of Interests

The authors declare that there is no conflict of interests regarding the publication of this paper.

## Acknowledgments

This work was supported by the National Natural Science Foundation of China (51472043, 51272035, and 51272037), China-Japan International Cooperation Program Funds (nos. 2010DFA61410 and 2011DFA50530), Program for New Century Excellent Talents in University (no. NCET-12-0097), and the Fundamental Research Funds for the Central Universities (no. ZYGX2014J023).

## References

- [1] M. Kouhnavard, S. Ikeda, N. A. Ludin et al., "A review of semiconductor materials as sensitizers for quantum dot-sensitized solar cells," *Renewable & Sustainable Energy Reviews*, vol. 37, pp. 397–407, 2014.
- [2] L. Wang, D. Zhao, Z. Su, B. Li, Z. Zhang, and D. Shen, "Enhanced efficiency of polymer/ZnO nanorods hybrid solar cell sensitized by CdS quantum dots," *Journal of the Electrochemical Society*, vol. 158, no. 8, pp. H804–H807, 2011.
- [3] C. H. Yang, A. W. Tang, and F. Tenga, "The solid-state electrochemistry of CdS and Cu(I)-doped cds nanocrystals," *Journal of the Electrochemical Society*, vol. 160, no. 2, pp. H121–H125, 2013.
- [4] C.-H. Chang and Y.-L. Lee, "Chemical bath deposition of CdS quantum dots onto mesoscopic TiO<sub>2</sub> films for application in quantum-dot-sensitized solar cells," *Applied Physics Letters*, vol. 91, no. 5, Article ID 053503, 2007.
- [5] S. Kohtani, A. Kudo, and T. Sakata, "Spectral sensitization of a TiO<sub>2</sub> semiconductor electrode by CdS microcrystals and its photoelectrochemical properties," *Chemical Physics Letters*, vol. 206, no. 1–4, pp. 166–170, 1993.
- [6] W. W. Yu, L. Qu, W. Guo, and X. Peng, "Experimental determination of the extinction coefficient of CdTe, CdSe, and CdS nanocrystals," *Chemistry of Materials*, vol. 15, no. 14, pp. 2854–2860, 2003.
- [7] Y. Chen, Q. Tao, W. Fu et al., "Enhanced photoelectric performance of PbS/CdS quantum dot co-sensitized solar cells via hydrogenated TiO<sub>2</sub> nanorod arrays," *Chemical Communications*, vol. 50, no. 67, pp. 9509–9512C, 2014.
- [8] S. Wang, W. Dong, X. Fang et al., "CdS and CdSe quantum dot co-sensitized nanocrystalline TiO<sub>2</sub> electrode: quantum dot distribution, thickness optimization, and the enhanced photovoltaic performance," *Journal of Power Sources*, vol. 273, pp. 645–653, 2015.
- [9] R. Asahi, T. Morikawa, T. Ohwaki, K. Aoki, and Y. Taga, "Visible-light photocatalysis in nitrogen-doped titanium oxides," *Science*, vol. 293, no. 5528, pp. 269–271, 2001.
- [10] H. Irie, Y. Watanabe, and K. Hashimoto, "Carbon-doped anatase TiO<sub>2</sub> powders as a visible-light sensitive photocatalyst," *Chemistry Letters*, vol. 32, no. 8, pp. 772–773, 2003.
- [11] Q. Zhang, J. Su, X. Zhang, J. Li, A. Zhang, and Y. Gao, "Bi<sub>2</sub>Se<sub>3</sub>/CdS/TiO<sub>2</sub> hybrid photoelectrode and its band-edge levels," *Journal of Alloys and Compounds*, vol. 545, pp. 105–110, 2012.
- [12] X. Chen, L. Liu, P. Y. Yu, and S. S. Mao, "Increasing solar absorption for photocatalysis with black hydrogenated titanium dioxide nanocrystals," *Science*, vol. 331, no. 6018, pp. 746–750, 2011.
- [13] G. Wang, H. Wang, Y. Ling et al., "Hydrogen-treated TiO<sub>2</sub> nanowire arrays for photoelectrochemical water splitting," *Nano Letters*, vol. 11, no. 7, pp. 3026–3033, 2011.
- [14] H. He, K. Yang, N. Wang, F. Luo, and H. Chen, "Hydrogenated TiO<sub>2</sub> film for enhancing photovoltaic properties of solar cells and self-sensitized effect," *Journal of Applied Physics*, vol. 114, no. 21, Article ID 213505, 2013.
- [15] H. Lee, M. Wang, P. Chen et al., "Efficient CdSe quantum dot-sensitized solar cells prepared by an improved successive ionic layer adsorption and reaction process," *Nano Letters*, vol. 9, no. 12, pp. 4221–4227, 2009.
- [16] K. Prabhakar, H. Seo, M. Son, and H. Kim, "CdS quantum dots sensitized TiO<sub>2</sub> photoelectrodes," *Materials Chemistry and Physics*, vol. 117, no. 1, pp. 26–28, 2009.
- [17] M. Grätzel, "Photoelectrochemical cells," *Nature*, vol. 414, no. 6861, pp. 338–344, 2001.
- [18] F. Fabregat-Santiago, G. Garcia-Belmonte, I. Mora-Seró, and J. Bisquert, "Characterization of nanostructured hybrid and organic solar cells by impedance spectroscopy," *Physical Chemistry Chemical Physics*, vol. 13, no. 20, pp. 9083–9118, 2011.
- [19] F. Fabregat-Santiago, J. Bisquert, G. Garcia-Belmonte, G. Boschloo, and A. Hagfeldt, "Influence of electrolyte in transport and recombination in dye-sensitized solar cells studied by impedance spectroscopy," *Solar Energy Materials and Solar Cells*, vol. 87, no. 1–4, pp. 117–131, 2005.
- [20] Q. Wang, J.-E. Moser, and M. Grätzel, "Electrochemical impedance spectroscopic analysis of dye-sensitized solar cells," *Journal of Physical Chemistry B*, vol. 109, no. 31, pp. 14945–14953, 2005.
- [21] S. Zhang, X. Yang, Y. Numata, and L. Han, "Highly efficient dye-sensitized solar cells: progress and future challenges," *Energy and Environmental Science*, vol. 6, no. 6, pp. 1443–1464, 2013.
- [22] T. Miyasaka, "Toward printable sensitized mesoscopic solar cells: light-harvesting management with thin TiO<sub>2</sub> films," *Journal of Physical Chemistry Letters*, vol. 2, no. 3, pp. 262–269, 2011.
- [23] J. Zhao, X. Shen, F. Yan, L. Qiu, S. Lee, and B. Sun, "Solvent-free ionic liquid/poly(ionic liquid) electrolytes for quasi-solid-state dye-sensitized solar cells," *Journal of Materials Chemistry*, vol. 21, no. 20, pp. 7326–7330, 2011.
- [24] A. Zaban, M. Greenshtein, and J. Bisquert, "Determination of the electron lifetime in nanocrystalline dye solar cells by open-circuit voltage decay measurements," *ChemPhysChem*, vol. 4, no. 8, pp. 859–864, 2003.

## Research Article

# Enhancement of Electrochemical Stability about Silicon/Carbon Composite Anode Materials for Lithium Ion Batteries

Wei Xiao, Chang Miao, Xuemin Yan, Qing Sun, and Ping Mei

College of Chemistry and Environmental Engineering, Yangtze University, Jingzhou 434023, China

Correspondence should be addressed to Wei Xiao; [xwylyq2009@gmail.com](mailto:xwylyq2009@gmail.com)

Received 2 December 2014; Revised 19 January 2015; Accepted 19 January 2015

Academic Editor: Jiayu Wan

Copyright © 2015 Wei Xiao et al. This is an open access article distributed under the Creative Commons Attribution License, which permits unrestricted use, distribution, and reproduction in any medium, provided the original work is properly cited.

Silicon/carbon (Si/C) composite anode materials are successfully synthesized by mechanical ball milling followed by pyrolysis method. The structure and morphology of the composite are characterized by X-ray diffraction and scanning electron microscopy and transmission electron microscope, respectively. The results show that the composite is composed of Si, flake graphite, and phenolic resin-pyrolyzed carbon, and Si and flake graphite are enwrapped by phenolic resin-pyrolyzed carbon, which can provide not only a good buffering matrix but also a conductive network. The Si/C composite also shows good electrochemical stability, in which the composite anode material exhibits a high initial charge capacity of  $805.3 \text{ mAh g}^{-1}$  at  $100 \text{ mA g}^{-1}$  and it can still deliver a high charge capacity of  $791.7 \text{ mAh g}^{-1}$  when the current density increases to  $500 \text{ mA g}^{-1}$ . The results indicate that it could be used as a promising anode material for lithium ion batteries.

## 1. Introduction

Rechargeable lithium ion batteries are key components of portable electronic devices and electrical vehicles due to their high energy density, long cycle life, and high power [1–3]. In this area, the anode materials play an important role in lithium ion batteries. Though graphite is now widely used as the commercial anode material, the low theoretical capacity about  $372 \text{ mAh g}^{-1}$  is still an obstacle for the lithium ion batteries to further develop [4, 5]. In this regard, Si has attracted much attention as anode material for its high theoretical capacity about  $4200 \text{ mAh g}^{-1}$  [6, 7]. However, some shortcomings, such as the poor capacity retention resulting from the low intrinsic electronic conductivity, the over three times volume change during the Li insertion and extraction processes and the unstable solid electrolyte interface (SEI), are still the thresholds that prevent the materials from practical application [8–11]. Therefore, various forms of Si-based materials have been explored to overcome these disadvantages, such as limiting the volume change by coating various materials [12, 13], buffering the volume expansion by constructing new frame work for Si grains [14, 15], and synthesizing nanodispersed Si particles to create enough interspace in anode materials by chemical vapor deposition

(CVD) and thermal vapor deposition (TVD) [16, 17]. And carbon coating has been considered as the most effective and feasible method to improve the performance of Si-based materials, which promotes extensive efforts in the development of synthesis methods, such as ball milling, mechanical milling, combination of pyrolysis with mechanical milling, sol-gel, pyrolysis, and CVD/TVD [18, 19]. Among these techniques, the mechanical milling combining with pyrolysis is a flexible and scalable process to prepare Si/C composite material at present. Therefore, the Si/graphite composite materials coated with carbon are prepared via mechanical milling followed by pyrolysis in this work. The obtained Si/C composite used as anode material for lithium ion batteries is studied in respect of structural, morphological, and electrochemical properties. The effect of carbon coating and mechanical milling on the electrochemical performance is also investigated in the paper.

## 2. Experimental

**2.1. Preparation of Si/C Composite.** Silicon/carbon (Si/C) composite was synthesized by mechanical milling followed by pyrolysis. The synthetic procedures can be briefly described as follows: (1) mixing raw materials of 1.00 g nano-Si (>99.9%,

~30 nm, Shuitian Materials Technology Co., Ltd., Shanghai, China), 4.00 g graphite (>99%, ~0.5  $\mu\text{m}$ , Qingdao Tianhe Graphite Co., Ltd., Shandong, China), and 3.85 g phenolic resin by magnetic stirring and ultrasonic treatment, using alcohol as dispersing agent; (2) ball milling for 10 h and drying in the oven at 90°C overnight (denoted as the precursor); (3) pyrolysis at 750°C for 2 h under argon atmosphere.

**2.2. Properties Characterization.** The powder X-ray diffraction (XRD, Rint-2000, Rigaku, Japan) using Cu K $\alpha$  radiation was employed to identify the crystalline phase of the synthesized materials. Thermal analysis of the as-prepared samples was performed on a SDT Q600 TG-DTA (TE, USA) apparatus between room temperature and 1000°C at a heating rate of 10°C min<sup>-1</sup> in argon atmosphere. The morphology of the samples was observed by scanning electron microscope (SEM, JEOL, JSM-5612LV) with an accelerating voltage of 20 kV, and the microstructure of the composite was investigated by transmission electron microscope (TEM, Tecnai G12, 200 kV).

The electrochemical performance was evaluated via a standard Li//LiPF<sub>6</sub> (EC:EMC:DMC = 1:1:1; v/v/v)//Si/C CR2025 coin cell. To fabricate the working electrode, 80 wt.% active materials, 10 wt.% acetylene black, and 10 wt.% poly(vinylidene fluoride) were firstly blended in *N*-methyl pyrrolidinone to obtain homogeneous slurry, and then the slurry was spread uniformly on a copper foil and dried at 120°C for 12 h in the air; the desirable working electrode can be obtained after being cut into round pieces with an area of 1.54 cm<sup>2</sup>. The whole assembling processes of the cell were carried out in a dry argon-filled glove box. The charge-discharge tests of the cell were performed on a Neware battery tester (Neware, Shenzhen) with cut-off voltage of 0.01–2.00 V at room temperature. The electrochemical impedance measurement was performed on a CHI660A electrochemical workstation (Chenhua, Shanghai), in which the impedance spectra were recorded with AC amplitude of 5 mV from 0.01 Hz to 100 kHz.

### 3. Results and Discussion

**3.1. Thermal Analysis of the Precursor.** The TG-DTA curves of the precursor are shown in Figure 1. It can be obviously observed that the TG curve presents three stages of weight loss at 25~260, 260~560, and 560~1000°C, which represent the loss of absorbed water, the decomposition of phenolic resin to form excess phenolic resin-pyrolyzed carbon, and the further evaporation of phenolic resin, respectively. DTA curve displays two distinctly corresponding endothermic peaks, which correspond to the aforementioned first two stages. As for the third stage, the weight loss is not remarkable in Figure 1. It is worthy to note that the change of weight loss becomes insignificant when the pyrolysis temperature is above 750°C. Therefore, in order to obtain desirable Si/C composites, the blended precursor was pyrolyzed at 750°C in this work.

**3.2. Structural Analysis of the Materials.** The XRD patterns of the precursor and Si/C composite material are shown in

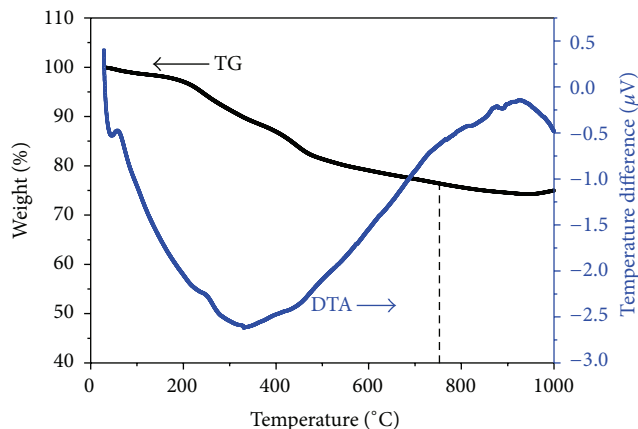


FIGURE 1: TG-DTA curves of the precursor.

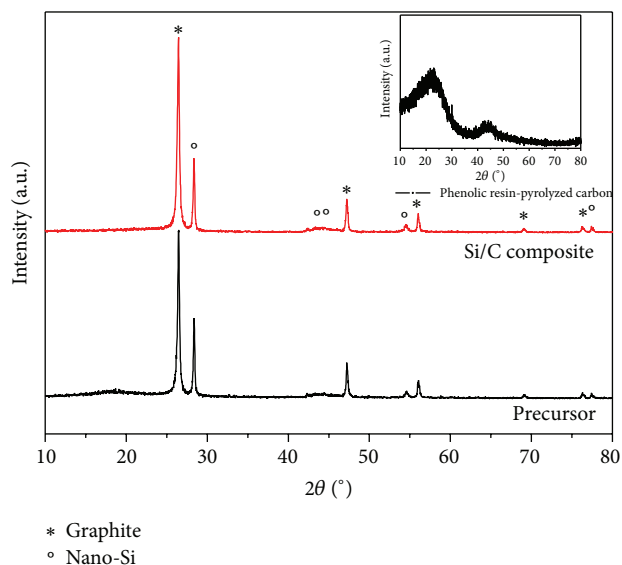


FIGURE 2: X-ray diffraction patterns of the precursor and the Si/C composite.

Figure 2. As demonstrated in Figure 2, both XRD patterns of the precursor and Si/C composite show the diffraction peaks of flake graphite ( $2\theta = 26.6, 42.5, 43.5, 54.7, \text{ and } 77.6^\circ$ , PDF#41-1487) and silicon ( $2\theta = 28.4, 47.3, 56.1, 69.1, \text{ and } 76.4^\circ$ , PDF#27-1407), which corresponds to the (002), (100), (101), (004), and (110) plane of flake graphite and the (111), (220), (311), (400), and (331) plane of Si, respectively [20]. These results indicate that the pyrolysis process would not destroy the basic structure of the composite material. Furthermore, the broadened diffraction peak around  $2\theta = 23^\circ$  comes from the amorphous phenolic resin-pyrolyzed carbon as shown on the upper right corner in Figure 2. The results suggest that no other impurity phase is detected in the composite and the composite is composed of flake graphite, nano-Si, and phenolic resin-pyrolyzed carbon, which can be explained that the desirable composite materials can be successfully prepared by the mechanical milling followed by pyrolysis method.

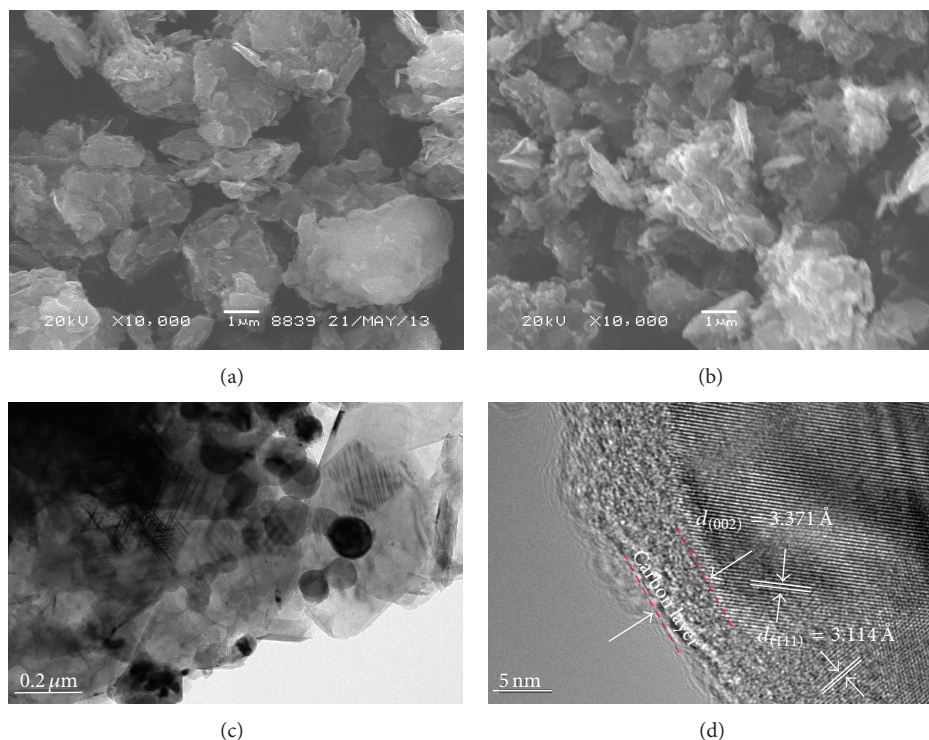


FIGURE 3: SEM images of the precursor (a) and the Si/C composite (b), TEM (c), and HRTEM (d) images of the Si/C composite.

**3.3. Morphology of the Materials.** The morphology of the precursor and the obtained Si/C composite material were observed by SEM as shown in Figures 3(a) and 3(b). The morphology of Si/C material inherits the morphology of the precursor; most of the particles exhibit scaly shape and are micron in dimension. It should be noted that Si/C material is looser than the precursor, which can be mainly attributed to the decomposition of phenolic resin during pyrolysis [21, 22]. Figures 3(c) and 3(d) show the TEM and HRTEM images of the Si/C composite, respectively. It can be obviously observed that the composite particles are composed of flake graphite, nano-Si, and phenolic resin-pyrolyzed carbon, which are in concordance with the results of XRD analysis. Furthermore, the phenolic resin-pyrolyzed carbon is coated on the surface of the composite sphere perfectly, which not only provides a good buffering matrix but also constructs the connection network of flake graphite and Si particles [23].

**3.4. Electrochemical Performance.** The cut-off voltages range of the cells was chosen as 0.01–2.00 V, and the discharge current density is limited at  $100 \text{ mA g}^{-1}$ . The voltage profiles of the Si/C composite for the 1st, 2nd, and 3rd cycle are presented in Figure 4(a), respectively. It can be seen that the first charge capacity (reversible capacity corresponding to lithium extraction) of the composite is about  $805.3 \text{ mAh g}^{-1}$ , and the initial coulombic efficiency is 74.26%, which is a little higher than the value of the previous report [23, 24]. As known to us, the irreversible capacity of the first cycle is mainly attributed to the formation of a solid electrolyte interphase (SEI) film on the surface of electrode at 0.6–0.8 V. It can be also seen from Figure 4(a) that there is a distinct

potential platform below 0.2 V during the first insertion process, which can be assigned to the alloying process of the composite with lithium and the insertion of lithium ions into the carbon host. And the shift of the subsequent discharge curves presented in the following cycles may be ascribed to the typical phase transformation of silicon from crystal to amorphous [23, 25, 26]. Another significant plateau at 0.45 V can also be found in Figure 4(a), which is attributed to the extraction processes of  $\text{Li}^+$  from silicon. The charge-discharge cycling and coulombic efficiency curves of the Si/C composite with and without ball milling at  $100 \text{ mA g}^{-1}$  are shown in Figure 4(b). The coulombic efficiency of the composite with ball milling can quickly achieve a steady value about 98% after only three cycles, which gains much improvement compared to the Si/C composite without ball milling. And the capacity of the composite can maintain above  $500 \text{ mAh g}^{-1}$  after 40 cycles. The results show that ball milling plays a vital role in the cycling performance of the composite, which may be ascribed to the more active points formation by the mechanical activation. In order to further study the electrochemical performance, rate performance is also conducted and the corresponding curves are demonstrated in Figure 4(c). It can be seen from Figure 4(c) that both the first charge capacity and initial coulombic efficiency decrease with increasing current density, in which the first charge capacity of the composite at 100, 200, and  $500 \text{ mA g}^{-1}$  is about 805.3, 797.4, and  $791.7 \text{ mAh g}^{-1}$ , respectively, and the corresponding initial coulombic efficiency is 74.26%, 74.20%, and 74.10%, respectively. The cyclic performance of the Si/C composite at different current densities is also shown in Figure 4(d), and the capacity retention ratio is 89.58%, 79.46%, and

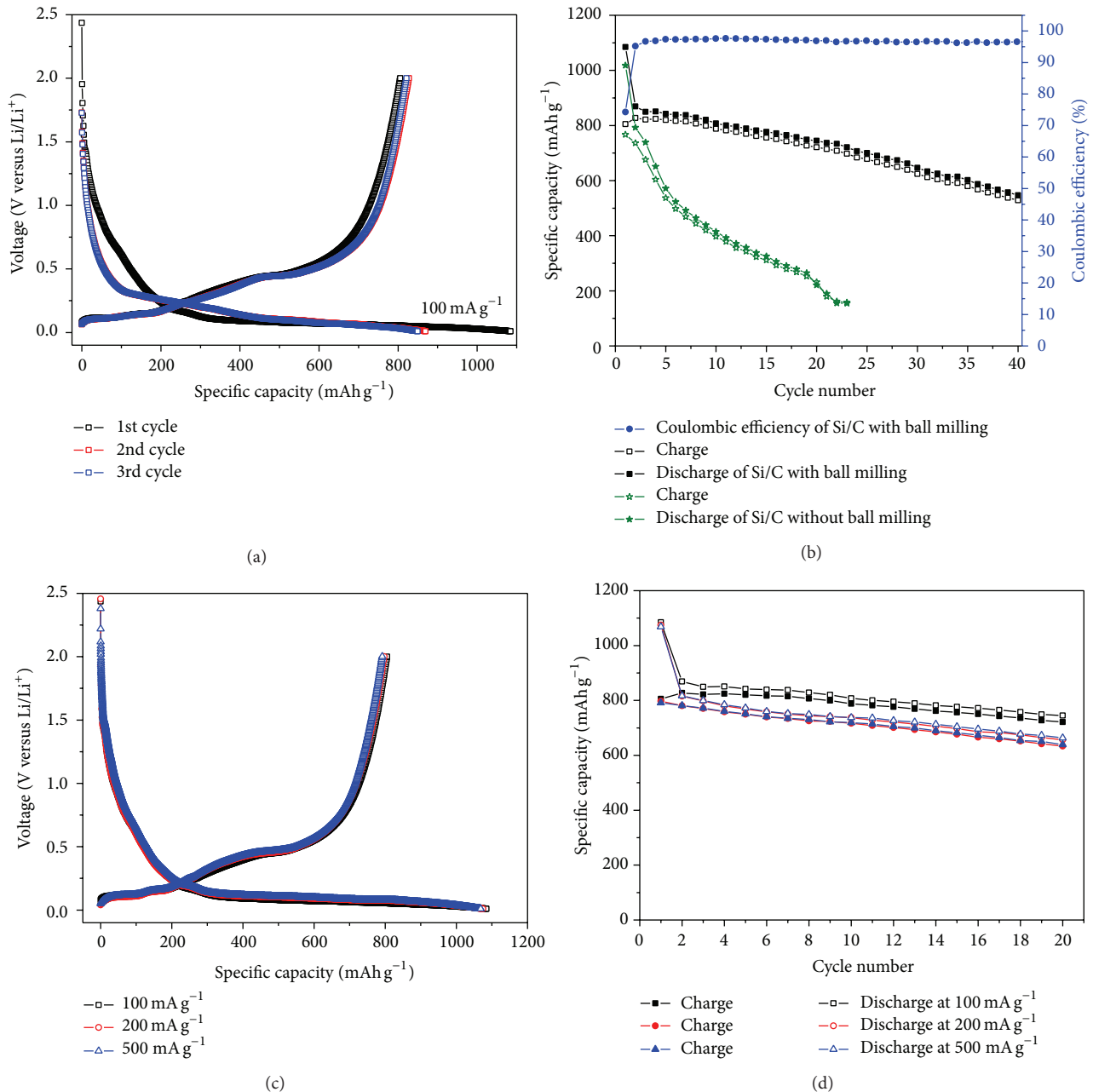


FIGURE 4: (a) The voltage profiles of Si/C composites at 100 mA g<sup>-1</sup>; (b) the charge-discharge cycling curves of the Si/C composite with and without ball milling at 100 mA g<sup>-1</sup>; (c) initial charge-discharge curves of the composites at different rates; (d) cycling curves of the composites at different rates.

80.69% after 20 cycles, respectively. Therefore, there are reasons to believe that the Si/C composite possesses better electrochemical performance, and this is associated with the effective attachment between Si, graphite, and phenolic resin-pyrolyzed carbon, which can provide good electronic conductivity and avoid direct contact between Si particles and the electrolyte to improve the electrochemical stability of the assembled cell.

The electrochemical impedance spectra of the composite anodes after different cycles are shown in Figure 5(a). It can be obviously seen that all plots are composed of a compressed

semicircle in high frequency and an inclined line in low frequency, which are attributed to the charge transfer process and lithium diffusion process, respectively. To investigate the charge-discharge behavior of the electrodes, the pattern in the impedance spectra can be fitted using the equivalent circuit described as  $R_s$  in series with parallel  $(CPE_1 R_{ct})$  and  $W_1$  elements  $\{R_s(CPE_1 R_{ct})W_1\}$  demonstrated in Figure 5(b), in which  $R_s$  is attributed to the ohmic resistance of the electrolyte and electrodes,  $R_{ct}$  represents the charge transfer resistance of electrochemical reactions, and  $CPE_1$  and  $W_1$  are the capacitance of the interface and Warburg

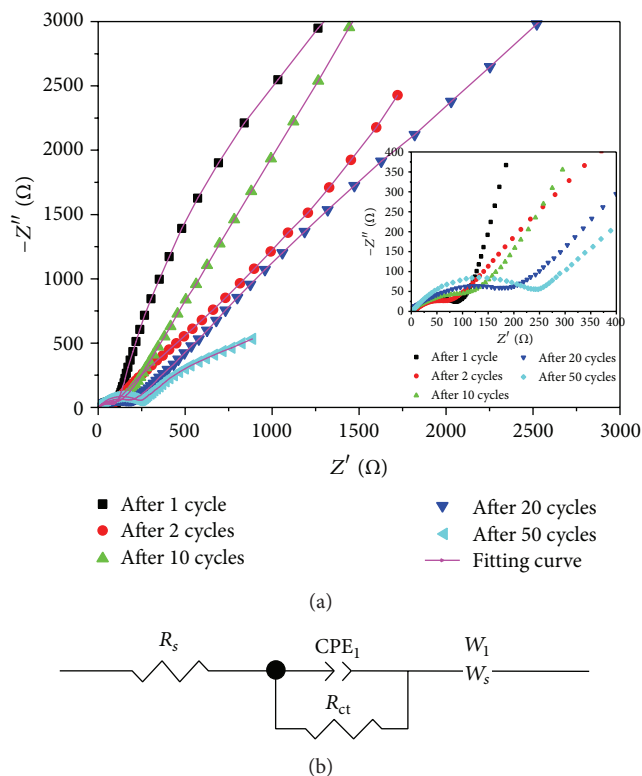


FIGURE 5: EIS curves of Si/C during different cycles (a) and the equivalent circuit for the impedance spectra (b).

diffusion-controlled resistance, respectively [27]. It is obviously observed that the EIS curves shown in Figure 5(a) can be well fitted by the equivalent circuit demonstrated in Figure 5(b). Furthermore, the resistance of  $R_s$ ,  $R_{ct}$ , and  $W_1$  increases obviously in the 20 cycles, which is due to the destruction of the electrode. However, the resistance can remain stable value after 20 cycles, which can be attributed to the buffering of the Si/C composite material to improve the electrochemical stability of the electrodes.

#### 4. Conclusions

Si/C composite anode material was successfully synthesized using the simple mechanical milling followed by pyrolysis method. The particles exhibit scaly shape and are micron in dimension; the phenolic resin-pyrolyzed carbon is coated on the surface of the composite sphere perfectly and constructs the connection network of flake graphite and nano-Si particles in the composite. Therefore, this composite shows good electrochemical performance, in which the composite exhibits not only high specific capacity with high coulombic efficiency in first cycle but also good cycle and rate performance. The primary results indicate that the as-prepared Si/C composite material can be a promising anode material for high energy density and power demanding lithium-ion batteries.

#### Conflict of Interests

The authors declare that there is no conflict of interests regarding the publication of this paper.

#### Acknowledgments

This work has been carried out with the financial support of the National Natural Science Foundation of China under Contract no. 51404038 and Scientific Research and Development Funds of Basic Subject in Yangtze University under Contract no. 2013cjp20.

#### References

- [1] P. G. Bruce, B. Scrosati, and J.-M. Tarascon, "Nanomaterials for rechargeable lithium batteries," *Angewandte Chemie—International Edition*, vol. 47, no. 16, pp. 2930–2946, 2008.
- [2] J. M. Tarascon and M. Armand, "Issues and challenges facing rechargeable lithium batteries," *Nature*, vol. 414, no. 6861, pp. 359–367, 2001.
- [3] M. Armand and J. M. Tarascon, "Building better batteries," *Nature*, vol. 451, no. 7179, pp. 652–657, 2008.
- [4] H. Fujimoto, "Development of efficient carbon anode material for a high-power and long-life lithium ion battery," *Journal of Power Sources*, vol. 195, no. 15, pp. 5019–5024, 2010.
- [5] Y. P. Wu, E. Rahm, and R. Holze, "Carbon anode materials for lithium ion batteries," *Journal of Power Sources*, vol. 114, no. 2, pp. 228–236, 2003.
- [6] J. R. Szczech and S. Jin, "Nanostructured silicon for high capacity lithium battery anodes," *Energy & Environmental Science*, vol. 4, no. 1, pp. 56–72, 2011.
- [7] J. Wang, Y. Chen, and L. Qi, "The development of silicon nanocomposite materials for Li-Ion secondary batteries," *Open Materials Science Journal*, vol. 5, pp. 228–235, 2011.
- [8] Y. Fan, Q. Zhang, C. Lu, Q. Xiao, X. Wang, and B. K. Tay, "High performance carbon nanotube-Si core-shell wires with a rationally structured core for lithium ion battery anodes," *Nanoscale*, vol. 5, no. 4, pp. 1503–1506, 2013.
- [9] J. Xiao, W. Xu, D. Wang et al., "Stabilization of silicon anode for Li-Ion batteries," *Journal of the Electrochemical Society*, vol. 157, no. 10, pp. A1047–A1051, 2010.
- [10] M. N. Obrovac and L. Christensen, "Structural changes in silicon anodes during lithium insertion/extraction," *Electrochemical and Solid-State Letters*, vol. 7, no. 5, pp. A93–A96, 2004.
- [11] J. W. Wang, Y. He, F. Fan et al., "Two-phase electrochemical lithiation in amorphous silicon," *Nano Letters*, vol. 13, no. 2, pp. 709–715, 2013.
- [12] Y. Hwa, W.-S. Kim, S.-H. Hong, and H.-J. Sohn, "High capacity and rate capability of core-shell structured nano-Si/C anode for Li-ion batteries," *Electrochimica Acta*, vol. 71, pp. 201–205, 2012.
- [13] K. Shin, D.-J. Park, H.-S. Lim, Y.-K. Sun, and K.-D. Suh, "Synthesis of silicon/carbon, multi-core/shell microspheres using solution polymerization for a high performance Li ion battery," *Electrochimica Acta*, vol. 58, no. 1, pp. 578–582, 2011.
- [14] J. Nanda, M. K. Datta, J. T. Remillard, A. O'Neill, and P. N. Kumta, "In situ Raman microscopy during discharge of a high capacity silicon-carbon composite Li-ion battery negative electrode," *Electrochemistry Communications*, vol. 11, no. 1, pp. 235–237, 2009.

- [15] J. K. Lee, K. B. Smith, C. M. Hayner, and H. H. Kung, "Silicon nanoparticles-graphene paper composites for Li ion battery anodes," *Chemical Communications*, vol. 46, no. 12, pp. 2025–2027, 2010.
- [16] L.-F. Cui, Y. Yang, C.-M. Hsu, and Y. Cui, "Carbon-silicon core-shell nanowires as high capacity electrode for lithium ion batteries," *Nano Letters*, vol. 9, no. 9, pp. 3370–3374, 2009.
- [17] T. Umeno, K. Fukuda, H. Wang, N. Dimov, T. Iwao, and M. Yoshio, "Novel anode material for lithium-ion batteries: carbon-coated silicon prepared by thermal vapor decomposition," *Chemistry Letters*, vol. 30, no. 11, pp. 1186–1187, 2001.
- [18] U. Kasavajjula, C. Wang, and A. J. Appleby, "Nano- and bulk-silicon-based insertion anodes for lithium-ion secondary cells," *Journal of Power Sources*, vol. 163, no. 2, pp. 1003–1039, 2007.
- [19] M. K. Datta and P. N. Kumta, "Silicon, graphite and resin based hard carbon nanocomposite anodes for lithium ion batteries," *Journal of Power Sources*, vol. 165, no. 1, pp. 368–378, 2007.
- [20] M. Su, Z. Wang, H. Guo et al., "Enhancement of the cyclability of a Si/Graphite@Graphene composite as anode for Lithium-ion batteries," *Electrochimica Acta*, vol. 116, pp. 230–236, 2014.
- [21] J. Bae, "Fabrication of carbon microcapsules containing silicon nanoparticles for anode in lithium ion battery," *Colloid and Polymer Science*, vol. 289, no. 11, pp. 1233–1241, 2011.
- [22] P. Gao, J. Fu, J. Yang et al., "Microporous carbon coated silicon core/shell nanocomposite via in situ polymerization for advanced Li-ion battery anode material," *Physical Chemistry Chemical Physics*, vol. 11, no. 47, pp. 11101–11105, 2009.
- [23] J. Lai, H. Guo, Z. Wang et al., "Preparation and characterization of flake graphite/silicon/carbon spherical composite as anode materials for lithium-ion batteries," *Journal of Alloys and Compounds*, vol. 530, pp. 30–35, 2012.
- [24] M. Su, Z. Wang, H. Guo et al., "Enhanced cycling performance of Si/C composite prepared by spray-drying as anode for Li-ion batteries," *Powder Technology*, vol. 249, pp. 105–109, 2013.
- [25] P. Limthongkul, Y.-I. Jang, N. J. Dudney, and Y.-M. Chiang, "Electrochemically-driven solid-state amorphization in lithium-silicon alloys and implications for lithium storage," *Acta Materialia*, vol. 51, no. 4, pp. 1103–1113, 2003.
- [26] Y. Liu, K. Hanai, J. Yang, N. Imanishi, A. Hirano, and Y. Takeda, "Morphology-stable silicon-based composite for Li-intercalation," *Solid State Ionics*, vol. 168, no. 1-2, pp. 61–68, 2004.
- [27] W. Xiao, X. Li, H. Guo, Z. Wang, Y. Zhang, and X. Zhang, "Preparation of core-shell structural single ionic conductor  $\text{SiO}_2$ @Li+ and its application in PVDF-HFP-based composite polymer electrolyte," *Electrochimica Acta*, vol. 85, pp. 612–621, 2012.

## Research Article

# Cauliflower-Like $\text{Co}_3\text{O}_4$ /Three-Dimensional Graphene Composite for High Performance Supercapacitor Applications

Huili Liu,<sup>1,2</sup> Xinglong Gou,<sup>2</sup> Yi Wang,<sup>1</sup> Xuan Du,<sup>1</sup> Can Quan,<sup>3</sup> and Tao Qi<sup>1</sup>

<sup>1</sup>National Engineering Laboratory for Hydrometallurgical Cleaner Production Technology, Institute of Process Engineering, Chinese Academy of Sciences, Beijing 100190, China

<sup>2</sup>College of Chemistry and Chemical Engineering, China West Normal University, 1 Shida Road, Nanchong 637000, China

<sup>3</sup>Division of Chemistry, National Institute of Metrology, Beijing 100013, China

Correspondence should be addressed to Yi Wang; wangyi@ipe.ac.cn and Can Quan; superfluidcan@hotmail.com

Received 5 December 2014; Accepted 11 February 2015

Academic Editor: Jiayu Wan

Copyright © 2015 Huili Liu et al. This is an open access article distributed under the Creative Commons Attribution License, which permits unrestricted use, distribution, and reproduction in any medium, provided the original work is properly cited.

Cauliflower-like  $\text{Co}_3\text{O}_4$ /three-dimensional (3D) graphene nanocomposite material was synthesized by a facile two-step synthesis route (heat reduction of graphite oxide (GO) and hydrothermal synthesis of  $\text{Co}_3\text{O}_4$ ). The phase composition, morphology, and structure of the as-obtained products were characterized by scanning electron microscopy (SEM), transmission electron microscope (TEM), and X-ray diffraction (XRD). Electrochemical properties as supercapacitor electrode materials were systematically investigated by cyclic voltammetry (CV) and constant current charge-discharge tests. It was found that the  $\text{Co}_3\text{O}_4$ /3D graphene composite showed a maximum specific capacitance of  $863 \text{ F g}^{-1}$ , which was obtained by means of CVs at a scan rate of  $1 \text{ mV s}^{-1}$  in 6 M KOH aqueous solution. Moreover, the composite exhibited improved cycling stability after 1,000 cycles. The good supercapacitor performance is ascribed to the combination of 3D graphene and cauliflower-like  $\text{Co}_3\text{O}_4$ , which leads to a strong synergistic effect to remarkably boost the utilization ratio of  $\text{Co}_3\text{O}_4$  and graphene for high capacitance.

## 1. Introduction

With the impending energy crisis, the concerns about the environment are increasing. The research on alternative energy conversion and storage systems which have high efficiency, low cost, and environmental benignity is urgently called for. Supercapacitors, also known as electrochemical capacitors or ultracapacitors, have been intensively investigated in the fields of energy storage and conversion [1, 2]. Compared with the conventional capacitors and secondary batteries, supercapacitors can provide high power density, strong cycle stability, and remarkable pulse charge-discharge properties [1–5]. They are being employed in different applications [1, 6–8], such as mobile electronic devices, back-up power supplies, and hybrid electric vehicles. The charge-storage mechanism in supercapacitor is usually electrical double-layer and Faradic capacitor [7, 9]. The electrical double-layer capacitor (EDLC) roots in charge separation at

the electrode/solution interface, whereas the Faradic pseudo-capacitance arises from the reversible redox reactions occurring within the supercapacitor electrode material [10, 11]. As the core component of supercapacitors, electrode material plays an important role in determining the performance of electrochemical capacitors. Recently, tremendous attention has been focused on the development of new materials for supercapacitor electrodes with higher specific capacitance and better cyclic life whilst using environmentally benign materials in easily processable ways.

Among the major materials studied for pseudo-capacitor electrodes, transition metal oxides, such as  $\text{RuO}_2$  [12],  $\text{InO}_2$  [13],  $\text{NiO}$  [14],  $\text{MnO}_2$  [15],  $\text{Co}_3\text{O}_4$  [16, 17], and  $\text{SnO}_2$  [18], have attracted much attention due to their high theoretical capacities and promising potential.  $\text{RuO}_2$  is known as an ideal electrode material for supercapacitors, which shows outstanding electrochemical properties. In some reports, the specific capacitance (SC) of  $\text{RuO}_2$ , which has a higher

conductivity than carbon materials and remarkable stability, shows as high as 720–768 F g<sup>-1</sup> [19, 20]. However, the high cost and toxic nature of ruthenium substantially limits its commercial application [21]. Hence, the relatively inexpensive metal oxides have been studied widely. Among them, cobalt oxide is considered as a promising electrode material for supercapacitors due to its relatively low cost, well-defined redox behavior, ultrahigh theoretical SC (~3560 F g<sup>-1</sup>), and environmental friendliness [22, 23]. For instance, it has been reported that the CoO<sub>x</sub> xerogels thermally treated at 150°C showed a good capacitive behavior with a SC value of 291 F g<sup>-1</sup> [24]. Tummala et al. [7] have synthesized nanostructured Co<sub>3</sub>O<sub>4</sub> by plasma spray technique and studied its capacitance properties. The results showed a high SC value of 162 F g<sup>-1</sup> in 6 M KOH electrolyte.

Graphene, as a new carbon material, has attracted much attention since it was isolated from layer-by-layer graphite in 2004 [25]. It is a promising electrode candidate for EDLCs due to its superb characteristics including the excellent mechanical strength and chemical stability, high electrical and thermal conductivity, and large surface area (a theoretical value of 2630 m<sup>2</sup> g<sup>-1</sup>) [25]. But the serious agglomeration and restacking between individual graphene sheets result in limited surface utilization percentage and a lower capacitance than the anticipated value [26]. In our recent work [27, 28], three-dimensional (3D) graphene (strictly speaking, it should be reduced graphene oxide (RGO), but it is still called graphene here for convenience) was acquired by heat reduction of graphite oxide in vacuum, which has a higher specific surface area (487 m<sup>2</sup> g<sup>-1</sup>). Different from Dong's work [29], it has a predominant mesoporosity which centers at 4 nm, and these mesopores can provide a high specific surface area while allowing good mass transport in an electrode process [30].

Recently, many researchers have constructed a graphene-based metal oxide composite structure [17, 31–34]. It was found that these composites showed improved performance with higher electron transport rate, electrolyte contact area, and structural stability. It can be attributed to the special composite structure in which metal oxides are attached on the surface or intercalated into the interlayer of large patches of graphene [31]. Yan et al. [17] reported that graphene nanosheet (GNS)/Co<sub>3</sub>O<sub>4</sub> composite has a maximum specific capacitance of 243.2 F g<sup>-1</sup> at a scan rate of 10 mV s<sup>-1</sup> in 6 M KOH aqueous solution. However, the composite of 3D graphene which was reported in our previous work [27] and Co<sub>3</sub>O<sub>4</sub> has never been investigated so far. Herein, a facile hydrothermal strategy was proposed to deposit cauliflower-like nanostructured Co<sub>3</sub>O<sub>4</sub> on 3D graphene nanosheets. Cyclic voltammetry (CV) and galvanostatic charge-discharge measurements were used to assess the electrochemical properties of the Co<sub>3</sub>O<sub>4</sub>/3D graphene composite in KOH solutions.

## 2. Experimental

**2.1. Materials Preparation.** In this study, deionized water was used throughout. Cobalt nitrate hexahydrate

(Co(NO<sub>3</sub>)<sub>2</sub>·6H<sub>2</sub>O), ammonia (37%, NH<sub>3</sub>·H<sub>2</sub>O) and potassium hydroxide (KOH) were obtained from Xilong Chemical Engineering Co., Ltd. Hydrochloric acid (37%) and ethanol were supplied by Chemical Plant of Beijing. All the reagents used in this experiment were of analytical grade and without further purification.

Graphene oxide was prepared from nature graphite by a modified Hummers' method. 3D graphene material was obtained by reducing graphite oxide powder in a glass bottle under vacuum followed by heating to 250°C from room temperature [27].

Co<sub>3</sub>O<sub>4</sub>/3D graphene composite was synthesized as follows. First, 15 mg of 3D graphene was dispersed in 15 mL ethanol with the assistance of ultrasonication for 60 min. Then, 0.5 mmol Co(NO<sub>3</sub>)<sub>2</sub>·6H<sub>2</sub>O and 34 μL of 37% ammonia were added to the 3D graphene suspension simultaneously. The as-obtained mixture was magnetically stirred for 20 min. After that, the above suspension was loaded into a 25 mL of Teflon-lined stainless steel autoclave and heated at 170°C for 5 h. The obtained black products were washed by centrifugation for several times using ethanol and deionized water to remove excess ions and then dried in a vacuum oven at 60°C. Afterwards, the material was calcined at 350°C for 3 h in air and then cooled to room temperature. For comparison, Co<sub>3</sub>O<sub>4</sub> was also prepared by the same steps without the addition of 3D graphene.

**2.2. Characterization Methods.** The crystallographic structures of the samples were determined by X-ray diffraction system (XRD, X<sup>3</sup> Pert-PRO MPD) equipped with Cu K<sub>α</sub> (λ = 1.5406 Å) radiation. The morphological analysis was conducted using scanning electron microscope (SEM, JEOL JSM-6700F) and transmission electron microscope (TEM, JEOL JEM-2011, 200 kV). The specific surface area and pore volume of the samples were determined by analyzing the standard nitrogen adsorption isotherm measured at 77 K. An electrochemical workstation system (CHI760D, Chenhua, Shanghai) was employed to study the electrochemical properties. The electrodes were fabricated by mixing 80 wt% active materials, 15 wt% acetylene black, and 5 wt% polyvinylidene fluoride (PVDF) as binder. The mixtures were well blended using alcohol, coated the paste onto nickel foam current collectors (1 cm × 1 cm), were dried at 100°C for 10 h, and were pressed under 20 MPa for 3–5 min. Each electrode contains 2–3 mg active materials. A conventional three-electrode system was employed to investigate the capacitive behaviors. Platinum foil and Hg/HgO (1 M KOH aqueous solution) electrodes were used as the counter and reference electrodes, respectively.

## 3. Results and Discussion

**3.1. Structure and Morphology of the Samples.** The XRD patterns of 3D graphene, Co<sub>3</sub>O<sub>4</sub>, and the as-prepared composite before and after calcination were shown in Figure 1. For 3D graphene, a broad peak was observed at 25.6°, which is attributed to the C (002) plane [31, 35]. The main peaks in the XRD pattern of pure Co<sub>3</sub>O<sub>4</sub> (JCPDS, number 42-1467) are located at 19.0, 31.3, 36.8, 44.8, 59.4, and 65.3°, which are

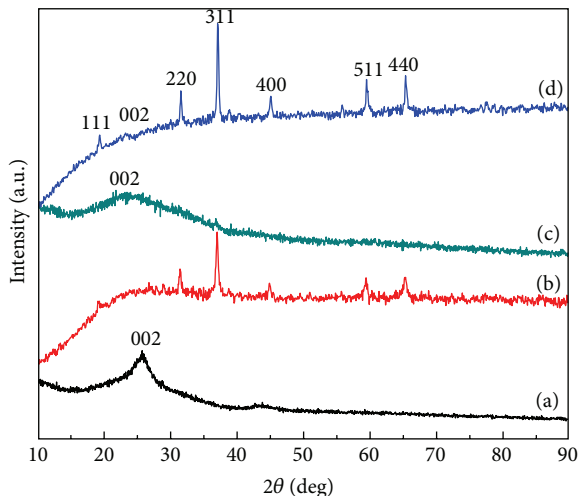
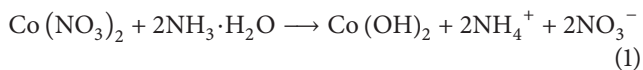


FIGURE 1: XRD patterns of (a) 3D graphene, (b)  $\text{Co}_3\text{O}_4$ , (c) the composite without calcination treatment, and (d) the composite after calcination treatment.

assigned to the crystal planes of (111), (220), (311), (400), (511), and (440) [36]. From Figure 1(c), it can be found that the XRD pattern of the as-prepared composite before calcination does not show any other peak except a broad hump at  $2\theta$  of about  $25.6^\circ$  which is attributed to the diffraction peak of C (002) in 3D graphene [35]. However, several peaks appear at  $2\theta$  of around  $19^\circ$ ,  $31^\circ$ ,  $37^\circ$ ,  $45^\circ$ ,  $59^\circ$ , and  $65^\circ$  obviously in the XRD pattern after calcination. These diffraction peaks are assigned to the crystal planes of (111), (220), (311), (400), (511), and (440), which agree with the typical spinel  $\text{Co}_3\text{O}_4$  [36]. Thus, the chemical reactions in the synthetic process are supposed as follows:



The absence of diffraction peaks of  $\text{Co}(\text{OH})_2$  in Figure 1(c) may result from the amorphous state of  $\text{Co}(\text{OH})_2$ . It is inferred that the composite before calcination consists of  $\text{Co}(\text{OH})_2$  and graphene.

Additionally, from the XRD pattern of the composite after calcination, the characteristic peak of 3D graphene for C (002) is also found. Based on these results, the as-obtained calcinate material can be undoubtedly identified as  $\text{Co}_3\text{O}_4/3\text{D}$  graphene composite. Moreover, it is notable that the C (002) peaks in Figures 1(c) and 1(d) shift toward left as compared to that in Figure 1(a), which indicates that  $\text{Co}(\text{OH})_2$  and  $\text{Co}_3\text{O}_4$  may lead to the increase of the unit cell volume of graphene because the shift of entire diffraction peaks toward lower  $2\theta$  usually suggests the increase of unit cell volume.

The morphology of the as-prepared materials was investigated by SEM, as shown in Figure 2. The graphene material has a 3D structure composed of homogeneous

micrometer-sized flakes (Figure 2(a)). Moreover, according to our previous work [27], the 3D graphene material has mesoporosity centered at 4 nm, demonstrating that it belongs to mesoporous materials. Figure 2(b) shows the SEM image of the composite before calcination (i.e., the precursor of  $\text{Co}_3\text{O}_4/3\text{D}$  graphene composite). It can be seen that the graphene skeleton maintains structural integrity except that the  $\text{Co}_3\text{O}_4$  particles are distributed over the graphene surface. After the calcination treatment, it seems that the morphology and structure are similar to those of the precursor of the composite (Figure 2(c)). The high-magnification SEM image in Figure 2(d) reveals that many small  $\text{Co}_3\text{O}_4$  granules agglomerated together to form some big circular particles with nonuniform diameters from 50 to 250 nm. However, from Figures 2(e) and 2(f), it is clearly seen that, without the addition of 3D graphene,  $\text{Co}_3\text{O}_4$  and its precursor display cubic morphology, and these particles have a size about 50–100 nm and were stacked irregularly. It indicates that the morphology of  $\text{Co}_3\text{O}_4$  in the composite material is different from that of pure  $\text{Co}_3\text{O}_4$ . This may be because of the effects of the electrostatic adsorption and other chemical bonds between the oxygen-containing functional groups on the surface of 3D graphene and the precursor of  $\text{Co}_3\text{O}_4$ .

TEM images of  $\text{Co}_3\text{O}_4$  and  $\text{Co}_3\text{O}_4/3\text{D}$  graphene composite are shown in Figure 3. Figures 3(a) and 3(b) display the TEM images of pure  $\text{Co}_3\text{O}_4$  with different magnification. It can be found that the pure  $\text{Co}_3\text{O}_4$  sample is composed of a great deal of irregular cubic particles. However, Figure 3(c) reveals that, in the  $\text{Co}_3\text{O}_4/3\text{D}$  graphene composite, many nearly spherical  $\text{Co}_3\text{O}_4$  particles are attached onto 3D graphene nanosheets, which is similar to the results of SEM. Furthermore, it can be seen that the  $\text{Co}_3\text{O}_4$  cubic particles with a size about 50–100 nanometers are complete and solid from the inset of Figure 3(a). However, from the high magnification TEM image of  $\text{Co}_3\text{O}_4/3\text{D}$  graphene composite shown in Figure 3(d), it can be found that the big spherical  $\text{Co}_3\text{O}_4$  particles in the composite are composed of numerous assembled nanoparticles with a size of 10–25 nanometers, and these small nanoparticles assemble together to display cauliflower-like morphology. This can lead to abundant pore structures, which is beneficial to the electrochemical utilization of metal oxides and the passing of the ions in the electrolyte. Additionally, the HRTEM image of the composite is presented in the inset of Figure 3(d). The  $\text{Co}_3\text{O}_4$  exhibits high crystallinity and the lattice spacing of 0.26 nm is corresponding to the interspacing of the (311) planes [35].

Nitrogen isotherms of  $\text{Co}_3\text{O}_4$  and  $\text{Co}_3\text{O}_4/3\text{D}$  graphene composite are presented in Figure 4. It is interesting to see that the composite adsorbs much more  $\text{N}_2$  than pure  $\text{Co}_3\text{O}_4$ . It suggests that the structural characteristics change greatly after the addition of 3D graphene. The BET surface area increases from 0.111 to  $69.7 \text{ m}^2 \text{ g}^{-1}$  while the pore volume increases from 0.0016 to  $0.17 \text{ cc g}^{-1}$ . This is the normal sequence since 3D graphene possesses a large specific surface area and pore volume, and the cauliflower-like morphology of  $\text{Co}_3\text{O}_4$  in the composite further contributes to the surface area and pore volume.

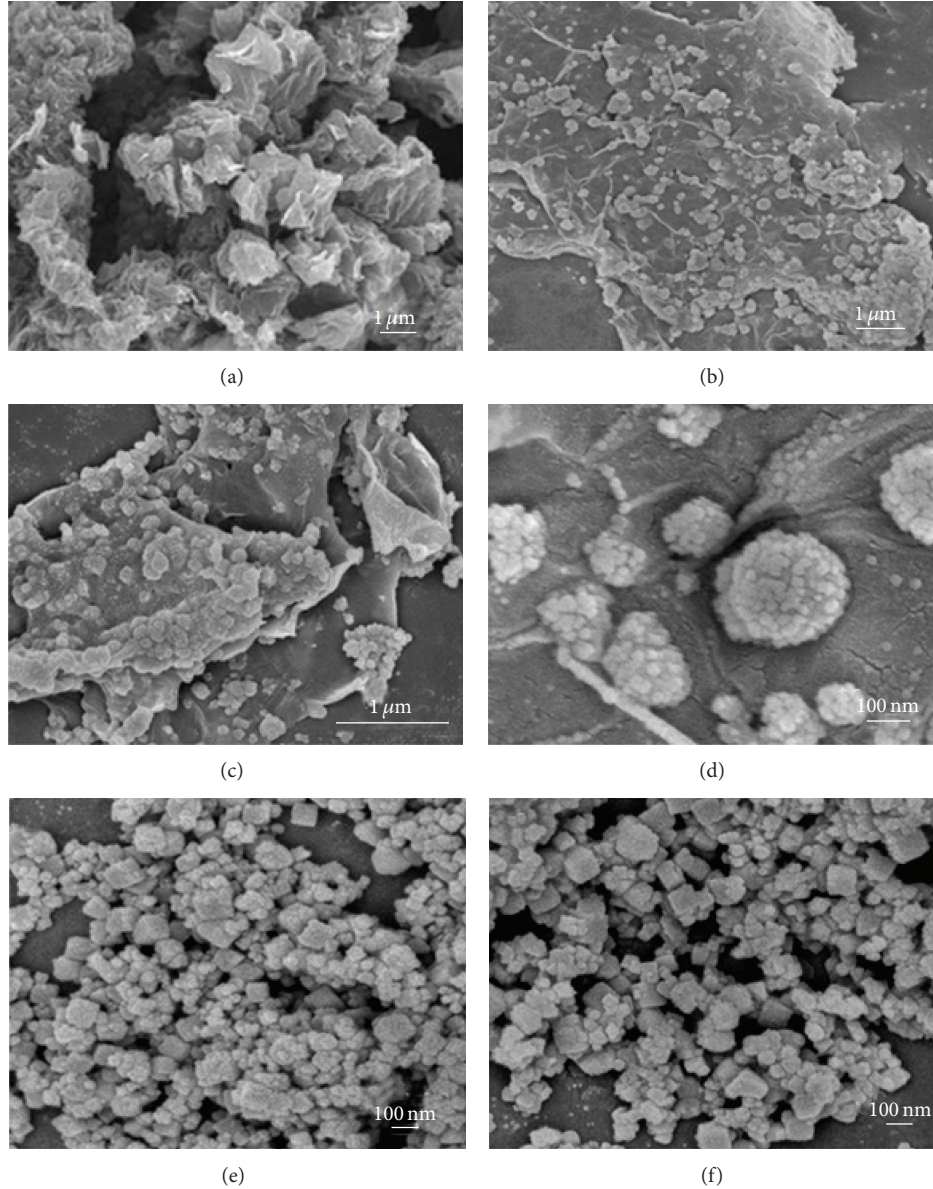


FIGURE 2: SEM images of (a) 3D graphene, (b) the precursor of  $\text{Co}_3\text{O}_4$ /3D graphene composite,  $\text{Co}_3\text{O}_4$ /3D graphene composite with (c) low and (d) high magnification, and (e) the precursor of  $\text{Co}_3\text{O}_4$  and (f)  $\text{Co}_3\text{O}_4$ .

**3.2. Electrochemical Properties.** For potential supercapacitor applications, the capacitor behaviors of the electrodes were examined.

**3.2.1. Cyclic Voltammetry (CV).** Figure 5(a) displays the CV curves of  $\text{Co}_3\text{O}_4$ /3D graphene composite,  $\text{Co}_3\text{O}_4$ , and 3D graphene at a scan rate of  $10 \text{ mV s}^{-1}$  in 1 M KOH electrolyte within the potential window of  $-0.2$ – $0.5 \text{ V}$ . Evidently, the area surrounded by the CV curve is dramatically enhanced by the introduction of  $\text{Co}_3\text{O}_4$  nanoparticles onto 3D graphene sheets as shown in Figure 5(a). This result indicates a large specific capacitance associated with the composite electrode. The CV curves are different from the ideal rectangular shape of the typical electric double-layer capacitance. Unlike 3D

graphene, two pairs of redox reaction peaks are visible in the CV curve of the composite, which can be ascribed to the redox process of  $\text{Co}_3\text{O}_4$ , suggesting that the capacitance mainly results from the pseudocapacitance of  $\text{Co}_3\text{O}_4$ . The mechanism of electrochemical reactions of  $\text{Co}_3\text{O}_4$  in alkaline electrolyte can be expressed as the following equations [36]:



The SC of the electrode, based on CV curves, can be calculated as

$$C = \frac{\left( \int IdV \right)}{vmV}, \quad (5)$$

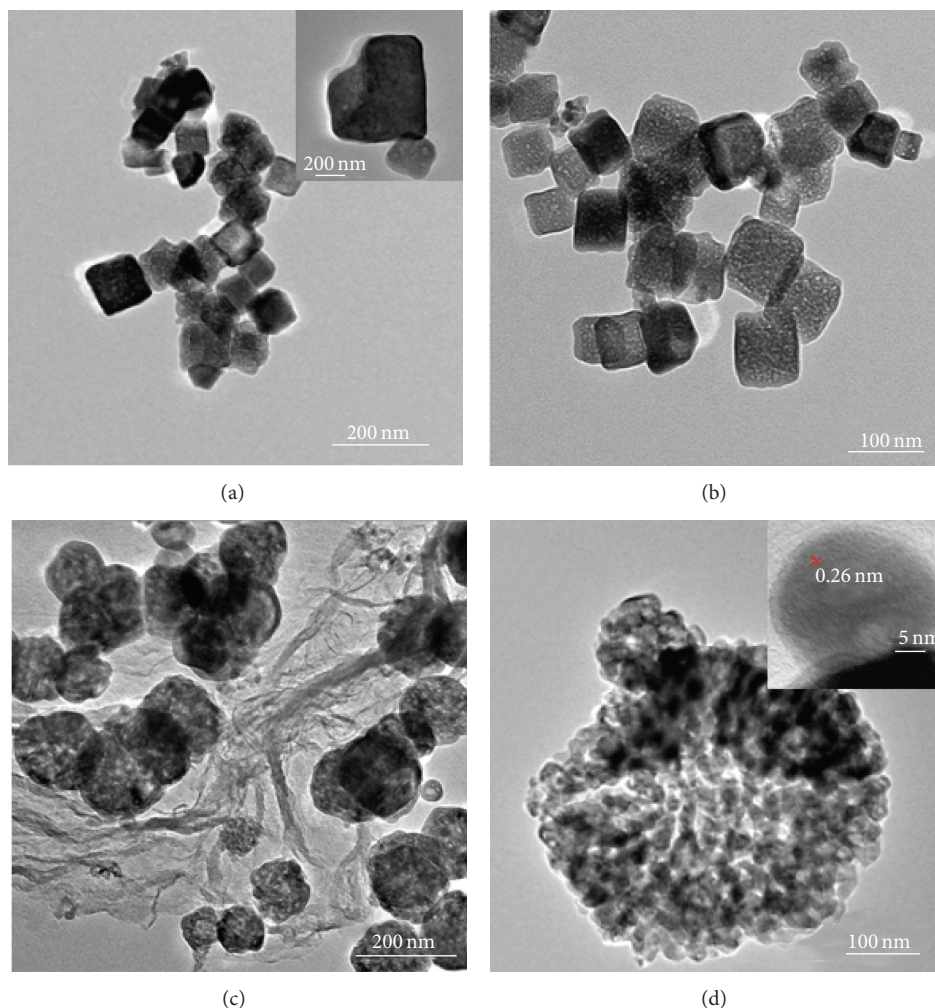


FIGURE 3: TEM images of  $\text{Co}_3\text{O}_4$  with (a) low and (b) high magnification and  $\text{Co}_3\text{O}_4/3\text{D}$  graphene composite with (c) low and (d) high magnification. Inset: high resolution TEM (HRTEM) images.

where  $C$  is the SC of electroactive materials ( $\text{F g}^{-1}$ ),  $I$  is the response current (A),  $V$  is the potential (V),  $\nu$  is the potential scan rate ( $\text{V s}^{-1}$ ), and  $m$  is the mass of the electrode materials (g). According to (5), the SCs of the  $\text{Co}_3\text{O}_4/3\text{D}$  graphene composite,  $\text{Co}_3\text{O}_4$ , and 3D graphene electrodes are calculated to be about 457, 134, and  $97 \text{ F/g}$  at a scan rate of  $10 \text{ mV s}^{-1}$ , respectively. If the SCs are represented by volumetric capacitance, these values are 965, 335, and  $103 \text{ F/cm}^3$ , respectively. Clearly, the SC of the composite is not simple sum of  $\text{Co}_3\text{O}_4$  and 3D graphene but significantly larger than expected. Moreover, the SC value is much higher than that of a  $\text{Co}_3\text{O}_4/\text{reduced graphene oxide}$  scrolled structure ( $163.8 \text{ F/g}$ ) reported recently [31]. The desirable performance could be attributed to the synergistic effect between graphene sheets and  $\text{Co}_3\text{O}_4$  nanoparticles in the nanocomposite [37]. This effect may be associated with the fact that conductive graphene is hydrophobic, while  $\text{Co}_3\text{O}_4$  is hydrophilic but has poor conductivity. It is very likely that  $\text{Co}_3\text{O}_4$  increases the graphene hydrophilicity for significantly increased utilization of the porous electrode and

the conductive graphene enhances the charge transfer rate of  $\text{Co}_3\text{O}_4$  for higher pseudocapacitance. Furthermore, the large specific surface area and pore volume resulting from the cauliflower-like morphology of  $\text{Co}_3\text{O}_4$  in the composite may also increase the utilization of  $\text{Co}_3\text{O}_4$  and thus further enhance the pseudocapacitance. These factors result in a much larger SC value of the composite than the sum of that of 3D graphene and  $\text{Co}_3\text{O}_4$ . Additionally, as compared to two-dimensional (2D) graphene which has been reported [38], 3D graphene has a much higher specific surface area ( $487 \text{ m}^2 \text{ g}^{-1}$ ) and larger pore volume ( $1.04 \text{ cc g}^{-1}$ ) [27]. The 3D graphene has predominant mesoporosity which centers at 4 nm, which is in favor of improving the electrochemical accessibility of electrolyte ions and providing preferable EDLCs [30]. Both the pseudocapacitance derived from the cauliflower-like  $\text{Co}_3\text{O}_4$  and the superior surface and pore properties of 3D graphene contribute to the high capacitance.

Figure 5(b) shows the variation of the calculated SC values of  $\text{Co}_3\text{O}_4/3\text{D}$  graphene composite as a function of scan rates in different concentration KOH electrolytes. Obviously,

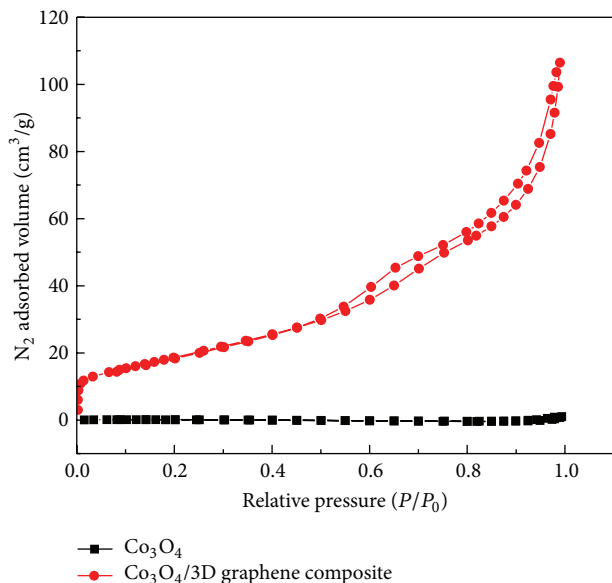


FIGURE 4:  $N_2$  adsorption-desorption isotherms of  $Co_3O_4$  and  $Co_3O_4/3D$  graphene composite.

the SC values of the composite decrease gradually with the increase of scan rate. This may be because, at high scan rates, diffusion limits the movement of electrolyte ions due to the time constraint, and only the outer active surface is utilized for charge storage. At lower scan rates, however, all the active surface area can be utilized for charge storage and the electrochemical utilization of  $Co_3O_4$  [39]. As shown in Figure 5(b), 6 M electrolyte provided the largest SC values. The maximum SC value is  $863 \text{ F g}^{-1}$  in 6 M KOH electrolyte at a scan rate of  $1 \text{ mV s}^{-1}$ . According to the equations of the electrochemical reactions of  $Co_3O_4$  in alkaline electrolyte, there is  $OH^-$  in the reactions. Thus, a high concentration of hydroxyl ions is in favor of increasing the reaction rate. This results in the largest SC value in 6 M KOH solution.

**3.2.2. Galvanostatic Charge-Discharge Measurement.** Furthermore, galvanostatic charge-discharge measurement was utilized to study the capacitor performance of the as-prepared samples.

Figure 6 depicts the charge-discharge behaviors of  $Co_3O_4$ , 3D graphene, and the  $Co_3O_4/3D$  graphene composite electrodes between 0 and 0.5 V at a constant current density of  $5 \text{ A g}^{-1}$  in 1 M KOH aqueous solution. From the charge-discharge curves of 3D graphene, it is evidently seen that the voltage decreases linearly along the discharge time, which shows an ideal double-layer capacitive behavior. However, the discharge curve of  $Co_3O_4/3D$  graphene composite consists of a slow potential drop from 0.5 to 0.2 V and a sudden potential decay from 0.2 to 0 V. The latter indicates short charge/discharge duration, which is a pure double-layer capacitance behavior from the charge separation at the electrode/electrolyte interface. However, the former is a typical pseudocapacitance behavior, caused by electrochemical adsorption/desorption or a redox reaction

at the electrode/electrolyte interface [40]. Usually, Faradaic redox reaction is accompanied by the double-layer charge-discharge process, and thus the combination of electric double-layer capacitance and Faradaic pseudocapacitance is responsible for the longer charge/discharge duration [17].

From the discharge curves, SC could also be calculated using the following equation:

$$C = \frac{I\Delta t}{m\Delta V}, \quad (6)$$

where  $C$  is the SC of the active materials ( $\text{F g}^{-1}$ ),  $I$ ,  $\Delta t$ ,  $\Delta V$ , and  $m$  are constant discharge current (A), discharge time (s), the voltage change after a full discharge (V), and the mass of the active material (g), respectively [41]. The SC values calculated from the galvanostatic charge and discharge curves are 40, 46, and  $337 \text{ F g}^{-1}$  for 3D graphene,  $Co_3O_4$ , and the composite, respectively, which are similar to the trend of those calculated from CVs. A larger specific capacitance value of  $402 \text{ F g}^{-1}$  for the composite is obtained at  $0.5 \text{ A g}^{-1}$ . The much larger SC value of the composite than the sum of that of graphene and pure  $Co_3O_4$  further proves that the combination of 3D graphene and cauliflower-like  $Co_3O_4$  is very beneficial to improving the supercapacitor performance.

Subsequently, the galvanostatic charge-discharge properties of the composite are investigated with different current density in different concentration of KOH electrolytes. The SC values are calculated in accordance with (6) and listed in Table 1. It is found that the SC of the electrode based on the as-prepared composite reached a maximum value of  $522 \text{ F g}^{-1}$  in 6 M KOH electrolyte at the current density of  $0.5 \text{ A g}^{-1}$ . The results are similar to the results obtained from the CVs, further indicating that a high concentration of hydroxyl ions is in favor of increasing the reaction rate.

To investigate the cycling performance of the  $Co_3O_4/3D$  graphene composite, the charge-discharge tests were performed at  $2 \text{ A g}^{-1}$  for 1,000 cycles. Figure 7 shows the results of cycling stability measurement. After 1,000 cycles, the specific capacitance of the  $Co_3O_4/3D$  graphene composite decreased apparently. An initial total capacitance of 75% was retained after the 1000th discharge cycle. The decay of capacitance can be ascribed to the increased impedance with increasing number of cycles, and it is inferred that the increased impedance could be due to fatigue of the active material during cycling [7]. As compared to some nanostructured  $Co_3O_4$  electrodes reported recently [7], the retention rate of capacitance of the  $Co_3O_4/3D$  graphene composite was improved a little, which may be attributed to the special structure of 3D graphene and cauliflower-like  $Co_3O_4$ . During cycling, the three-dimensional nanoporous structure of 3D graphene, as well as the cauliflower-like morphology of  $Co_3O_4$ , can inhibit the volume change and detachment of  $Co_3O_4$  particles more effectively and thus result in a better cyclic life.

## 4. Conclusions

In this work, a  $Co_3O_4/3D$  graphene composite was synthesized via a facile two-step synthesis route (heat reduction

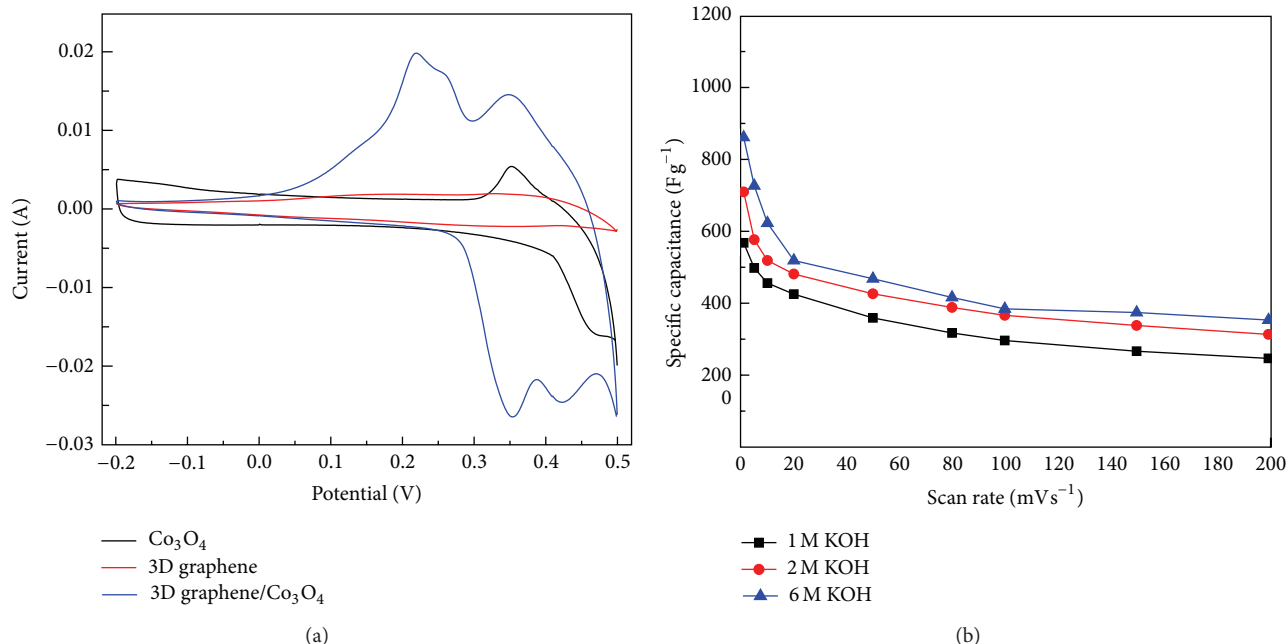


FIGURE 5: (a) CV curves of 3D graphene,  $\text{Co}_3\text{O}_4$ , and  $\text{Co}_3\text{O}_4/3\text{D graphene}$  composite at a scan rate of  $10 \text{ mV s}^{-1}$ , (b) the SC of  $\text{Co}_3\text{O}_4/3\text{D graphene}$  composite at various scan rates of 1, 5, 10, 20, 50, 80, 100, and  $200 \text{ mV s}^{-1}$  within the potential window of  $-0.2$ – $0.5 \text{ V}$ .

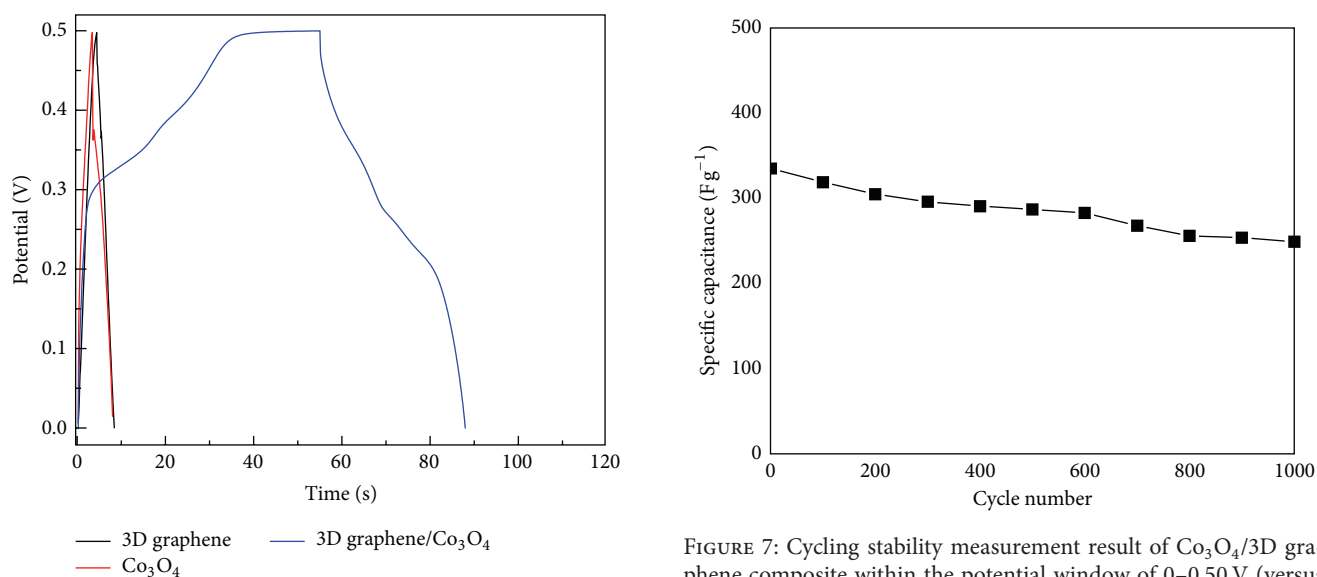


FIGURE 6: Galvanostatic charge/discharge curves of 3D graphene,  $\text{Co}_3\text{O}_4$ , and  $\text{Co}_3\text{O}_4/3\text{D graphene}$  composite at a current density of  $5 \text{ A g}^{-1}$ .

FIGURE 7: Cycling stability measurement result of  $\text{Co}_3\text{O}_4/3\text{D graphene}$  composite within the potential window of  $0$ – $0.50 \text{ V}$  (versus  $\text{Hg/HgO}$ ) at a current density of  $2 \text{ A g}^{-1}$ .

of GO and hydrothermal synthesis of  $\text{Co}_3\text{O}_4$ ). SEM and TEM images showed that, in the composite, many small nanoparticles with a size of  $10$ – $25 \text{ nm}$  assemble together to display cauliflower-like morphology. The supercapacitor performance of the composite, 3D graphene, and  $\text{Co}_3\text{O}_4$  was investigated and compared by CV and constant current charge-discharge tests. It was found that the composite

showed much larger specific capacitance than the sum of that of 3D graphene and  $\text{Co}_3\text{O}_4$ . Moreover, the composite exhibited better cycling stability. The good supercapacitor performance is ascribed to the combination of 3D graphene and cauliflower-like  $\text{Co}_3\text{O}_4$ , which leads to a strong synergistic effect to remarkably boost the utilization ratio of  $\text{Co}_3\text{O}_4$  and graphene. The cauliflower-like  $\text{Co}_3\text{O}_4/3\text{D graphene}$  composite is believed to be a promising electrode material for supercapacitors.

TABLE 1: SC values ( $\text{F g}^{-1}$ ) of  $\text{Co}_3\text{O}_4/3\text{D}$  graphene composite at different current density in different concentration electrolytes within the potential window of 0–0.5 V.

	1 M KOH	2 M KOH	6 M KOH
$0.5 \text{ A g}^{-1}$	402	458	522
$1 \text{ A g}^{-1}$	380	431	478
$5 \text{ A g}^{-1}$	337	367	396
$10 \text{ A g}^{-1}$	296	338	363

## Conflict of Interests

The authors declare that there is no conflict of interests regarding the publication of this paper.

## Acknowledgments

The authors are grateful for the financial support by One Hundred Talent Program of Chinese Academy of Sciences as well as by the NSFC (51302264) of China.

## References

- [1] P. Simon and Y. Gogotsi, "Materials for electrochemical capacitors," *Nature Materials*, vol. 7, no. 11, pp. 845–854, 2008.
- [2] J. Yan, Z. Fan, W. Sun et al., "Advanced asymmetric supercapacitors based on  $\text{Ni}(\text{OH})_2/\text{graphene}$  and porous graphene electrodes with high energy density," *Advanced Functional Materials*, vol. 22, no. 12, pp. 2632–2641, 2012.
- [3] L. H. Bao, J. F. Zang, and X. D. Li, "Flexible  $\text{Zn}_2\text{SnO}_4/\text{MnO}_2$  core/shell nanocable-carbon microfiber hybrid composites for high-performance supercapacitor electrodes," *Nano Letters*, vol. 11, no. 3, pp. 1215–1220, 2011.
- [4] L. T. Lam and R. Louey, "Development of ultra-battery for hybrid-electric vehicle applications," *Journal of Power Sources*, vol. 158, no. 2, pp. 1140–1148, 2006.
- [5] M. Winter and R. J. Brodd, "What are batteries, fuel cells, and supercapacitors?" *Chemical Reviews*, vol. 104, pp. 4245–4269, 2004.
- [6] E. Faggioli, P. Rena, V. Danel, X. Andrieu, R. Mallant, and H. Kahlen, "Supercapacitors for the energy management of electric vehicles," *Journal of Power Sources*, vol. 84, no. 2, pp. 261–269, 1999.
- [7] R. Tummala, R. K. Guduru, and P. S. Mohanty, "Nanostructured  $\text{Co}_3\text{O}_4$  electrodes for supercapacitor applications from plasma spray technique," *Journal of Power Sources*, vol. 209, pp. 44–51, 2012.
- [8] Y. Hou, Y. Cheng, T. Hobson, and J. Liu, "Design and synthesis of hierarchical  $\text{MnO}_2$  nanospheres/carbon nanotubes/conducting polymer ternary composite for high performance electrochemical electrodes," *Nano Letters*, vol. 10, no. 7, pp. 2727–2733, 2010.
- [9] B. E. Conway, "Transition from 'supercapacitor' to 'battery' behavior in electrochemical energy storage," *Journal of the Electrochemical Society*, vol. 138, no. 6, pp. 1539–1548, 1991.
- [10] T. Xue, C.-L. Xu, D.-D. Zhao, X.-H. Li, and H.-L. Li, "Electrodeposition of mesoporous manganese dioxide supercapacitor electrodes through self-assembled triblock copolymer templates," *Journal of Power Sources*, vol. 164, no. 2, pp. 953–958, 2007.
- [11] B. E. Conway, V. Birss, and J. Wojtowicz, "The role and utilization of pseudocapacitance for energy storage by supercapacitors," *Journal of Power Sources*, vol. 66, no. 1–2, pp. 1–14, 1997.
- [12] J. P. Zheng, P. J. Cygan, and T. R. Jow, "Hydrous ruthenium oxide as an electrode material for electrochemical capacitors," *Journal of the Electrochemical Society*, vol. 142, no. 8, pp. 2699–2703, 1995.
- [13] J. Chang, W. Lee, R. S. Mane, B. W. Cho, and S.-H. Han, "Morphology-dependent electrochemical supercapacitor properties of indium oxide," *Electrochemical and Solid-State Letters*, vol. 11, no. 1, pp. A9–A11, 2008.
- [14] I. Jung, J. Choi, and Y. Tak, "Nickel oxalate nanostructures for supercapacitors," *Journal of Materials Chemistry*, vol. 20, no. 29, pp. 6164–6169, 2010.
- [15] O. Ghodbane, J.-L. Pascal, and F. Favier, "Microstructural effects on charge-storage properties in  $\text{MnO}_2$ -based electrochemical supercapacitors," *ACS Applied Materials & Interfaces*, vol. 1, no. 5, pp. 1130–1139, 2009.
- [16] V. R. Shinde, S. B. Mahadik, T. P. Gujar, and C. D. Lokhande, "Supercapacitive cobalt oxide ( $\text{Co}_3\text{O}_4$ ) thin films by spray pyrolysis," *Applied Surface Science*, vol. 252, no. 20, pp. 7487–7492, 2006.
- [17] J. Yan, T. Wei, W. Qiao et al., "Rapid microwave-assisted synthesis of graphene nanosheet/ $\text{Co}_3\text{O}_4$  composite for supercapacitors," *Electrochimica Acta*, vol. 55, no. 23, pp. 6973–6978, 2010.
- [18] R. K. Selvan, I. Perelshtein, N. Perkas, and A. Gedanken, "Synthesis of hexagonal-shaped  $\text{SnO}_2$  nanocrystals and  $\text{SnO}_2/\text{C}$  nanocomposites for electrochemical redox supercapacitors," *The Journal of Physical Chemistry C*, vol. 112, no. 6, pp. 1825–1830, 2008.
- [19] J. P. Zheng and T. R. Jow, "High energy and high power density electrochemical capacitors," *Journal of Power Sources*, vol. 62, no. 2, pp. 155–159, 1996.
- [20] J. P. Zheng, J. Huang, and T. R. Jow, "The limitations of energy density for electrochemical capacitors," *Journal of the Electrochemical Society*, vol. 144, no. 6, pp. 2026–2031, 1997.
- [21] G. P. Wang, L. Zhang, and J. J. Zhang, "A review of electrode materials for electrochemical supercapacitors," *Chemical Society Reviews*, vol. 41, no. 2, pp. 797–828, 2012.
- [22] M.-J. Deng, F.-L. Huang, I.-W. Sun, W.-T. Tsai, and J.-K. Chang, "An entirely electrochemical preparation of a nanostructured cobalt oxide electrode with superior redox activity," *Nanotechnology*, vol. 20, no. 17, Article ID 175602, 2009.
- [23] Y. Liu, W. W. Zhao, and X. G. Zhang, "Soft template synthesis of mesoporous  $\text{Co}_3\text{O}_4/\text{RuO}_2 \cdot x\text{H}_2\text{O}$  composites for electrochemical capacitors," *Electrochimica Acta*, vol. 53, no. 8, pp. 3296–3304, 2008.
- [24] C. Lin, J. A. Ritter, and B. N. Popov, "Characterization of sol-gel-derived cobalt oxide xerogels as electrochemical capacitors," *Journal of the Electrochemical Society*, vol. 145, no. 12, pp. 4097–4103, 1998.
- [25] K. S. Novoselov, A. K. Geim, S. V. Morozov et al., "Electric field in atomically thin carbon films," *Science*, vol. 306, no. 5696, pp. 666–669, 2004.
- [26] Y. Wang, Z. Q. Shi, Y. Huang et al., "Supercapacitor devices based on graphene materials," *The Journal of Physical Chemistry C*, vol. 113, no. 30, pp. 13103–13107, 2009.
- [27] Y. Wang, C. Guan, K. Wang, C. X. Guo, and C. M. Li, "Nitrogen, hydrogen, carbon dioxide, and water vapor sorption

- properties of three-dimensional graphene,” *Journal of Chemical and Engineering Data*, vol. 56, no. 3, pp. 642–645, 2011.
- [28] Y. Wang, C. X. Guo, J. Liu, T. Chen, H. Yang, and C. M. Li, “CeO<sub>2</sub> nanoparticles/graphene nanocomposite-based high performance supercapacitor,” *Dalton Transactions*, vol. 40, no. 24, pp. 6388–6391, 2011.
- [29] X. C. Dong, J. X. Wang, J. Wang et al., “Supercapacitor electrode based on three-dimensional graphene–polyaniline hybrid,” *Materials Chemistry and Physics*, vol. 134, no. 2-3, pp. 576–580, 2012.
- [30] C. X. Guo, F. P. Hu, X. W. Lou, and C. M. Li, “High-performance biofuel cell made with hydrophilic ordered mesoporous carbon as electrode material,” *Journal of Power Sources*, vol. 195, no. 13, pp. 4090–4097, 2010.
- [31] W. Zhou, J. Liu, T. Chen et al., “Fabrication of Co<sub>3</sub>O<sub>4</sub>-reduced graphene oxide scrolls for high-performance supercapacitor electrodes,” *Physical Chemistry Chemical Physics*, vol. 13, no. 32, pp. 14462–14465, 2011.
- [32] A. Pendashteh, M. F. Mousavi, and M. S. Rahmanifar, “Fabrication of anchored copper oxide nanoparticles on graphene oxide nanosheets via an electrostatic coprecipitation and its application as supercapacitor,” *Electrochimica Acta*, vol. 88, pp. 347–357, 2013.
- [33] S. X. Deng, D. Sun, C. H. Wu et al., “Synthesis and electrochemical properties of MnO<sub>2</sub> nanorods/graphene composites for supercapacitor applications,” *Electrochimica Acta*, vol. 111, pp. 707–712, 2013.
- [34] X. Dai, W. Shi, H. Cai, R. Li, and G. Yang, “Facile preparation of the novel structured  $\alpha$ -MnO<sub>2</sub>/graphene nanocomposites and their electrochemical properties,” *Solid State Sciences*, vol. 27, pp. 17–23, 2014.
- [35] X.-C. Dong, H. Xu, X.-W. Wang et al., “3D graphene-cobalt oxide electrode for high-performance supercapacitor and enzymeless glucose detection,” *ACS Nano*, vol. 6, no. 4, pp. 3206–3213, 2012.
- [36] X. Wang, S. Liu, H. Wang, F. Tu, D. Fang, and Y. Li, “Facile and green synthesis of Co<sub>3</sub>O<sub>4</sub> nanoplates/graphene nanosheets composite for supercapacitor,” *Journal of Solid State Electrochemistry*, vol. 16, no. 11, pp. 3593–3602, 2012.
- [37] G. He, J. Li, H. Chen et al., “Hydrothermal preparation of Co<sub>3</sub>O<sub>4</sub>@graphene nanocomposite for supercapacitor with enhanced capacitive performance,” *Materials Letters*, vol. 82, pp. 61–63, 2012.
- [38] Y. Wang, J. H. Liu, K. Wang, T. Chen, X. Tan, and C. M. Li, “Hydrogen storage in Ni-B nanoalloy-doped 2D graphene,” *International Journal of Hydrogen Energy*, vol. 36, no. 20, pp. 12950–12954, 2011.
- [39] J. Li, H. Xie, Y. Li, J. Liu, and Z. Li, “Electrochemical properties of graphene nanosheets/polyaniline nanofibers composites as electrode for supercapacitors,” *Journal of Power Sources*, vol. 196, no. 24, pp. 10775–10781, 2011.
- [40] S.-J. Bao, C. M. Li, C.-X. Guo, and Y. Qiao, “Biomolecule-assisted synthesis of cobalt sulfide nanowires for application in supercapacitors,” *Journal of Power Sources*, vol. 180, no. 1, pp. 676–681, 2008.
- [41] R. Z. Ma, J. Liang, B. Q. Wei, B. Zhang, C. L. Xu, and D. H. Wu, “Study of electrochemical capacitors utilizing carbon nanotube electrodes,” *Journal of Power Sources*, vol. 84, no. 1, pp. 126–129, 1999.